1994

Aluminum, Silicon, Phosphorus And Sulfur K- And L-edge X-ray Absorption Spectroscopy Of Minerals And Glasses: Applications In Mineralogy And Geochemistry

Dien Li

Al, Si, P and S K- and L-edge X-ray Absorption Spectroscopy of Minerals and Glasses: Applications in Mineralogy and Geochemistry

by

Dien Li

Department of Chemistry

Submitted in partial fulfilment
of the requirements for the degree of
Doctor of Philosophy

Faculty of Graduate Studies
The University of Western Ontario
London, Ontario

July 1994

ISBN 0-315-93186-8

ABSTRACT

Al, Si, P and S K- and L-edge X-ray absorption near-edge structure (XANES) spectra of a large selection of metal sulfide and silicate minerals and some glasses have been studied using monochromatized synchrotron radiation.

S K- and L-edge XANES spectra of metal sulfides are qualitatively interpreted based on MO/energy band models, reveal the DOS of unoccupied S s-, p- and d-like states, provide new insight into the electronic structure of the conduction band, and demonstrate the bonding interaction of metal d electrons with S 3s and 3p electrons. The S K- and L-edges shift to high energy with increase in oxidation state of sulfur from sulfides to sulfur, sulfite and sulfates, and also with increase in energy gap and decrease in reflectivity of metal sulfides.

Si K- and L-edge and Al K-edge XANES of silica polymorphs, silicate and aluminosilicate minerals are interpreted based on the qualitative MO calculation of MO_4 and MO_6 ($M = Si^{4+}$ and Al^{3+}) clusters, multiple scattering effects, and comparison with the spectra of model gas phase molecules. Four- and six-coordinated Si and Al in minerals can be unambiguously distinguished based on the chemical shift of the edge features. The chemical shifts of the Si K- and L-edges and Al K-edge also correlate with the polymerization of the MO_4 clusters, substitution of Al for Si, M-O bond distance, bond valence, distortion of the polyhedra and cation compositions of the second coordination shell. Al K-edge spectra can now be used to determine the distribution of Al between tetrahedral and octahedral sites in minerals and glasses.

Precious opals are shown to contain structural units of amorphous and crystalline cristobalite, the proportions of which can be estimated semi-quantitatively, using the Si K- and L-edge spectra. Si and P K- and L-edge XANES spectra of SiO_2-P_2O_5 and Na_2O-SiO_2-P_2O_5 glass systems with $P_2O_5 \leq 30$ mol% show that Na_2O depolymerizes silicate melts, PO_4^{3-} copolymerizes the silicate melts; and the speciation of P in these systems are monophosphate, pyrophosphate and metaphosphates with different chain length, depending on the content of P_2O_5.

ACKNOWLEDGEMENTS

I sincerely thank my research supervisor, Professor G.M. Bancroft, for his endless guidance, support, encouragement and enthusiasm throughout my Ph.D. program.

I thank Professor M.E. Fleet, for his guidance and help, particularly in polishing my English; Professor M.J. Stillman, for his attention to the progress of my research; Dr. M. Kasrai, for his assistance with experimental aspects; and Professor T.K. Sham and Dr. B.X. Yang, for their advice for my research and my carrier.

I appreciate the technical assistance from B.X. Yang, X.H. Feng and K.H. Tan in the Canadian Synchrotron Radiation Facility, and other staff in the Synchrotron Radiation Center, University of Wisconsin.

I would like to thank D. Dillon of the Department of Earth Sciences, UWO; and F. Wicks, R. Ramik and T. Ottawa of the Department of Mineralogy, Royal Ontario Museum; and Professor Lin-gun Liu of Research School of Earth Sciences, Australian National University for the provision of samples, J. Forth, Y.C. Chen and R.L. Barnett of Department of Earth Sciences, UWO; Y. Pan of Department of Geological Sciences, University of Saskatchewan for their assistance in making thin sections, collecting powder x-ray diffraction spectra and electron microprobe analysis, respectively.

I would like to acknowledge the help and friendship of other members of the Chemistry Department and fellow graduate students: John Bozek, Jeff Cutler, Marina Fuller, Zigi Gui, Yongfeng Hu, Detong Jiang, Jim Johnson, Stephan Knipe, Xiaorong Li, Zhifeng Liu, Leone Maddox, Jay Mycroft, Jamie Price, Mike Scaini, Doug Sutherland, Zhanfeng Yin, Jianzhang Xiong, and the assistance of Edna Dell and Cheryl O'Meara.

Finally, special thanks must go to my parents, brothers and sisters for their love, understanding and encouragement; to my former mentor, Professor Mingsheng Peng, for her guidance, encouragement and inspiration of my research interests; to my former teachers, Manjun Huang and Zhongyang He, for their encouragement. I dedicated this work to my mother, Jinlian Wang, my late father, Hechun Li, and my late stepfather, Debao Zhang. Of course, my most special thanks must go to my wife, Yan Qiu, for her love and encouragement.

TABLE OF CONTENTS

CERTIFICATE OF EXAMINATION ii

ABSTRACT iii

ACKNOWLEDGEMENTS iv

TABLE OF CONTENTS v

LIST OF FIGURES ix

LIST OF TABLES xiii

CHAPTER 1 - Introduction 1

1.1 X-ray Absorption Spectroscopy (XAS) 1

1.1.1 X-ray Absorption Near-edge Structure (XANES) 1

1.1.2 Extended X-ray Absorption Fine Structure (EXAFS) 2

1.2 Experimental 4

1.2.1 Synchrotron Radiation and the Storage Ring 4

1.2.2 Double Crystal Monochromator (DCM) 4

1.2.3 Mark IV Grasshopper Beamline 5

1.2.4 Total Electron Yield (TEY) Detection 6

1.3 Applications of XAS in Mineralogy and Geochemistry 9

1.4 Significance, Purposes and Outline of the Thesis 10

1.4.1 Significance of this Study 10

1.4.2 Purposes and Outline of this Thesis 11

1.5 References 13

CHAPTER 2 - S K and L-edge XANES of Zn, Cd and Hg Monosulfides 17

2.1 Introduction 17

2.2 Experimental 18

2.3 Results and Discussion 18

2.3.1 Near-edge Features and Electronic Structure 21

2.3.2 Post-edge XANES Features 32

2.4 Conclusions 36

2.5 References 36

CHAPTER 3 - S K- and L-edge XANES and Electronic Structure of Copper and/or Iron Sulfide Minerals 40
3.1 Introduction 40
3.2 Experimental 41
3.3 Results and Spectral Assignments 43
3.3.1 Chalcopyrite, Cubanite and Bornite 43
3.3.2 Chalcocite, Covellite and Enargite 48
3.3.3 Stannite and Tetrahedrite 52
3.3.4 Carrollite and Linnaeite 56
3.3.5 Pyrrhotite and Pyrite 58
3.4 Discussion 63
3.5 Conclusions 66
3.6 References 66
CHAPTER 4 - Polarized X-ray Absorption Spectroscopy and the Electronic Structure of Molybdenite: 2H-MoS_2 70
4.1 Introduction 70
4.2 Experimental 71
4.3 Results and Discussion 72
4.3.1 Interpretation of XANES 72
4.3.2 Polarized XANES 75
4.4 Conclusions 84
4.5 References 84
CHAPTER 5 - Applications of S K- and L-edge X-ray Absorption Spectroscopy in Mineralogy and Geochemistry 87
5.1 Introduction 87
5.2 Experimental 87
5.3 Results and Discussion 88
5.3.1 S K- and L-edge XANES Spectra of Sulfates 88
5.3.2 Chemical Shift in S K- and L-edges and Oxidation State of Sulfur 91
5.3.3 Chemical Shift in S K- and L-edges versus Energy Gap (E_g) and

Reflectivity of Metal Sulfides 96
5.3.4 EXAFS Analysis of Some Sulfide Minerals of Known Crystal Structure 99
5.4 Conclusions 103
5.5 References 103
CHAPTER 6 - X-ray Absorption Spectroscopy of SiO_2 Polymorphs: Structural Characterization of Opal 105
6.1 Introduction 105
6.2 Experimental 106
6.3 Results and Discussion 107
6.3.1 Interpretation of XANES Spectra 107
6.3.2 XANES Spectra and Crystal Chemistry 113
6.3.3 Structural Characterization of Opal 118
6.4 Conclusions 123
6.5 References 124
CHAPTER 7 - Si K-edge XANES Spectra of Silicate Minerals 127
7.1 Introduction 127
7.2 Experimental 127
7.3 Results and Discussion 128
7.3.1 Interpretation of Si K-edge XANES spectra 128
7.3.2 Chemical Shift of Si K-edge versus Polymerization 131
7.3.3 Chemical Shift of Si K-edge versus Substitution of Al for Si . . . 137
7.3.4 Chemical Shift of Si K-edge versus d_{Si-O} and s_{Si-O} 137
7.3.5 Chemical Shift of Si K-edge Cations in the More Distant Atom Shells 137
7.3.6 Comparison of Si K-edge XANES technique with ^{29}Si NMR and XPS 140
7.4 Conclusions 141
7.5 References 142
CHAPTER 8 - Al K-edge XANES Spectroscopy of Aluminosilicates 144

8.1 Introduction 144
8.2 Experimental 146
8.3 Results and Discussion 147
8.3.1 Al K-edge XANES of 4-coordinated Al (Al^{IV}) 147
8.3.2 Al K-edge XANES of 6-coordinated Al (Al^{VI}) 150
8.3.3 Chemical Shift of Al K-edge and coordination number of Al . . . 154
8.3.4 Chemical shift of Al K-edge versus d_{Al-O}, s_{Al-O} Δ_{Al-O} and Compositions 161
8.3.5 The Intensity of Al K-edge and the Content of Al 161
8.4 Conclusions 164
8.5 References 165
CHAPTER 9 - Local Structures of Silicon and Phosphorus in Glasses 167
9.1 Introduction 167
9.2 Experimental 168
9.3 Results and Discussion 168
9.3.1 Interpretation of Spectra 168
9.3.2 Structure of SiO_2-P_2-O_5 Glasses 173
9.3.3 Structure of Na_2O-SiO_2-P_2O_5 Glasses 178
9.4 Conclusions 183
9.5 References 185
VITA 188

List of Figures

Figure 1.2.1 Schematic diagrams showing the core-hole production and annihilation processes when x-rays interact with a target sample 7
Figure 1.2.2 Si K-edge XANES spectra of a Si (100) film collected by TEY (solid line) and transmission detection (dash line) modes 8
Figure 2.3.1 S K-edge XANES spectra of sphalerite, wurtzite, greenockite, metacinnabar and cinnabar 19
Figure 2.3.2 S L-edge XANES spectra of sphalerite, wurtzite, greenockite, metacinnabar and cinnabar 20
Figure 2.3.3 Near-edge structures of S K- and L-edge, Fe and Zn K-edge XANES spectra of sphalerite 23
Figure 2.3.4 S K- and L-edge XANES spectra of synthetic ZnS and (Zn,Fe)S samples containing FeS up to 40.1 mol% 27
Figure 2.3.5 Near-edge structures of S K- and L-edge XANES spectra of sphalerite, wurtzite, greenockite, metacinnabar and cinnabar 30
Figure 2.3.6 Correlations of post-edge features of S K- and L-edge XANES with reciprocal interatomic and lattice plane distances for sphalerite, wurtzite, greenockite and metacinnabar 34
Figure 3.3.1 S K- and L-edge, and Fe K-edge XANES spectra of chalcopyrite . . 44
Figure 3.3.2 S K- and L-edge XANES spectra of chalcopyrite, cubanite and bornite 46
Figure 3.3.3 S K- and L-edge XANES spectra of chalcocite, covellite and enargite 50
Figure 3.3.4 S K- and L-edge XANES spectra of stannite and tetrahedrite 53
Figure 3.3.5 S K- and L-edge XANES spectra of carrollite, together with Cu and Co K-edge XANES spectra 57
Figure 3.3.6 S K and L-edge XANES spectra of pyrrhotite, together with Fe K-edge spectra 59
Figure 3.3.7 S K- and L-edge XANES spectra of pyrite, together with

Fe K-edge spectra 61
Figure 3.4.1 Qualitative energy band scheme of Cu and Cu-Fe sulfides 64
Figure 4.2.1 Geometrical scheme for polarized XANES measurements of molybdenite 72
Figure 4.3.1 S K- and L-edge, Mo, L_2- and L_3-edge spectra of molybdenite compared with XPS and XES spectra 73
Figure 4.3.2 Polarized S K-edge XANES spectra of molybdenite 77
Figure 4.3.3 Deconvolution of peak a into peaks a_1 and a_2 in the polarized S K-edge spectra of molybdenite 78
Figure 4.3.4 Variation of the area ratio of peaks a_1 and a_2 in the S K-edge spectra of MoS_2 with $\cos^2\theta$ 79
Figure 4.3.5 Polarized S L-edge XANES spectra of molybdenite 81
Figure 4.3.6 Polarized Mo L_3-edge and L_2-edge XANES spectra of molybdenite . 82
Figure 5.3.1 S K- and L-edge XANES spectra of $MgSO_4 \cdot 2H_2O$, gypsum, anhydrite, celestite and barite 89
Figure 5.3.2 Correlation of S K- and L-edges of sulfides, sulfur, sulfite and sulfates 93
Figure 5.3.3 Correlations of S K- and L-edges with oxidation state of sulfur species 93
Figure 5.3.4 Correlations of S K- (a) and L-edges (b) with the respective S 1s and 2p BE for $CuFeS_2$, ZnS, FeS_2, native sulfur, $FeSO_3$ and $FeSO_4$ 95
Figure 5.3.5 Correlation of S K- and L-edges of metal sulfide minerals 96
Figure 5.3.6 Correlations of S K- and L-edges with the E_g of metal sulfides 97
Figure 5.3.7 Correlation of S K-edge with reflectivity of metal sulfides 98
Figure 5.3.8 S K-edge EXAFS analysis of sphalerite 101
Figure 6.3.1 Si K- and L-edge XANES spectra of α-quartz and stishovite 108
Figure 6.3.2 Si K-edge XANES spectra of α-quartz, cristobalite, coesite, stishovite and opals 114
Figure 6.3.3 Si L-edge XANES spectra of α-quartz, cristobalite, coesite, stishovite and opals 116

Figure 6.3.4 Si K-edge XANES spectra of cristobalite and a-SiO_2, together with the composite spectra for different proportions of cristobalite and a-SiO_2 120
Figure 6.3.5 Si L-edge XANES spectra of cristobalite and a-SiO_2, together with the composite spectra for different proportions of cristobalite and a-SiO_2 121
Figure 6.3.6 The Si K- and L-edge XANES spectra of two opal samples compared with the composite spectra of different proportions of cristobalite and a-SiO_2 122
Figure 7.3.1 Si K-edge XANES spectra of some representative silicate minerals with different degrees of polymerization 129
Figure 7.3.2 Si K-edge of representative silicate minerals on an expanded scale . 130
Figure 7.3.3 Variations of Si K-edge positions with polymerization and O:Si ratio of silicates 134
Figure 7.3.4 Shifts of Si K-edge to lower energy with substitution of Al for Si for Q^3 and Q^4 silicates 135
Figure 7.3.5 Correlations of Si K-edge with Si-O bond distance (d_{Si-O}) and Si-O bond valence (s_{Si-O}) 136
Figure 7.3.6 Si K-edge shift and substitution of Al for Mg in octahedral sites in various Q^2 and Q^3 structures 138
Figure 7.3.7 Correlation of Si K-edge (eV) with ^{29}Si MAS NMR chemical shift δ (ppm) 139
Figure 7.3.8 Correlation Si K-edge (eV) and Si 1s BE (eV). The Si 1s BE is calculated by adding the Si 2p BE and Si $K\alpha_1$ x-ray emission energy 139
Figure 8.3.1 Al K-edge XANES spectra of anorthite, microcline and biotite, compared to Si K-edge spectra of these minerals and α-quartz 148
Figure 8.3.2 Al K-edge XANES spectra of some representative aluminosilicates containing Al^{VI}, compared to Si K-edge spectrum of stishovite 152
Figure 8.3.3 Al K-edge XANES spectra of microcline (Al^{IV} only), andalusite (both Al^{V} and Al^{VI}), corundum (Al^{VI} only) and omphacite, sillimanite and muscovite (both Al^{IV} and Al^{VI}) 155
Figure 8.3.4 Chemical shifts of Al K-edges for all studied aluminosilicates with

coordination number of Al 157
Figure 8.3.5 Correlation of Al K-edges with the MAS NMR chemical shift for Al^{IV}, Al^{V} and Al^{VI} in aluminosilicates 159
Figure 8.3.6 Correlations of Al K-edge with d_{Al-O}, s_{Al-O} and Δ_{Al-O} of aluminosilicates 160
Figure 8.3.7 Correlations of the intensity of Al K-edge with the content of Al in octahedral and tetrahedral sites 162
Figure 9.3.1 Si K- and L-edge XANES spectra of c-SiP_2O_7 and SiO_2-P_2O_5 glass . 169
Figure 9.3.2 P K- and L-edge XANES spectra of c-SiP_2O_7 and SiO_2-P_2O_5 glass . . 172
Figure 9.3.3 The near-edge features in Si K- and L-edge XANES spectra of SiO_2-P_2O_5 glasses 174
Figure 9.3.4 P L-edge spectra of SiO_2-P_2O_5 glasses, compared with that of c-SiP_2O_7 177
Figure 9.3.5 The near-edge features in Si K- and L-edge XANES spectra of Na_2O-SiO_2-P_2O_5 glasses 180
Figure 9.3.6 P L-edge spectra of Na_2O-SiO_2-P_2O_5 glasses 181
Figure 9.3.7 Composite Si K-edge spectra of Si^{IV} and Si^{VI}, simulated with different proportion of c-SiP_2O_7 and SiO_2-P_2O_5 containing Si^{IV} 182

List of Tables

Table 2.3.1 S K- and L-edge features and qualitative assignments of Zn, Cd and Hg sulfides 25

Table 2.3.2 The post-edge features of S K- and L-edge XANES of sphalerite, wurtzite, greenockite and metacinnabar 35

Table 3.2.1 Occurrences and chemical compositions of copper sulfides 42

Table 3.3.1 S K- and L-edge XANES of chalcopyrite, cubanite and bornite . . . 47

Table 3.3.2 S K- and L-edge XANES of chalcocite, covellite and enargite 51

Table 3.3.3 S K- and L-edge XANES of stannite, tetrahedrite and carrollite . . . 54

Table 5.3.1 S K- and L-edge XANES spectra of some sulfates 90

Table 5.3.2 S K- and L-edges, energy gap and reflectivity of sulfides 92

Table 5.3.3 S K-edge EXAFS analysis of sphalerite, chalcopyrite and stannite . . 102

Table 6.3.1 Si K- and L-edge XANES of SiO_2 polymorphs 109

Table 6.3.2 Si K- and L-edge XANES and crystal chemical parameters of SiO_2 polymorphs 118

Table 7.3.1 Si K-edge XANES and crystal chemical parameters of silicates . . . 132

Table 8.2.1 Electron microprobe analyses of aluminosilicate minerals 145

Table 8.3.1 Assignments of Al K-edge XANES of aluminosilicates containing 4-coordinated Al (Al^{IV}) 149

Table 8.3.2 Assignments of Al K-edge XANES of representative aluminosilicates containing 6-coordinated Al (Al^{IV}) 153

Table 8.3.3 Al K-edge and crystal chemical parameters, NMR δ and the content of Al (wt%) of aluminosilicates 156

Table 9.3.1 Assignments for Si K- and L-edge spectra of c-SiP_2O_7 and SiO_2-P_2O_5 glasses 170

Table 9.3.2 Si K- and L-edges, P L-edge and chemical composition of glasses . . 175

CHAPTER 1

Introduction

1.1 X-ray Absorption Spectroscopy (XAS)

X-ray absorption spectroscopy measures the absorbance of x-rays by matter (gas, liquid or solid) as a function of photon energy. The absorption coefficient generally decreases with increase of photon energy until a certain critical energy is reached where the absorption coefficient increase abruptly, this discontinuity is called the absorption edge. The x-ray absorption spectrum is comprised of x-ray absorption near-edge structure (XANES), also called near edge x-ray absorption fine structure (NEXAFS), or traditionally the Kossel structure, that extends from the absorption edge to about 40 eV above the edge; and the extended x-ray absorption fine structure (EXAFS), traditionally called the Kronig structure, from about 40 eV to as much as 1000 eV above the edge.

1.1.1 X-ray Absorption Near-edge Structure (XANES)

XANES can usually be divided into two sub-regions: the near-edge, or main-edge region, up to about 10 eV above the edge, and the post-edge region from about 10 to 40 eV above the edge. The first XAS spectrum was reported by Fricke[1] and Hertz[2], and explained by Kossel[3]. The near-edge XANES concerns the study of electronic transitions from atomic inner shells of an absorber to unoccupied states. However, the actual physical origin of the absorption features in the near-edge region is different in different classes of materials: Rydberg states in atoms, bound valence states in molecules, core excitons in ionic crystals, many-body singularities in metals, and bound atom-like localized excitations in solids[4]. Theoretically the near-edge features, even for a very simple system, are not fully understood.

Basically, there are two complementary interpretations for XANES features. One is the molecular orbital (MO) interpretation[5,6], which assigns the XANES features to electron transitions from an inner shell of an absorber atom to antibonding orbitals. This explanation is readily accepted by chemists, even though physically there are no discrete energy levels in the continuum. From this point of view, the XANES features can provide information on the absorber-ligand bonding and electronic structure. Nefedov[7] and Dehmer[8] were the first to assign XANES features to "inner well resonances" induced by an electronegative potential barrier on the first-neighbor atoms. The other interpretation is multiple scattering (MS) theory[9-11], in which XANES features arise from the strong MS of outgoing photoelectrons with moderate kinetic energy from atoms surrounding the absorber. This MS process even involves next nearest-neighbor atoms extending beyond the first shell of ligands. Therefore, XANES features are sensitive to the geometrical arrangement of the first and more distant neighbor shells around the central absorber, and can provide information on site geometry, bond angle, and even bond distance. In order to obtain information on the electronic and local structure from XANES, the spectra must be collected in high-resolution mode with high intensity incident radiation. Hence, XANES studies have benefited greatly from the advances in synchrotron radiation sources.

1.1.2 Extended x-ray absorption fine structure (EXAFS)

EXAFS refers to weak oscillations of the final state wave function of the photoelectron caused by backscattering from the surrounding atoms[12], as a result of interference between the wave functions of the outgoing photoelectron and backscattered electron by the surrounding atoms. Kronig[13] first attempted an explanation of EXAFS in condensed matter, that depended explicitly on the long-range order (LRO) in solids. This LRO theory was fundamentally incorrect; however, it took about 40 years for this to be appreciated[14].

Kronig[15] also germinated the idea of short-range order (SRO) theory to explain EXAFS in molecules. Peterson[16] introduced the idea of adding the phase shift in the

photoelectron wave function caused by the potentials of the absorbing atom and the backscattering atom. Kostarev[17] extended the Kronig-Peterson SRO theory to condensed matter. Shiraiwa et al.[18] first accounted for the lifetime of the excited photoelectron and core-hole state through a mean free path. Shmidt[19] introduced a Debye-Waller factor to account for the effect of thermal disorder on the interference of the backscattered waves from ligand atoms. About 1966, Levy[20] calculated first coordination distances from the energy separation between the first EXAFS maximum and the next minimum. The real breakthrough in EXAFS theory happened when Sayers et al.[21] pointed out the Fourier transform of EXAFS data with respect to the photoelectron wave number will peak at distances corresponding approximately to the nearest-neighbor coordination shell of atoms. Lytle et al.[22] further developed this to make EXAFS a quantitative tool for determining short-range structural parameters. The EXAFS technique matured with the research work of Kincaid and Eisenberger[23], Ashley and Doniach[24], Lee and Pentry[25], and others.

In general, the current EXAFS theory has been established based on the following assumptions: (1) the photoelectron has a large enough kinetic energy so that it is assumed to be a free electron in the interatomic potential, (2) the process producing the oscillations is a single-electron process, (3) only single scattering is considered, so that EXAFS can be regarded as a simple sum of waves due to various types of neighboring atoms and the amplitude and phase shift function are transferable from model to unknown for each pair of absorber-ligands, even though some recent theoretical methods are now used to assess multiple scattering which can be important in the EXAFS region. EXAFS has now become a routine structural technique for determining the absorber-ligand bond distance, the coordination number of the absorber and the static and thermal disorder of the ligands (from the Debye-Waller factor)[12]. Of course, because the EXAFS signal is very weak, representing only a few percent of the total absorbance, and extends up to 1000 eV above the edge, a very bright and tunable incident light source is necessary for the collection of high-quality EXAFS data. Synchrotron radiation has been critical for making EXAFS analysis a routine structural technique experimentally.

1.2 Experimental

1.2.1 Synchrotron Radiation and the Storage Ring

Synchrotron radiation (SR) is electromagnetic radiation emitted by charged particles, such as electrons and positrons, moving in circular orbits with high velocities[26]. Modern dedicated SR is produced from a storage ring, a closed, continuous high-vacuum chamber threaded through various ring elements. The basic elements of a storage ring are: (1) bending magnets that make the electron travel in circular arcs producing SR; (2) special insertion devices, such as wigglers and undulators, that produce modified or enhanced SR; (3) a radio-frequency cavity and associated power supply, which replenishes the energy lost by the electron beam to the SR; (4) vacuum pumps to evacuate the chamber; and (5) an injector that permits electrons from a separate accelerator to be injected into the storage ring[27]. The SR has many outstanding properties[26-28]: very bright, broad spectral range from infrared to x-ray regions, high degree of collimation, strong polarization, pulse time structure, and high-vacuum environment, small source spot size and good stability. These features of SR have overcome the shortcomings of conventional x-ray sources, and revolutionized x-ray absorption spectroscopy. In fact, SR sources have provided tremendous impetus for the development of experimental methods in x-ray absorption spectroscopy.

The x-ray absorption spectra reported in this thesis were collected on a Double Crystal Monochromator (DCM) and Mark IV Grasshopper grazing incidence beamlines, which are affiliated with Canadian Synchrotron Radiation Facility (CSRF), and accommodated on the Aladdin storage ring, Synchrotron Radiation Center (SRC), University of Wisconsin. The Aladdin storage ring is operated at either 800 meV with current from about 60 to 180 mA, or 1 GeV with current from 40 to 80 mA.

1.2.2 Double Crystal Monochromator (DCM)

The advent of SR has indeed brought forth revolutionary changes to XAS.

However, the changes took place much more rapidly in the hard x-ray region (5-22 KeV) than in the soft x-ray region ($\leq$ 4000 eV) due to the technical difficulties related to the stringent vacuum requirement in the lower energy region. The majority of XAS studies in mineralogy and geochemistry have involved the hard x-ray region. A recently constructed DCM beam line[29,30] covers the energy range of 1700-3500 eV using InSb (111) crystals as the monochromators, and provides a good opportunity to study Si, P, S and Cl K-edges, which are very important for studies of XAS in mineralogy and geochemistry. The DCM monochromator consists of two parallel InSb (111) crystals, which can rotate and translate mechanically. The SR beam is first monochromatized by the first InSb crystal in the DCM directly, and the second InSb crystal is used to maintain the monochromatized beam parallel to the incident SR beam direction. The monochromatized beam is then focused by a bent cylindrical mirror to the experimental target with a spot size less than 1.5x3 mm^2. Vertical collimation is obtained by narrowing down the entrance and exit apertures, at the expense of a lower photon flux. An electronic feedback system is employed to maintain the stability of the beam. The energy resolution of the DCM is about 0.8 eV at 1840 eV[29]. Also two α-quartz ($10\bar{1}0$) crystals, instead of InSb crystals, were used in the monochromator system to cover the energy range of 1500-1800 eV and collect Al K-edge XANES spectra. Al, Si, P and S K-edge XAS spectra reported in this thesis were taken on the DCM beam line using Total Electron Yield (TEY) at the chamber pressure of 10^{-6} Torr and room temperature.

1.2.3 Mark IV Grasshopper Beamline

The Mark IV Grasshopper beam line uses a grazing incidence monochromator with an 1800 grooves/mm grating covering the energy range from 50 to 800 eV[30], which covers the Al, Si, P, S and Cl L-edge regions. The basic working procedures for this beamline are: (1) a Mo mirror collects the SR beam from the storage ring and focuses it into the monochromator; (2) inside the monochromator, the SR beam is first focused by a mirror, then passes the entrance slit and impinges on the grating. The grating disperses the white light into its constituent wavelengths and the monochromatized beam

passes the exit slit and enters the experimental chamber for the data collection. The energy resolution of the Grasshopper beamline is about 0.1 eV at 100 eV. All L-edge spectra were taken using TEY at a room temperature and a chamber pressure of 10^{-8} torr.

1.2.4 Total Electron Yield (TEY) Detection

In general, when monochromatized x-rays interact with the target sample, a number of processes take place simultaneously. For example, as shown in Figure 1.2.1, when the energy, $h\upsilon$, of the incident x-ray photons is higher than the binding energy, E_b, of the inner shell electrons of the absorber atom, the inner shell electrons are excited to become photoelectrons with kinetic energy $E_k = h\upsilon - E_b$. In the de-excitation, or so-called core-hole annihilation, processes, the outer shell electrons will fill the hole created in the inner shell. The extra energy is released as the fluorescence emission (Figure 1.2.1b), or to excite the outer shell electrons, which are called Auger electrons (see Figure 1.2.1c). Moreover, the hole produced in the outer shell can further be filled by electrons from the more distant shells and the extra energy is used to excite the outer shell electrons, which are called secondary electrons (see Figure 1.2.1d).

Traditionally, x-ray absorption spectroscopy directly measures the intensity of the incident beam (I_0) and that of the transmitted beam (I). However, the preparation of ultrathin samples ($\sim$ 1000 Å thick) for XAS is a great challenge, particularly for solid samples like minerals and glasses. Therefore, indirect measurement techniques of absorption have been widely used. The fluorescence yield (I_f) is directly proportional to the number of absorption events for dilute samples, and I_f/I_0 is proportional to absorption coefficient, μ, although recent research work has shown that fluorecence yield for L-edge is not proportional to absorbance. However, for the element of interest which is concentrated, this proportionality changes. Thus, the fluorescence method is suitable to the study of dilute and small samples. The main disadvantage of this technique is that fluorescent yield is very small for the light elements, such as Si and Al, which have K-edge energy below 2000 eV. In addition, the Auger electron yield detection technique has also been used, especially for the XAS study of surfaces and interfaces.

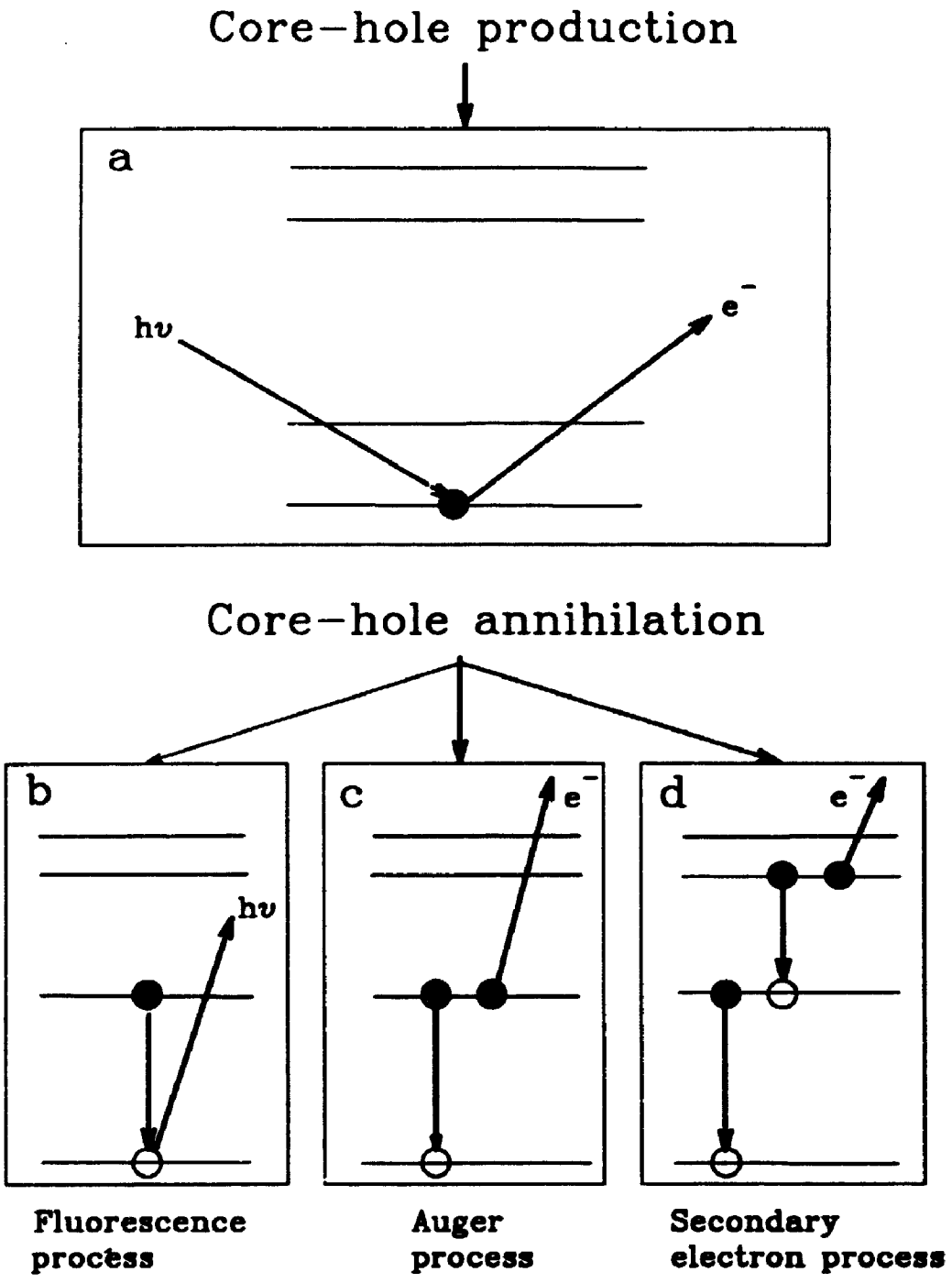

Figure 1.2.1 Schematic diagrams showing the core-hole production and annihilation processes when monochromatized x-rays interact with the target sample.

The other simple detection technique consists of collecting electrons of all energies from the samples. This technique is referred to as Total Electron Yield (TEY) However, the TEY signal is dominated by low energy electrons. The method is also very efficient, because of the large total count-rate, and provides structural information for absorber atoms in the top 20 Å of the samples. The disadvantage of TEY is the high background. The TEY signal is also directly proportional to the absorption coefficient. For example, Figure 1.2.2 shows the Si K-edge x-ray absorption spectra of a Si (100) film, collected by TEY (solid line) and transmission detection (dash line) modes. These two spectra were digitized from Yang et al.[29] and are almost identical. All the K and L-edge x-ray absorption spectra presented in this thesis were collected using TEY mode and synchrotron radiation, even though the fluorescence yield spectra, which are almost identical to the TEY spectra, were also collected for most samples investigated.

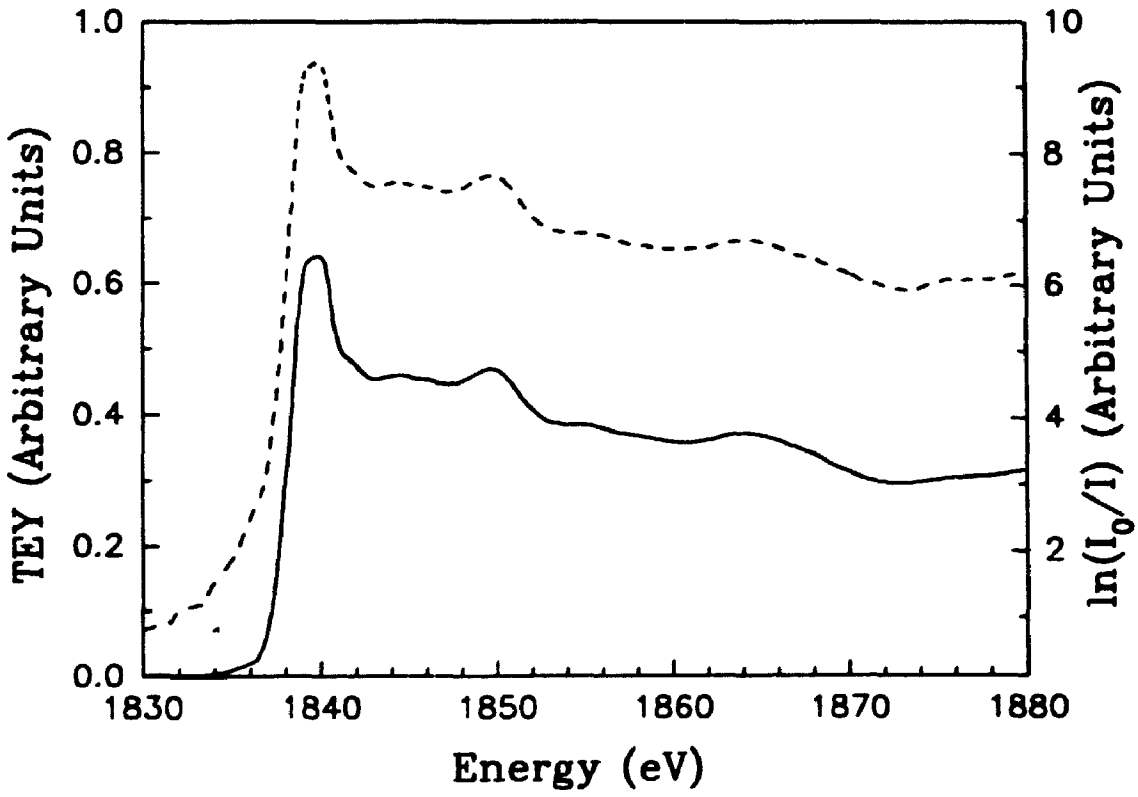

Figure 1.2.2 Si K-edge XANES spectra of Si (100) film collected by Total Electron Yield (TEY) (solid line) and transmission (dash line) detection modes.

1.3 Applications of XAS in Mineralogy and Geochemistry

Even though the first XAS was reported in the early 1920's, XAS was not as widely used as x-ray diffraction (XRD) in physics and chemistry, because of difficulties in theoretical interpretations, limitations of exciting light sources, and the indirect and implicit nature of the structural information obtained. In the 1970's, bright and polarized synchrotron radiation tunable over a large photon energy range became available for XAS measurements[31], and a short-range single-electron scattering theory for EXAFS was proposed[21,22]. Since then, XAS has been applied in biology and medical sciences, material sciences, mineralogy and geochemistry, as well as in physics and chemistry.

Most types of spectroscopy now used for mineralogical and geochemical studies have one or more severe limitations. For example, Mössbauer spectroscopy[32,33] is limited to specific nuclides, mainly ^{57}Fe and ^{119}Sn. Visible spectroscopy[34,35] requires that the species in question be colored. Electron paramagnetic resonance[36] requires unpaired electron spins, and so forth. In contrast with the other spectroscopic techniques, XAS has many advantages for mineralogical and geochemical studies. First, XAS is essentially not limited to specific elements, and can be used to study all the elements, except for H and He, in the periodic table. Second, XAS is also not limited to specific states of materials studied, and can be used to investigate any kind of materials — gases, liquids and crystalline or amorphous solids. Third, XAS can provide new information and information compatible with other techniques. Meanwhile, XAS using synchrotron radiation in structural studies is element-specific, it can select the components of density of states (DOS) to be studied, and allows fast acquisition of high-resolution spectra over a wide energy range.

Applications of XAS in the earth sciences were initiated and have been developed mainly by two groups, one in Stanford University, led by Professor G.E. Jr. Brown and the other in the University of Paris, led by Professor G. Calas. Even though XAS using synchrotron radiation has been applied in the earth sciences for only about 15 years, the advantages of XAS and the availability of synchrotron facilities around the world have led to its widespread application in mineralogical and geochemical studies. There are

several excellent reviews on the applications of XAS to mineralogical and geochemical problems[37-43]. These studies include the following aspects: (1) determination of local structure and cation oxidation states in silicate minerals[44-49], (2) short-range order of cations in silicate minerals and clays[50,51], (3) site occupancy and oxidation states, electronic structure and bonding in metal sulfide minerals[52-55], (4) local structure of highly disordered materials, such as glasses[56-58], melts[59,60], gels[61] and aqueous solution[62], (5) nucleation and crystallization processes[63], (6) adsorption of cations on mineral surfaces and mineral-water interfaces[64-68].

1.4 Significance, Purposes and Outline of the Thesis

1.4.1 Significance of this Study

Most of the previous XAS studies in earth sciences have involved hard x-rays and the metal K-edge EXAFS spectra. Al, Si, P and S K- and L-edge XANES of geological materials (the subject of this thesis) have been seldom reported.

The metal sulfides, silicate minerals and glasses we are investigating in this thesis are also important materials. The metal sulfides are important industrial minerals and semiconducting materials. Therefore, an understanding of the electronic structure and bonding of these materials is very important for the development of their industrial material properties and for beneficiation of sulfide ores. Molecular orbital and energy band calculations, and experimental x-ray photoelectron spectroscopy (XPS), ultraviolet photoelectron spectroscopy (UPS) and x-ray emission spectroscopy (XES) have indeed provided valuable information on the electronic structure and bonding of these materials. However, the information obtained is mainly limited to the valence band (VB), and is not complete; the understanding of the conduction band (CB) of these materials is very limited, because of difficulties in theoretical calculations and experimental techniques. Near-edge XANES spectroscopy has proved to be a very useful technique to probe the electronic structure and the density of states (DOS) near and above the Fermi level of semiconducting metal sulfides, and this is further confirmed in this thesis studies. On

the other hand, sulfur is an important component in various geological systems, and the determination of oxidation state and chemical form of sulfur has important geochemical and environmental applications.

Silicate minerals and melts are major components of the earth, and silicate glasses are also important natural and industrial materials. Physical properties of aluminosilicate glasses are related to the coordination geometries of Al, and phase transformations of silicates at lower crust and upper mantle pressures are pressure-induced and associated with change in coordination of Si. ^{29}Si and ^{27}Al magic angle spinning (MAS) NMR spectroscopy has been a well-known technique for study of the coordination geometries and local structure of Si and Al, respectively, in solid materials including minerals and glasses. However, a large amount of samples (normally $\geq$ 1 g) is required for ^{29}Si MAS NMR measurements, because of low natural abundance of ^{29}Si. This large sample size is sometimes very difficult to obtain, particularly, for example, in high temperature and pressure experimental studies. Also, features in ^{27}Al MAS NMR spectra are often not well resolved, because of quadruple broadening. Therefore, there is an urgent need to develop new techniques to investigate coordination changes of Si and Al.

1.4.2 Purposes and Outline of this Thesis

This thesis investigate Al, Si, P and S K- and L-edge XANES spectra of metal sulfides, silicate minerals and glasses. It consists of nine chapters. The first chapter is an overview of x-ray absorption spectroscopy (XAS), including XANES and EXAFS, the DCM and Mark IV Grasshopper beamlines accommodated on the Aladdin storage ring and used for the present experiments, and applications of XAS in mineralogy and geochemistry. The next eight chapters are divided into three parts based on the nature of samples investigated.

The first part, including chapters 2 to 5, reports S K- and L-edge XAS of metal sulfide minerals. S K- and L-edge XANES spectra of these metal sulfides are qualitatively interpreted based on MO/energy band calculation models. The main purposes of this part are to establish correlations of chemical shifts in S K- and L-edges

with oxidation state of sulfur, and to investigate the electronic structure and DOS features of unoccupied S 3s-, 3p- and 3d-like states near and above the Fermi level of the metal sulfides, based on the near-edge XANES spectra. Chapter 2 studies Zn ($3d^{10}$), Cd ($4d^{10}$) and Hg ($5d^{10}$) monosulfides. Chapter 3 presents and interprets S K- and L-edge spectra of Cu and/or Fe sulfides. In chapter 4, polarized S K- and L-edge, Mo L_2- and L_3-edge spectra of molybdenite are investigated. Chapter 5 is focused on applications of S K- and L-edge XANES and S K-edge EXAFS spectroscopy in mineralogy and geochemistry.

The second part, including chapters 6, 7 and 8, reports Si K- and L-edge XANES spectra of crystalline silica and silicates, and Al K-edge spectra of aluminosilicates. The Si and Al K- and L-edge XANES spectra are qualitatively interpreted based on molecular orbital diagrams for MO_4 and MO_6 (M = Si and Al) clusters and the spectra of model molecules. The main purposes of the second part are to establish correlations of chemical shifts in Si and Al K- and L-edges with their coordination geometries for silicate and aluminosilicate minerals of known crystal structures, and to correlate chemical shifts of Si K-edge with the polymerization of SiO_4 clusters and with the substitution of Al for Si. Chapter 6 reports Si K- and L-edge XANES of silica polymorphs, presents detailed qualitative interpretation of the XANES spectra, and characterizes the structure of precious opal using Si K- and L-edge XANES spectra. Chapter 7 reports the Si K-edge spectra of silicate minerals and discusses correlations of chemical shift in Si K-edge with the polymerization and crystal chemistry of silicate minerals. Chapter 8 investigates the Al K-edge XANES of aluminosilicate minerals.

Part three, including chapter 9, studies the local structure and coordination of Si and P in silicate-phosphate glasses and melts of unknown structure, using Si and P K- and L-edge XANES, based on results for silicate minerals of known crystal structure in chapters 6, 7 and 8. The preliminary results are reported for SiO_2 - P_2O_5 and Na_2O - SiO_2 - P_2O_5 glass systems containing P_2O_5 below 30 mol%.

Crystal structures of the numerous minerals considered in this study are not reproduced in this thesis. However, excellent illustrations of these familiar crystal structures are given in standard textbooks, such as "Crystal Structure" by Wyckoff[69] and "Crystal Structures and Cation Sites of the Rock-forming Minerals" by Smyth and Bish[70].

1.5 References

1. H. Fricke, *Phys. Rev.* **16**, 202 (1920).
2. G. Hertz, *Z. Phys.* **3**, 19 (1920).
3. W. Kossel, *Z. Phys.* **1**, 119 (1921).
4. A. Bianconi, J. Gaicia and M. Benfatto, *Topics in Current Chemistry* **145**, Springer-Verlag, Berlin, 1988, pp. 29.
5. G.L. Glenn and C.G. Dodd, *J. Appl. Phys.* **39**, 5372 (1968).
6. W. Seka and H.P. Hanson, *J. Chem. Phys.* **50**, 344 (1969).
7. V.I. Nefedov, *J. Struct. Chem.* **11**, 277 (1970).
8. J.L. Dehmer, *J. Chem. Phys.* **56**, 4496 (1972).
9. C.R. Natoli, In *EXAFS and Near Edge Structure* (Ed. by Bianconi A., Incoccia L. and Stipcich S.), Springer-Verlag, Berlin, 1988. pp. 43.
10. C.R. Natoli and M. Benfatto, *J. Phys. Colloq.* **47**, 11 (1986).
11. P.J. Durham, In *X-ray absorption: Principles, Applications, Techniques of EXAFS, SEXAFS and XANES* (Ed. by Koningsberger D.C. and Prins R.). Wiley and Sons, New York, 1988, pp. 53.
12. B.K. Teo, *EXAFS: Basic Principles and Data Analysis*. Springer-Verlag, Berlin, 1986.
13. R. de L. Kronig, *Z. Phys.* **70**, 317 (1931).
14. E.A. Stern, *Phys. Rev.* **B10**, 3027 (1974).
15. R. de L. Kronig, *Z. Phys.* **75**, 468 (1932).
16. H. Peterson, *Z. Phys.* **76**, 768 (1932).
17. A.I. Kostarev, *Zh. Eksp. Teor. Fiz.* **11**, 60 (1941).
18. T. Shiraiwa, T. Ishimura and M. Sawada, *J. Phys. Soc. Jpn.* **12**, 788 (1957).
19. V.V. Shmidt, *Bull. Acad. Sci. USSR, Phys. Ser.* **25**, 998 (1961).
20. R.M. Levy, *J. Chem. Phys.* **43**, 1846 (1965).
21. D.E. Sayers, E.A. Stern and F.W. Lytle, *Phys. Rev. Lett.* **27**, 1204 (1971).
22. F.W. Lytle, D.E. Sayers and E.A. Stern, *Phys. Rev.* **B11**, 4825 (1975).

23. B.M. Kincaid and P. Eisenberger, *Phys. Rev. Lett.* **34**, 1361 (1975).

24. C.A. Ashley and S. Doniach, *Phys. Rev.* **B11**, 1279 (1975).

25. P.A. Lee and J.B. Pendry, *Phys. Rev.* **B11**, 2795 (1975).

26. C. Kunz, *Synchrotron Radiation: Techniques and Applications*. Springer-Verlag, New York, 1979.

27. H. Winick and S. Doniach, *Synchrotron Radiation Research*. Plenum Press, New York, 1980.

28. E.E. Koch, Handbook in *Synchrotron Radiation IA*. North-Holding Publishing Company, Amsterdam, 1983.

29. B.X. Yang, F.H. Middleton, B.G. Olsson, G.M. Bancroft, J.M. Chen, T.K. Sham, K. Tan and D.J. Wallace, *Nucl. Instrum. Meth. Phys. Res.* **A316**, 422 (1992).

30. G.M. Bancroft, *Can. Chem. News* **44**, 15 (1992).

31. T. Miyahara, H. Kitamura, T. Katayama, M. Watababe, S. Sato, E. Ishiguro, M. Endo, Shigeo Yamaguchi, T. Yamakawa, Seitaro Yamaguchi and T. Sasaki *Part. Accel.* **7**, 163 (1976).

32. G.M. Bancroft, *Mössbauer Spectroscopy. An Introduction for Inorganic Chemists and Geochemists*. McGraw Hill, New York, 1973.

33. F.C. Hawthorne, In *Spectroscopic Methods in Mineralogy and Geology* (Ed. by Hawthorne F.C.). Mineralogical Society of America, 1988, pp. 255.

34. R.G. Burns, *Mineralogical Applications of Crystal Field Theory*, Cambridge University Press, Cambridge, 1970.

35. G.R. Rossman, In *Spectroscopic Methods in Mineralogy and Geology* (Ed. by Hawthorne F.C.). Mineralogical Society of America, 1988, pp. 207.

36. G. Calas, In *Spectroscopic Methods in Mineralogy and Geology* (Ed. by Hawthorne F.C.). Mineralogical Society of America, 1988, pp. 513.

37. G. Calas., W.A. Bassett., J. Petiau, D. Steinberg, D. Tchoubar and A. Zarka *Phys. Chem. Minerals* **11**, 17 (1984).

38. G.A. Waychunas and Brown G.E. Jr., In *EXAFS and Near-Edge Structure* (Ed.

by Hodgson K.O., Hedman B. and Penner-Hahn J.E.). Springer-Verlag, New York, 1984, pp. 336.

39. G. Calas, G.E. Jr. Brown, G.A. Waychunas and J. Petiau, *Phys. Chem. Minerals* **15**, 19 (1987).

40. G.E. Jr. Brown, G. Calas, G.A. Waychunas and J. Petiau, In *Spectroscopic Methods in Mineralogy and Geology* (Ed. by Hawthorne F.C.). Mineralogical Society of America, 1988, pp. 431.

41. G.E. Jr. Brown and G.A. Parks, *Rev. Geophys.* **27**, 519 (1989).

42. G.E. Jr. Brown, G.A. Parks and C.J. Chisholm-Brause, *Chimia* **43**, 248 (1989).

43. G.E. Jr. Brown, In *Mineral-Water Interface Geochemistry* (Ed. by Hochella M.F. Jr. and White A.F.). Mineralogical Society of America, 1990, pp. 309.

44. G.A. Waychunas, M.J. Apted and G.E. Jr. Brown, *Phys. Chem. Minerals* **10**, 1 (1983).

45. D. Bonnin, G. Calas, H. Suquet and H. Pezerat, *Phys. Chem. Minerals* **12**, 55 (1985).

46. G.A. Waychunas, G.E. Jr. Brown and M.J. Apted, *Phys. Chem. Minerals* **13**, 31 (1986).

47. A. Manceau, S. Llorca and G. Calas, *Geochim. Cosmochim. Acta* **5**, 105 (1987).

48. G.A. Waychunas, *Am. Mineral.* **72**, 89 (1987).

49. G. Cressey, C.M.B. Henderson and G. van der Laan, *Phys. Chem. Minerals* **20**, 111 (1993).

50. G.A. Waychunas, W.A. Dollase and C.R. Ross, *J. Phys. Collog.* **47**, C8, 845 (1986).

51. A. Manceau and G. Calas, *Am. Mineral.* **70**, 549 (1985).

52. G.N. Charnock, C.G. Garner, P.A.D. Patrick and D.J. Vaughan, *Phys. Chem. Minerals* **15**, 296 (1988).

53. J. Petiau, P. Sainctavit and G. Calas, *Mater. Sci. Eng.* **B1**, 237 (1988) .

54. D.A. McKeown, *Phys. Rev.* **B45**, 2648 (1992).

55. R.A.D. Patrick, G. van der Laan, D.J. Vaughan and C.M.B. Henderson, *Phys.*

Chem. Minerals **20**, 395-401 (1993).

56. G.N. Greaves, A. Fontaine, P. Lagarde, D. Raous and S.J. Gurman, *Nature* **293**, 611 (1981).

57. D.A. McKeown, G.A. Waychunas and G.E. Jr. Brown, *J. Non-Cryst. Solids* **74**, 325 (1985).

58. C.W. Ponader and G.E. Jr. Brown, *Geochim. Cosmochim. Acta* **53**, 2893 (1988).

59. G.A. Waychunas, G.E. Jr. Brown, C.W. Ponader and W.E. Jackson, *Nature* **332**, 251 (1988).

60. W.E. Jackson, J. Mustre de Leon, G.E. Jr. Brown, G.A. Waychunas, S.D. Conradson and J.M. Combes, *Science* **262**, 229 (1993).

61. J.M. Combes, G. Manceau, G. Calas and J.Y. Bottero, *Geochim. Cosmochim. Acta* **53**, 583 (1988).

62. M.J. Apted, G.A. Waychunas and G.E. Jr. Brown, *Geochim. Cosmochim. Acta* **49**, 2081 (1985).

63. J. Petiau and G. Calas, *J. Phys. Colloq.* **46**, C8, 41 (1985).

64. K.F. Hayes, A.L. Roe, G.E. Jr. Brown, K.O. Hodgson, J.O. Leckie and G.A. Parks, *Science* **238**, 783 (1987).

65. C.J. Chisholm-Brause, P.A. O'Day, Brown G.E. Jr. and Parks G.A., *Nature* **348**, 528 (1990).

66. C.J. Chisholm-Brause, K.F. Hayes, A.L. Roe, G.E. Jr. Brown, G.A. Parks and J.O. Leckie, *Geochim. Cosmochim. Acta* **54**, 1897 (1990).

67. A.L. Roe, K.F. Hayes, C.J. Chisholm-Brause, G.E. Jr. Brown, G.A. Parks, K.O. Hodgson and J.O. Leckie, *Langmuir* **7**, 367 (1991).

68. G.A. Waychunas, B.A. Rea, C.C. Fuller and J.A. Davis, *Geochim. Cosmochim. Acta* **57**, 2251 (1993).

69. R.N.G. Wyckoff (1965) *Crystal Structure* (2nd Edition), John Wiley & Sons, New York.

70. J.R. Smyth and D.L. Bish (1988) *Crystal Structures and Cation Sites of the Rock-Forming Minerals*. Allen & Unwin, London.

CHAPTER 2

S K- and L-edge XANES of Zn, Cd and Hg Monosulfides

2.1 Introduction

ZnS occurs in nature as cubic sphalerite and hexagonal wurtzite, CdS as cubic hawleyite and hexagonal greenockite, and HgS as trigonal cinnabar and cubic metacinnabar. Extensive studies have been made on the electronic structure of ZnS, CdS and HgS, due to their importance in industry, technology and structural chemistry. These studies include energy band calculations of ZnS[1-8], CdS[1-4, 8-12] and HgS[2,6,8], using various approaches, x-ray photoelectron spectra (XPS) of HgS[13], S K_β x-ray emission spectra (XES) for ZnS[14-16], CdS[14], and cinnabar[16], S $L_{2,3}$ XES of hawleyite[17], S K-edge x-ray absorption near-edge structure (XANES) spectra of ZnS and CdS[14], S $L_{2,3}$ edge XANES of hawleyite[17], and UV absorption and reflectivity spectra of ZnS and CdS[18]. These studies provided valuable information on the valence band (VB) of these sulfides.

Recently, S, Zn and Fe K-edge XANES[19,20], S L-edge XANES of sphalerite[21], and electron energy loss spectra (EELS) of cinnabar and metacinnabar[13] have been reported with synchrotron radiation. However, S K- and L-edge XANES of cinnabar and metacinnabar have not been reported, and the interpretations of the previous XANES spectra are incomplete. Also the conduction band (CB) structures of these semiconductor minerals are not well understood. In this chapter, high-resolution S K- and L-edge XANES of sphalerite (cubic ZnS), wurtzite (hexagonal ZnS), greenockite (hexagonal CdS), cinnabar (trigonal HgS) and metacinnabar (cubic HgS) are presented using synchrotron radiation. The purposes of this chapter are to qualitatively interpret the S K- and L-edge XANES spectra, to investigate the unoccupied S 3s, 3p and 3d states and the electronic structures of the CB, to compare the bonding of metal d electrons in these semiconductor minerals and to study the effect of Fe^{2+} on the electronic structure and bonding of sphalerite.

2.2 Experimental

Samples of natural sphalerite, wurtzite, greenockite and cinnabar were provided by the Department of Earth Sciences, UWO, and metacinnabar by the Department of Mineralogy, Royal Ontario Museum (M 7372). ZnS-FeS solid solutions were prepared by reacting synthetic ZnS and FeS in evacuated sealed silica-glass tubes at 800 °C for a total of 9 days, with grinding and mixing after 3 days. The ZnS and FeS starting materials were synthesized from high-purity Zn, Fe and S. All sample materials were characterized by powder x-ray diffraction (PXRD) and electron microprobe analysis (EMPA) and shown to be single phase and homogeneous.

The samples were finely ground in air to approximately 10 μm in particle size. The powder sample was spread uniformly on conducting carbon tape supported on a stainless steel sample holder. S K-edge XANES spectra were collected using the Double Crystal Monochromator (DCM), and the S L-edge XANES were collected using the Grasshopper beamline. All the spectra shown were taken by Total Electron Yield (TEY) using synchrotron radiation.

2.3 Results and Discussion

Figure 2.3.1 shows the S K-edge XANES of sphalerite, wurtzite, greenockite, metacinnabar and cinnabar. The S 1s binding energy (BE) is also indicated. Because the S 2p BE of ZnS, CdS and HgS are close within 0.2 eV of each other[22], the S 1s BE for all these materials was calculated by adding the S $2p_{3/2}$ BE of (Zn,Fe)S at 161.4 eV[23] and the S $K\alpha_1$ x-ray emission energy of 2307.8 eV. The spectra are normalized by I/I_0, where I_0 is the intensity of photon flux and I is the intensity of Total Electron Yield (TEY), and calibrated using the S K-edge of native sulfur at 2472 eV. The peak positions for the near-edge region (up to 15 eV above the edge) are summarized in Table 2.3.1, in which ΔE for each peak is the difference between the peak energy and S 1s BE. The peak positions for the post-edge region (from 15 to about 50 eV) are given in Table 2.3.2. The spectra of wurtzite and sphalerite are similar. Peak c, with fine features c_1,

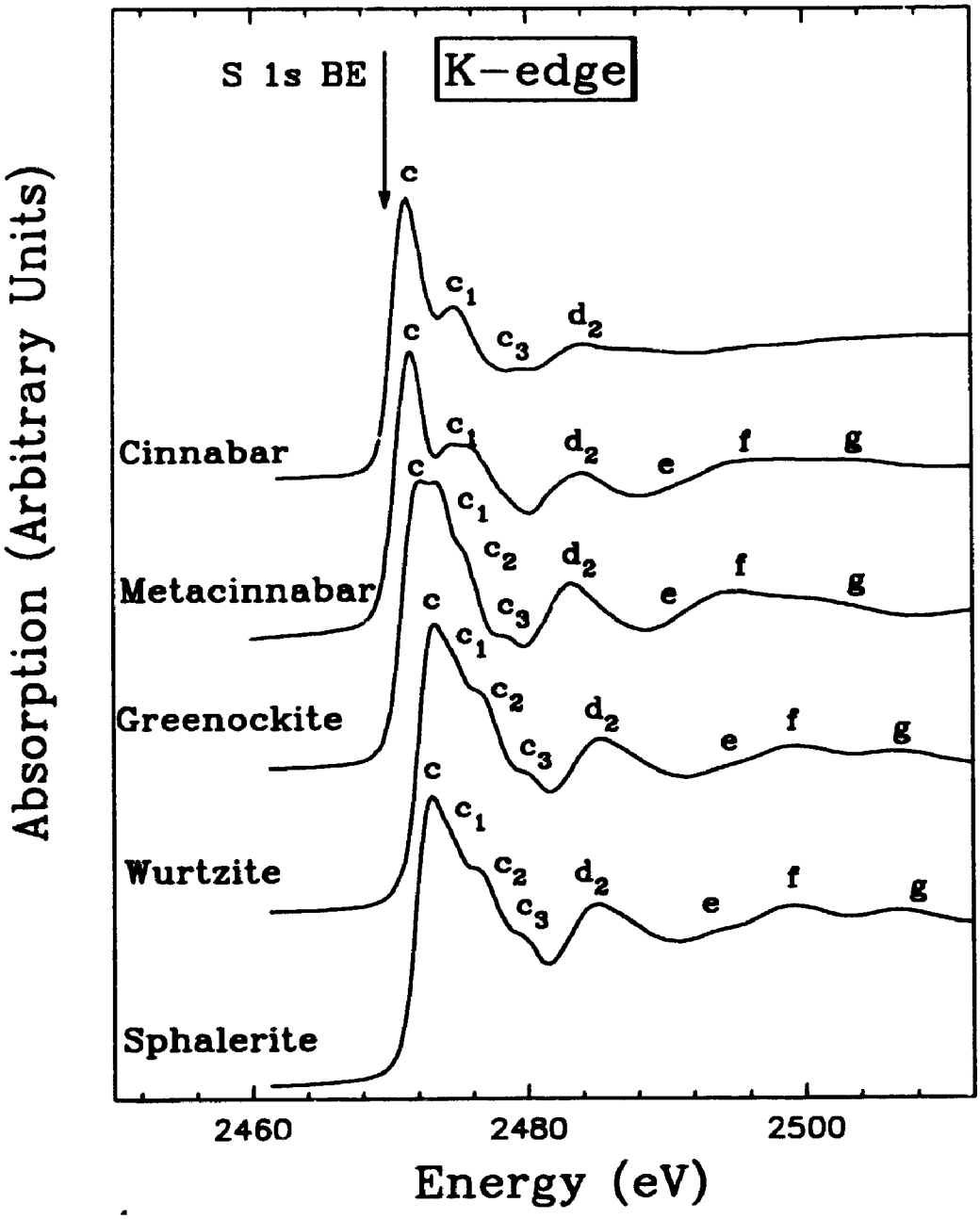

Figure 2.3.1 S K-edge XANES spectra of sphalerite, wurtzite, greenockite, metacinnabar and cinnabar. The S 1s BE is indicated by an arrow line.

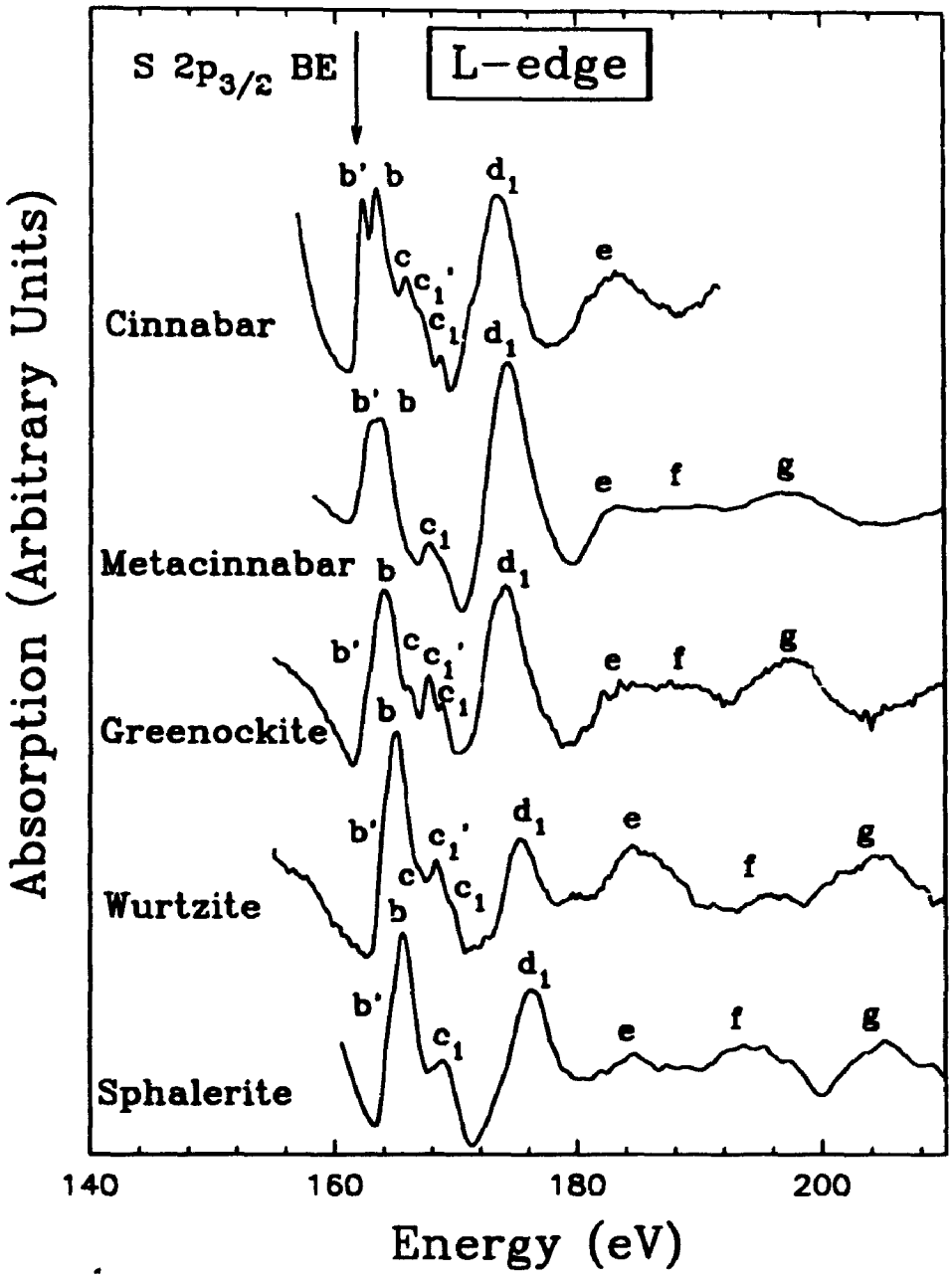

Figure 2.3.2 S L-edge XANES spectra of sphalerite, wurtzite, greenockite, metacinnabar and cinnabar. The S $2p_{3/2}$ BE of these materials is indicated by an arrow line.

c_2 and c_3, is at 2473.4 eV for sphalerite and 2473.2 eV for wurtzite. These four features are also present in the spectrum for greenockite; however, peak c shifts to 2472.3 eV, and the intensity of peak c_1 becomes almost equal to that of peak c. Peak c for metacinnabar and cinnabar is shifted to lower energy, at 2471.7 and 2471.1 eV, respectively. Peak d_2 is prominent for all these sulfides and shifts in the same way as peak c. The post-edge features are similar for sphalerite, wurtzite, greenockite and metacinnabar, and the resonance strength tends to decrease in this sequence. The post-edge features for cinnabar are weak.

Figure 2.3.2 shows the S L-edge XANES of sphalerite, wurtzite, greenockite, metacinnabar and cinnabar. The S $2p_{3/2}$ BE of (Zn,Fe)S is also indicated at 161.4 eV[23]. A spline background has been subtracted in each of the spectra shown, and the spectra are calibrated by the first peak in the S L-edge spectrum of native sulfur at 162.7 eV. The peak positions are given in Table 2.3.1 for the near-edge region and in Table 2.3.2 for the post-edge region. In the near-edge region, peaks b, c and d_1 are aligned well for all these materials. Also, the post-edge features for these minerals are similar.

2.3.1 Near-edge Features and Electronic Structure

XANES features involve complicated processes, and are not fully understood theoretically. For molecules, Nefedov and Fomichev[24] compared the inner-shell spectra of several molecules with semi-empirical molecular orbital (MO) calculations. Nefedov[25] also proposed the existence of effective potential barriers in octahedral molecules and pointed out that such a barrier could account for the large absorption features in the continuum above the S L-edge in SF_6. Dehmer[26] further used the effective potential barrier model to interpret about twenty K- and L-edge XANES spectra of small molecules of different structure and composition, as well as the S L-edge XANES spectrum of solid SF_6, and pointed out that this model can possibly interpret strong near edge features in XANES of solids. For semiconductors and insulators, Poumellec et al.[27] have suggested that the XANES of Ti and V oxides are dominated by the multi-electron effects and the one-electron transition model is no longer satisfactory. However, Sugiura

and Muramatsu[28] showed that the XANES spectrum of FeS_2 compares well with the results of one-electron calculations. Kisiel et al.[29] also confirmed that in general, the XANES spectra for semiconductors can be satisfactorily described within the one-electron approximation. In addition, Tossell[30,31], Tossell and Vaughan[2], Tossell et al.[32], Vaughan and Tossell[33] were successful in interpreting XPS and XES and in describing electronic structures of some sulfide and oxide minerals using qualitative MO/energy calculations. Filatova et al.[34] proposed a quasi-molecular approach to interpret the main near Si L-edge XANES features of silicon and its compounds. Therefore, for semiconducting and insulating solids, the strong near-edge features, like the strong line structures in XANES of molecules, correspond to transitions to unoccupied states in the CB. These transitions are also governed by dipole selection rules, $\Delta L = \pm 1$, $\Delta S = 0$ and $\Delta J = \pm 1$.

It is not possible to interpret the near-edge spectra quantitatively without a detailed band structure calculation. No such interpretation has been given for Zn, Cd and Hg monosulfides, even though there are MS Xα calculations for sphalerite[20,35]. However, The crystal chemistry of sphalerite (and wurtzite), greenockite and metacinnabar are conventionally discussed based on tetrahedral ZnS_4^{6-}, CdS_4^{6-} and HgS_4^{6-} clusters, respectively[2]. The charges assigned to these clusters are for electron count purpose only, of course, are saturated themselves in the crystal structure. The qualitative MO/energy band structure models of these systems have been calculated[2].

Figure 2.3.3 shows the expanded S K- and L-edge structures of sphalerite before background subtraction, as well as the Zn and Fe K-edge spectra[19]. The peak positions are summarized in Table 2.3.1. The S L- and K-edge structures were aligned to zero energy by taking the S $2p_{3/2}$ BE at 161.4 eV from XPS[23], and the S 1s BE was calculated by adding the S $K\alpha_1$ x-ray emission energy at 2307.8 eV and the above S $2p_{3/2}$ BE, respectively. The Zn and Fe K-edge spectra were digitized from Petiau et al.[36] and calibrated using the K-edge of metallic Fe at 7112 eV. The spectra were aligned by Zn and Fe 1s BE. The Zn 1s BE was calculated by adding the XPS Zn $2p_{3/2}$ BE of 1021.3 eV[37] plus $K\alpha_1$ x-ray emission energy at 8638.9 eV; the Fe 1s BE was calculated by adding the XPS Fe 3p BE of 54.14 eV[37] and the $K\beta_1$ x-ray emission energy at 7058.0 eV. The qualitative MO/energy band diagram of sphalerite[38] is included in this figure. The

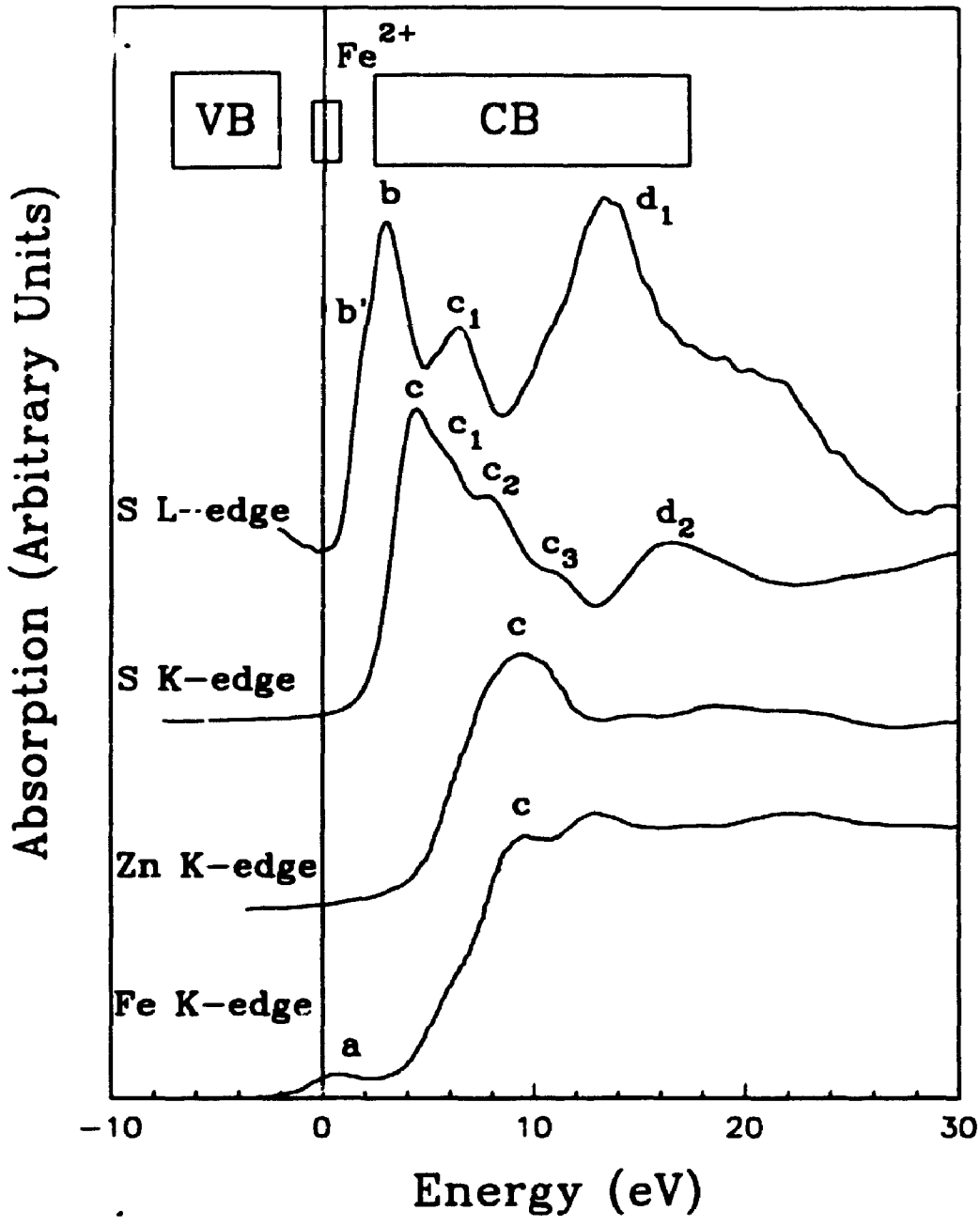

Figure 2.3.3 Near-edge structures of S K- and L-edge, Fe and Zn K-edge XANES spectra of sphalerite. The qualitative MO/energy band diagram for sphalerite[38] is included in this figure.

energy zero point is close to the Fermi level and the Fe^{2+} 3d crystal field band.

The S K-edge spectra of sphalerite (ZnS) and ferroan sphalerite ((Zn,Fe)S) containing 15.0 mol% FeS are very similar. Peak c in S K-edge XANES of sphalerite can be attributed to transitions from S 1s to the bands characterized by S 3p antibonding states in the CB minimum, which is about 4.2 eV above the Fermi level of sphalerite. Peak d_2 is also mainly due to the transition to empty S p-like states. In the S L-edge XANES of sphalerite, peak b indicates the existence of an antibonding S 3s state at the CB minimum, and the splitting of peak b into b and b' is due to the spin-orbit interaction of the S 2p orbitals. Peak c_1 and d_1 are probably attributable to transitions to the empty S 3d states[39], and also peak d_1 has significant contribution from multiple scattering. Fe^{2+} is the most important substituting impurity in natural sphalerite. Fe^{2+} 3d crystal field band lies in the fundamental gap of sphalerite[38]. However, the absence of the low energy peak a in the S K- and L-edge XANES of sphalerite demonstrates that the Fe^{2+} 3d band in the gap has little or no bonding hybridization with S 3s and 3p orbitals. These interpretations are in good qualitative agreement with the MO/energy band calculation[18]. The pre-edge (peak *a*) in the Fe K-edge XANES corresponds to the transition of Fe 1s electrons to the Fe 3d crystal field band in the fundamental gap. No pre-edge is observed in the Zn K-edge XANES, because the Zn 3d band is full and located at much lower energy below the VB maximum. The strong jumps in the Fe and Zn K-edge XANES are due to the allowed transitions of the metal 1s electrons to the metal p-like bands in the CB, which constitute the major features of the CB of sphalerite. The qualitative assignments of the S near-edge structures of sphalerite are summarized in Table 2.3.1.

In order to confirm the conclusion that the Fe^{2+} 3d crystal field band in sphalerite has little S 3s- and 3p-like DOS, one pure ZnS and four (Zn,Fe)S samples were synthesized with contents of FeS from 13.7 mol% up to 40.1 mol%, and the S K- and L-edge XANES spectra of these samples were collected at similar conditions. The S K- (at the top) and L-edge (at the bottom) spectra are shown in Figure 2.3.4. The S K- and L-edge XANES spectra of these samples are similar each other, and also show little difference from the results of the other two natural sphalerites with different contents of Fe. These results indicate that the Fe^{2+} 3d crystal field band in sphalerite indeed has

Table 2.3.1 S K- and L-edge features and qualitative assignments of Zn, Cd and Hg sulfides

Samples	Labels	K-edge (±0.2 eV)*			L-edge (±0.2 eV)*		
		Positions	ΔE	Assignments	Positions	ΔE	Assignments
Sphalerite	b'				163.0	1.6	S $2p_{3/2}$ → S 3s-like
	b				164.2	2.8	S $2p_{1/2}$ → S 3s-like
	c	2473.4	4.2	S 1s → S 3p-like			
	c_1	2475.0	5.8	S 1s → S 3p-like	167.6	6.2	S 2p → e (S 3d-like)
	c_2	2476.9	7.7	S 1s → S 3p-like			
	c_3	2479.9	10.7	S 1s → S 3p-like			
	d_1				174.6	13.2	S 2p → t_2 (S 3d-like) + M.S.
	d_2	2485.2	16.0	S 1s → empty S p-like + M.S.			
Wurtzite	b'				162.9	1.5	S $2p_{3/2}$ → S 3s-like
	b				164.1	2.7	S $2p_{1/2}$ → S 3s-like
	c	2473.2	4.0	S 1s → S 3p-like	166.0	4.6	S 2p → S s-like
	c_1	2475.1	5.9	S 1s → S 3p-like	167.5	6.1	S $2p_{3/2}$ → e (S 3d-like)
	c_2	2477.0	7.8	S 1s → S 3p-like	168.7	7.3	S $2p_{1/2}$ → e (S 3d-like)
	c_3	2480.5	11.3	S 1s → S 3p-like			
	d_1				174.2	12.8	S 2p → t_2 (S 3d-like) + M.S.
	d_2	2485.7	16.5	S 1s → empty S p-like + M.S.			

Table 2.3.1 continue

Greenockite	b'				161.6	0.2	$S\ 2p_{3/2} \rightarrow S\ 3s$-like
	b				162.8	1.4	$S\ 2p_{1/2} \rightarrow S\ 3s$-like
	c	2472.3	3.1	S 1s → S 3p-like	163.8	2.4	S 2p → S s-like
	c_1	2474.2	5.0	S 1s → S 3p-like	166.4	5.0	$S\ 2p_{3/2} \rightarrow e$ (S 3d-like)
	c_2	2476.0	6.8	S 1s → S 3p-like	167.5	6.1	$S\ 2p_{1/2} \rightarrow e$ (S 3d-like)
	c_3	2479.2	10.0	S 1s → S 3p-like			
	d_1				172.7	11.3	S 2p → t_2 (S 3d-like) + M.S.
	d_2	2483.8	14.6	S 1s → empty S p-like + M.S.			
Metacinnabar	b'				161.5	0.1	$S\ 2p_{3/2} \rightarrow S\ 3s$-like
	b				162.6	1.2	$S\ 2p_{1/2} \rightarrow S\ 3s$-like
•	c	2471.7	2.5	S 1s → S 3p-like			
	c_1	2474.4	5.2	S 1s → S 3p-like	166.5	5.1	S 2p → e (S 3d-like)
	c_2	2476.1	6.9	S 1s → S 3p-like			
	c_3	2479.2	10.0	S 1s → S 3p-like			
	d_1				172.8	11.4	S 2p → t_2 (S 3d-like) + M.S.
	d_2	2484.1	14.9	S 1s → empty S p-like + M.S.			
Cinnabar	b'				161.2	-0.2	$S\ 2p_{3/2} \rightarrow S\ 3s$-like
	b				162.4	1.0	$S\ 2p_{1/2} \rightarrow S\ 3s$-like
	c	2471.1	1.9	S 1s → S 3p-like	164.7	3.3	$S\ 2p_{3/2} \rightarrow S$ s-like
	c_1	2474.5	5.3	S 1s → S 3p-like	166.1	4.7	$S\ 2p_{1/2} \rightarrow S$ s-like
	c_2				167.7	6.3	S 2p → e (S 3d-like)
	c_3	2479.3	10.1	S 1s → S 3p-like			
	d_1				172.4	11.0	S 2p → t_2 (S 3d-like) + M.S.
	d_2	2483.5	14.3	S 1s → empty S p-like + M.S.			

• The reading error of the edge peak is ±0.1 eV.

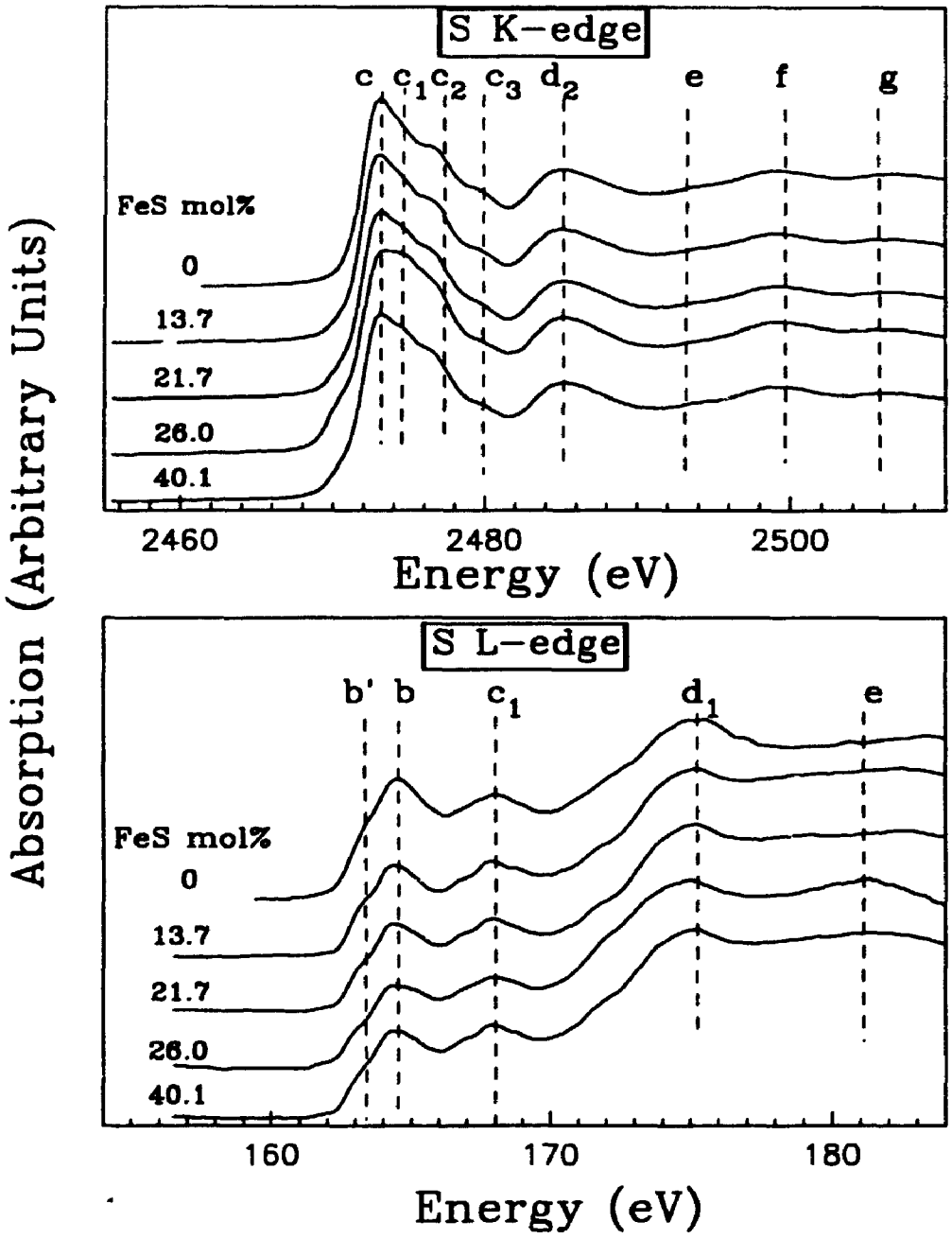

Figure 2.3.4 S K- (at the top) and L-edge (at the bottom) XANES spectra of synthetic ZnS and (Zn,Fe)S samples containing FeS up to 40.1 mol%.

little S 3s- and 3p-like DOS. The substitution of FeS for ZnS up to 40.1 mol% in this structure has little influence on the metal-sulfur bonding, and Fe^{2+} 3d electrons are not significantly involved in the metal-sulfur bonding.

By comparison with the S K- and L-edge spectra of sphalerite, the S K- and L-edge XANES spectra of wurtzite, greenockite, cinnabar and metacinnabar, which have similar geometrical and electronic structures to those of sphalerite, are interpreted as in Table 2.3.1. For S K-edge spectra, peak c is attributable to transitions of S 1s electrons to S 3p-like states in the CB, but the origins of peaks c_1, c_2 and c_3 are not clear, although probably related to transitions to S p-like states and multiple scattering (MS) with the more distant atom shells. Peak d_2 is also assigned to transition of S 1s electrons to the S p-like (probably 4p) state. However, peak d_2 must have a contribution from the MS effect from more distant atom shells. In the S L-edge spectra, peak b is assigned to transitions of S 2p electrons to the S 3s-like states in the CB. Peak b is split into peaks b' and b by about 1.2 eV, apparently due to the spin-orbit interaction of S 2p orbitals. Peak c_1 is also split by about 1.1 eV for wurtzite, greenockite and cinnabar, also due to spin-orbit splitting of S 2p orbitals. Peak c is observed for wurtzite, greenockite, and cinnabar, and tends to increase in intensity in this sequence. Peaks c_1 and d_1 are at least partly attributable to transitions of S 2p electrons to empty S 3d bands in the CB. In tetrahedral symmetry, S 3d orbitals are split into e and t_2 states, and the e state is favored in energy over the t_2 state. Therefore, peak c_1 is assigned to transition of S 2p electron to the e state, and peak d_1 to the t_2 state (so called shape resonances). Peaks c_1 and d_1 are separated from 7.0 eV for sphalerite and wurtzite to about 5.6 eV for greenockite and metacinnabar. This is in qualitative agreement with the crystal field strength, because Zn-S bond length (2.34 Å) in sphalerite and wurtzite is somewhat smaller than Cd-S bond length (2.53 Å) in greenockite and Hg-S bond length (2.53 Å) in metacinnabar, and the crystal field strength is proportional to $1/R^5$. Such crystal field splitting has been observed in Si, P and S L-edge spectra of gases and solids[39]. However, intense shape resonance peaks are always associated with electronegative ligands (e.g. F, Cl and O) bonded to the [illegible] and S. In our compounds containing electropositive atoms surrounding the S atom, we should not expect the shape resonance peaks to be intense.

Thus, peak d_1 can not be attributed exclusively to a t_2 shape resonance, and must reflect significant contribution from MS with more distant atom shells.

The CB electronic structures of semiconducting and insulating solids are not well understood. Optical and core-level reflection spectroscopy[40], bremsstrahlung isochromat spectroscopy (BIS)[41], electron energy loss spectroscopy (EELS)[42] and XANES spectroscopy are the common techniques used to analyze the unoccupied densities of states (DOS). Low-energy optical reflection spectroscopy has very high resolution (better than 0.1 eV), but it provides limited information on the CB DOS because it depends on the joint DOS of the VB and CB rather than the CB DOS alone[40]. The BIS reflects the total CB DOS with a resolution of about 0.7 eV, and can be used to trace the band dispersion in ordered crystals, but the acquisition time of a spectrum is very long[41]. EELS can also provide information on the CB DOS and atomic arrangements, but the resolution of EELS is often poor[42]. XANES spectroscopy using synchrotron radiation permits measurements of high accuracy, high sensitivity, short acquisition time, wide energy range and broad selectivity of atomic species and DOS components. The XANES provide good insight into the CB electronic structures of the presently investigated solids.

Figure 2.3.5 shows the near S K- and L-edge features of the Zn, Cd and Hg monosulfides. The K- and L-edge spectra are aligned to zero by the S 1s BE and S 2p BE, respectively. The energy position and ΔE for each peak in the K and L-edge spectra are summarized in Table 2.3.1. In general, the near-edge peaks in the S K and L-edge spectra correspond well. The slight differences in ΔE for equivalent peaks are probably due to different core-hole relaxation energies in the K- and L-edge spectra, although the very similar term value for peaks in the Si L- and K-edge spectra of $SiCl_4$ and $Si(CH_3)_4$ show that such differential relaxation is < 1 eV[43]. The near-edge features of S K- and L-edge XANES reflect the partial DOS of unoccupied S 3s, 3p and 3d states in the CB and provide qualitative information on the CB structures. For the Zn, Cd and Hg monosulfides, the antibonding S 3s-like states, 3p-like are close to the CB minimum; while the empty S 3d-like and p-like states are in the upper part of the CB. The antibonding S 3s- and 3p-like states are very close to each other and are apparently overlapping, and the S 3d-like and p-like states also overlap. These results indicate the

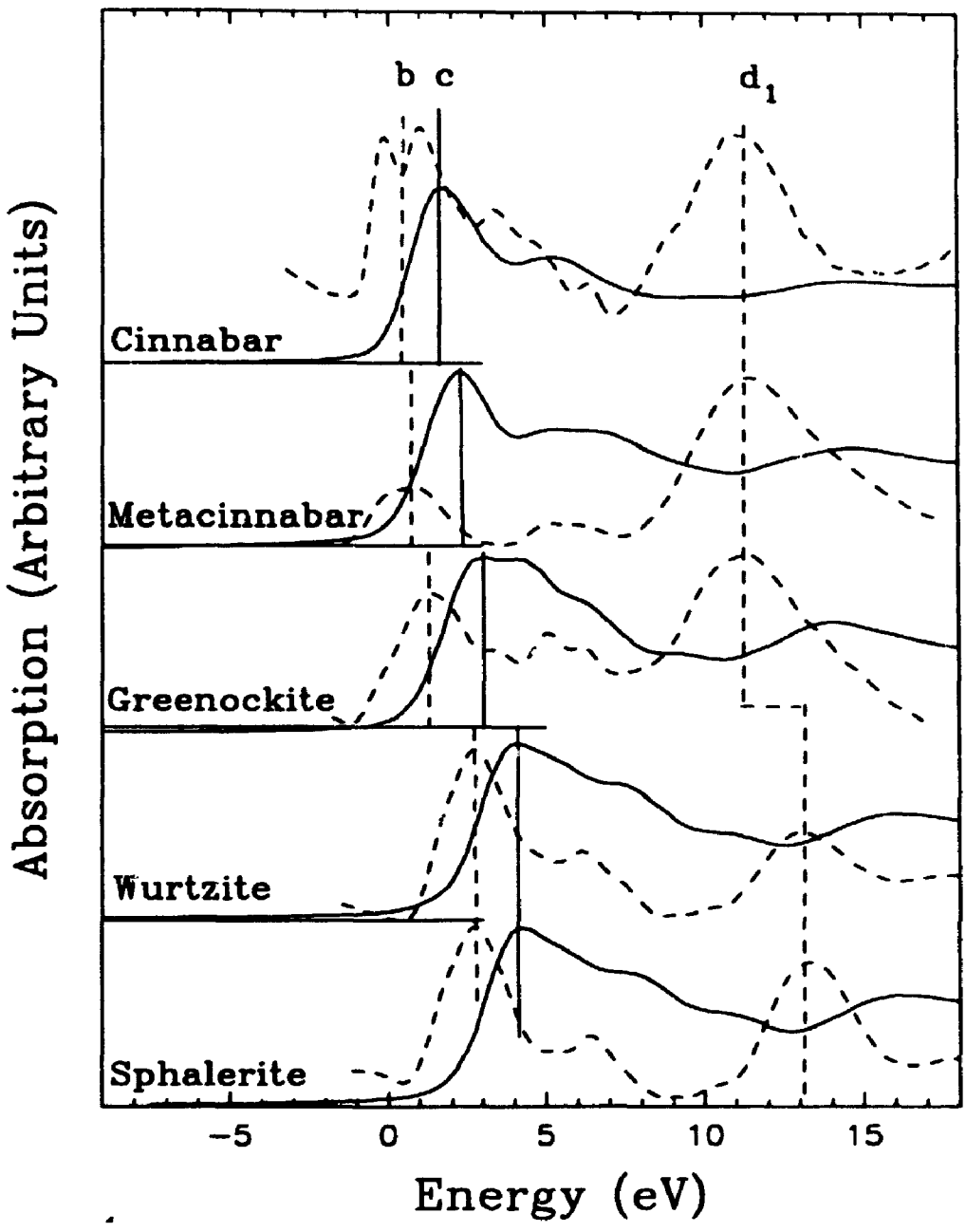

Figure 2.3.5 Near-edge structures of S K- (solid lines) and L-edge (dash lines) XANES spectra of sphalerite, wurtzite, greenockite, metacinnabar and cinnabar. The near-edge structures reflect the partial DOS of unoccupied S 3p- and 3s-like states at the CB minimum of these semiconducting materials.

mixture between S s- and p-like states, and between the S p- and d-like states in the CB. As in the foregoing analysis, because the XANES spectroscopy using synchrotron radiation allows us to select the atomic species and the DOS components, the Zn, Cd, Hg K- and L-edge XANES spectra must reflect the DOS of the unoccupied s-, p- and d-like states of the corresponding metals in the CB. Therefore, the whole structure of the CB and the metal-sulfur bonding of these sulfides can be described. Unfortunately, the metal K- and L-edge spectra of these materials are not available, so that the whole structure of the CB can not appropriately described. However, the S K- and L-edge spectra must reveal the DOS of unoccupied S s-, p- and d-like states in the CB.

Comparing the S K- and L-edge XANES spectra of Zn, Cd and Hg monosulfides, the most apparent change is the shift to lower energy of the corresponding edge features from ZnS to CdS and to HgS. For example, peak c shifts by 2.3 eV in the K-edge spectra from sphalerite (2473.4 eV) to greenockite (2472.3 eV) and cinnabar (2471.1 eV), and peak b shifts by 1.8 eV in the L-edge spectra from sphalerite (163.6 eV) to greenockite (162.2 eV) and cinnabar (161.8 eV) (see Table 2.3.1). On the other hand, from sphalerite to greenockite and to cinnabar, the energy gap decreases from 3.8 eV to 2.5 eV and to about 2.0 eV. Therefore, the S K- and L-edge spectra indicate that the CB minimum moves down from ZnS, CdS to HgS, and the bonding of Zn^{2+} ($3d^{10}$), Cd^{2+} ($4d^{10}$) and Hg^{2+} ($5d^{10}$) with sulfur is different. For Zn, Cd and Hg monosulfides, the Zn $3d^{10}$, Cd $4d^{10}$ and Hg $5d^{10}$ crystal field bands lie below the metal-S bonding bands in the VB, rather than in the fundamental gap[2]. Although the XPS, S K_β and L XES results have demonstrated the participation of d electrons of metals in the chemical bonding with sulfur for these compounds[44], S K- and L-edge XANES spectra provide little evidence for this conclusion. However, the S 3s and 3d DOS are strongly overlapped with the S 3p DOS in the CB.

The S K- and L-edge XANES spectra for sphalerite, wurtzite, greenockite and metacinnabar are generally very similar, and the S K-edge spectra are also similar to the Cl K-edge of CuCl[45], P K edge of InP and Si K-edge XANES of silicon. Among these compounds, wurtzite and greenockite have the wurtzite structure; sphalerite, hawleyite, metacinnabar, CuCl and InP have the sphalerite structure; and silicon has the sphalerite-

like diamond structure. Although the precise origins of these features are unclear, they must be related to the transitions of 1s electrons to the p-like states in the CB. From this point of view, the XANES spectra demonstrate that the CB structures of the present II-IV semiconducting compounds are similar, and for both ZnS and CdS, the energy band structures of the cubic and hexagonal modifications are similar also. This argument is also in agreement with a recent energy band calculation of these II-IV semiconductors[4]. Hence, the near K-edge features of these semiconductors are mainly related to the local tetrahedral structure of sulfur, and can probably be used as structural fingerprint for semiconductors with the sphalerite structure. This may be of significance for studying structure of unknown materials, such as chalcogenide glasses and metalloproteins.

2.3.2 Post-Edge XANES Features

Figures 2.3.1 and 2.3.2 show the post-edge features, as well as the near-edge structures, of S K- and L-edge XANES spectra for Zn, Cd and Hg monosulfides. The post-edge features (peaks d, e, f and g) for these minerals are very similar, in both position and intensity (Table 2.3.2), as expected by similarity in crystal structures and the local tetrahedral coordination of sulfur.

The post-edge XANES features have been interpreted as multiple scattering resonances[46]. However, no simple theoretical formalism has been developed to describe the experimental XANES features. The correlation of interatomic distances and multiple scattering resonances has attracted much interest[47]. A linear relation between k_r, the wavevector of the photoelectron, and 1/R, where R is the interatomic distance, was found. Multiple scattering theory also justified this relation[48] and showed that a similar relation $k_b \cdot R = C_b$ may hold for a bound state at k_b. A new relation $(E_r - E_b) \cdot R^2 = C$ was proposed, where C is a constant, E_r and E_b are energies of post-edge features and the bound state, respectively, obtained from the experimental XANES spectrum, and used to determine the interatomic distances in unknown systems[47]. This new model was recently extended to determination of interatomic distances for coordination shells of sulfur in ZnS, MoS_2 and PbS[49] and chlorine in LiCl, NaCl, KCl and CsCl[50].

Recently, a Bragg single reflection model under the nearly free electron approximation was suggested to interpret the XANES spectra of crystalline solids. The basic assumption follows from the Bragg condition $\mathbf{k}_i - \mathbf{k}_r = \mathbf{G}$, where $\mathbf{k}_i$ and $\mathbf{k}_r$ are the wavevectors of the incident and reflected electrons, respectively, and G is a reciprocal lattice vector. The constructive interference between the incident wave and the reflected wave from the lattice planes produces resonances in the XANES, and the maximum constructive interference will occur for directly backward scattering of the reflected wave. In this case, a formula $\mathbf{k}_i = \mathbf{G}/2$ is obtained[51].

The models $\mathbf{k}_r \cdot \mathbf{R}$ = constant and $(E_r - E_b) \cdot R^2$ = constant have been shown to be valid for the XANES spectra of molecules and condensed systems. The Bragg reflection model was in principle established using single scattering processes under the nearly free electron approximation, but the formulism, $\mathbf{k}_i = \mathbf{G}/2$, is similar to $\mathbf{k}_r \cdot \mathbf{R}$ = constant in the multiple scattering theory. Therefore, these models were essentially unified as $(E_r - E_b) \cdot R^2$ = constant in the interpretation of XANES features[49,50], where E_r and E_b are energies for post-edge features and bound states respectively, and R is the interatomic distance or lattice spacing.

For Zn, Cd and Hg monosulfides, the E_r, resonance energies in the post S K- and L-edge region, are measured in the experimental spectra. The interatomic distances or lattice spacing (R) are calculated from x-ray structure data. $E_r - E_b$ for the resonances in the S K- and L-edge XANES spectra are compared with $1/R^2$ in Table 2.3.2; E_b is the energy of the first peak in each XANES spectrum[49,50]. The resonance energies correlate linearly with the squared reciprocal interatomic distances for S K- and L-edge spectra (see Figure 2.3.6), with correlation coefficients larger than 0.99. The left-hand plots are for K-edge XANES, and the right-hand plots are for the L-edge XANES. All the lattice planes and interatomic shells in this region of R are in this correlation, confirming that absorption of backscattered photoelectrons occurs at $\lambda = d_{hkl}$ as well as $\lambda = R_a$[50]. Some of the linear correlation lines do not pass through the energy origin, but this is probably attributable to error in estimating peak position in the completely overlapped spectra. These results confirm that peak d_1 in the L-edge and peak d_2 in the K-edge spectra reflect contributions from multiple scattering with more distant atom shells.

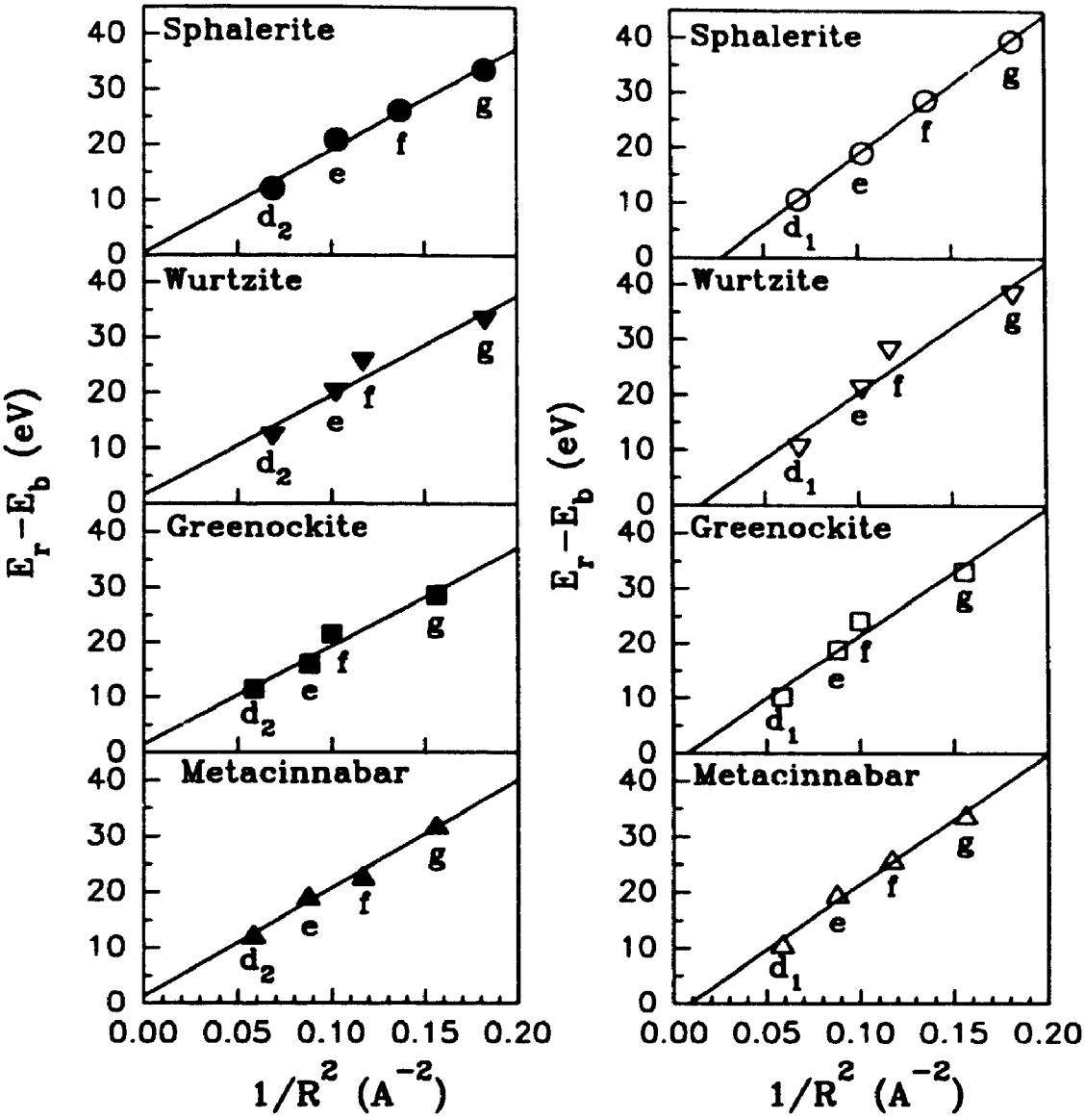

Figure 2.3.6 Correlations of post-edge features of S K- (left hand) and L-edge (right-hand) XANES with reciprocal interatomic and lattice plane distances for sphalerite, wurtzite, greenockite and metacinnabar.

Table 2.3.2 The post-edge features of S K- and L-edge XANES of Zn, Cd and Hg monosulfides

Minerals	Labels	K-edge (eV ±0.5)		L-edge (eV ±0.5)		R (Å)	$1/R^2$ ($Å^{-2}$)	Assignments
		Energy	E_r-E_0	Energy	E_r-E_0			
Sphalerite	g	2507.0	33.6	203.1	39.5	2.34	0.1826	1st shell
	f	2499.5	26.1	192.2	28.6	2.71	0.1367	d_{200}
	e	2494.2	20.8	182.6	19.0	3.12	0.1027	d_{111}
	d	2485.4	12.0	174.2	10.6	3.81	0.0689	2nd shell
Wurtzite	g	2506.3	33.1	201.7	38.2	2.34	0.1826	1st shell
	f	2499.2	26.0	192.8	29.3	2.93	0.1165	d_{101}
	e	2493.2	20.0	184.6	21.1	3.13	0.1028	d_{002}
	d	2485.3	12.1	173.9	10.4	3.81	0.0689	2nd shell
Greenockite	g	2501.0	28.7	195.4	33.2	2.53	0.1562	1st shell
	f	2494.8	22.5	188.2	26.0	3.16	0.1001	d_{101}
	e	2487.4	15.1	181.0	18.8	3.37	0.0881	d_{002}
	d	2483.7	11.4	172.4	10.2	4.14	0.0583	2nd shell
Metacinnabar	g	2503.7	32.0	196.1	34.0	2.53	0.1562	1st shell
	f	2494.6	22.9	188.0	25.9	2.93	0.1165	d_{200}
	e	2490.9	19.2	181.8	19.7	3.38	0.0875	d_{111}
	d	2484.1	12.4	172.8	10.7	4.14	0.0583	2nd shell

2.4 Conclusions

Major features in the near-edge region of the S K- and L-edge XANES for sphalerite, wurtzite, greenockite, cinnabar and metacinnabar are interpreted by qualitative MO/energy band calculations within the one-electron-transition model. XANES using synchrotron radiation is superior to any other technique in providing information on the unoccupied electron states and the CB electronic structure of solids. The near-edge features reflect the DOS of unoccupied S 3s, 3p and 3d states in the CB. From sphalerite to greenockite and to cinnabar, the S K- and L-edges shift toward lower energy by about 2.3 and 1.8 eV, respectively, and the energy gap decreases by about 1.9 eV, indicating that the unoccupied S 3s and 3p states, and the CB minimum move down to lower energy in this sequence. In these metal sulfides, the bonding behavior of Zn $3d^{10}$, Cd $4d^{10}$ and Hg $5d^{10}$ electrons is distinct, but the participation of the metal d electrons in the bonding of the metals with sulfur is not evident. The Fe^{2+} 3d crystal field band in the fundamental gap of (Zn,Fe)S has little DOS involving S 3s- and 3p-like states. Meanwhile, for tetrahedrally-coordinated sphalerite, wurtzite, greenockite and metacinnabar, the post-edge features of the S K and L-edge XANES are linearly correlated with the reciprocal interatomic distances and lattice plane distances. Hence, the S K- and L-edge XANES of Zn, Cd and Hg monosulfides provide information on the local structure and coordination of sulfur. The K-edge XANES of different anions in ZnS-structure compounds are qualitatively similar, and may be used as a structural fingerprint for studying local structure of unknown materials, such as chalcogenides glasses and metalloproteins.

2.5 References

1. O.V. Farberovich, S.I. Kurganskii and E.P. Domashevskaya, *Phys. Status. Solidi.* **B97**, 631 (1980).
2. J.A. Tossell and D.J. Vaughan, *Inorg. Chem.* **20**, 3333 (1981).
3. R. Eppenga, M.F.H. Schuurmans and H.W.A.M. Rompa, *J. Phys. Chem. Solids*

49, 1119 (1988).

4. Ming-zhu Huang and W.Y. Ching, *J. Phys. Chem. Solids.* **46**, 977 (1985).
5. J.E. Bernard and A. Zunger, *Phys. Rev.* **B36**, 3199 (1987).
6. C.S. Wang and B.M. Klein, *Phys. Rev.* **B24**, 3393 (1981).
7. H.Y. Chung and S.K. Kim, *Sue. Mulli.* **29**, 743 (1989).
8. H. Aourag, B. Khelifa, L. Hamerlaine, H. Belarbi and A. Belaidi, *Phys. Lett.* **A145**, 455 (1990).
9. A. Zunger and A.J. Freeman, *Phys. Rev.* **B17**, 4850 (1978).
10. K.J. Chang, S. Froyen and M.L. Cohen, *Phys. Rev.* **B28**, 4736 (1983).
11. A.I. Ali Dahr and P.M. Lee, *Phys. Scrip.* **38**, 441 (1988).
12. H.Y. Chung and S.K. Kim, *Sue. Mulli.* **28**, 494 (1988).
13. M. Scrocco, *J. Electron Spectrosc. Relat. Phenom.* **49**, 139 (1989).
14. C. Sugiura, Y. Gohshi and I. Suzuki, *Phys. Rev.* **B10**, 338 (1974).
15. S.A. Nemnonov and S.S. Mikhailova, *Bull. Acad. Sci. USSR. Phys. Ser.* **38**, 56 (1974).
16. K.I. Narbutt, *Bull. Acad. Sci. USSR. Phys. Ser.* **38**, 104 (1974).
17. C. Sugiura, Y. Hayasi, H. Konuma and S. Kiyono, *J. Phys. Soc. Japan.* **31**, 1748 (1971).
18. M. Cardona and G. Harbeke, *Phys. Rev.* **A137**, 1467 (1965).
19. P. Sainctavit, G. Calas, J. Petiau, R. Karnatak, J.M. Esteva and G.E. Jr. Brown, *J. Phys. Colloq.* **47**, 411 (1986).
20. P. Sainctavit, J. Petiau, G. Calas, M. Benfatto and C.R. Natoli, *J. Phys. Colloq.* **48**, 1109 (1987).
21. M. Kasrai, M.E. Fleet, T.K. Sham, G.M. Bancroft, K.H. Tan and J.R. Brown, *Solid State Commun.* **68**, 507 (1988).
22. X.R. Yu, F. Liu, Z.Y. Wang and Y. Chen, *J. Electron Spectrosc. Relat. Phenom.* **50**, 159 (1990).
23. M.M. Hyland and G.M. Bancroft, *Geochim. Cosmochim. Acta* **53**, 367 (1988).
24. V.I. Nefedov and V.A. Fomichev, *Zh. Strukt. Khim.* **9**, 279, (*J. Struct. Chem.*

9, 217) (1968).

25. V.I. Nefedov, *Zh. Strukt. Khim.* **11**, 299, (*J. Struct. Chem.* **11**, 277) (1970).
26. J.L. Dehmer, *J. Chem. Phys.* **56**, 4496 (1972).
27. B. Poumellec, J.F. Marucco and B. Touzelin, *Phys. Rev.* **B 35**, 2284 (1987).
28. C. Sugiura and S. Muramatsu, *Phys. Status Solidi* **B129**, K157 (1985).
29. A. Kisiel, G. Dalba, P. Fornasini, M. Podgórny, J. Oleszkiewicz, F. Rocca and E. Burattini, *Phys. Rev.* **B39**, 7895 (1989).
30. J.A. Tossell, *J. Am. Chem. Soc.* **97**, 4840 (1975).
31. J.A. Tossell, *J. Phys. Chem. Solid.* **36**, 1273 (1975).
32. J.A. Tossell, D.S. Urch, D.J. Vaughan and G. Wiech, *J. Chem. Phys.* **77**, 77 (1982).
33. D.J. Vaughan and J.A. Tossell, *Phys. Chem. Minerals.* **9**, 253 (1983).
34. E.O. Filatova, A.S. Vinogradov and T.M. Zimkina, *Sov. Phys. Solid State* **27**, 606 (1985).
35. D.A. McKeown, *Phys. Rev.* **B45**, 2648 (1992).
36. J. Petiau, P. Sainctavit and G. Calas, *Mater. Sci. Eng.* **B1**, 237 (1988).
37. R.K. Clifford, K.L. Purdy and J.D. Miller, *AIChE Symposium Series* **71**, 138 (1975).
38. D.J. Vaughan and J.A. Tossell, *Can. Mineral.* **18**, 157 (1980).
39. Z.F. Liu, J.N. Cutler, G.M. Bancroft, K.H. Tan, R.G. Cavel and J.S. Tse, *Chem. Phys.* **168**. 133 (1992).
40. A. Kisiel, M. Zimnal-Starnawska, E. Antonangeli, M. Piacentini and N. Zema, *Nuovo Cimento* **D8**, 436 (1984).
41. Y. Gao, B. Smandek, T.J. Wagener, J.H. Weaver, F. Levy and G. Margaritondo, *Phys. Rev.* **B35**, 9357 (1987).
42. J. Taftø and J. Zhu, *Ultramicroscopy* **9**, 349 (1982).
43. J.D. Bozek, K.H. Tan, G.M. Bancroft and J.S. Tse, *Chem. Phys. Lett.* **138**, 33 (1987).
44. E.P. Domashevskaya, V.A. Terekhov, L.N. Marshakova, Y.A. Ugai, V.I.

Nefedov and N.P. Sergushin, *J. Electron Spectrosc. Relat. Phenom.* **9**, 261 (1976).

45. S. Hamza, M.A. Khan, S. Lewonczuk, J. Ringeissen, J. Petiau and P. Sainctavit, *Solid State Commun.* **75**, 29 (1990).

46. C.R. Natoli, In *EXAFS and Near-edge Structure III* (Ed. by Hodgson K.O., Hedman B. and Penner-Hahn J.E.). Springer-Verlag, Berlin, 1984, pp. 38.

47. A. Bianconi, E. Fritsch, G. Calas and J. Petiau, *Phys. Rev.* **B32**, 4292 (1985).

48. C.R. Natoli and M. Benfatto, *J. Phys. Colloq.* **47**, 11 (1986).

49. M. Kasrai, M.E. Fleet, T.K. Sham, G.M. Bancroft, K.H. Tan and J.R. Brown, *Solid State Commun.* **68**, 507 (1988).

50. M. Kasrai, M.E. Fleet, G.M. Bancroft, K.H. Tan and J.M. Chen, *Phys. Rev.* **B43**, 1763 (1991).

51. T. Tiedje, J.R. Dahn, Y. Gao, K.M. Colbow, E.D. Crozier, D.T. Jiang and W. Eberhardt, *Solid State Commun.* **85**, 161 (1993).

CHAPTER 3

S K- and L-edge XANES and Electronic Structure of Copper and/or Iron Sulfide Minerals

3.1 Introduction

Cu and/or Fe sulfides are among the most important metal sulfide minerals. Some Cu-containing sulfides have simple chemical compositions, but extremely complicated crystal structures, bonding and phase transformations[1-4]. Among these sulfides, the electronic structure and bonding of chalcopyrite ($CuFeS_2$) have been extensively studied using a qualitative MO/energy band structure calculation[5-7], a self-consistent-charge discrete-variation Xα calculation[8], X-ray photoelectron spectra (XPS)[9] and S K_β x-ray emission spectra (XES)[10]. Tossell et al.[11] systematically interpreted the S K_β, S L, Cu K_β, Cu L, Fe K_β and Fe L XES based on the MO/energy band structure. Recently, Cu, Fe and S K-edge x-ray absorption near-edge structure (XANES) of $CuFeS_2$ have been studied using synchrotron radiation[12-14] and a multiple scattering calculation[15].

For the other copper-containing sulfides, S K_β XES have been obtained for Cu_2S by Domashevskaya et al.[16], and Sugiura and Gohshi[17]; and for CuS by Nemnonov and Mikhailova[18] and Sugiura et al.[19]. Tossell[5] presented MO calculation for CuS_4^{7-}, CuS_4^{6-}, CuS_3^{5-} and CuS_3^{4-} clusters, interpreted the XES and studied the electronic structures of CuS and Cu_2S. The Cu and S K-edge XANES of CuS and Cu_3AsS_4 have also been reported[13]. The energy band and bonding models for tetrahedrite[20,21] and thiospinel minerals[22-24] including carrollite and linnaeite have also been proposed. The metal K-edge EXAFS of tetrahedrite[25,26] and thiospinel minerals[27] have been reported. More recently, the oxidation states and electronic configuration of Cu in tetrahedrite have been determined using Cu L-edge XANES spectra[28]. XPS and XES provide information on the bonding VB, and XANES yields information on the unoccupied states in the CB.

Pyrite (FeS_2) and pyrrhotite ($Fe_{1-x}S$) are the two most important Fe sulfide

minerals. The electronic structures and bonding models of pyrite and marcasite[29-35], and pyrrhotite[36-38] have been calculated or proposed using various qualitative MO/energy band calculation approaches. S K_β XES of pyrite[39] and pyrrhotite[40] were reported, the S XES and XPS spectra of pyrite and pyrrhotite were also interpreted on the basis of the MO calculation and provided important information on the electronic structure of the VB[41-43]. Fe K-edge[44] and S K-edge[45,46] XANES spectra of pyrite and pyrrhotite were also reported, and the interpretation of the S K-edge XANES spectrum of pyrrhotite was attempted by multiple scattering calculation[47]. However, this calculation did not give clear assignments for the near-edge features.

In this chapter, S K- and L-edge XANES of chalcopyrite ($CuFeS_2$), cubanite ($CuFe_2S_3$), and low bornite (Cu_5FeS_4); low chalcocite (Cu_2S), covellite (CuS), and enargite (Cu_3AsS_4); stannite (Cu_2FeSnS_4); tetrahedrite ($Cu_{12}Sb_4S_{13}$); carrollite ($CuCo_2O_4$) and linnaeite (Co_3S_4); pyrrhotite ($Fe_{1-x}S$) and pyrite (FeS_2), are reported and qualitatively interpreted based on MO/energy band models, in order to study the electronic structure and bonding, and the DOS of unoccupied S 3s-, 3p- and 3d-like states near and above the Fermi level of these transition metal sulfides.

3.2 Experimental

The sample materials for XANES measurements were characterized by x-ray diffraction and electron microprobe analysis to be essentially of end-member composition and homogeneous (see Table 3.2.1). The S K-edge XANES spectra of powder samples were collected by Total Electron Yield (TEY) with the Double Crystal Monochromator (DCM). The spectra shown were calibrated against the K-edge of native sulfur at 2472 eV. S L-edge XANES spectra were taken by TEY on the Grasshopper beamline, and calibrated by the first sharp peak in the S L-edge XANES of native sulfur at 162.7 eV.

Table 3.2.1. Occurrences and chemical compositions* of copper sulfides

Samples	Ideal formula	Locality	Cu	Fe	As	Sb	S	Total
Bornite	Cu_5FeS_4	Falconbridge Ontario, Canada	62.6	11.6			25.7	99.9
Cubanite	$CuFe_2S_3$	Strathcona Ontario, Canada	23.1	41.5			35.3	99.9
Chalcopyrite	$CuFeS_2$	Noranda Quebec, Canada	34.6	30.7			34.7	100.0
Chalcocite	Cu_2S	Butte Montana, USA	80.2				19.0	99.2
Covellite	CuS	Butte Montana, USA	66.9				33.1	100.0
Enargite	Cu_3AsS_4	Butte Montana, USA	48.9			18.7	32.4	100.0
Tetrahedrite	$Cu_{12}Sb_4S_{13}$	Premier Mine B.C. Canada	41.8	3.3	0.8	29.2	24.8	99.9
Tetrahedrite	$Cu_{12}(Sb,As)_4S_{13}$	Sells Mine Utah, USA	42.2	3.3	10.9	13.7	26.3	96.4

* By electron microprobe analysis, using a JEOL JXA 8600 superprobe, in wt%.

3.3 Results and Spectral Assignments

3.3.1 Chalcopyrite, Cubanite and Bornite

The electronic configuration of S^{2-} in metal sulfides is $1s^22s^22p^63s^23p^6$. The S K- and L-edge XANES features are closely related to the transition of electrons from the inner shells to the antibonding states and the electronic structure of the conduction bands (CB). A simplified MO/energy band model[6,7] is very helpful for the qualitative interpretation of the near-edge features (see chapter 2). However, it is not possible to interpret these near-edge spectra quantitatively without a detailed band structure calculation. Such a calculation is not available for most metal sulfides, even for very simple and typical sphalerite structure. It is fortunate that a DVXα calculation exists for chalcopyrite[8], and the calculated DOS of unoccupied states has been used to interpret the S, Cu and Fe K-edge XANES for chalcopyrite[13].

Figure 3.3.1 shows the S K- and L-edge structures of chalcopyrite before background subtraction, together with the Fe K-edge spectra. The S K- and L-edge peak positions and the positions relative to the BE (ΔE) are summarized in Table 3.3.1. The S K- and L-edge structures of chalcopyrite are aligned using the S 1s BE of 2468.9 eV and $2p_{3/2}$ BE at 161.1 eV, respectively, where the S 1s BE is calculated by adding the S $K\alpha_1$ x-ray emission energy at 2307.8 eV and the S $2p_{3/2}$ BE. The qualitative MO/energy band diagram calculated by Vaughan and Tossell[6] is shown at the top. In general, the near-edge peaks in the S K- and L-edge spectra correspond well. The slight differences in ΔE for equivalent peaks are probably due to different core-hole relaxation energies in the K and L-edge spectra. The near-edge features are related to transitions from core levels to unoccupied Fe or Cu 3d orbitals in the fundamental gap, or to unoccupied orbitals (e.g. Fe p, Cu p or S s, p and d) in the CB. More quantitatively, the DOS calculation[8] can be directly compared with near-edge structures, and this comparison has already shown reasonable agreement for the S K-edge and Fe K-edge spectra[13]. For example, peaks a and c in the S K-edge spectrum correspond to the S 1s $\rightarrow$ Fe 3d/S 3p band and S 1s $\rightarrow$ S 3p-like states, respectively; while the Fe K-edge peak

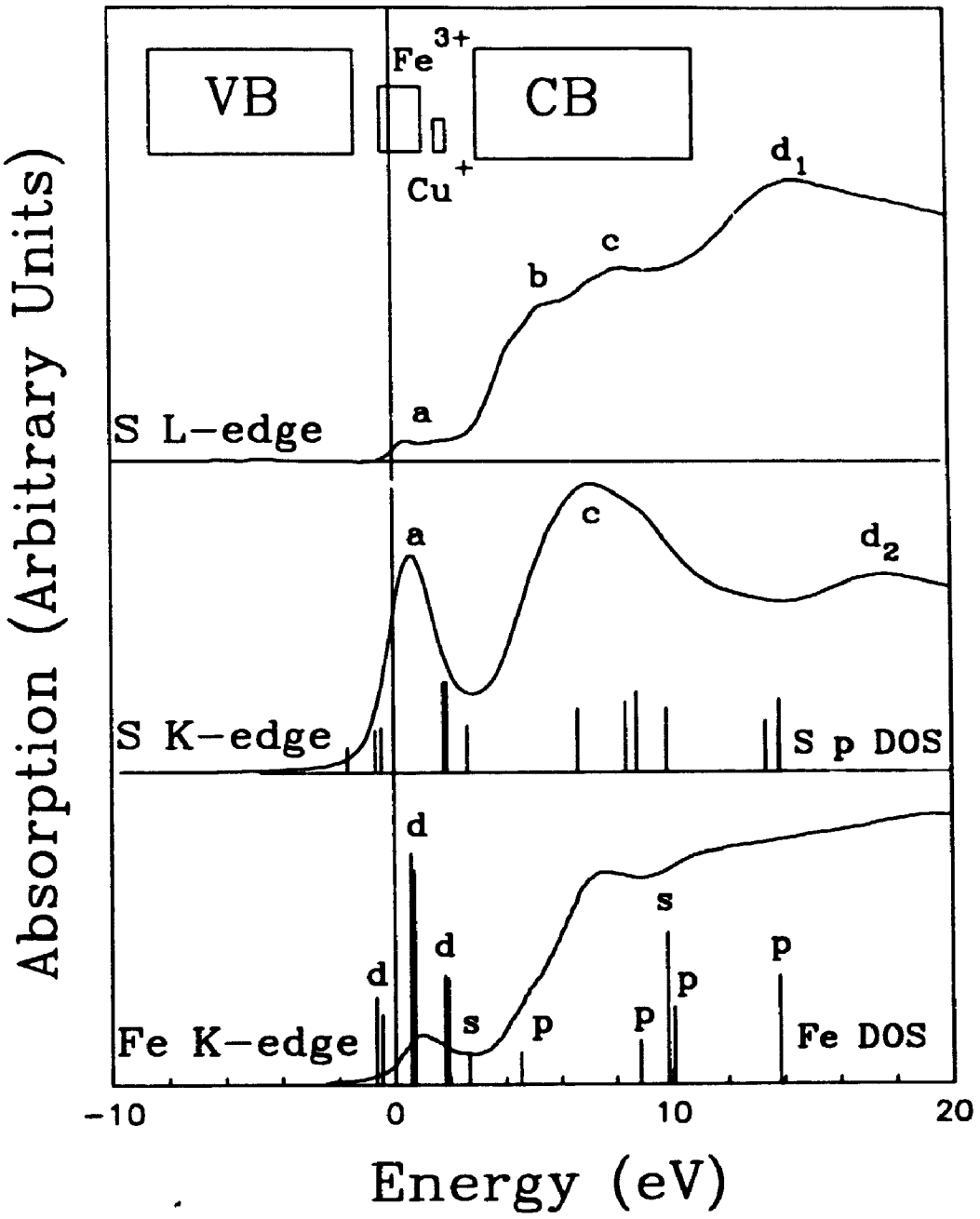

Figure 3.3.1 S K- and L-edge, and Fe K-edge XANES spectra of chalcopyrite. The spectra are aligned by the subtracting the corresponding binding energy (BE). The qualitative MO/energy band diagram[6] and calculated S p and Fe 3d DOS[8] are also shown in this figure.

near the Fermi level corresponds to an Fe 1s → 3d crystal field band in chalcopyrite[6-8]. As shown in Figure 3.3.1 (top), the Cu^{+} and Fe^{3+} 3d crystal field bands are in the fundamental gap,separated by about 1.1 eV, and hybridize with S 3s and 3p orbits[6-8]. Peak d_2 is attributable to transition of S 1s electrons to the S p-like state, and probably also reflects contributions from multiple scattering with more distant atom shells.

Peak a in the S L-edge spectrum corresponds closely in energy to the low energy peak in the S K-edge, Cu K-edge, and Fe K-edge spectra, and must correspond to the transition of S 2p electrons to the S 3s-like states hybridized into the Fe 3d and Cu 3d bands. Peak a is actually split by 1.2 eV, which corresponds to the S 2p spin-orbit splitting. Peaks b, c and d_1 in the S L-edge spectrum cannot be assigned with confidence without a detailed calculation; peak d_1 is strong and is far more intense than the comparable peak in the K-edge spectra (Figure 3.3.1). It is suggest that the stronger peak b is due to the transition to antibonding S 3s or 3p states allowed by vibronic coupling, and that peaks c and d_1 are at least partly due to transitions to e and t_2 states, respectively, from the splitting of the S 3d band in the CB (so called shape resonance)[48].

Cubanite and bornite also have derivative sphalerite structures[49-51]. These crystal structures can be regarded as approximate cubic close-packing of the sulfur atoms, with tetrahedrally-coordinated sulfur and metal atoms. Also, Cu atoms in these minerals are monovalent and Fe atoms are trivalent, but half of the Fe atoms in cubanite must be divalent[9,52,53]. It is expected that these three minerals have similar bonding properties and electronic structure. Figure 3.3.2 shows the S K- and L-edge XANES of low bornite, cubanite and chalcopyrite. The S L-edge spectra (solid curves) are aligned to zero by subtracting the XPS S 2p BE of 161.1 eV for chalcopyrite and cubanite, and 161.5 eV for bornite[9]. The S K-edge spectra (dash curves) are correlated with the L-edge spectra by the S $K\alpha_1$ XES at 2307.8 eV. The energy zero point is close to the Fermi level. The peak positions and assignments are summarized in Table 3.3.1, where ΔE is the energy difference between the peak position and the S 1s BE for the K-edge spectra or the S 2p BE for the L-edge spectra.

By comparing the corresponding S K- and L-edge XANES spectra, it is immediately apparent that the main spectral features of these minerals are very similar.

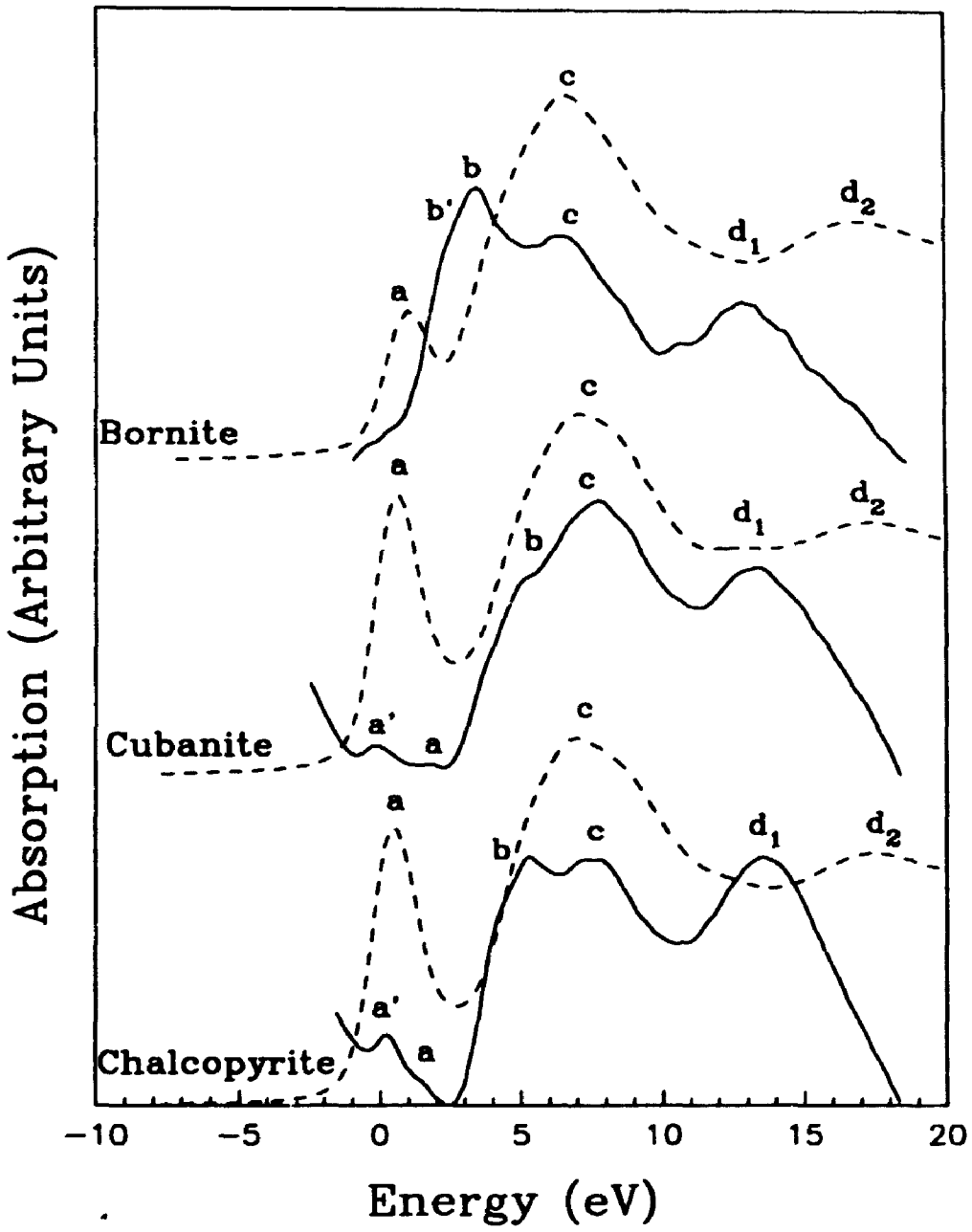

Figure 3.3.2 S K- (dash lines) and L-edge (solid lines) XANES spectra of chalcopyrite, cubanite and bornite. The S K- and L-edge spectra are aligned on a common scale by the S $K\alpha_1$ x-ray emission energy at 2307.8 eV.

Table 3.3.1. S K- and L-edge XANES of chalcopyrite, cubanite and bornite

Minerals	Labels	K-edge (±0.2 eV)*			L-edge (±0.2 eV)*		
		Positions	ΔE	Assignments	Positions	ΔE	Assignments
Chalcopyrite	a'	2469.6	0.7	S 1s → Fe^{3+} 3d + S 3p/3s	161.1	0.0	S $2p_{3/2}$ → Fe^{3+} 3d + S 3s/3p
	a				162.3	1.2	S $2p_{1/2}$ → Fe^{3+} 3d + S 3s/3p
	b'				165.2	4.1	S $2p_{3/2}$ → S 3s/3p-like
	b				166.4	5.3	S $2p_{1/2}$ → S 3s/3p-like
	c	2475.8	6.9	S 1s → S p-like	169.9	8.8	S 2p → e (S 3d-like)
	d				174.8	13.7	S 2p → t_2 (S 3d-like)
	e	2486.5	17.6	S 1s → S p-like			
Cubanite	a'	2469.5	0.6	S 1s → Fe^{3+} 3d + S 3s/3p	161.0	-0.1	S $2p_{3/2}$ → Fe^{3+} 3d + S 3s/3p-like
	a				162.2	1.1	S $2p_{1/2}$ → Fe^{3+} 3d + S 3s/3p-like
	b'				165.3	4.2	S $2p_{3/2}$ → S 3s/3p-like
	b				166.7	5.5	S $2p_{1/2}$ → S 3s/3p-like
	c	2476.0	7.1	S 1s → S p-like	169.3	8.3	S 2p → e (S 3d-like)
	d_1				174.9	13.8	S 2p → t_2 (S 3d-like)
	d_2	2486.7	17.8	S 1s → S p-like			
Bornite	a	2470.0	0.7	S 1s → Fe^{3+} 3d + S 3s/3p			
	b'				162.6	1.1	S $2p_{3/2}$ → S 3s/3p-like
	b				163.9	2.3	S $2p_{1/2}$ → S 3s/3p-like
	c	2475.6	6.3	S 1s → S 3p-like	166.9	5.4	S 2p → e (S 3d-like)
	d_1				173.4	11.9	S 2p → t_2 (S 3d-like)
	d_2	2485.9	16.6	S 1s → S p-like			

* The reading error of the edge peak is ±0.1 eV.

However, for bornite, peak a becomes weak in the S K-edge spectrum, and essentially vanishes in the S L-edge spectrum. These results indicate that in bornite, the S 3p-like DOS decreases in the Fe^{3+} 3d band and the S 3s-like states are minimally mixed into the Fe^{3+} 3d band, probably related to the crystal structure and metal:sulfur ratio of bornite. Frueh[54] computed the principal Brillouin zones of bornite and chalcopyrite and the electron/atom ratios necessary to fill these zones. In order to exactly fill the principal zones, the metal:sulfur ratio must increase from 1:1 for chalcopyrite to 6:4 for bornite. Hence, bornite is a metal-excess sulfide with metal-metal bonds and ordered arrangements of vacancies. The sulfur atoms appear to be five or seven-coordinate while the metals are in tetrahedral coordination. The bonding of sulfur atoms has been described by the sp^3 hybridization scheme, without the participation of S 3d orbitals[55]. Therefore, each sulfur atom in bornite forms four covalent bonds with metals, with one or three ionic bonds. Second, peak b in the L-edge spectrum of bornite increases in intensity and shifts towards lower energy, and peaks c and d_1 also shift to lower energy, but the energy separation between them is similar to that in chalcopyrite and cubanite. A weak peak d_1 in the K-edge spectrum of cubanite indicates some DOS of S p-like states in the t_2 states characteristic of S 3d orbitals. However, the overlapping between the S s-like or empty S 3d-like states and S 3p-like states seems to indicate direct participation of S 3d orbitals in the bonding of sulfur atoms with metals in these sulfides.

3.3.2 Chalcocite, Covellite and Enargite

The structures of low chalcocite (Cu_2S), enargite (Cu_3AsS_4) and covellite (CuS) are based on approximate hexagonal close-packing of the sulfur atoms and three- and four-coordinated geometries for metal atoms. In addition, covellite also contains the covalently bonded S_2^{2-} group. The S K- (dash curves) and L-edge (solid curves) XANES spectra of these minerals and S K-edge spectrum of pyrite (FeS_2) are shown in Figure 3.3.3, in which the alignments of the spectra are similar to Figure 3.3.2 and the S 2p BE values are cited from Nakai et al.[9]. Peak positions and assignments are also summarized in Table 3.3.2. The crystal structure of low chalcocite is very complex. However,

copper and sulfur atoms mainly occupy triangular interstices, with 21 out of the 24 non-equivalent copper atoms forming triangular CuS_3 groups[56]. Peak a in the K-edge spectrum, assigned to the transition of S 1s electrons to the S 3p-like states mixed into a Cu^+ 3d crystal field band, lies at lower energy (2470.1 eV). It is apparent that the Cu^+ 3d crystal field band has a small DOS of S 3p-like states and has little DOS of the S 3s-like states. On the other hand, peak c in the L-edge spectrum is very weak. Only peak d_1 is attributable to transition of S 2p electrons to empty S 3d states. This is also in agreement with S L-edge spectra of the other two- or three-coordinated sulfides, such as native sulfur, realgar (AsS) and orpiment (As_2S_3). These spectral features are closely related to the triangular coordination of Cu with sulfur in chalcocite, and can be used as a structural fingerprint for triangular CuS_3 groups.

Covellite contains layers of planar CuS_3 triangles, the sulfur atoms of which form the apices of pairs of CuS_4 tetrahedra extending above and below[57]. Tetrahedral Cu^+ has R (Cu-S) = 2.31 Å and triangular Cu^{2+} R (Cu-S) = 2.19 Å. Two thirds of the sulfur atoms are combined in S_2^{2-} anions with R (S-S) = 2.07 Å, and one thirds of the sulfur atoms are isolated S^{2-}. In the S K-edge spectrum of covellite, a shoulder at the low energy side of the first peak is observed; these two features are now labelled as peaks a_1 and a_2 and are separated by about 1.4 eV. By comparing the K-edge spectra of chalcocite and pyrite, peaks a_1 and a_2 in the covellite K-edge spectrum correspond to peak a in the K-edge spectra of chalcocite and pyrite, respectively. Hence, peaks a_1 and a_2 are assigned to transition of S 1s electrons to S 3p-like states hybridized with the Cu 3d band in $Cu^{2+}S_3$ and Cu^+S_4 clusters, respectively. The intensity ratio (approximately 1:2) of peak a_1 and a_2 is also in agreement with the atomic ratio of the corresponding sulfur species. Thus, peaks a_1 and a_2 in the S K-edge spectrum clearly determine the identities of isolated S^{2-} and S_2^{2-} species in CuS. Also, the Cu 3d crystal field band for the CuS_3 cluster has little DOS of S 3s-like states; therefore, peak a_1 is not present in the L-edge spectrum of covellite. However, for the tetrahedral CuS_4 cluster, like the tetrahedral FeS_4 cluster in chalcopyrite and cubanite, the Cu 3d crystal field band has significant DOS of S 3s-like states. Peak a_2 is present in the L-edge spectrum of covellite, and its splitting is also due to the spin-orbit interaction of S 2p orbitals.

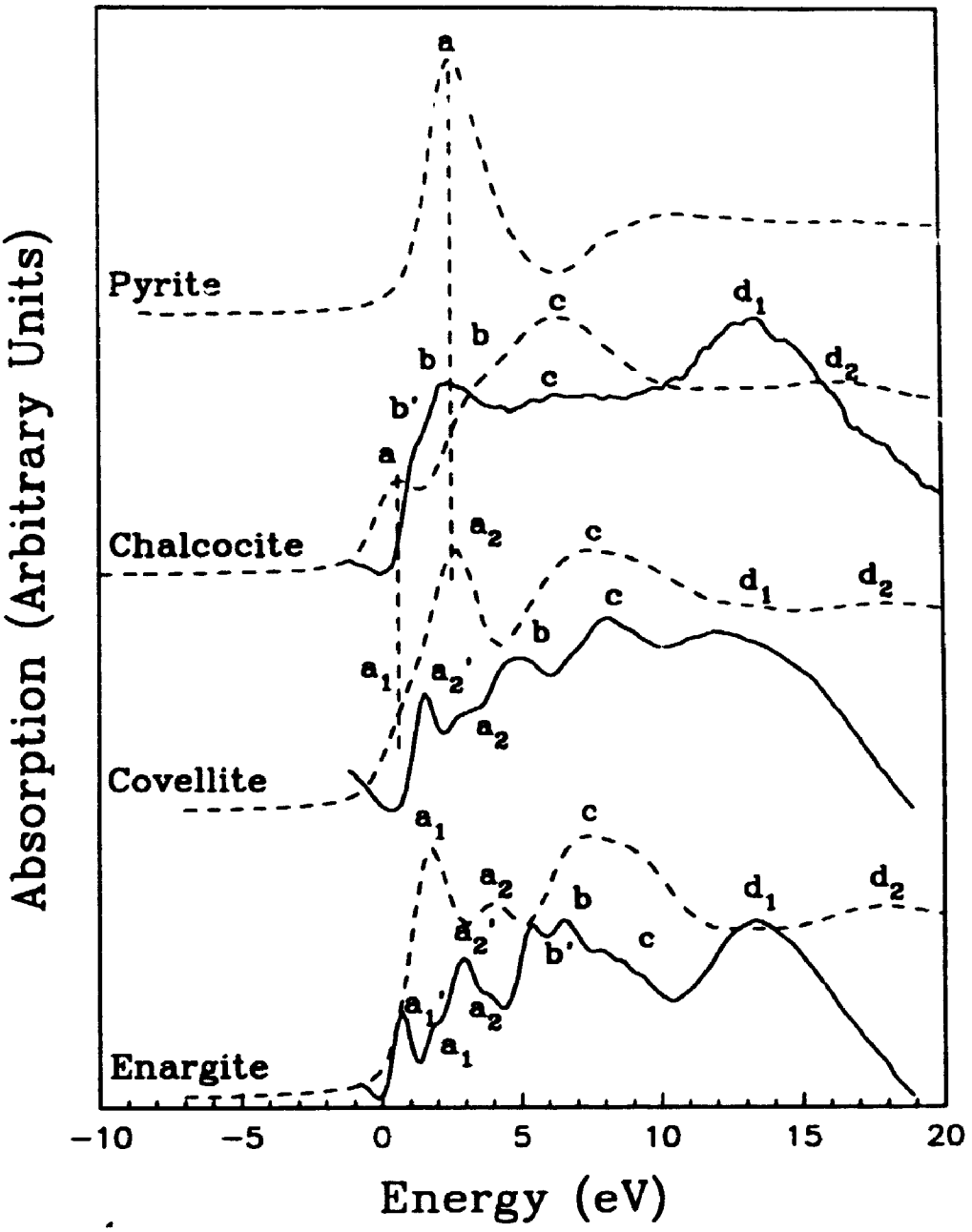

Figure 3.3.3 S K- (solid lines) and L-edge (dash lines) XANES spectra of chalcocite, covellite and enargite. The S K- and L-edge spectra are aligned on a common scale by the S $K\alpha_1$ x-ray emission energy at 2307.8 eV.

Table 3.3.2 S K- and L-edge XANES of chalcocite, covellite and enargite

Minerals	Labels	K-edge (±0.2 eV)*			L-edge (±0.2 eV)*		
		Positions	ΔE	Assignments	Positions	ΔE	Assignments
Chalcocite	a	2470.1	0.8	S 1s → Cu' 3d + S 3p/3s			
	b'				161.6	0.1	S $2p_{3/2}$ → S 3s/3p-like
	b	2472.5	3.2	S 1s → S 3p/3s-like	162.8	1.3	S $2p_{1/2}$ → S 3s/3p-like
	c	2475.1	5.8	S 1s → S p-like	167.1	5.6	S 2p → S 3d-like
	d_1				173.9	12.4	S 2p → S 3d-like
	d_2	2484.6	15.3	S 1s → S p-like			
Covellite	a_1	2470.1	0.5	S 1s → Cu' 3d + S 3p-like			
	a_2'				161.9	0.5	S $2p_{3/2}$ → Cu' 3d + S 3s/3p-like
	a_2	2472.0	1.9	S 1s → Cu' 3d + S 3p/3s	163.1	1.7	S $2p_{1/2}$ → Cu' 3d + S 3s/3p-like
	b'	2474.4	5.2	S 1s → S 3p-like	165.2	3.8	S 2p → S 3s-like
	b	2476.7	7.5	S 1s → S 3p-like			
	c	2478.4	9.2	S 1s → S p-like	168.4	7.0	S 2p → S 3d-like
	d_1				174.6	13.2	S 2p → S 3d-like
	d_2	2487.5	18.3	S 1s → S p-like			
Enargite	a_1'				161.4	0.0	S $2p_{3/2}$ → Cu' 3d + S 3s/3p-like
	a_1	2470.1	0.9	S 1s → Cu' 3d + S 3p/3s	162.6	1.2	S $2p_{1/2}$ → Cu' 3d + S 3s/3p-like
	a_2'				163.6	2.2	S $2p_{3/2}$ → Cu' 3d + S 3s/3p-like
	a_2	2472.3	3.1	S 1s → Cu' 3d + S 3p/3s	164.7	3.3	S $2p_{1/2}$ → Cu' 3d + S 3s/3p-like
	b'				166.1	4.7	S 2p → S 3s-like
	b	2476.0	6.8	S 1s → S 3p-like	167.3	5.9	S 2p → S 3s-like
	c	2478.1	8.9	S 1s → S p-like	169.5	8.1	S 2p → S 3d-like
	d_1	2482.2	13.0	S 1s → S p-like	174.1	12.7	S 2p → S 3d-like
	d_2	2487.0	17.8	S 1s → S p-like			

* The reading error of the edge peak is ±0.1 eV.

Enargite has a monoclinic structure in which there are three non-equivalent sulfur atoms[58]. Two sulfur atoms are triangularly coordinated with three Cu^+ atoms or two Cu^+ atoms plus one As^{5+} atom, while the other sulfur atom is tetrahedrally coordinated with three Cu^+ atoms and one As^{5+} atom. The observation of a distinct peak a_2 in the K-edge spectrum of enargite is unique, compared to the K-edge spectra of the other samples. However, as in covellite, peaks a_1 and a_2 in the S K-edge spectrum of enargite are separated by 2.2 eV, and attributed to transitions of S 1s electrons to S 3p-like states mixed into a Cu^+ crystal field band. Furthermore, peak a_1 corresponds to sulfur atoms in a triangular group, and peak a_2 to sulfur atoms in a tetrahedral group. This assignment is confirmed by the relative intensities of peaks a_1 and a_2 and by MO calculations for CuS_4^{7-} and CuS_3^{5-} clusters. First, the relative intensities of peaks a_1 and a_2 are in qualitative agreement with the atomic ratio (2:1) of triangular and tetrahedral sulfur species. Second, MO calculations also indicated that the Cu^+ crystal field band for the tetrahedral CuS_4^{7-} cluster is about 1.6 eV above that for the triangular CuS_3^{5-} cluster[5], in qualitative agreement with the energy separation of peaks a_1 and a_2.

The S L-edge spectrum of enargite has rich features. Peaks a_1 and a_2 are aligned well in both K- and L-edge spectra, peaks a_1 and a_2 in the L-edge spectrum are also attributable to the transitions of S 2p electrons to the S 3s-like states mixed into a Cu^+ crystal field band. Peak a_1 corresponds to triangular sulfur atoms, and peak a_2 to tetrahedral sulfur atoms. Again peaks a_1 and a_2 are split by about 1.1 eV, due to the spin-orbit interaction of S 2p orbitals. Peak b in the L-edge spectrum is due to transition of S 2p electrons to S 3s-like states, and also is split by spin-orbit interaction of S 2p orbitals.

3.3.3 Stannite and Tetrahedrite

Figure 3.3.4 shows S K- and L-edge XANES spectra of stannite and tetrahedrite. The peak positions and assignments are also summarized in Table 3.3.3. Stannite also has a derivative sphalerite structure[63]. The Cu atom is monovalent[9], and the Fe atom is divalent[56]. It is expected that it should have similar electronic structure and spectral

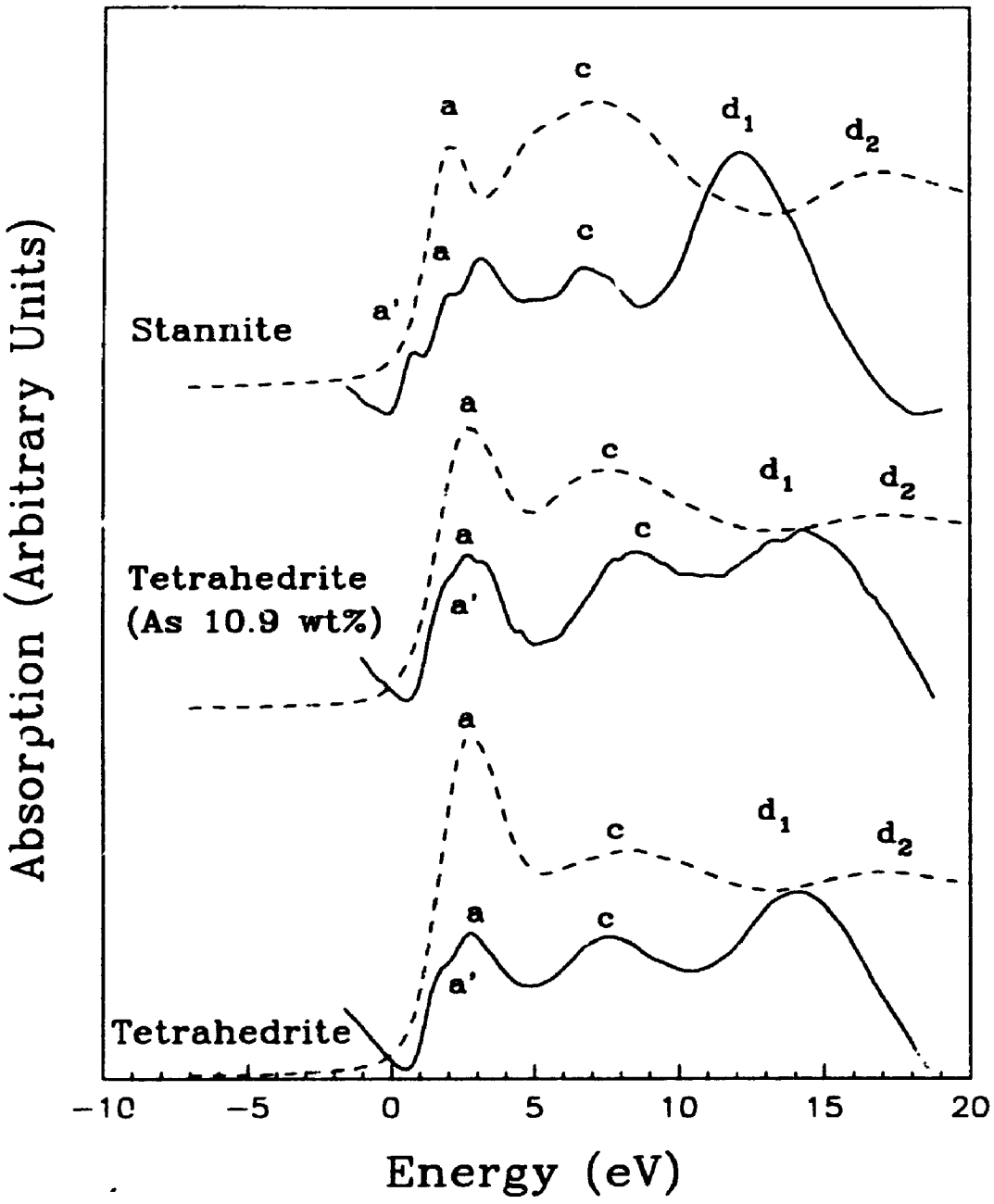

Figure 3.3.4 S K- (solid lines) and L-edge (dash line) XANES spectra of stannite and tetrahedrite. The S K- and L-edge spectra are aligned by the S $K\alpha_1$ x-ray emission energy at 2307.8 eV.

Table 3.3.3 S K- and L-edge XANES of stannite, tetrahedrite and carrollite

Minerals	Labels	K-edge (±0.2 eV)*			L-edge (±0.2 eV)*		
		Positions	ΔE	Assignments	Positions	ΔE	Assignments
Stannite	a'	2470.8	1.9	S 1s → Cu' 3d + S 3p/3s	161.7	0.6	S $2p_{3/2}$ → Cu' 3d + S 3s/3p-like
	a				162.8	1.7	S $2p_{1/2}$ → Cu' 3d + S 3s/3p-like
	b				163.8	2.7	S 2p → S 3s-like
	c	2475.7	6.8	S 1s → S p-like	166.6	5.5	S 2p → e (S 3d-like)
	d_1				173.3	11.2	S 2p → t_2 (S 3d-like)
	d_2	2485.5	16.6	S 1s → S p-like			
Tetrahedrite	a'				161.5	0.2	S $2p_{3/2}$ → Cu' 3d + S 3s/3p-like
	a	2470.9	1.8	S 1s → Cu' 3d + S 3p/3s	162.8	1.5	S $2p_{1/2}$ → Cu' 3d + S 3s/3p-like
	c	2476.6	7.5	S 1s → S p-like	168.2	6.9	S 2p → e (S 3d-like)
	d_1				174.7	13.4	S 2p → t_2 (S 3d-like)
	d_2	2485.2	16.1	S 1s → S p-like			
Carrollite	a'				161.1	0.0	S $2p_{3/2}$ → M 3d + S 3s/3p-like
	a	2469.7	0.8	S 1s → M 3d + S 3p/3s	162.3	1.2	S $2p_{1/2}$ → M 3d + S 3s/3p-like
	b	2477.1	8.2	S 1s → S p-like	168.2	7.1	S 2p → S 3s-like
	c	2480.3	11.4		171.7	10.6	S 2p → e (S 3d-like)
	d_1				176.2	15.1	S 2p → t_2 (S 3d-like)
	d_2	2487.3	18.4	S 1s → S p-like			

* The reading error of the edge peak is ±0.1 eV.

features to chalcopyrite. However, peak a in both K- and L-edge spectra of stannitemoves up by about 1.2 and 0.6 eV, respectively, compared to chalcopyrite, and is close to peak a in the spectra of the other sulfides containing CuS_4^{7-} cluster. Therefore, peak a in the S K- and L-edge spectra of stannite is assigned to the transition of S 1s and 2p electrons, respectively, to the S 3p- and 3s-like states mixed into a Cu^+ crystal field band, instead of a Fe^{2+} crystal field band. This assignment is in agreement with MO calculations for FeS_4^{6-} (Fe^{2+}), CuS_4^{7-} (Cu^+) and FeS_4^{5-} (Fe^{3+})[6]. These results also confirm that in the tetrahedral structure, the Fe^{2+} crystal field band has little DOS of S 3s- and 3p-like states.

The general formula representing the naturally occurring tetrahedrite-tennantite is $(Cu,Ag)_{10}(Zn,Fe,Cd,Hg,Cu)_2(Sb,As,Bi)_4S_{13}$ and denoted as $M_{10}^{+}M_2^{2+}M_4^{3+}S_{13}$. The mineral has a cubic structure based on that of sphalerite. The crystal chemistry of tetrahedrite has been studied in detail[60-64]. In a half unit cell of end-member tetrahedrite, 12 S atoms are 4-coordinated and the other single S atom is 6-coordinated; 6 Cu^+ atoms are 3 coordinated; 2 Cu^{2+} and 4 Cu^+ atoms are 4 coordinated; and the Sb atoms occupy the equivalent of a tetrahedral site in sphalerite but are bonded to only three sulfur atoms with a lone pair of electrons.

The S K- and L-edge XANES spectra of two tetrahedrite samples, one of which contains As up to 13 wt%, are shown in Figure 3.3.4. The peak positions and assignments are summarized in Table 3.3.3. The spectra basically reflect the features of four-coordinate sulfur atoms in a CuS_4 cluster. Peak a becomes broad, probably related to the presence of six-coordinate sulfur atoms. However, peak a in both K- and L-edge spectra move up by about 1.3 eV, compared to chalcopyrite, because peak a is assigned to transitions of S 1s (for K-edge) or 2p (for L-edge) electrons to the S 3p-like and 3s-like states, respectively, mixed into a Cu^+ crystal field band, rather than a Fe^{3+} crystal field band. In fact, MO calculations[6] indicated the Cu^+ 3d crystal field band lies about 1.2 eV above the Fe^{3+} 3d crystal field band in chalcopyrite. Compared to chalcocite, peak a shifts to higher energy by about 0.8 eV, in good agreement with the MO/energy band calculation[5]. Also peak a is more intense in tetrahedrite than in chalcocite, indicating the higher DOS of S 3s- and 3p-like states in the Cu^+ crystal field

band and the stronger metal-sulfur bonding in tetrahedrite. The S K- and L-edge XANES of both tetrahedrite samples are very similar, indicating that the substitution of As atoms for Sb atoms in tetrahedrite has little influence on the XANES spectra, and also on the electronic structure of tetrahedrite. However, some minor changes are observed; for example, peak c in the K-edge spectrum shifts to lower energy by about 1 eV, and peak d_1 in the L-edge spectrum to higher energy by about 1 eV, with the substitution of Al for Sb.

3.3.4 Carrollite and Linnaeite

The thiospinel minerals (AB_2S_4) have the spinel structure in which S atoms form a cubic-closest-packed sublattice, with half of the octahedral holes and one-eight of the tetrahedral holes occupied by metal ions. The qualitative bonding models of thiospinel minerals have been described by Goodenough[22] and Vaughan et al.[23]. More recently, Vaughan and Tossell[24] carried out MO calculations employing the SCF-X_α scattered-wave cluster method to model the electronic structure of the thiospinel minerals linnaeite (Co_3S_4), carrollite ($CuCo_2S_4$) and greigite (Fe_3S_4).

S K- and L-edge XANES spectra of carrollite and linnaeite are very similar, and the spectra of carrollite are shown in Figure 3.3.5, together with the Co and Cu K-edge spectra. The S L- and K-edge spectra are aligned to zero by the $2p_{3/2}$ BE of 162.3 eV[9] and S 1s BE calculated by the sum of the S $2p_{3/2}$ BE and S $K\alpha_1$ x-ray emission energy at 2307.8 eV, respectively. The Co and Cu K-edge spectra are digitized from Charnock et al.[27] and realigned with the S K- and L-edge spectra by an approximate 5 eV shift toward higher energy, because the main edge was taken as energy zero in Charnock et al.[27]. The peak positions and assignments are summarized in Table 3.3.3.

Carrollite has the normal spinel structure, with low-spin Co^{3+} occupying half of the octahedral sites, and Cu^{2+} occupying one-eight of the tetrahedral sites. The Co^{3+} in the octahedral (B) sites has bonding (σ_B) and antibonding (σ_B^*) molecular orbitals formed by overlap of Co^{3+} e_g, 4s, 4p orbitals with S 3s and 3p orbitals. Filled t_{2g} orbitals probably remain essentially non-bonding. For Cu^{2+} in the tetrahedral (A) sites, the e

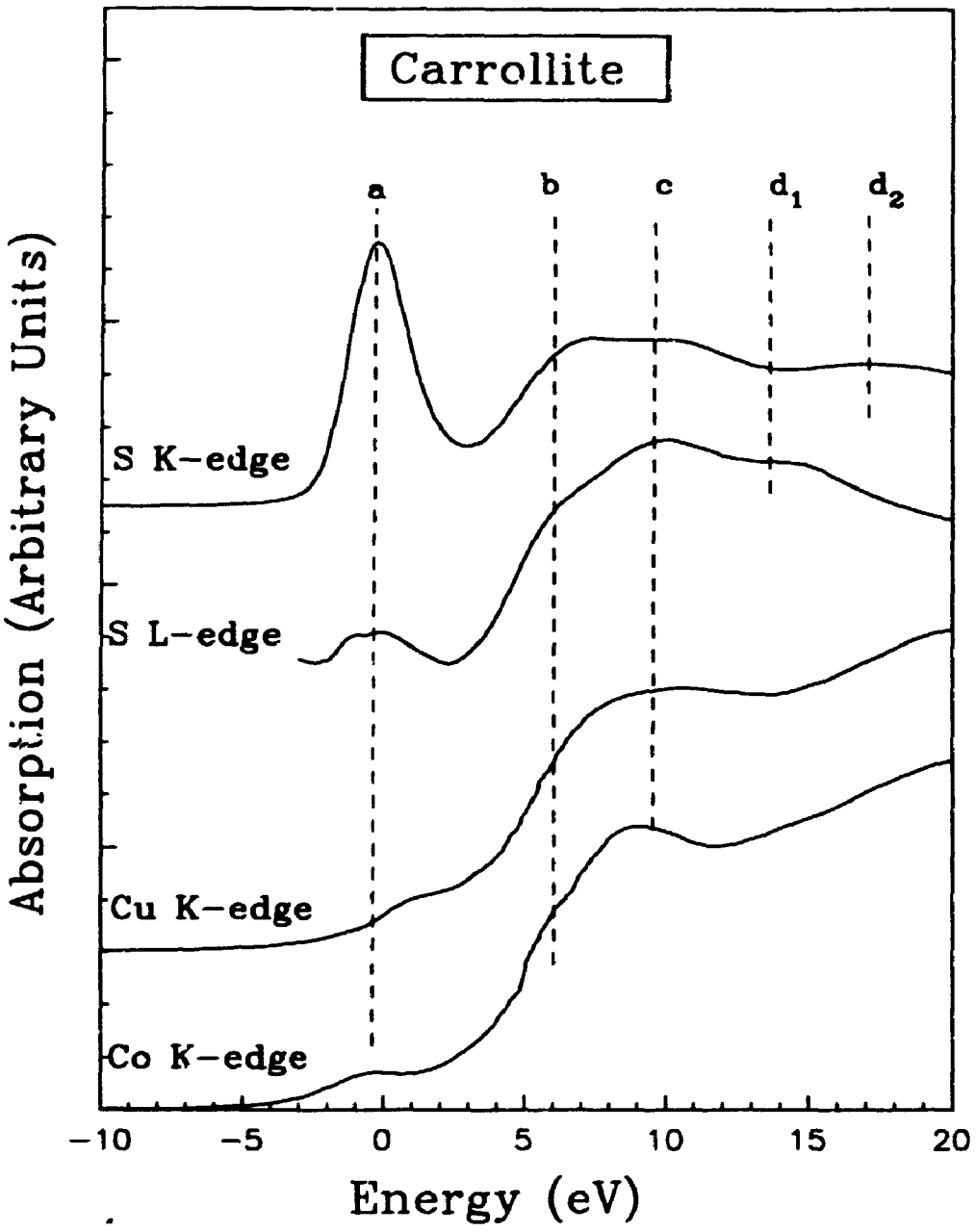

Figure 3.3.5 S K- and L-edge XANES spectra of carrollite, together with Cu and Co K-edge XANES spectra. The spectra are aligned by subtracting the S 1s, S 2p, Cu and Co 1s BE, respectively.

orbitals remain non-bonding, whereas t_2, 4s and 4p orbitals form σ_A and σ_A^*. The pre-edge in the Cu and Co K-edge spectra of carrollite is assigned to Cu 1s → 3d and Co 1s → 3d transitions, respectively. Peak a in both S K- and L-edge spectra are well aligned, and also approximately correspond to the pre-edge in the Cu and Co K-edge spectra. Hence, peak a in the S K- and L-edge spectra are assigned to transitions of S 1s and 2p electrons to S 3p- and 3s-like states, respectively, mixed into the σ_B^* and/or σ_A^* bands. The interpretations of peaks b, c, d_1 and d_2 in the XANES spectra are also similar to those for the other Cu-containing sulfides. The S K- and L-edge spectra of carrollite are in good agreement with the qualitative bonding models[22,23] and MO calculations[24], but provide new experimental information on the bonding and the CB structure of carrollite. First, the unoccupied Co and Cu 3d crystal field bands have a large contribution of S 3p states and some feature of S 3s states, and the metal 3d electrons involve the bonding of the metals with S atoms. Second, the CB bottom, characterized by metal sp states[22,23], has high DOS of S 3s- and 3p-like states, also indicating strong mixing of the metal sp states and S 3s- and 3p-like states.

3.3.5 Pyrrhotite and Pyrite

Figure 3.3.6 shows the S K- and L-edge XANES spectra of pyrrhotite, together with Fe K-edge XANES of FeS. The S L-edge spectrum is aligned to zero by subtracting the S $2p_{3/2}$ BE of FeS at 161.2 eV, and the S K- and L-edge spectra are correlated by the S $K\alpha_1$ XES energy at 2307.8 eV. The Fe K-edge spectrum of FeS is digitized from Sugiura[44], and aligned to zero by subtracting the Fe 1s BE calculated by the sum of the Fe $2p_{3/2}$ BE of 710.1 eV and $K\alpha_1$ x-ray emission energy at 6403.8 eV. The S K-edge spectra of pyrrhotite is also similar to previous results[45-47].

Pyrrhotite has a NiAs-type structure, in which each Fe atom is coordinated to six S atoms at the corners of a distorted octahedron, and each S atom is coordinated to six Fe atoms at the corners of a trigonal prism. The six Fe^{2+} $3d^6$ electrons in pyrrhotite have high spin t_{2g}^4-e_g^2 configuration, so that the majority spin t_{2g}^{α} and e_g^{α} bands are filled, while the minority spin t_{2g}^{β} is partly filled, and the minority spin e_g^{β} is completely

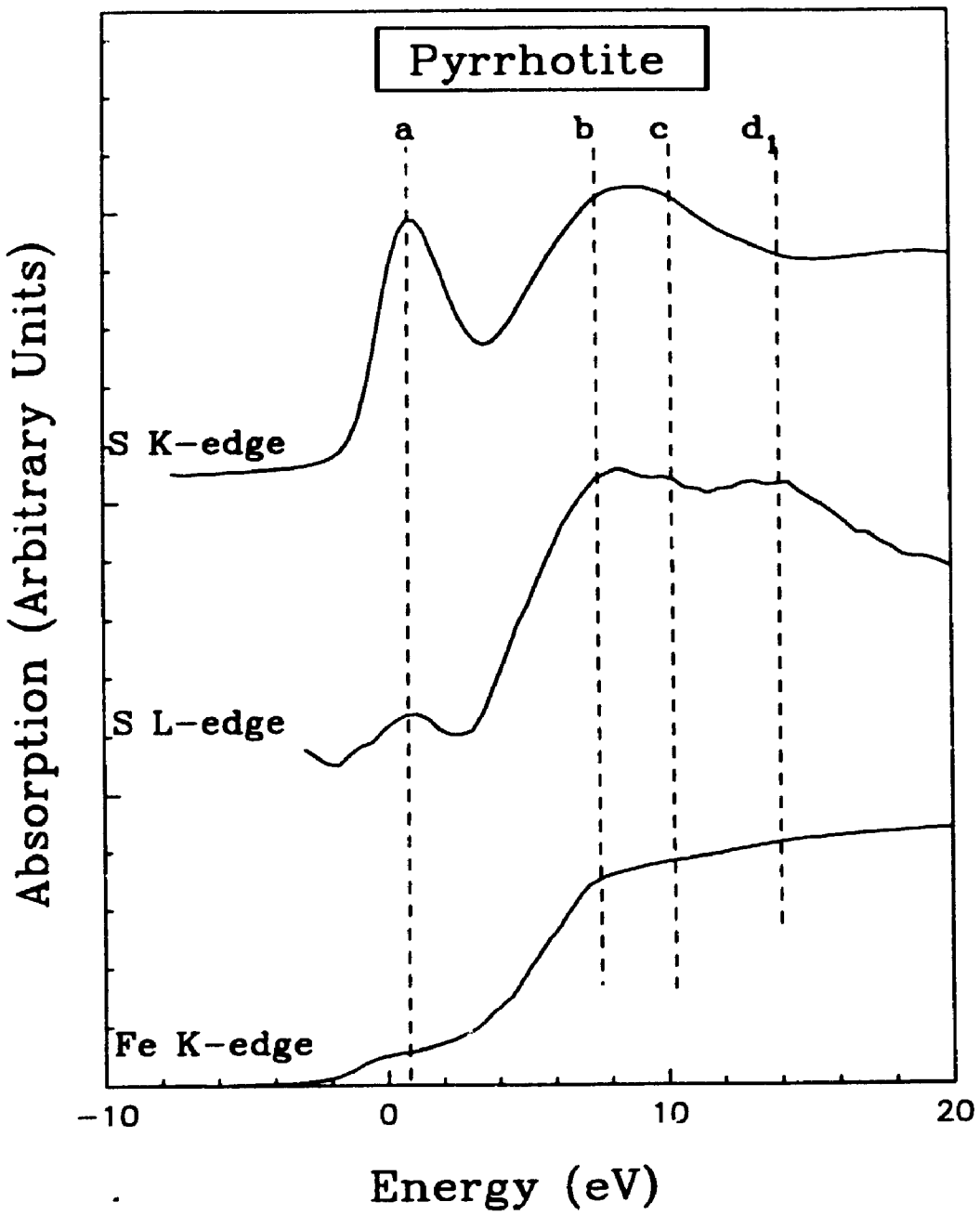

Figure 3.3.6 S K- and L-edge XANES spectra of pyrrhotite, together with Fe K-edge spectra. The spectra are aligned by subtracting the S 1s, S 2p and Fe 1s BE, respectively.

empty[37,41]. In the Fe K-edge spectrum, peak a is assigned to the transition of Fe 1s electrons to unoccupied 3d orbitals (t_{2g}^{β} and e_g^{β}). This transition is forbidden by quantum selection rules, however, the distortion of the coordination octahedra of the Fe atom mixes the Fe 3p and 3d orbitals, and makes this Fe 1s → 3d transition possible, even though its intensity is weak. Peak a in both S K- and L-edge spectra corresponds to peak a in the Fe K-edge spectrum, within ±0.5 eV, and is assigned to transitions of S 1s and 2p electrons, to S 3p- and 3s-like states, respectively, mixed into the unoccupied Fe 3d crystal field bands in the fundamental gap. Peak c in the S K-edge spectrum is assigned to transition of S 1s electrons to the S 3p-like states. In the L-edge spectrum, peak b is due to transition to S 3s-like states, and peaks c and d_1 are attributed to transitions of S 2p electrons to the S 3d-like t_{2g} and e_g bands, so called shape resonances. These results indicate that the Fe 3d crystal field band in the fundamental gap is hybridized with S 3p and 3s states, and the CB minimum is characterized by Fe s- and p-like states whose DOS is also overlapped with S 3s-, 3p- and even 3d-like states. This seems contrary to recent electronic band calculation of cubic and tetragonal FeS which claimed that the Fe-S bond is mainly ionic with little covalent mixing[38].

Figure 3.3.7 compares the S K- and L-edge XANES spectra of pyrite, and the Fe K-edge spectrum of pyrite digitized from Drager et al.[65]. The S L-edge spectrum is aligned to zero by subtracting the S $2p_{3/2}$ BE of 162.4 eV[66], and the S K-edge spectrum is correlated with the L-edge spectrum by S $K\alpha_1$ x-ray emission energy at 2307.8 eV. The Fe K-edge spectrum is aligned to zero by the Fe 1s BE calculated by adding Fe $2p_{1/2}$ BE of 706.5 eV and $K\alpha_1$ x-ray emission energy at 6304.8 eV. The partial DOS of S 3p and Fe 3d states in the first empty band of pyrite, digitized from Bullett[33] and aligned by calibrating the Fermi level (E_F) to energy zero, are included for comparison. The S K- and L-edge spectra of native sulfur are also shown as dash curves for comparison. The S K- and L-edge spectra of pyrite are in good agreement with the previous results[45,46].

In the structure of pyrite each Fe atom is coordinated to six S atoms at the corners of a slightly distorted octahedron with a Fe-S distance of 2.26 Å, while each S atom is bound to another S atom with the S-S distance of 2.08 Å and three Fe atoms. Pyrite is a semiconductor, because the Fe 3d crystal field band lies in the fundamental gap. The

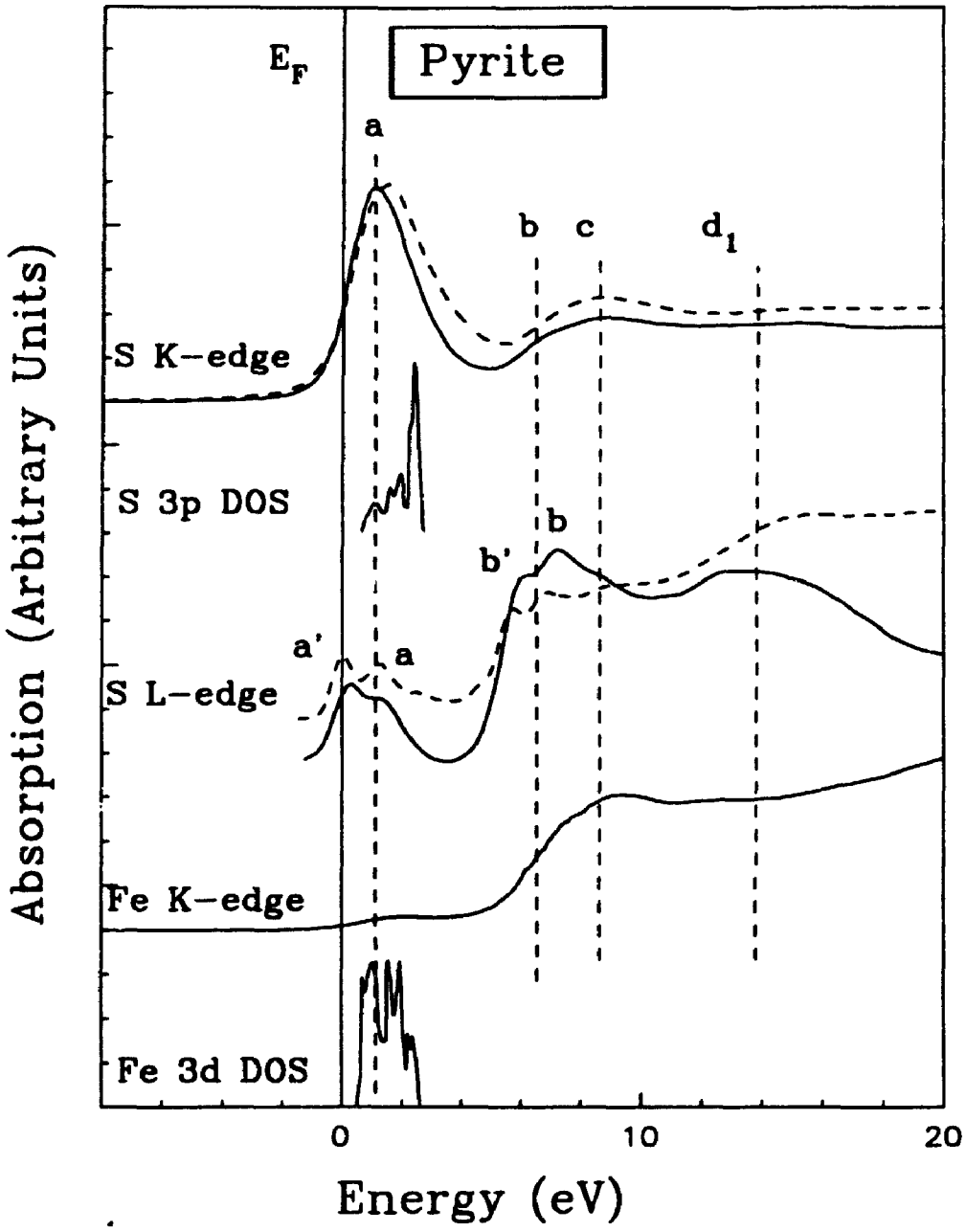

Figure 3.3.7 S K- and L-edge XANES spectra of pyrite, together with Fe K-edge spectrum. The spectra are aligned by subtracting S 1s, S 2p and Fe 1s BE, respectively. S K-edge spectra of native sulfur, and the S 3p-like and Fe 3d DOS calculated[33] are also included in this figure for comparison.

Fe^{2+} 3d electrons have low spin t_{2g}^6-e_g^0 configuration, and the filled t_{2g}^6 and empty e_g^0 are separated by about 0.7 eV defining the indirect energy gap of pyrite[33]. On the other hand, the MO calculation on the S_2^{2-} ion also indicated that there is no complete distinction between the antibonding S $p\sigma^*$ band and the empty Fe e_g^0 (3d) band, even though the former orbitals contribute principally at the top of the first unoccupied band[29,32,33]. By comparison with the calculated DOS, peak a in the S K-edge spectrum is assigned to transition of S 1s electrons to the S 3p-like states in the first unoccupied Fe e_g and S $p\sigma^*$ band, in agreement with Fe K-edge spectrum. Although calculated DOS of the S s- and d-like states are not available, peak a in both S K- and L-edge spectra are aligned well, within 0.4 eV, so that peak a in the S L-edge spectrum also appears to be attributable to the transition of S 2p electrons to S 3s-like states in this empty band. Peak b in the S L-edge spectrum is assigned to transition of S 2p electrons to the antibonding S 3s-like states at the CB minimum, and peaks c and d_1 to the S 3d-like e and t_2 states, respectively. Peaks a and b are each split by 1.2 eV, apparently due to the spin-orbit interaction of S 2p orbitals. These results also demonstrate that the first unoccupied state of pyrite is the Fe^{2+} 3d crystal field band strongly mixed with S 3s- and 3p-like states, and there is a strong overlap between the Fe p-like states and S 3s- and 3p-like states at the CB minimum.

The S K- and L-edge spectra of marcasite, the other important polymorph of FeS_2, are very similar to those of pyrite, except for a shift of about 0.2 eV to low energy, which is also in agreement with the electronic structure calculation of pyrite- and marcasite-type sulfides[33]. On the other hand, the S K- and L-edge spectra of pyrite and pyrrhotite are, in general, very similar, because their basic structural unit is the FeS_6^{10-} cluster. However, there are two significant differences. First, peak a in both S K- and L-edge spectra of pyrite shifts to high energy by about 1.5 eV. This is mainly dependent on the difference in Fe-S bond distances in pyrite and pyrrhotite. The MO/energy band calculation indicated that the unoccupied Fe e_g sub-band moves to high energy by about 1.2 eV when the Fe-S bond distance decreases from 2.38 Å in monoclinic pyrrhotite to 2.26 Å in pyrite, in good agreement with the S K- and L-edge spectra. Second, peak a in the S K-edge spectrum of pyrite greatly increases in intensity; peak a is much more

intense than peak c for pyrite, while peak a is somewhat weaker than peak c for pyrrhotite; also peak a in the S L-edge spectrum of pyrite is much stronger than that for pyrrhotite. This indicates stronger mixing of S 3s and 3p states into the Fe 3d band in pyrite, which is apparently attributed to the presence of the S_2^{2-} ion, giving overlapping of the antibonding S $p\sigma^*$ band with the empty Fe e_g (3d) band. The similarity between both S K- and L-edge spectra of pyrite and native sulfur (see Figure 3.3.7) also supports this interpretation of the spectral features and emphasizes that the molecular S_2^{2-} ion is a dominant feature in the electronic structure of pyrite.

3.4 Discussion

Figure 3.4.1 shows schematic MO/energy band models for Cu^+-Fe^{3+} sulfides[6] on the left hand side, and for trigonally- and tetrahedrally-coordinate Cu^+ sulfides[5] on the right hand side. The qualitative assignment of peak a in both S K- and L-edge XANES spectra of these sulfides is also indicated. The S K- and L-edge spectra of these Cu sulfides are in very good agreement with MO/energy band calculations[6,8].

The results indicate that the Fe^{3+} 3d crystal field band in the fundamental energy gap of Cu^+-Fe^{3+} sulfides with tetrahedral structure have significant DOS of S 3s- and 3p-like states. However, the Cu^+ 3d crystal field band has little DOS of S 3s- and 3p-like states. This is in agreement with the DOS calculated by Hamajima et al.[8], although the relative energy positions of Cu^+ and Fe^{3+} 3d bands in that calculation[8] differ from Vaughan and Tossell's calculation[6].

In transition metal sulfides, the roles of metal d electrons in the metal-sulfur bonding have long been controversial. The S K- and L-edge XANES spectra of Cu and/or Fe sulfides reflect the partial DOS of unoccupied S 3p- and 3s- or 3d-like states near and above the Fermi level of these sulfides, and certainly provide important information on the bonding roles of Cu or Fe 3d electrons. For Cu^+-Fe^{3+} sulfides having derivative sphalerite structures with the tetrahedral MS_4 cluster, such as chalcopyrite, cubanite and bornite, stannite, the S K- and L-edge XANES spectra show that the Cu^+ 3d band lies above the Fe^{3+} 3d band by about 1.3 eV, in agreement with

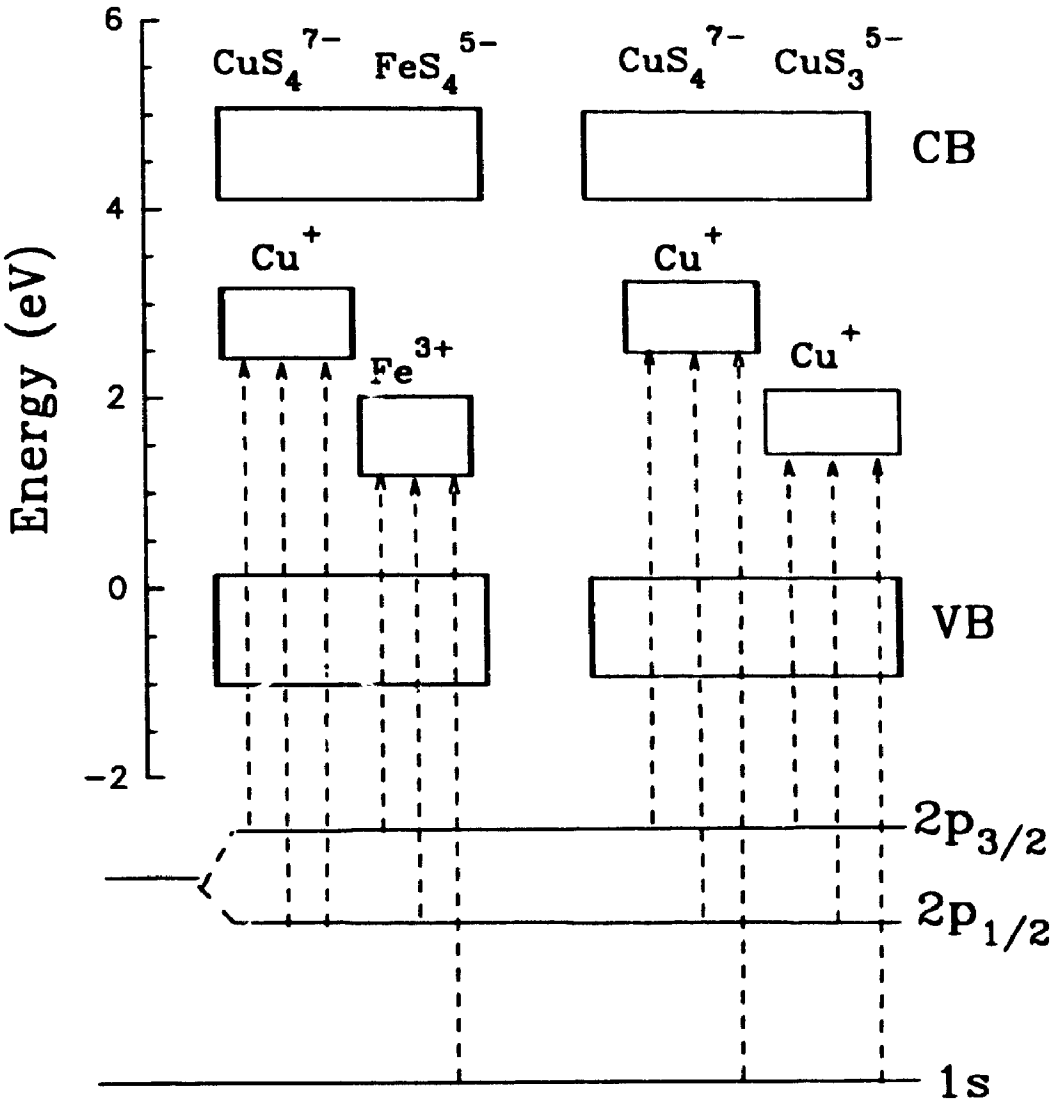

Figure 3.4.1 Qualitative energy band scheme of Cu and Cu-Fe sulfides. The transitions corresponding to peak a in both S K- and L-edge spectra of Cu sulfide minerals are indicated by arrow lines.

the MO/energy band calculation[6]. On the other hand, the Fe^{3+} 3d crystal field band contains significant DOS of unoccupied S 3p- and 3s-like states, whereas the Cu^{+} 3d crystal field band probably has little DOS of the S 3p- and 3s-like states, in agreement with the DOS calculated by Hamajima et al.[8]. These results indicate that Fe^{3+} 3d electrons more strongly involve the bonding of metal with sulfur than Cu^{+} 3d electrons in these minerals. This is probably related to the smaller Fe 3d MO energy and the fact that the Fe^{3+} 3d orbitals are half filled, so that the S 3p- and 3s-like states favor mixing with the Fe^{3+} 3d orbital, rather than the Cu^{+} 3d orbitals. For stannite containing Cu^{+} and Fe^{2+}, rather than Fe^{3+}, the Fe^{2+} 3d crystal field band has little or no DOS of S 3p- and 3s-like states, which is similar to sphalerite containing Fe^{2+}. Hence, the Fe^{2+} 3d electrons in these sulfides with tetrahedral structure probably play little role in the bonding of metal with sulfur.

For the remaining Cu^{+} sulfides, such as chalcocite, covellite, enargite, carrollite, and tetrahedrite, the S K- and L-edge XANES also demonstrate that the Cu^{+} 3d crystal field band has apparent DOS of S 3s- and 3p-like states. Also, the Cu^{+} 3d band is at higher energy and has much higher DOS of S 3s- and 3p-like states in sulfides containing CuS_4 cluster that in sulfides containing CuS_3 cluster. These results a in agreement with MO/energy band calculation[5], and indicate that the Cu^{+} 3d electrons strongly participate in the bonding of Cu with sulfur in metal sulfides. Particularly in sulfides of tetrahedral coordination geometry, the bonding participation of Cu^{+} 3d electrons with S 3p and 3s states becomes much stronger. For both Cu^{+} and Fe^{3+}, tetrahedral coordination geometry apparently favors the mixing of both S 3p and 3s states into the metal 3d crystal field bands and the bonding involvement of the metal 3d electrons with S 3p and 3s states.

Although in the tetrahedral structure, the Fe^{2+} 3d crystal field band has little DOS of S 3p- and 3s-like states, in octahedral structures, such as pyrite and pyrrhotite, the S K- and L-edge XANES spectra demonstrate that the Fe^{2+} 3d crystal field bands have a very high DOS of S 3p- and 3s-like states, particularly for the pyrite structure containing S_2^{2-} group. Therefore, in the octahedral coordination structure, Fe^{2+} 3d electrons apparently do contribute to the bonding of Fe^{2+} with sulfur in the Fe sulfide minerals.

3.5 Conclusions

S K- and L-edge XANES spectra of Cu and/or Fe sulfides are interpreted based on MO/energy band diagrams. These reflect the DOS of S s-, p- and d-like states in the CB, and provide important information on the roles of transition metal 3d electrons in the bonding of the metals with sulfur and the electronic states near and above the Fermi level. In sulfides containing both Fe^{3+} and Cu^{+}, the DOS of 3p- and 3s-like states are much more strongly mixed into the Fe^{3+} 3d crystal field band which is half filled, rather than into the full Cu^{+} 3d band. For Cu sulfide minerals, although the Cu^{+} 3d crystal field band is full, the S 3p- and 3s-like state can be hybridized into it, their DOS is dependent on the coordination geometries of Cu. The DOS of S 3p- and 3s-like states mixed into the Cu^{+} 3d band is much higher in the sulfides containing the CuS_4^{7-} cluster than in the sulfides containing the CuS_3^{5-} clusters. The first unoccupied states move to higher energy for CuS_4^{7-} clusters compared to that for CuS_3^{5-} clusters. For Fe sulfides with tetrahedral structures, the Fe^{2+} 3d crystal field band has little DOS of S 3s- and 3p-like states in tetrahedral structure. The Fe^{3+} 3d band is at low energy and has a very high DOS of S 3s- and 3p-like states. However, the Fe^{2+} crystal field band is shown to be mixed with significant DOS of S 3s- and 3p-like states, and moves to higher energy in the pyrite structure than in the pyrrhotite structure. Therefore, as a simple fingerprint, the S K and L-edge XANES spectra provide information on the local structure of sulfur atoms in these sulfides, can distinguish between Fe^{2+} and Fe^{3+} atoms in tetrahedral symmetry, between tetrahedral and octahedral geometries of Fe^{2+}, and between CuS_4^{7-} and CuS_3^{5-} clusters in metal sulfides.

3.6 References

1. P.L. Ribbe, *Sulfide Mineralogy*. Mineralogical Society of America, 1977.
2. D.J. Vaughan and J.R. Craig, *Mineral Chemistry of Metal Sulfides*. Cambridge University Press, Cambridge, London, 1978.
3. J.A. Tossell and D.J. Vaughan, *Theoretical geochemistry: Application of Quantum*

Mechanics in the Earth and Mineral Sciences. Oxford University Press. New York-Oxford, 1992, pp. 274.

4. R.J. Goble, *Can. Mineral.* **23**, 61 (1985).
5. J.A. Tossell, *Phys. Chem. Minerals* **2**, 225 (1978).
6. D.J. Vaughan and J.A. Tossell, *Can. Mineral.* **18**, 157 (1980).
7. D.J. Vaughan and J.A. Tossell, *Phys. Chem. Minerals* **9**, 253 (1983).
8. T. Hamajima, T. Kambara, K.I. Gondaira and T. Oguchi, *Phys. Rev.* **B24**, 3349 (1981).
9. I. Nakai, Y. Sugitani, K. Nagashima and Y. Niwa, *J. Inorg. Nucl. Chem.* **40**, 789 (1978).
10. K.I. Narbutt, *Izv. Akad. Nauk SSSR, Ser. Fiz.* **38**, 104 (1974).
11. J.A. Tossell, D.S. Urch, D.J. Vaughan and G. Wiech, *J. Chem. Phys.* **77**, 77 (1982).
12. P. Sainctavit, G. Calas, J. Petiau, P. Karnatak, J.M. Esteva and G.E. Jr. Brown, *J. Phys. Colloq.* **47**, 411 (1986).
13. J. Petiau, P. Sainctavit and G. Calas, *Mater. Sci. Eng.* **B1**, 237 (1988).
14. P. Sainctavit, J. Petiau, A.M. Flank, J. Ringeissen and S. Lewonczuk, *Physica* **B158**, 623 (1989).
15. D. A. McKeown, *Phys. Rev.* **B45**, 2648 (1992).
16. E.P. Domashevskaya, V.A. Terekhov, L.N. Marshakova, Y.A. Ugai, V.I. Nefedov and N.P. Sergushin, *J. Electron Spectrosc. Relat. Phenom.* **9**, 261 (1976).
17. C. Sugiura and Y. Gohshi, *J. Chem. Phys.* **74**, 4204 (1981).
18. S.A. Nemnonov and S.S. Mikhailova, *Izv. Akad. Nauk SSSR, Ser. Fiz.* **38**, 493 (1974).
19. C. Sugiura, Y. Gohshi and I. Suzuki, *Phys. Rev.* **B10**, 338 (1974).
20. D W. Bullett and W.G. Dawson, *J. Phys. C: Solid State Phys.* **19**, 5837 (1986).
21. D.W. Bullett, *Phys. Chem. Minerals* **14**, 485 (1987).
22. J.B. Goodenough, *J. Phys. Chem. Solids* **30**, 261 (1968).

23. D.J. Vaughan, R.G. Burns and V.M. Burns, *Geochim. Cosmochim. Acta* **35**, 365 (1971).

24. D.J. Vaughan and J.A. Tossell, *Am. Mineral.* **66**, 1250 (1981).

25. J.M. Charnock, C.D. Garner, R.A.D. Pattrick and D.J. Vaughan, *Mineral. Mag.* **53**, 193 (1989).

26. J.M. Charnock, C.D. Garner, R.A.D. Pattrick and D.J. Vaughan, *J. Solid State Chem.* **82**, 279 (1989).

27. J.M. Charnock, C.D. Garner, R.A.D. Pattrick and D.J. Vaughan, *Am. Mineral.* **75**, 247 (1990).

28. R.A.D. Pattrick, G. van der Laan, D.J. Vaughan and C.M.B. Henderson, *Phys. Chem. Minerals* **20**, 395 (1993).

29. J.B. Goodenough, *J. Solid State Chem.* **5**, 144 (1972).

30. L. Pauling, *Can. Mineral.* **16**, 447 (1978).

31. E.D. Stevens, M.L. DeLucia and P. Coppens, *Inorg. Chem.* **19**, 813 (1980).

32. J.A. Tossell, D.J. Vaughan and J.K. Burdett, *Phys. Chem. Minerals* **7**, 177 (1981).

33. D.W. Bullett, *J. Phys.C: Solid State Phys.* **15**, 6163 (1982).

34. S.D. Wijeyesekera and R. Hoffmann, *Inorg. Chem.* **24**, 3197 (1983).

35. P. Schmitt-Beurmann and W. Lottermoser, *Phys. Chem. Minerals* **19**, 571 (1993).

36. S.P. Freidman and V.A. Gubanov, *J. Phys. Chem. Solids* **44**, 187 (1983).

37. S. Sakkopoulos, E. Vitoratos and T. Argyreas, *J. Phys. Chem. Solids* **45**, 923 (1984).

38. D. Welz and M. Rosenberg, *J. Phys.C: Solid State Phys.* **20**, 3911 (1987).

39. C. Sugiura, I. Suzuki and J. Kashiwakura, *J. Phys. Soc. Japan* **40**, 1720 (1976).

40. C. Sugiura, Y. Gohshi and I. Suzuki, *Phys. Rev.* **B10**, 338 (1974).

41. J.A. Tossell, *J. Chem. Phys.* **66**, 5712 (1977).

42. S.P. Freidman and V.A. Gubanov, *Russ. J. Inorg. Chem.* **30**, 1421 (1985).

43. S.P. Freidman and V.A. Gubanov, *Russ. J. Inorg. Chem.* **30**, 1424 (1985).

44. C. Sugiura, *J. Chem. Phys.* **80**, 1047 (1984).

45. C. Sugiura, *J. Chem. Phys.* **74**, 1047 (1981).

46. C. Sugiura and S. Muramatsu, *Phys. Status Solidi* **B74**, K157 (1985).

47. M. Kitamura, C. Sugiura and S. Muramatsu, *Solid State Commun.* **67**, 313 (1988).

48. Z.F. Liu, J.N. Cutler, G.M. Bancroft, K.H. Tan, R.G. Cavell, J.S. Tse, *Chem. Phys.* **168**, 133 (1992).

49. S.R. Hall J.M. Steward, *Acta Crystal.* **B29**, 579 (1973).

50. M.E. Fleet, *Zeitsch Kristal.* **132**, 276 (1970).

51. K. Koto and N. Morimoto, *Acta Crystal.* **B31**, 2268 (1975).

52. R.K. Clifford, K.L. Purdy and J.D. Miller, *AIChE Symp. Ser.* **71**, 138 (1975).

53. A.S. Marfunin A.R. Mkrtchyan, *Geokhimiya* **10**, 1094 (1967). (Transl. *Geochem. Int.* **4**, 980)

54. A.J. Frueh, *Geochim. Cosmochim. Acta* **6**, 79 (1954).

55. P.G. Manning, *Can. Mineral.* **9**, 85 (1967).

56. H.T. Jr. Evans, *Zeit. Kristal.* **150**, 299 (1979).

57. R. Kalbskopf, F. Pertlik and J. Zemann, *Tsch. Mineral. Petrol. Mitt.* **22**, 242 (1975).

58. V.G. Adiwidjaja and J. Löhn, *Acta Crystal.* **B26**, 1878 (1970).

59. S.R. Hall, J.T. Szymanski and J.M. Steward, *Can. Mineral.* **16**, 131 (1978).

60. R.A. Pattrick and A.J. Hall, *Mineral. Mag.* **47**, 441(1983).

61. R.C. Peterson and I. Miller, *Mineral. Mag.* **50**, 717 (1986).

62. N.E. Johnson, J.R. Craig and J.D. Rimstidt, *Can. Mineral.* **25**, 237 (1987).

63. N.E. Johnson, J.R. Craig and J.D. Rimstidt, *Am. Mineral.* **73**, 389 (1988).

64. E. Makovicky, K. Forcher, W. Lottermoser and G. Amthauer, *Mineral. Petrol.* **43**, 73 (1990).

65. G. Drager, R. Frahm, G. Materlik and O. Brummer, *Phys. State. Sol.* **b146**, 287 (1988).

66. M.M. Hyland and G.M. Bancroft, *Geochim. Cosmochim. Acta* **53**, 367 (1987).

CHAPTER 4

Polarized X-ray Absorption Spectroscopy and the Electronic Structure of Molybdenite (2H-MoS_2)

4.1 Introduction

The electronic structure and physical (optical, electric and magnetic) properties of layered transition metal dichalcogenides, MX_2, in which M is a IVb, Vb and VIb transition metal (Ti, Zr, Hf, V, Nb, Ta, Mo, and W) and X is a chalcogen (S, Se and Te), have been reviewed by Wilson and Yoffe[1] and Calais[2]. In these compounds, there are two different coordi nations for metal atoms, either trigonal prismatic (e.g. NbS_2, MoS_2, WS_2, $NbSe_2$, $MoSe_2$, WSe_2), or octahedral (e.g. Ti, Zr, Hf and V dichalcogenides). Both coordinations are present in TaS_2, $TaSe_2$ and $MoTe_2$. The coordination polyhedra form chalcogen-metal-chalcogen "sandwich" layer units with strong covalent bonding, and the individual layers are linked to each other by weak Van der Waals-type forces, leading to the striking anisotropy of these compounds. Some of these dichalcogenides, such as $NbSe_2$ and NbS_2, are metallic and show superconducting behavior at low temperature, and the others are semiconductors. However, ZrS_2 and MoS_2 can become metallic by the intercalation of alkali metals or organic molecules into the weakly bonded interlayers.

2H-MoS_2 is a model compound for these transition metal dichalcogenides, both experimentally and theoretically, because of its natural occurrence as molybdenite, and its interesting optical and electrical properties. A qualitative electronic band model of molybdenite has been proposed by Wilson and Yoffe[1], based on the optical data of molybdenite and crystal field theory. The electronic structure of molybdenite has also been studied using various energy band calculation methods[3-11], x-ray photoelectron spectra (XPS)[12], ultraviolet photoemission spectra (UPS)[13-21], S K_β x-ray emission spectra (XES)[22-25], S $L_{2,3}$, Mo L_β and Mo 5p → 3d XES[26,27]. These studies have provided detailed

information on the valence band (VB) structure of molybdenite.

Sonntag and Brown[28] first measured the S L-edge XANES spectrum of molybdenite and qualitatively interpreted it based on the DOS calculated by Mattheiss[6,7]. Recently, Ohno et al.[29,30] reported S K-edge XANES and Mo L-edge XANES of molybdenite. Ohno[31] also studied the S L-edge inner-shell-electron energy-loss spectra (ISEELS) of 2H-MoS_2. Sancrotti et al[32] investigated the empty electron-states of MoS_2 using k-integrated Bremsstrahlung isochromat spectra (BIS) of 2H-MoS_2. Our group[33] also reported S L-edge spectrum of MoS_2. However, polarized S K- and L-edge, Mo L_2- and L_3-edge XANES spectra have not been reported so far, and the conduction band (CB) structure of molybdenite is not fully understood.

In this chapter, polarized S K- and L-edge, and Mo L_3 and L_2-edge XANES of natural molybdenite (2H-MoS_2) are interpreted, based on the energy band model, and the unoccupied electronic states of molybdenite are studied. The empty Mo 4d crystal field bands are qualitatively characterized and the S $p_{x,y}$ and p_z components in the CB of molybdenite are differentiated using the polarized S K-edge spectra.

4.2 Experimental

A natural molybdenite sample was provided by the Department of Earth Sciences, UWO. A 15x15 mm^2 molybdenite crystal was cleaved from this aggregate sample, and mounted on a stainless steel washer with electric carbon tape. The geometry for the XANES measurements is shown in Figure 4.2.1, where θ is the angle between the c-axis of the crystal and the electric vector E of synchrotron radiation. The polarized XANES spectra were collected at the different values of θ, while the crystal was rotated about the b-axis. S K-edge and Mo L-edge XANES were collected using the DCM, and S L-edge XANES were taken using the Grasshopper monochromator. All the spectra were recorded by TEY using synchrotron radiation.

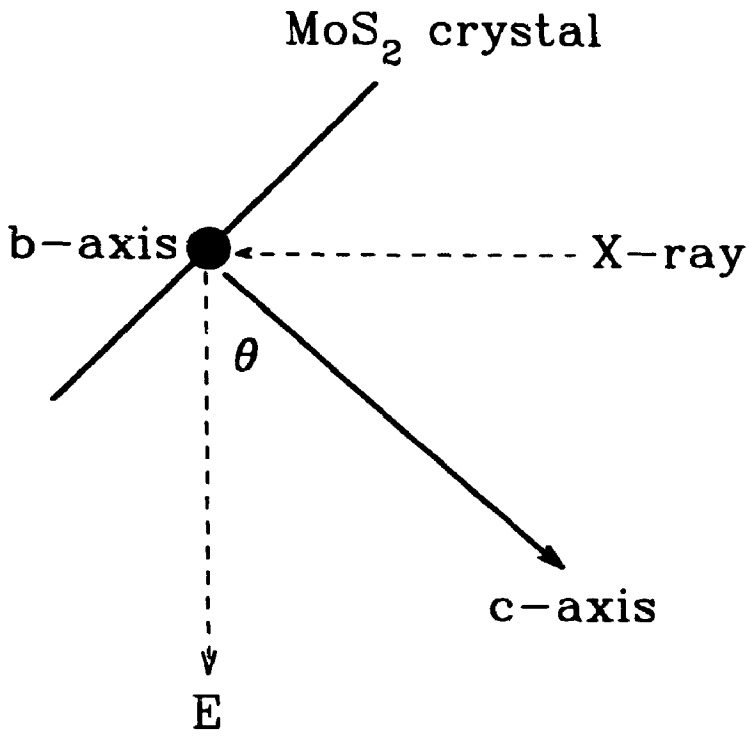

Figure 4.2.1 Geometrical scheme for polarized XANES measurements of molybdenite.

4.3 Results and Discussion

4.3.1 Interpretation of XANES

The XANES, XES and UPS of molybdenite are compared on a common energy scale in Figure 4.3.1. The measured S L- and K-edge, Mo L_3- and L_2-edge XANES (solid lines) are aligned on the upper right hand side, by subtracting the S $2p_{3/2}$, S 1s, Mo $2p_{3/2}$ and Mo $2p_{1/2}$ BE, respectively. The S $2p_{3/2}$ BE is 160.4 eV cited from Yu et al.[12], the S 1s BE is 2468.2 eV calculated by adding the S $K\alpha_1$ XES of 2307.8 eV and the S $2p_{3/2}$ BE. The UPS (dot line), S $K\beta_{1,3}$ XES, S $L_{2,3}M$ XES, Mo $L\beta_{1,}$ XES and Mo 5p → $3d_{5/2}$ XES (dash lines) are assembled on the upper left-hand side. The UPS was digitized

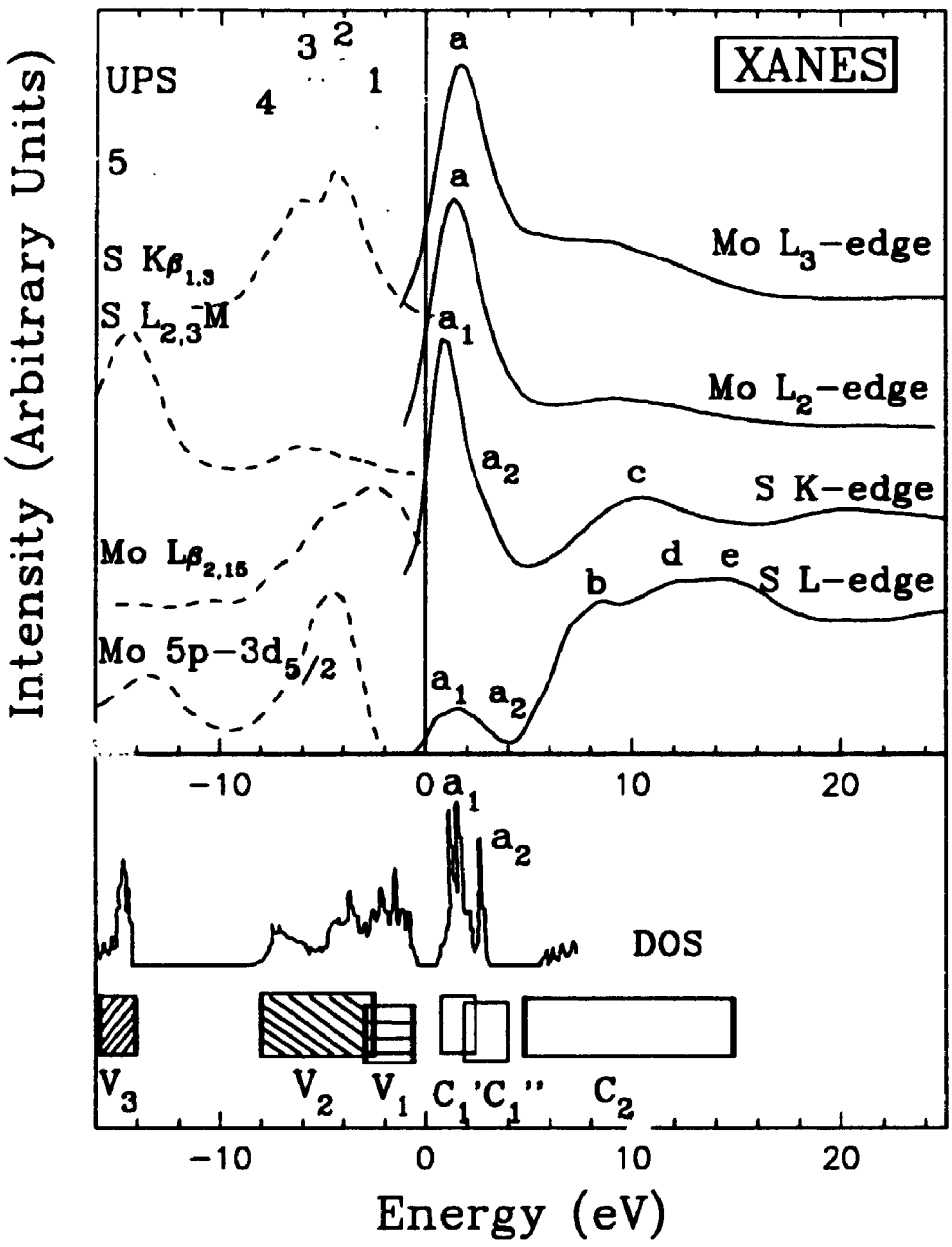

Figure 4.3.1 S K- and L-edge, Mo L_2- and L_3-edge spectra of molybdenite are compared with its XPS[14] and XES spectra[25,27] on a common scale. The total DOS calculated[10] and an empirical energy band model[1,17] are also presented at the bottom.

from Wertheim et al.[14], in which the energy zero is the Fermi level. The S $K\beta_{1,3}$ XES was digitized from Simunek and Wiech[25] and the remaining XES digitized from Haycock et al.[27]. All the XES spectra are aligned with the UPS spectra[27]. The DOS calculated by Bullett[10] and an empirical energy band model[1,17] are shown at the bottom for comparison. The energy zero in this figure is close to the Fermi level.

The UPS represents total DOS in the VB of molybdenite, and is in good agreement with the calculated DOS[10]. Peak 1 is assigned to the Mo $4d_{z^2}$ band, peaks 2, 3 and 4 correspond to S 3p bonding states, and peak 5 is attributed to S 3s states in the VB[13-20]. The XES spectra reflect the partial DOS of the corresponding VB states. For example, the S $K\beta_{1,3}$ XES reflect the S 3p bonding states, S $L_{2,3}M$ XES reveals S 3s states, Mo $L\beta_{2,15}$ and Mo $5p \rightarrow 3d_{5/2}$ XES are related to Mo d and p electron states, respectively. The XES spectra confirm the assignments of the UPS and reveal detailed information on the VB of molybdenite. In summary, based on the UPS, XES and energy band calculation of molybdenite, the VB maximum of molybdenite (V_1) is the non-bonding Mo $4d_{z^2}$ band, band V_2 is characterized by S 3p bonding states, and also has significant features of Mo 5p and 4d states. The band V_3 is characterized by S 3s orbitals.

S K-edge XANES features are attributed to transitions of S 1s electrons to unoccupied S p-like states, and S L-edge XANES to transitions of S 2p electrons to unoccupied S s- or d-like states. In Figure 4.3.1, peak a in the Mo L_3- and L_2-edge XANES of molybdenite is assigned to transitions of electrons from the Mo $2p_{3/2}$ and Mo $2p_{1/2}$, respectively, to the Mo 4d band at the CB minimum. Peak a in the S K- and L-edge XANES spectra is aligned with the Mo L-edge spectra well within 0.4 eV, and attributed to transitions of S 1s and 2p electrons, respectively, to S 3p- and S 3s-like states mixed into the Mo 4d band. These assignments are in good agreement with the calculated DOS[6,7,10] and the qualitative energy band model[1,17]. Hence, the band C_1 is characterized by Mo 4d-like states[1,10], but also has significant features of S 3p-like and 3s-like states. In addition, feature b in the S L-edge XANES is assigned to transition of S 2p electrons to unoccupied S 3s-like states, and peaks c and d_1 to transitions of S 2p electrons to empty S 3d states. Peak c in the S K-edge XANES probably corresponds

to transition of S 1s electrons to antibonding S 3p-like states, and peak c in the Mo L_2- and L_3-edge XANES to transition of Mo $2p_{1/2}$ and Mo $2p_{3/2}$ electrons, respectively, to unoccupied Mo 5s-like states.

A shoulder (a_2) at the higher energy side of peak a in the S K-edge XANES indicates the further splitting of the unoccupied Mo 4d band, probably into $4d_{x^2-y^2}$ and $4d_{xy}$ bands[1,10], which have different DOS of S 3p states. This splitting of Mo 4d orbitals is further confirmed by the S L-edge XANES of molybdenite. Peak a in the S L-edge XANES is an envelope of several features, and can be fitted into two doublets, corresponding to the transitions of S 2p electrons to unoccupied S 3s-like states mixed into these two Mo 4d sub-bands. Each doublet is caused by the spin-orbit interaction of S 2p orbitals. The splitting of the unoccupied Mo 4d band is also confirmed by k-integrated BIS of 2H-MoS_2[32] and the DOS calculated using the simple *ab initio* atomic orbital method[10] (see Figure 4.3.1). The splitting of the unoccupied Mo 4d bands is not observed in the Mo L_2- and L_3-edge XANES, because peak a in the Mo L_2- and L_3-edge spectra is broadened by both the reduced resolution of the beamline and larger intrinsic core-hole width at the Mo L_2 and L_3-edges.

The S K-edge XANES qualitatively reveals the DOS of unoccupied S p-like states, while the S and Mo L-edge XANES highlight the DOS of unoccupied S and Mo s- and d-like states, respectively, in the CB of molybdenite. Obviously, the largest densities of unoccupied S p-like and Mo d-like states are located in the lower CB, and the empty S p-like states have the two maximum densities in the upper CB. The S s-like states have significant DOS at the lower CB, but its maximum density is about 8 eV above the Fermi level. The band for empty S 3d states has maximum DOS at the upper CB. Therefore, the upper CB is basically composed of S 3s-like and 3d-like states, and probably has contributions from Mo p-like and S p-like states. Both S 3s- and 3p-like states are strongly mixed into the Mo 4d crystal field band.

4.3.2 Polarized XANES

Figure 4.3.2 shows polarized S K-edge XANES of molybdenite at θ = 90°, 75°,

60°, 45° and 30°, with the estimated experimental values of θ accurate to $\pm 3°$. All of the present polarized spectra are averages of three measurements and normalized by I/I_0, before a simply linear background subtraction. The variation of the full width at half maximum (FWHM) for peak a with θ is shown in the inset. The experimental set-up did not allow us to collect XANES spectra at the limiting case of $\theta = 0°$ (E parallel to the c-axis and normal to the layers). However, it is known that the x-ray absorption coefficient μ has no polarization dependence in the plane of the layer, but in the plane normal to the layers, it varies as:

$$\mu(\theta) = \mu_{\parallel} + (\mu_{\perp} - \mu_{\parallel})\cos^2\theta$$

where $\mu_{\parallel}$ and $\mu_{\perp}$ are the absorption coefficients with the E vector parallel ($\theta = 90°$) and perpendicular ($\theta = 0°$) to the layers[34], respectively. This allows us to deduce the limiting case spectrum at $\theta = 0°$ based on the XANES spectra collected at $\theta = 90°$ ($\mu_{\parallel}$) and $\theta \neq 90°$.

The general profiles of S K-edge XANES of molybdenite are similar to each other for different values of θ. However, peaks a and c show some interesting variations. First, as seen in Figure 4.3.2, the FWHM for peak a decreases, indicating that one peak, a_2, becomes weaker, as the angle θ increases from 30° to 90°. Peak a has been deconvoluted into peaks a_1 and a_2 by fitting Gaussian profiles, as shown in Figure 4.3.3, where solid dot lines are the experimental spectra, the dash lines are the two fitted peaks a_1 and a_2, and the solid lines are the envelopes of the fitted spectra. The energy positions of peaks a_1 and a_2 are at 2470.5 and 2472.0 eV, respectively, separated by 1.5 eV, and their FWHM are set at 1.65 and 2.15 eV, respectively. The relative intensity of peak a_2 dramatically increases when θ decreases from 90° to 30°. The area ratio of peaks a_1 and a_2 (I_{a_1}/I_{a_2}) essentially varies linearly with $\cos^2\theta$ (see Figure 4.3.4).

At $\theta = 90°$, the electric vector E of the x-ray radiation is parallel to the basal plane of the molybdenite crystal, and the absorption of x-ray photons causes the excitation of electrons to the states of $p_{x,y}$ character. Conversely, at $\theta = 0°$, transitions to p_z states are excited[23-25,34,35]. Therefore, the symmetry of the final p-like states can be determined using polarized S K-edge XANES. The results indicate that both S $p_{x,y}$ and p_z characters are mixed into the two unoccupied Mo 4d sub-bands; however, the lower

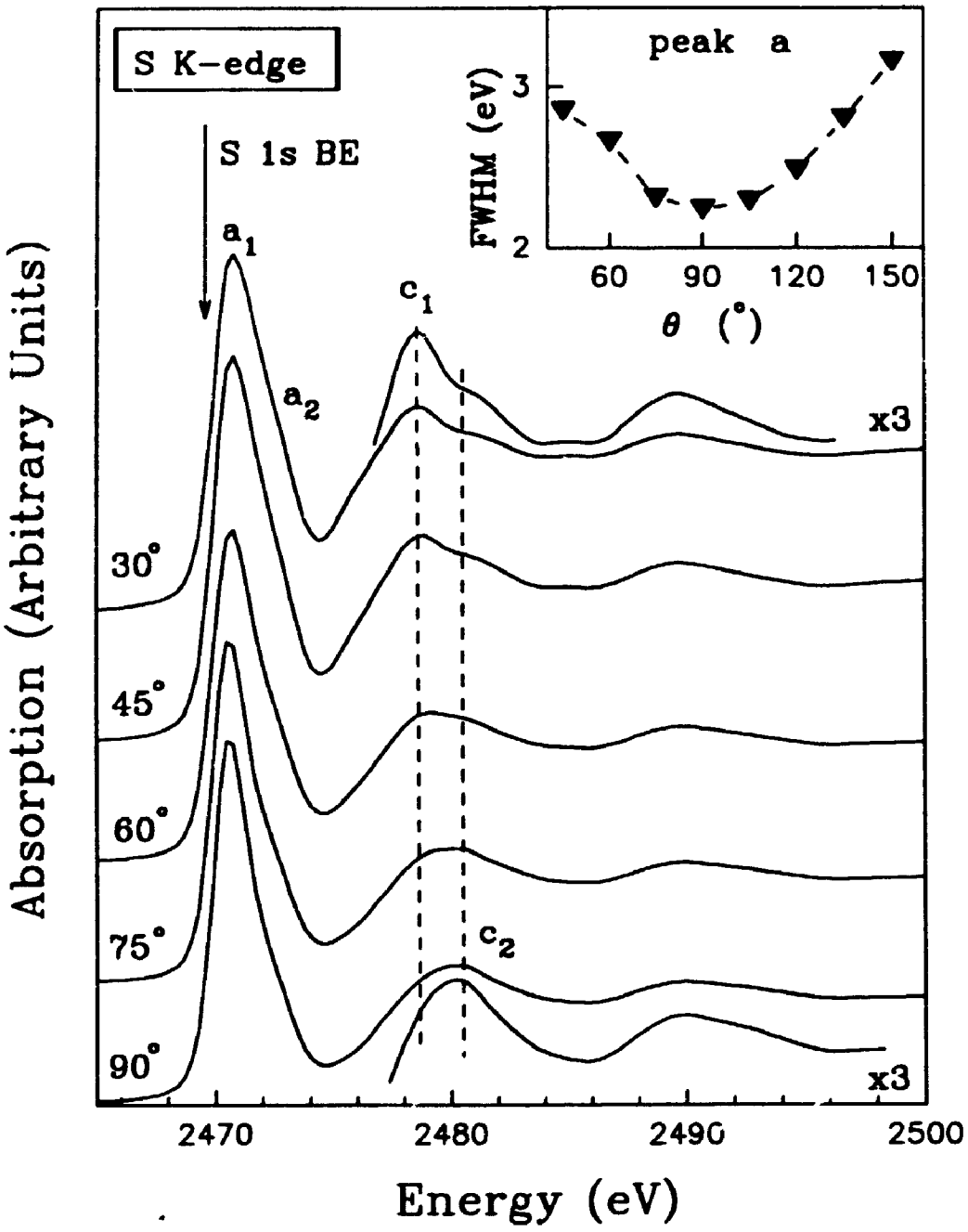

Figure 4.3.2 Polarized S K-edge XANES spectra of molybdenite. The variation of the full width at half maximum (FWHM) of peak a with the θ values is shown in the inset.

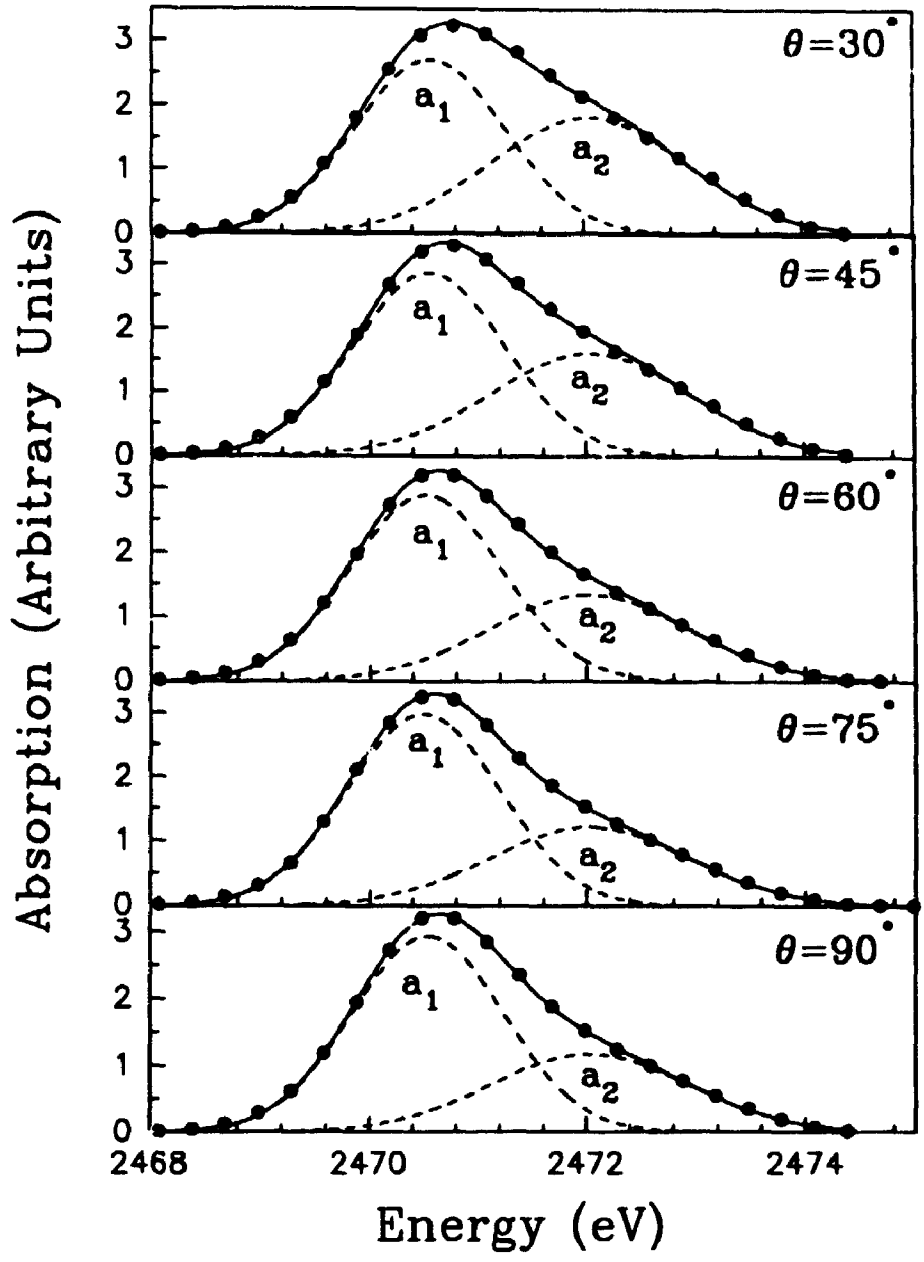

Figure 4.3.3 Deconvolution of peak a into peaks a_1 and a_2 in polarized S K-edge spectra of molybdenite. The dot lines are the experimental results, and the solid lines are the fitted envelops of peaks a_1 and a_2.

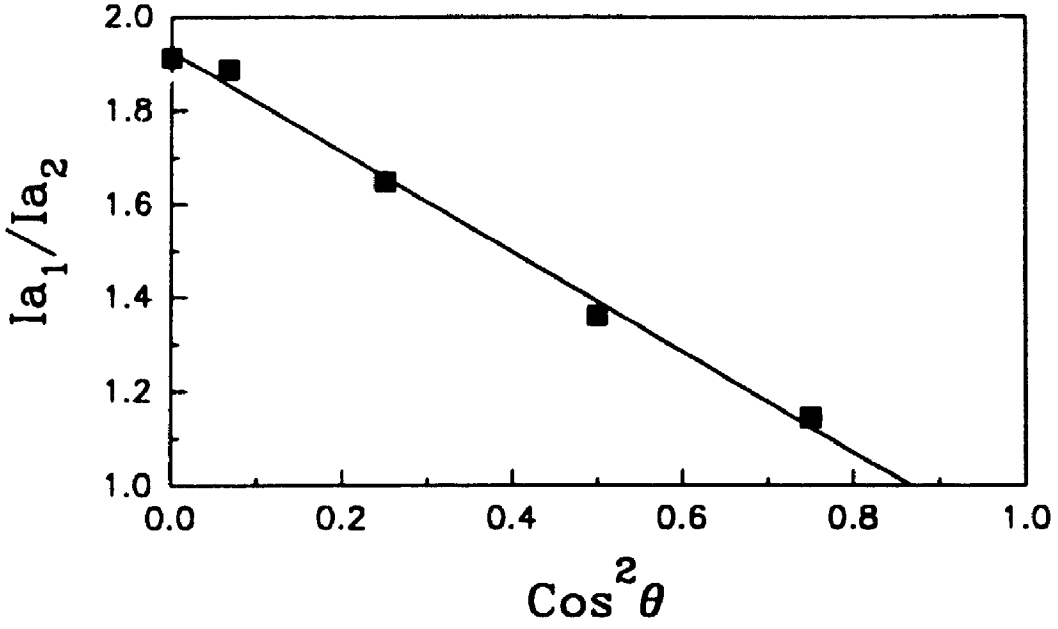

Figure 4.3.4 Variation of the area ratio of peaks a_1 and a_2 in the S K-edge spectra of MoS_2 with $\cos^2\theta$.

energy Mo 4d sub-band has very similar DOS of both $p_{x,y}$- and p_z-like states, while the higher energy sub-band has significantly higher DOS for p_z states than for $p_{x,y}$ states.

Another important feature in the polarized S K-edge XANES of molybdenite is that peak c is a single broad peak (c_2) in the $\theta = 90°$ spectrum; while at $\theta = 30°$, its maximum shifts toward lower energy by about 2 eV, and becomes sharper and stronger (c_1). In addition, there are two other distinct features above peak c_1 in the $\theta = 30°$ spectrum. As discussed above, peak c was assigned to the transition of S 1s electron to p-like states; therefore, single peak c_2 in the $\theta = 90°$ S K-edge spectrum basically represents the feature of S $p_{x,y}$-like states. Peak c_1 in the $\theta = 30°$ spectrum more likely reflects the S $3p_z$-like final states. The other two weak features above peak c_1 probably indicate the presence of S $3p_{x,y}$-like states, and also more contribution from empty S 3d orbitals, as is evident in the S L-edge XANES. Therefore, peaks c_1 and c_2 are assigned to transitions of S 1s electrons to p_z- and $p_{x,y}$-like states, respectively. It is expected that peak c_1 would shift further to lower energy in the $\theta = 0°$ spectrum.

The intensity of a pure 1s → π (p_z) transition should be proportional to $\cos^2\theta$, while the intensity of a pure 1s → σ ($p_{x,y}$) transition should be proportional to $\sin^2\theta$ [5]. In fact, it is observed that the intensity of peak c_1 decreases, and the intensity of peak c_2 increases, from $\theta = 30°$ to $\theta = 90°$, confirming the above assignment of peaks c_1 and c_2 to p_z- and $p_{x,y}$-like states, respectively. In addition, angle-dependent S K_β XES of molybdenite and the DOS calculated using the self-consistent pseudopotential method[21,25] showed that the bonding S $3p_z$ states shifts toward higher energy by about 2 eV relative to the bonding S $3p_{x,y}$, in good agreement with the polarized S K-edge XANES spectra of molybdenite and the qualitative MO scheme. The carbon K-edge XANES spectra of graphite indicated that the C 1s → π transition occurs at lower energy than the C 1s → σ transition, and also the intensity of the former is directly proportional to $\cos^2\theta$ [5], also in good agreement with the polarized S K-edge XANES spectra.

Figure 4.3.5 shows the polarized S L-edge XANES of molybdenite; the $\theta = 30°$ spectrum and its differential curve are expanded in the inset. Generally, the spectra are similar to each other for different values of θ. Peaks a and b show no significant change with the angle θ, because they are attributed to transitions of S 2p electrons to S s-like states which have spherical symmetry. For peaks c and d_1, which were attributed to transitions of S 2p electrons to empty S 3d-like states, the relative intensity does vary with the angle θ. Peaks c and d_1 have similar intensities at $\theta = 90°$; however, peak c becomes markedly stronger than peak d_1 at $\theta = 30°$.

Figure 4.3.6 shows the polarized Mo L_3-edge (A) and Mo L_2-edge (B) XANES of molybdenite. A strong peak a, another weak peak c and a broad band at about 45 eV above peak a are evident. The profiles of the spectra are similar for different values of θ, and also for both Mo L_3- and L_2-edge XANES spectra. The Mo L_3- and L_2-edge XANES spectra show little variation with the angle θ, and thus indicate that the final unoccupied Mo 4d states are unlikely to be simply $4d_{x^2-y^2}$ and $4d_{xy}$.

It is well known that the d orbitals of transition metals under octahedral ligand field (O_h) are split into triple-degenerate t_{2g} (d_{xy}, d_{yz}, d_{xz}) and double-degenerate e_g ($d_{x^2-y^2}$, d_{z^2}) sets. Considering the distortion of O_h ligand field along the threefold axis that is used as the axis of quantization, the t_{2g} set is split into one single degenerate a_{1g} and one

Figure 5.3.6 shows the correlation of the S K- (a) and L-edges (b) with the energy gaps (E_g) of metal sulfides, where the energy gaps are cited mainly from Shuey[11]. First, it is apparent that for Cu and Cu-Fe sulfides which have small electrical resistance[12], both S K- and L-edges lie at lower energy and E_g is also smaller. For Zn, Cd, Hg, As and Sb sulfides with higher electrical resistance[9], the E_g is larger, and both S K- and L-edges are also at higher energy. Second, of all the sulfides studied, both S K- and L-edges are linearly correlated with E_g. In general, the correlations of S K- and L-edges with the energy gap of metal sulfides appear quite acceptable, because some of small deviations from linearity are no doubt due to very approximate E_g values, and establish a potential application of S K- and L-edge spectra in the determination of the E_g of semiconducting metal sulfides.

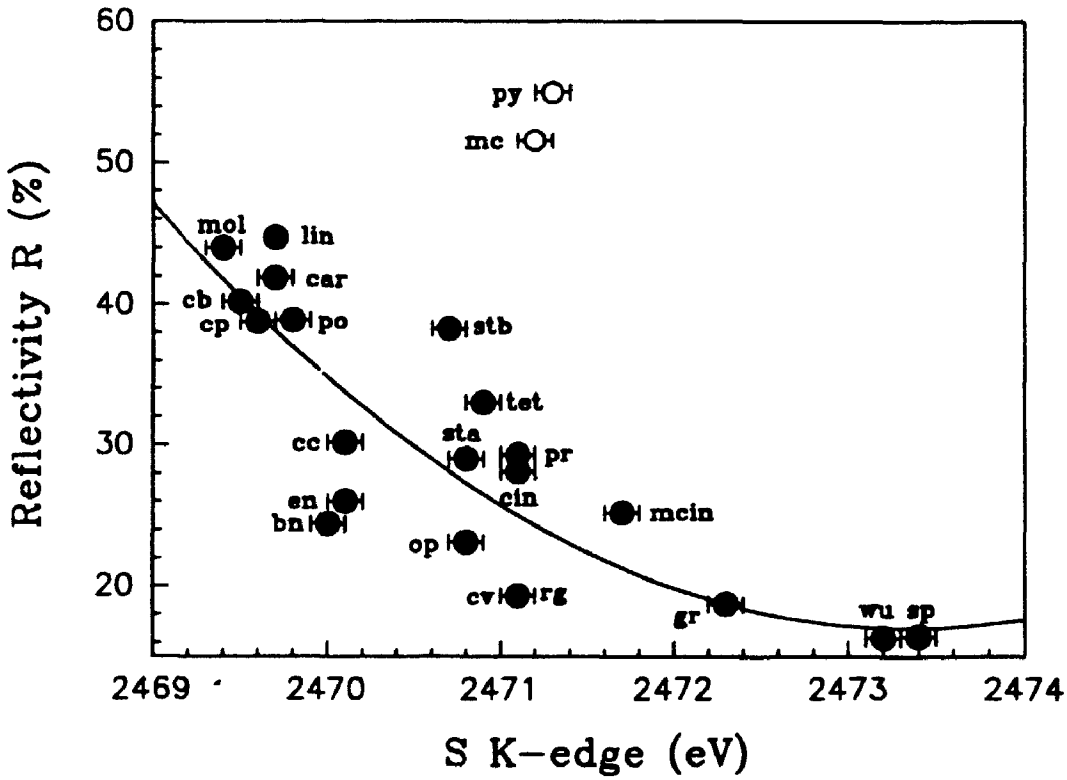

Figure 5.3.7 Correlation of S K-edge with reflectivity of metal sulfides.

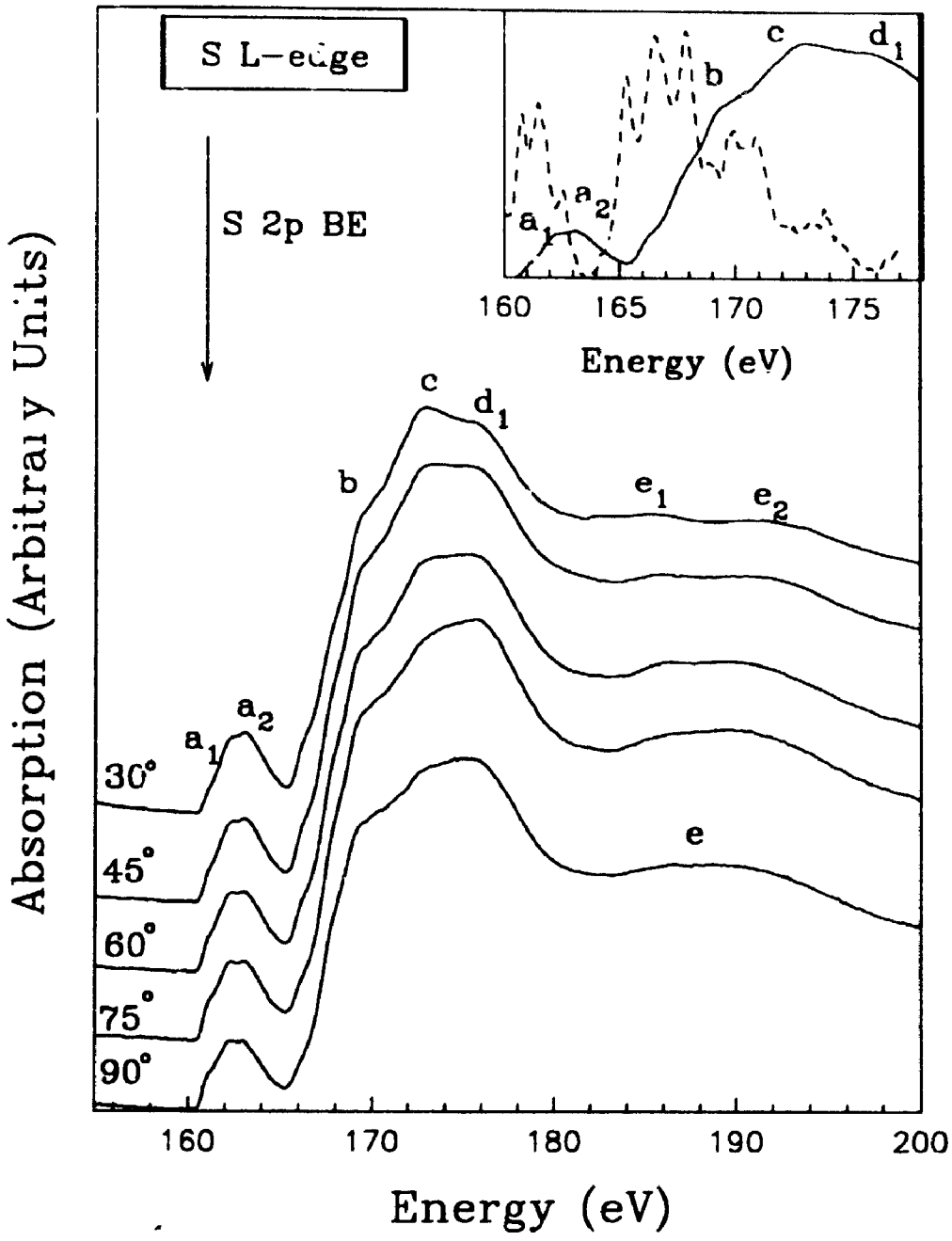

Figure 4.3.5 Polarized S L-edge XANES spectra of molybdenite. The near-edge features and the derivative (dash line) curve are shown in the inset.

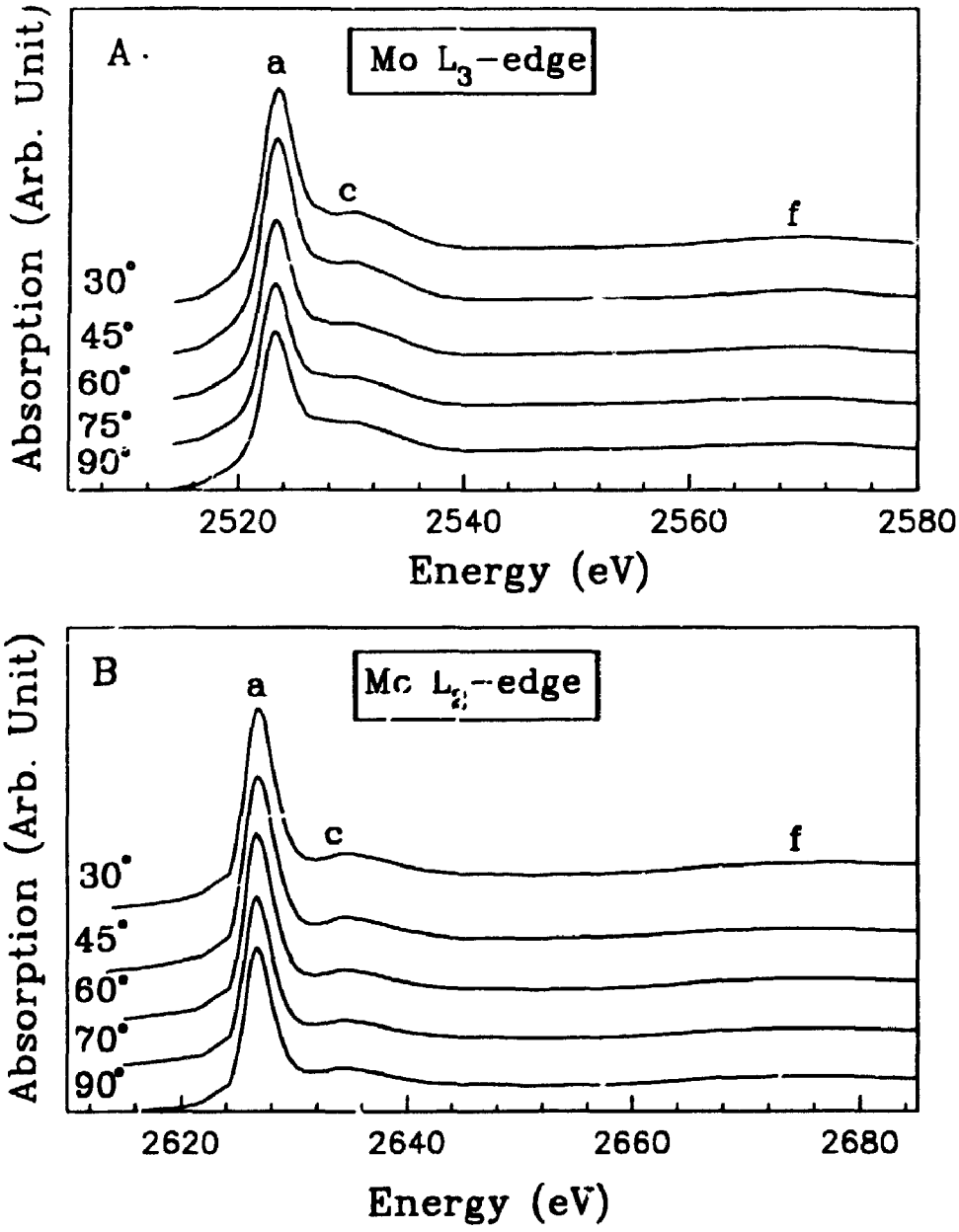

Figure 4.3.6 Polarized Mo L_3-edge (A) and L_2-edge (B) XANES spectra of molybdenite.

double degenerate e_g, and the e_g set remains degenerate. The wave functions of the d states of transition metals under the trigonal ligand field are described by the following five equations[36]. The t_{2g}^0 wave function is equivalent to the single-degenerate a_{1g}. It is dominated by the d_z state and has the lowest energy. The t_{2g}^+ and t_{2g}^- are degenerate and equivalent to the double-degenerate e_g split from the t_{2g} set; and the e_g^+ and e_g^- remain double-degenerate and equivalent to the other e_g set. It seems hard to evaluate exactly the relative energy of the two double degenerate e_g state (t_{2g}^+/t_{2g}^- and e_g^+/e_g^-), although the t_{2g}^+/t_{2g}^- set probably has the lower energy. However, these states have mixed wave functions of different d orbital components.

$$t_{2g}^0 = d(z^2)$$

$$t_{2g}^- = \sqrt{2/3}\,d(xy) + \sqrt{1/3}\,d(yz)$$

$$t_{2g}^+ = \sqrt{2/3}\,d(x^2-y^2) - \sqrt{1/3}\,d(xz)$$

$$e_g^- = \sqrt{1/3}\,d(xy) - \sqrt{2/3}\,d(yz)$$

$$e_g^+ = \sqrt{1/3}\,d(x^2-y^2) + \sqrt{2/3}\,d(xz)$$

In the crystal structure of molybdenite, the local symmetry of Mo^{4+} ($4d^2$) is D_{3h}. The Mo 4d orbitals are split into one single degenerate a_{1g} and two double degenerate e_g. The a_{1g} state is dominated by the Mo $4d_{z^2}$ and has the lowest energy. Because the Mo^{4+} has $4d^2$ configuration, the Mo $4d_{z^2}$ is fully occupied and constitutes the VB maximum of molybdenite. The unoccupied Mo 4d states in the molybdenite are very complicated and poorly understood. However, the S K- and Mo L-edge XANES spectra indeed provide very important information on the Mo 4d states, and also in good agreement with the above classic analysis based on the ligand field theory. In summary, the unoccupied Mo 4d states are split into two double-degenerate states, which were designated as t_{2g}^-/t_{2g}^+

and e_g^-/e_g^+ as above. Although the relative energy of these two sets are difficult to be evaluated, probably the former has lower energy than the latter. More importantly, these two states have the combination wave functions of the other different Mo 4d components, except for the d_{z^2} state. Each of these two sets has Mo 4d components along and normal to the c-axis, so that the polarized Mo L-edge XANES spectra are apparently similar for different values of θ. Also, both S $p_{x,y}$ and p_z states can be mixed into the two unoccupied Mo 4d sub-bands, even though the DOS of S $p_{x,y}$ and p_z states in these two sub-bands could be different.

4.4 Conclusions

S K- and L-edge, and Mo L_3- and L_2-edge XANES spectra of molybdenite are qualitatively interpreted based on the energy band model, and indicate that the CB minimum of molybdenite is characterized by unoccupied Mo 4d states. The Mo 4d band is split into two sub-bands, which are separated by about 1.5 eV and partly overlapped, with the widths of about 1.7 and 2.2 eV, respectively. However, these two unoccupied Mo 4d bands are unlikely to be simply $4d_{x^2-y^2}$ and $4d_{xy}$, respectively. The unoccupied Mo 4d states are strongly hybridized with S 3s-like and 3p-like states. For the lower energy sub-band, the DOS of both S p_z- and $p_{x,y}$-like states are very similar, while for the higher energy sub-band, the DOS of the S p_z-state is dramatically higher than that for the S $p_{x,y}$-like states. The polarized S K-edge XANES of molybdenite not only confirm the assignments of the near-edge features, but also provide direct experimental evidence on polarization of the bonding between the Mo 4d orbitals and 3p states. The polarized S K-edge XANES also indicate that the feature due to transition to the p_z states is stronger and sharper, and shifts toward lower energy by about 2 eV relative to the $p_{x,y}$ states.

4.5 References

1. J.A. Wilson and A.D. Yoffe, *Adv. Phys.* **18**, 193 (1969).

2. J.L. Calais, *Adv. Phys.* **26**, 847 (1977).

3. R.A. Bromley, R.B. Murray and A.D. Yoffe, *J. Phys. C: Solid State Phys.* **5**, 759 (1972),.

4. D.R. Edmondson, *Solid State Commun.* **10**, 1085 (1972).

5. R. Huisman, R. De Jonge, C. Haas and F. Jellinek, *J. Solid State Chem.* **3**, 56 (1971).

6. L.F. Mattheiss. *Phys. Rev. Lett.* **30**, 784 (1973).

7. L.F. Mattheiss, *Phys. Rev.* **B8**, 3719 (1973).

8. R.V. Kasowski, *Phys. Rev. Lett.* **30**, 1175 (1973).

9. K. Wood and J.B. Pendry, *Phys. Rev. Lett.* **31**, 1400 (1973).

10. D.W. Bullett, *J. Phys. C: Solid State Phys.* **11**, 4501 (1978).

11. R. Coehoorn, C. Haas, J. Dijkstra C.J.F. Flipse, R.A. De Groot and A. Wold, *Phys. Rev.* **B35**, 6195 (1987).

12. X.R. Yu, F. Liu, Z.Y. Wang and Y. Chen, *J. Electron Spectrosc. Relat. Phenom.* **50**, 159 (1990).

13. R.H. Williams, J.M. Thomas, M. Barber and N. Alford, *Chem. Phys. lett.* **17**, 142 (1972).

14. G.K. Wertheim, F.J. DiSalvo and D.N.E. Buchanan, *Solid State Commun.* **13**, 1225 (1973).

15. R.B. Murray and R.H. Williams, *Phil. Mag.* **29**, 473 (1974).

16. R.H. Williams, P.C. Kemeny and L. Ley, *Solid State Commun.* **19**, 495 (1976).

17. J.C. McMenamin and W.E. Spicer, *Phys. Rev.* **B16**, 5474 (1977).

18. I.T. McGovern, R H Williams and A.W. Parke, *J. Phys. C: Solid State Phys.* **12**, 2689 (1979).

19. I.T. McGovern, K.D. Childs, H.M. Clearfield and R.H. Williams, *J. Phys. C: Solid State Phys.* **14**, L243 (1981).

20. I. Abbati, L. Braicovich, C. Carbone, J. Nogami, I. Lindau and U. Del Pennino, *J. Electron Spectrosc. Relat. Phenom.* **40**, 353 (1986).

21. R. Mamy, A. Boufelja and B. Carricaburu, *Phys. Status Solidi* **B141**, 467 (1987).

22. C. Sugiura, I. Suzuki, J. Kashiwakura and Y. Gohshi, *J. Phys. Soc. Japan* **40**,

1720 (1976).

23. W. Müller, G. Wiech and A. Šimůnek, *Phys. Lett.* **A98**, 66 (1983).

24. Yu. M. Yarmoshenko, V.M. Cherkashenko and E.Z. Kurmaev, *J. Electron Spectrosc. Relat. Phenom.* **32**, 103 (1983).

25. A. Šimůnek and G. Wiech, *Phys. Rev.* **B30**, 923 (1984).

26. W. Ormerod and D.S. Urch, In *Inner-shell X-ray Physics of Atoms and Solids* (Ed. by Fabian, D.J., Kleinpoppen, H. and Watson, L.M.). Plenum, New York, 1981, pp. 829.

27. D.E. Haycock, D.S. Urch and G. Wiech, *J. Chem. Soc., Faraday Trans. II* **75**, 1692 (1979).

28. G.B. Sonntag and F.C. Brown, *Phys. Rev.* **B10**, 2300 (1974).

29. Y. Ohno, K. Hirama, S. Nakai, C. Sugiura and S. Okada, *Phys. Rev.* **B27**, 3811 (1983).

30. Y. Ohno, K. Hirama, S. Nakai, C. Sugiura and S. Okada, *J. Phys. C: Solid State Phys.* **16**, 6695 (1983).

31. Y. Ohno, *Phys. Rev.* **B36**, 7500 (1987).

32. M. Sancrotti, L. Braicovich, C. Chemelli and G. Trezzi, *Solid State Commun.* **66**, 593 (1988).

33. M. Kasrai, M.E. Fleet, T.K. Sham, G.M. Bancroft, K.H. Tan and J.R. Brown, *Solid State Commun.* **68**, 507 (1988).

34. S.M. Heald and E.A. Stern, *Phys. Rev.* **B16**, 5549 (1977).

35. R.A. Rosenberg, P.J. Love and V. Rehn, *Phys. Rev.* **B33**, 4034 (1986).

36. C.J. Ballhausen, *Introduction to Ligand Field Theory*. McGraw-Hill, New York, 1962.

CHAPTER 5

Applications of S K- and L-edge X-ray Absorption Spectroscopy in Mineralogy and Geochemistry

5.1 Introduction

In the previous three chapters, S K- and L-edge XANES spectra of a range of metal sulfide minerals have been presented and qualitatively interpreted based on MO/ energy band models. The near-edge features reflect the DOS of unoccupied S 3p-and 3s/3d states near and above the Fermi level, and provide information on the roles of metal d electrons in the bonding of metal with sulfur. In this chapter, first, S K- and L-edge XANES spectra of several sulfate minerals are presented and qualitatively explained based on a MO scheme and a comparison with the spectra of model gas phase molecules. Second, chemical shifts of the S K- and L-edges and their applications in mineralogy and geochemistry are discussed; for example, the chemical shift and the oxidation states of sulfur species, the chemical shift and the energy gap and the reflectivity of metal sulfide minerals. Third, S K-edge EXAFS analyses of some sulfide minerals are reported and illustrate the kind of structural information that can be derived from EXAFS analysis, with estimation of reliability from comparison with the minerals of known crystal structure.

5.2 Experimental

The $MgSO_4.2H_2O$ investigated was analytical grade reagent, and the remaining sulfates were natural minerals, gypsum ($CaSO_4 \cdot H_2O$), anhydrite ($CaSO_4$), celestite ($SrSO_4$) and barite ($BaSO_4$). All mineral samples were characterized by XRD to be essentially of single phase composition. The S K- and L-edge XANES spectra were collected using the DCM and grasshopper beamlines, respectively, as described above.

The S K-edge EXAFS spectra were collected on the DCM, over the energy range from 2400 to 3200 eV. The energy interval between each data point was set from 0.2 to 3 eV, and the time set for each data point from 1 to 5 seconds, so that after Fourier transform, each data point has an equal-interval in k space.

5.3 Results and Discussion

5.3.1 S K- and L-edge XANES spectra of sulfates

Figure 5.3.1 compares the S K- (dash curves) and L-edge (solid curves) XANES spectra of $MgSO_4 \cdot 2H_2O$, gypsum, anhydrite, celestite and barite, correlated by the S $K\alpha_1$ x-ray emission energy at 2307.8 eV. The peak positions and assignments are summarized in Table 5.3.1, where ΔE is the energy difference between a peak and S 1s BE (for K-edge spectra) or $2p_{3/2}$ BE (for L-edge spectra). The assignments are based on comparison with the spectra of other systems containing tetrahedrally coordinated S or Si, such as Na_2SO_4 [1], gaseous SF_4 [2], SO_2Cl_2 [3] and SiF_4 [4] and α-quartz [5]. Peak A in the L-edge spectra is assigned to the transition of S 2p electrons to the S 3s-like a_1 states, and it is split by about 1.2 eV, apparently due to the spin-orbit interaction of S 2p orbitals. Peak A is absent in the K-edge spectra, because the S 1s → 3s transition is forbidden by the selection rules. Peak C in the K-edge spectra is, of course, attributed to the transition of S 1s electrons to the S 3p-like t_2 states; this peak is weak in the L-edge spectra, because the S 2p → 3p transition is forbidden by the selection rules. Peaks E and G are assigned to the S 3d-like e and t_2 states, and are weak in the K-edge spectra, because the S 1s → 3d transitions are forbidden. However, once again there is a problem with the intensity of peak E, which suggests a strong multiple scattering (MS) contribution to both peaks E and G. As shown in Table 5.3.1, two features D and F in the K-edge spectra are not assigned with any confidence; however, they are probably related to the MS effect[5].

Some systematic changes in the S K- and L-edge spectra are observed from $MgSO_4 \cdot 2H_2O$ and gypsum to anhydrite, celestite and barite. For $MgSO_4 \cdot 2H_2O$ and

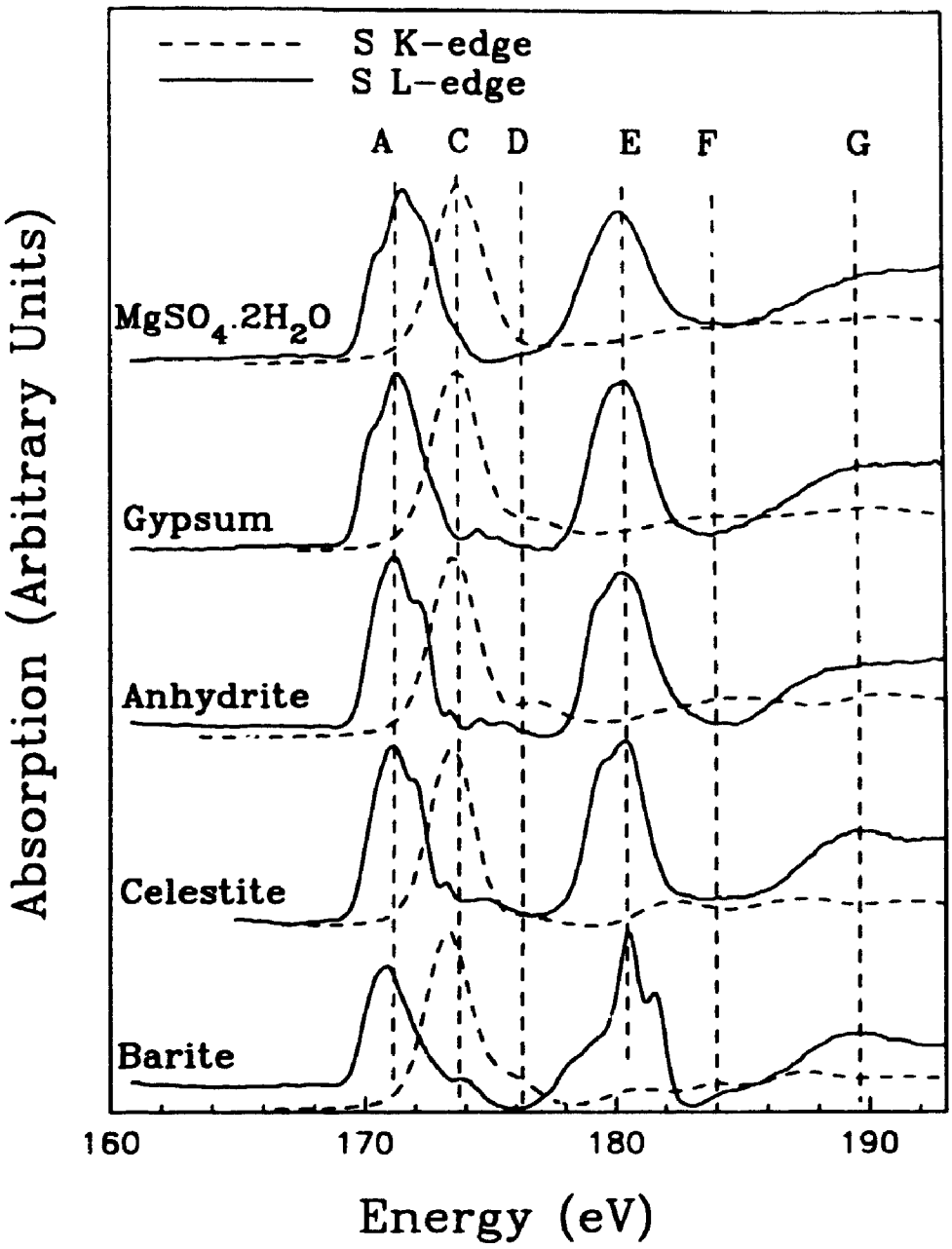

Figure 5.3.1 S K- and L-edge XANES spectra of $MgSO_4 \cdot 2H_2O$, gypsum, anhydrite, celestite and barite. The S K- and L-edge spectra are aligned on a common scale using S $K\alpha_1$ x-ray emission energy at 2307.8 eV.

Table 5.3.1 S K- and L-edge XANES spectra (±0.2 eV) of some sulfates

Samples	Label	Assignments	ΔE	K-edge	L-edge	ΔE	Assignments
$MgSO_4 \cdot 2H_2O$	A				171.1	2.1	S $2p_{3/2} \rightarrow a_1$ (3s-like)
					172.3	3.3	S $2p_{1/2} \rightarrow a_1$ (3s-like)
	C	S 1s → t_2 (3p-like)	4.7	2481.5	173.3	4.3	S $2p_{3/2} \rightarrow t_2$ (3p-like)
					174.6	5.6	S $2p_{1/2} \rightarrow t_2$ (3p-like)
	D	M.S.	9.3	2486.1	177.0	8.0	M.S.
	E	S 1s → e (3d-like)	13.4	2490.2	181.0	12.0	S 2p → e (3d-like)
	F	M.S.	16.8	2493.6			
	G	S 1s → t_2 (3d-like)	22.0	2498.8	190.5	21.5	S 2p → t_2 (3d-like)
Gypsum	A				170.9	1.9	S $2p_{3/2} \rightarrow a_1$ (3s-like)
					172.1	3.1	S $2p_{1/2} \rightarrow a_1$ (3s-like)
	C	S 1s → t_2 (3p-like)	4.7	2481.5	173.7	4.7	S $2p_{3/2} \rightarrow t_2$ (3p-like)
					175.3	6.3	S $2p_{1/2} \rightarrow t_2$ (3p-like)
	D	M.S.	7.9	2484.7	177.4	8.4	M.S.
	E	S 1s → e (3d-like)	11.0	2487.8	181.1	12.1	S 2p → e (3d-like)
	F	M.S.	14.5	2491.3			
	G	S 1s → t_2 (3d-like)	21.1	2497.9	189.7	20.7	S 2p → t_2 (3d-like)
Anhydrite	A				171.8	2.8	S $2p_{3/2} \rightarrow a_1$ (3s-like)
					173.0	4.0	S $2p_{1/2} \rightarrow a_1$ (3s-like)
	C	S 1s → t_2 (3p-like)	4.5	2481.3	174.0	5.0	S $2p_{3/2} \rightarrow t_2$ (3p-like)
					175.2	6.2	S $2p_{1/2} \rightarrow t_2$ (3p-like)
	D	M.S.	7.8	2484.6	177.1	8.1	M.S.
	E	S 1s → e (3d-like)	12.5	2489.3	180.8	11.8	S 2p → e (3d-like)
	F	M.S.	15.7	2492.5			
	G	S 1s → t_2 (3d-like)	21.7	2498.5	189.0	20.0	S 2p → t_2 (3d-like)
Celestite	A				171.4	2.4	S $2p_{3/2} \rightarrow a_1$ (3s-like)
					172.6	3.6	S $2p_{1/2} \rightarrow a_1$ (3s-like)
	C	S 1s → t_2 (3p-like)	4.5	2481.3	173.6	4.6	S $2p_{3/2} \rightarrow t_2$ (3p-like)
					175.2	6.2	S $2p_{1/2} \rightarrow t_2$ (3p-like)
	D	M.S.	7.6	2484.4	179.7	10.7	S $2p_{3/2} \rightarrow$ e (3d-like)
	E	S 1s → e (3d-like)	13.3	2490.1	180.8	11.8	S $2p_{1/2} \rightarrow$ e (3d-like)
	F	M.S.	18.4	2495.2			
	G	S 1s → t_2 (3d-like)	22.7	2499.5	189.5	20.5	S 2p → t_2 (3d-like)
Barite	A				171.6	2.6	S 2p → a_1 (3s-like)
	C	S 1s → t_2 (3p-like)	4.3	2481.1	174.0	5.0	S 2p → t_2 (3p-like)
	D	M.S.	7.1	2483.9	178.0	9.0	M.S.
	E	S 1s → e (3d-like)	11.7	2488.5	180.5	11.5	S $2p_{3/2} \rightarrow$ e (3d-like)
					181.6	12.6	S $2p_{1/2} \rightarrow$ e (3d-like)
	F	M.S.	15.0	2491.8			
			18.3	2495.1	189.1	20.1	S 2p → t_2 (3d-like)
	G	S 1s → t_2 (3d-like)	22.6	2499.4			

gypsum, which contain structurally-bound H_2O, peak A in the L-edge spectra shifts to low energy by about 0.9 eV, and the first peak of this doublet is weaker; the spin-orbit splitting of peak E is not observed. For anhydrite and celestite, peak A is at higher energy; the relative intensity of this doublet is reversed; and the spin-orbit splitting of peak E is resolved. For barite, peak A also shifts to lower energy, as for gypsum, but is not apparently split, whereas peak E moves to higher energy and is apparently split by the spin-orbit interaction of S 2p orbitals. Peak C in the K-edge spectra tends to shift to lower energy, and the post-edge features become more complicated, from $MgSO_4 \cdot 2H_2O$ to barite, probably related to the greater backscattering efficiency of the heavier cations beyond the first shell.

5.3.2 Chemical Shift in S K- and L-edges and Oxidation State of Sulfur

The first peak in both S K- and L-edge XANES spectra represents the transition of S 1s (for K-edge) or 2p (for L-edge) electrons to the first unoccupied states, and is tentatively regarded as the K- and L-edge of these materials. The S K- and L-edges of all the sulfides, sulfur, sulfite and sulfates, together with the $^{-}E_g$, reflectivity and abbreviations of metal sulfides, are summarized in Table 5.3.2.

Figure 5.3.2 correlates the S K- and L-edges of sulfides, sulfite and sulfates, and indicates that both S K- and L-edges shift toward high energy in sequence from sulfides to sulfur, sulfite and sulfates.

The variations of both S K- (solid dots) and L-edges (circles) with the oxidation state of sulfur are given in Figure 5.3.3; the S K- and L-edges for S^{2-} are averages of 22 metal sulfides, and the data for S^{6+} are the averages of 10 sulfates. Both S K- and L-edges shift toward higher energy by about 10 eV from S^{2-} to S^{6+} species. The chemical shift in x-ray absorption edge depends on the initial and final states involving the transition. When a valence electron is removed from an atom, the screening of core electrons by valence electrons is reduced, and the core energy levels become more tightly bound. Therefore, the binding energy of the inner shell S 2p increases with increase in its oxidation state, as evident it is in the XPS chemical shift. On the other hand, the

Table 5.3.2 S K- and L-edges (±0.1 eV), energy gap (eV) and reflectivity (R %) of sulfides

Minerals	Formula	K-edge	L-edge	E_g	R (%)	Keys
Sphalerite	ZnS	2473.4	163.6	3.8	16.4	sp
Wurtzite	ZnS	2473.2	163.5	3.9	16.3	wz
Greenockite	CdS	2472.3	162.2	2.5	18.7	gr
Metacinnabar	HgS	2471.7	162.0	2.3	25.2	mcin
Orpiment	As_2S_3	2470.8	161.6	2.4	23.1	op
Realgar	As_4S_4	2471.1	161.8	2.2	19.4	rg
Cinnabar	HgS	2471.1	161.8	2.0	28.1	cin
Proustite	Ag_3AsS_3	2471.1	162.0	2.0	29.3	pr
Stibnite	Sb_2S_3	2470.7	161.7	1.7	38.3	stb
Molybdenite	MoS_2	2469.4	161.9	1.0	44.0	mol
Pyrrhotite	$Fe_{1-x}S$	2469.8	161.7	1.0	38.9	po
Covellite	CuS	2471.1	162.5	2.0	19.3	cv
Tetrahedrite	$Cu_{12}Sb_4S_{13}$	2470.9	162.1	1.8	33.0	tet
Stannite	Cu_2FeSnS_4	2470.8	162.3	1.5	29.0	sta
Chalcocite	Cu_2S	2470.1	162.2	1.1	30.2	cc
Enargite	Cu_3AsS_4	2470.1	162.0	1.0	26.0	en
Bornite	Cu_5FeS_4	2470.0		1.0	24.4	bn
Cubanite	$CuFe_2S_3$	2469.5	161.6	0.7	40.2	cb
Chalcopyrite	$CuFeS_2$	2469.6	161.7	0.7	38.8	cp
Linnaeite	Co_3S_4	2469.8	161.7		44.7	lin
Carrollite	$CuCo_2S_4$	2469.7	161.6		41.9	car
Pyrite	FeS_2	2471.3	163.0	0.9	55.0	py
Marcasite	FeS_2	2471.2	163.0	0.9	51.6	mc
Sulfur	S_8	2472.0	163.3			
Na_2SO_3		2477.4	168.6			
Barite	$BaSO_4$	2481.1	171.6			
Celestite	$SrSO_4$	2481.2	172.0			
Anhydrite	$CaSO_4$	2481.3	172.4			
Gypsum	$CaSO_4.2H_2O$	2481.5	171.5			
	$MgSO_4.2H_2O$	2481.6	171.7			
	$MnSO_4$	2481.2	171.8			
	$FeSO_4$	2481.7	171.5			
	$CoSO_4$	2481.5	171.4			
	$NiSO_4$	2481.5	171.5			
	$Na_2S_2O_3$	2479.3	169.5			
		2470.8	162.9			

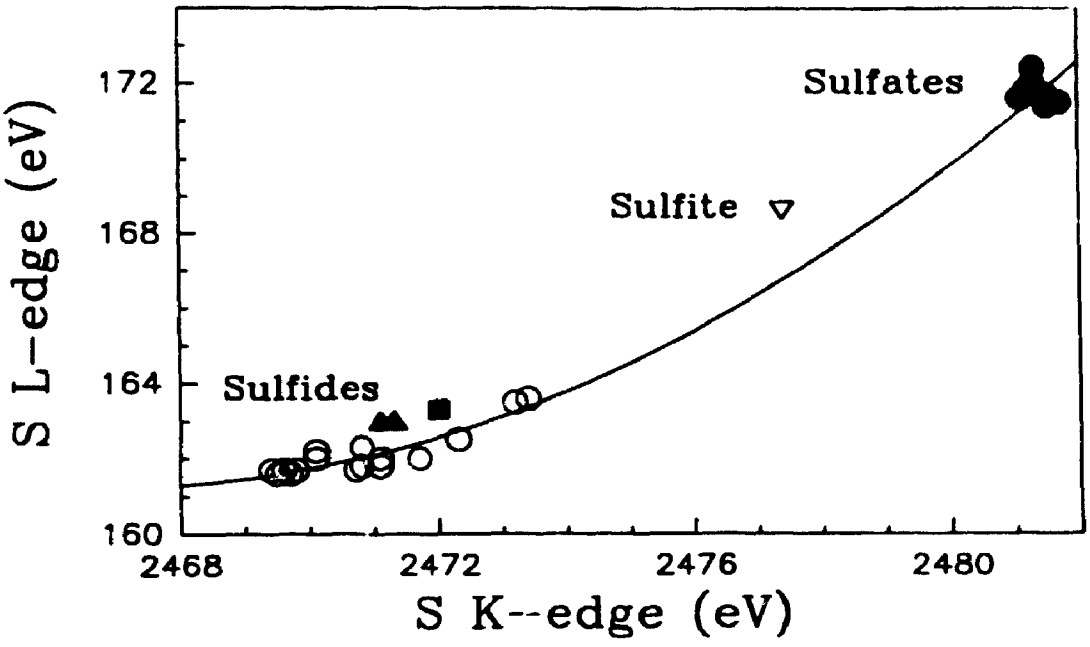

Figure 5.3.2 Correlation of S K- and L-edges of sulfides, sulfur, sulfide and sulfates.

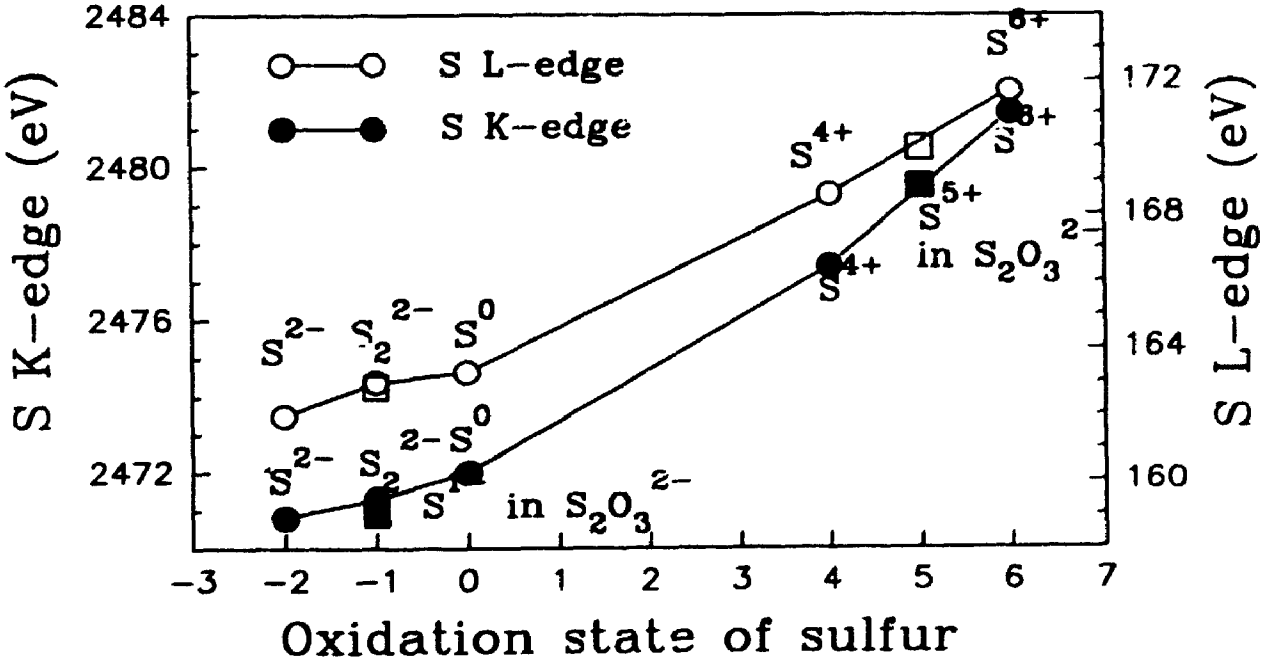

Figure 5.3.3 Correlations of S K- and L-edges with oxidation state of sulfur species.

more oxidized sulfur species form stronger bond with the same ligand, promoting greater overlap of sulfur and the ligand orbitals. This gives more stable bonding orbitals, and less stable anti-bonding orbitals. Consequently, the S K- and L-edges are expected to shift towards higher energy with increase in the oxidation state of sulfur. Thus, the correlation in Figure 5.3.3 unambiguously determines the oxidation state and form of sulfur in any kind of substance and state of matter. For example, in sodium thiosulfate ($Na_2S_2O_3$), it is commonly accepted that there are two different sulfur species, S^{2-} and S^{6+}. However, the S K and L-edge values of this compound are plotted in Figure 5.3.3, as empty and solid square, respectively, which shows that one of the sulfur species in $Na_2S_2O_3$ is better described as S^{5+}, and the other one is S^{-}, similar to sulfur in pyrite[6,7].

The shifts of S K- and L-edges with oxidation state of sulfur are extremely similar to that of S 2p BE. Figure 5.3.4 shows that the correlations (solid circles) of S K- (a) and L-edges (b) with the S 1s and 2p BE, respectively. The experimental S K- and L-edge data are shown as solid circles, and the open circles and the regression lines show the correlations when the relative S K- and L-edge values are assumed to equal to the respective S 1s and 2p BE (the slopes of the open circle lines are one). The S 2p BE were measured by XPS and cited from Hyland and Bancroft[8] for ZnS, FeS_2 and native sulfur, and from Fleet et al.[9] and Richardson and Vaughan[10] for $FeSO_3$ and $FeSO_4$. The S 1s BE is calculated by adding the S 2p BE and the S $K\alpha_1$ x-ray emission energy at 2307.8 eV. In general, the S K-edge and S 1s BE, as well as S L-edge and S 2p BE shift toward higher energy with oxidation state of sulfur. However, the shifts of S K- and L-edges are larger, because they depend on the shifts of the unoccupied final states, as well as the BE of the inner shells. It is very hard to quantitatively evaluate the contributions of the initial and final states to the shifts of S K- and L-edges. However, as shown in Figure 5.3.4, the BE shifts of the S 1s and 2p mainly contribute to the absorption edge shifts, but the shifts of the final states also make some contributions. As an example, the S 2p BE of ZnS and $CuFeS_2$, both of which contains S^{2-}, are very close, but the S K- and L-edges of ZnS shifts to much higher energy than those of $CuFeS_2$. Therefore, the shifts of the final unoccupied states must make significant contribution.

5.3.3 Chemical Shifts in S K- and L-edges versus Energy gap (E_g) and Reflectivity of Metal Sulfides

Figure 5.3.5 shows a positive linear correlation between S K- and L-edges of metal sulfides in an expanded scale, where the mineral name abbreviations are keyed in Table 5.3.2. This indicates that even for sulfides containing only S^{2-} species, the S K- and L-edges also shift significantly. Although small differences probably exist due to different geometrical and electronic structures, the inner S 1s and S 2p shells must be very similar for different sulfides. The chemical shifts in the S K- and L-edges of sulfides are mainly dependent on the final states, that is, the first unoccupied states which are the metal d crystal field bands mixed with the S 3p- and 3s-like states below the CB minimum for transition metal (Fe, Co, Ni, Cu and Mo) sulfides, and the antibonding S 3p- and 3s-like states at the CB minimum for Zn, Cd, Hg, As and Sb sulfides with fully occupied d orbitals. Therefore, the S K- and L-edges lie to lower energy for the former (empty circles) and at higher energy for the latter (filled circles). Therefore, the chemical shifts in the S K- and L-edges are related to the crystal chemistry, electronic structure, energy gap and reflectivity of these semiconducting materials.

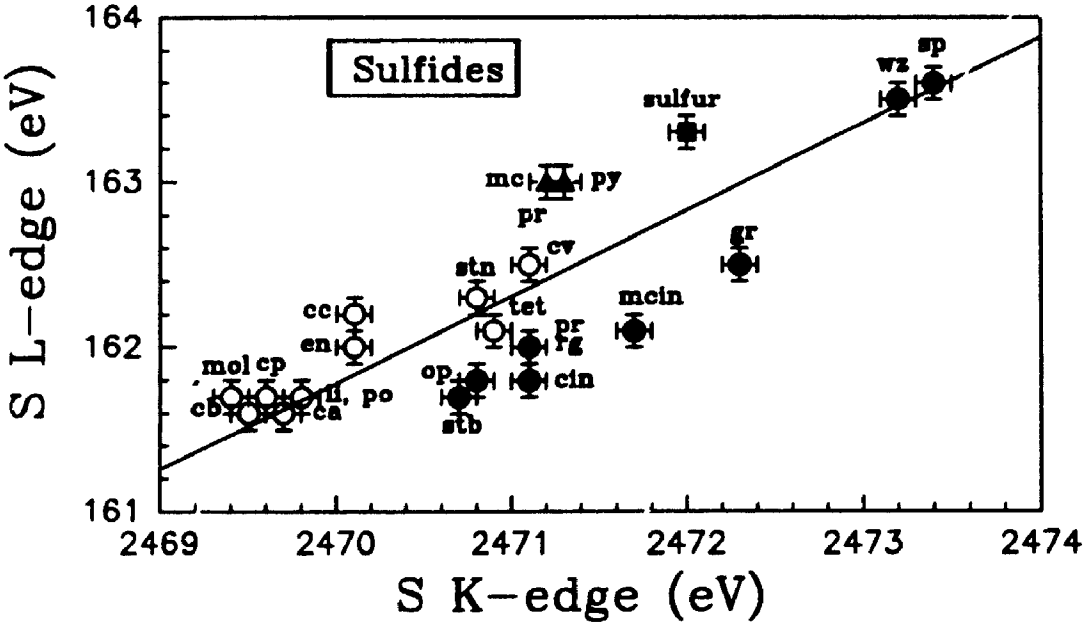

Figure 5.3.5 Correlation of S K- and L-edges of metal sulfide minerals

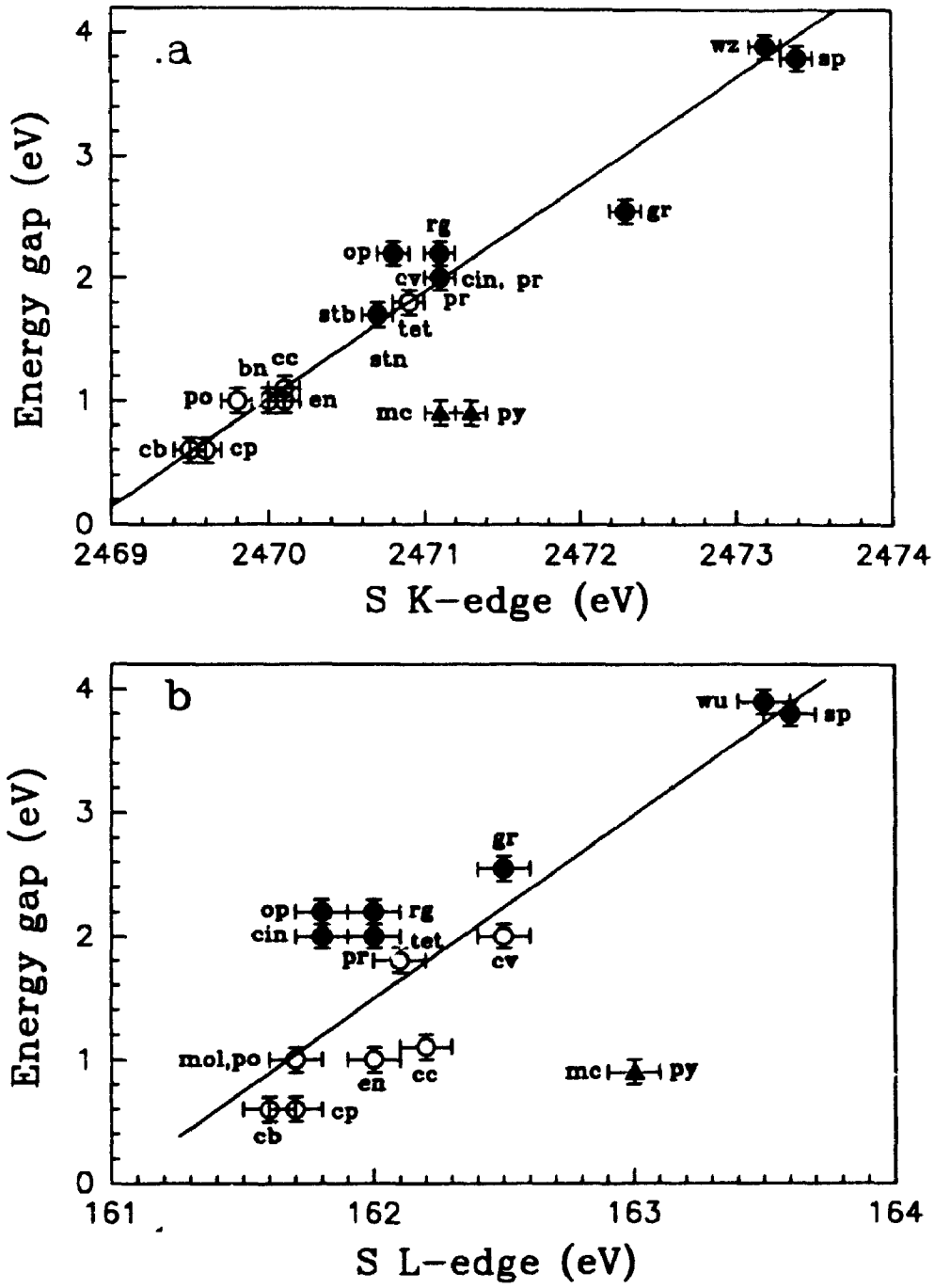

Figure 5.3.6 Correlations of S K- (a) and L-edges (b) with the E_g of metal sulfides.

Figure 5.3.6 shows the correlation of the S K- (a) and L-edges (b) with the energy gaps (E_g) of metal sulfides, where the energy gaps are cited mainly from Shuey[11]. First, it is apparent that for Cu and Cu-Fe sulfides which have small electrical resistance[12], both S K- and L-edges lie at lower energy and E_g is also smaller. For Zn, Cd, Hg, As and Sb sulfides with higher electrical resistance[9], the E_g is larger, and both S K- and L-edges are also at higher energy. Second, of all the sulfides studied, both S K- and L-edges are linearly correlated with E_g. In general, the correlations of S K- and L-edges with the energy gap of metal sulfides appear quite acceptable, because some of small deviations from linearity are no doubt due to very approximate E_g values, and establish a potential application of S K- and L-edge spectra in the determination of the E_g of semiconducting metal sulfides.

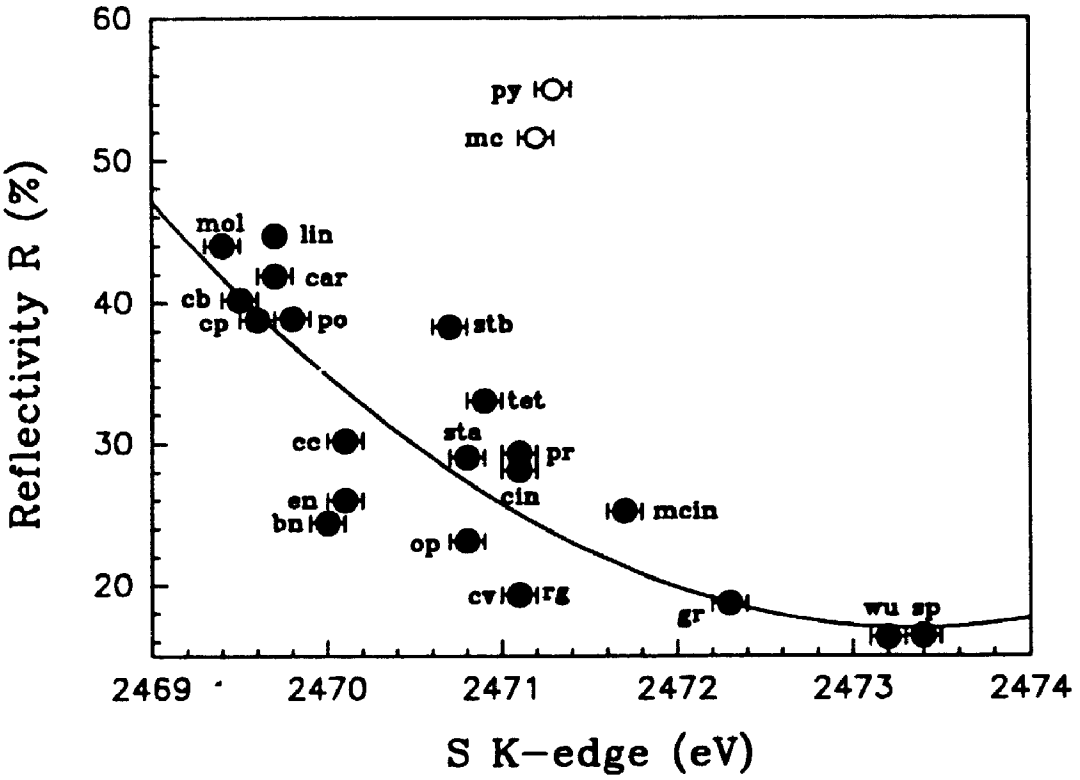

Figure 5.3.7 Correlation of S K-edge with reflectivity of metal sulfides.

Figure 5.3.7 shows the correlation of the S K-edge with the reflectivity (%) of the present metal sulfides, where the reflectivity values are cited from Anthony et al.[13]. This correlation is apparently non-linear. However, for simple sulfides, the S K-edge tends to shift toward higher energy with decrease in reflectivity. Also the S L-edge (not shown) tends to have a higher energy shift for metal sulfides with lower reflectivity.

Pyrite and marcasite deviate from the linear correlations of the S K- and L-edges with E_g (see Figure 5.3.6) and the curvilinear correlation between the S K-edge and reflectivity, because they contain S_2^{2-} species, rather than simple S^{2-} species.

5.3.4 EXAFS analysis of Some Sulfide Minerals of Known Crystal Structure

EXAFS analysis has become a routine technique in structural studies, following the development of synchrotron radiation sources and the single-electron single scattering theory[14]. EXAFS analyses yield bond distance (BD), coordination number (CN) of absorber atoms, and Debye-Waller factor (σ^2). Although the crystal structures of metal sulfide minerals investigated have long been known, the EXAFS analysis of these materials of known crystal structure is important for studying chalcogenide glasses, interfaces between sulfide minerals and solution, and metal proteins.

In the crystal structure of sphalerite, both sulfur and zinc atoms are four-fold coordinated and their site symmetries are T_d. Figure 5.3.8 shows the calibrated and normalized average EXAFS spectrum of sphalerite, containing 0.53 wt% of iron, and the EXAFS data reduction. The EXAFS analysis was done using program BAN[15]. The experimental average spectrum is normalized using I/I_0 (see Figure 5.3.8a). Following background subtraction, the spectrum is converted from energy space into k space by $\chi(k)=[\mu(E)-\mu_0(E)]/\mu_0(E)$, where, μ_0 is the background absorption above the edge without the EXAFS modulations, μ is the experimental absorption coefficient, k is the photoelectron wave vector defined as: $k = [0.262(E-E_0)]^{1/2}$, E is the incident photon energy, and E_0 is the threshold energy for photoelectron ejection. The weighted $k\chi(k)$ is shown as the solid line in Figure 5.3.8b. According to the single electron scattering model, the EXAFS modulations are described as[16]:

$$\chi(k) = \sum_j N_j S_i(k) F_j(k) \exp(-2\sigma_j^2 k^2 - 2r_j/\lambda(k)) \cdot [\sin(2kr_j + \phi_i(k) + \phi_j(k)]/kr_j^2$$

where, N_j is coordination number of backscattering atoms at distance r_j, $S_i(k)$ is a correction factor for absorber atom multielectron effects, $F_j(k)$ is the backscattering amplitude function, σ^2 is the EXAFS Debye-Waller factor, $\lambda(k)$ is a parameter which allows for loss of backscattering amplitude due to electron inelastic scattering effects, r_j is the distance of backscatterer j from the absorber atom, and $\phi_i(k)$ is a function for phase shift of the photoelectron wave during backscattering from neighbor atom j. The Fourier transform of the S K-edge EXAFS for sphalerite is shown in Figure 5.3.8c. The structure function in R space clearly indicates the three interatomic shells and even more distant shells. Figures 5.3.8d, 5.3.8e and 5.3.8f show the back Fourier transforms for windowing the first, second and third shells, respectively. The sum of the back Fourier transforms for the three shells is shown as the dash line in Figure 5.3.8b. This sum is obviously a good fit to the experimental structure function with the exception that the low *k* modulations have some contribution from more distant interatomic shells. Finally using Rehr and McKale phase shifts and amplitude correction[17,18], the average BD, CN and Debye-Waller factor σ^2 for each shell in sphalerite have been calculated. The EXAFS parameters of sphalerite, chalcopyrite and stannite are reported in Table 5.3.3.

Analysis of the second and even more distant neighbor shells of an absorbing atom is important for studying effects such as clustering and ordering, and interconnection of polyhedra in glasses. Use of the theoretical phase shift and amplitude may not apply well to the second shell, because the multiple scattering from the first shell atoms is not considered in the usual single scattering EXAFS formalism, but this is not a serious problem for the sphalerite structure. When the theoretical functions are used to fit the back Fourier transforms for the second and the third neighbor shells, good curve fitting and close similarity of structural parameters to x-ray structure values are obtained. Therefore, sphalerite is a useful model compound for EXAFS structure analysis of related systems, such as chalcogenide glasses and metalloproteins.

Comparison of the structural parameters obtained using the theoretical Rehr and McKale phase shifts and amplitudes indicates that for the first shell, and perhaps the

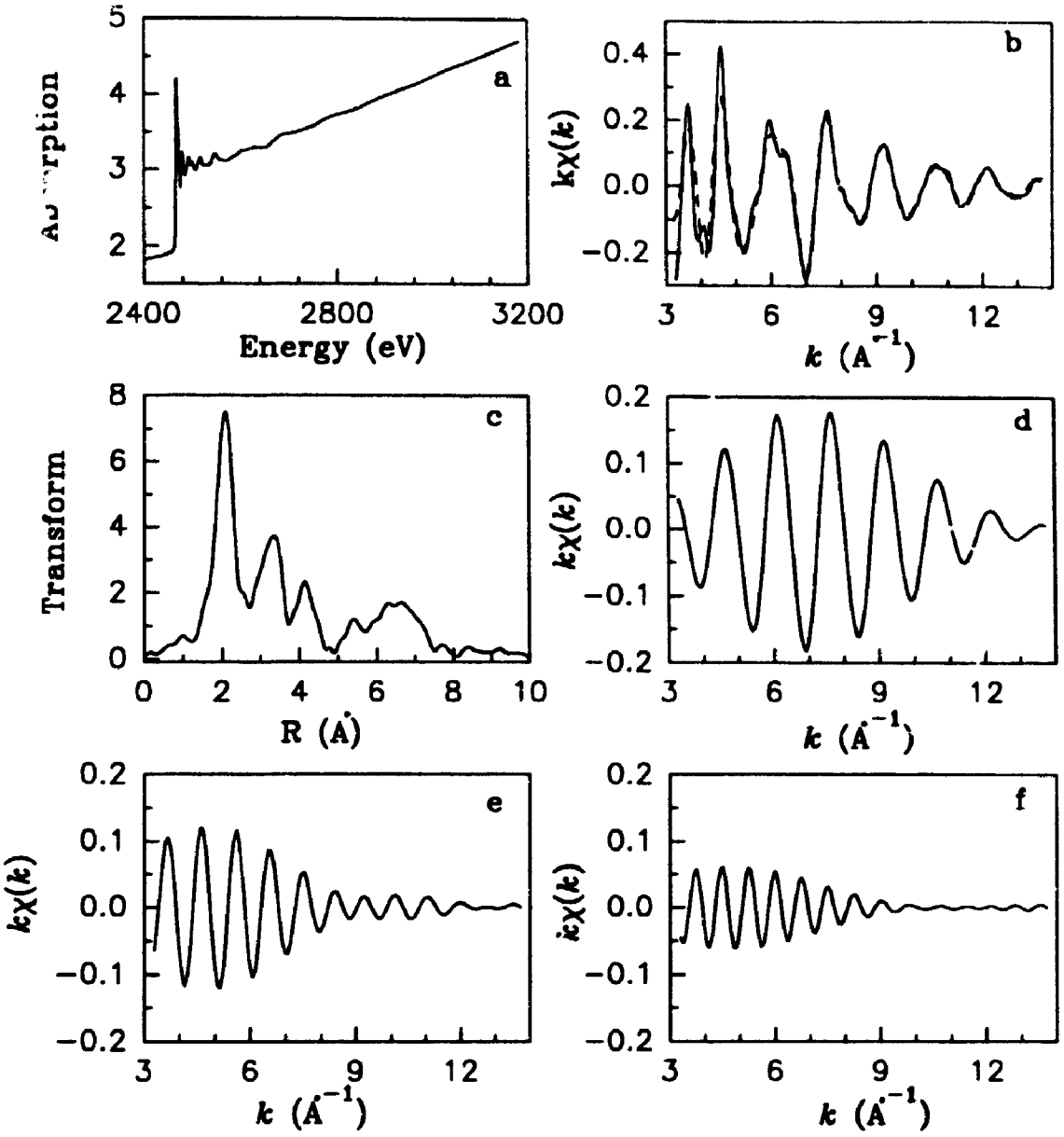

Figure 5.3,8 EXAFS analysis of sulfur in sphalerite. (a) Experimental spectrum; (b) Experimental structure function (solid line) in k space, the dash line is the sum of the back Fourier transforms for the first three neighbour shells; (c) Fourier transform of the structure function; (d) The back Fourier transform for the first shell; (e) The back Fourier transform for the second shell; (f) The back Fourier transform for the third shell.

Table 5.3.3 S K-edge EXAFS analysis of sphalerite, chalcopyrite and stannite

Minerals	Atomic shells		X-ray structure		EXAFS analysis*					
					Rehr et al. (1991)[15]			McKale et al. (1988)[14]		
			BD	CN	BD	CN	σ^2	BD	CN	σ^2
Sphalerite	1st	S-Zn	2.34	4	2.35	3.4	0.0045	2.35	3.5	0.0051
	2nd	S-S	3.83	12	3.82	7.3	0.0072	3.83	8.4	0.0076
	3rd	S-Zn	4.48	12	4.48	16.1	0.0197	4.44	16.0	0.0214
Chalcopyrite	1st	S Cu	2.30	2	2.28	1.90	0.0058	2.28	1.85	0.0063
		S-Fe	2.26	2	2.23	1.90	0.0058	2.23	1.85	0.0063
	2nd	S-S	3.74	12	3.62			3.62		
	3rd	S-Cu,Fe	4.38	12	4.31			4.33		
Stannite	1st	S-Fe	2.34	1	2.34	0.58	0.0077	2.33	0.61	0.0081
		S-Cu	2.33	2	2.33	1.17	0.0077	2.33	1.22	0.0081
		S-Sn	2.40	1	2.41	0.60	0.0077	2.40	0.65	0.0081

* BD — Bond distance (Å); CN — Coordination number; σ^2 — Debye-Waller factor

second shell, the two sets of values are closely compatible, Although in principle the theoretical phase shifts and amplitudes may not apply for the more distant neighbor shells. For the first shell of the absorbing atom, the BD derived from the EXAFS analysis using theoretical phase shifts and amplitudes are accurate to ± 0.02 Å, compared to the x-ray structure data, and the CN is accurate to about ± 20 percent.

Interestingly, the Debye-Waller factor for sphalerite increases from the first shell to the third shell. This may reflect the lack of direct bonding to more distant back scatterers; sample cooling should have a greater effect on the more distant shells.

5.4 Conclusions

Both S K- and L-edges shift to higher energy with increase in oxidation state of sulfur, from sulfides, sulfur, sulfite and sulfates. Two different sulfur species in $Na_2S_2O_3$ are most likely closer S^{1-} and S^{5+}, rather than S^{2-} and S^{6+} as previously recognized, based on the S K- and L-edge spectra. Also both S K- and L-edges of metal sulfides are positively correlated, and shift to higher energy with increase in the energy gap and with decrease in reflectivity of these semiconducting materials. These results demonstrate the potential of S K- and L-edge XANES spectroscopy in determining qualitatively or even quantitatively the sulfur species in geological samples such as marine sediments, coal and petroleum, and providing information on the electronic structures and semiconducting properties of metal sulfide materials. Compared with x-ray photoelectron spectroscopy (XPS), S K- and L-edge XANES spectroscopy has many advantages. First, it can study gas, liquid, crystalline and amorphous solid materials; second, it can be used to study inorganic and organic sulfur, and sulfur species of low or high concentrations; it just takes several minutes to collect a spectrum.

5.5 References

1. J.L. Dehmer, *J. Chem. Phys.* **56**, 4496 (1972).

2. S. Bodeur and A.P. Hitchcock, *Chem. Phys.* **111**, 467 (1987).

3. A.P. Hitchcock, S. Bodeur and M Tronc, *Chem. Phys.* **115**, 93 (1987).

4. H. Friedrich, B. Pittel, P. Rabe, W.H.P. Schwarz and B. Sonntag, *J. Phys. B: Atoms Molec. Phys.* **13**, 25 (1980).

5. Dien Li, G.M. Bancroft G.M., Kasrai M., Fleet M.E. Feng X.H., Tan, K.H. and B.X. Yang, *Solid State Commun.* **87**, 613 (1993).

6. H. Sekiyama, N. Kosugi, H. Kuroda and T. Ohta, *Bull. Chem. Soc. Japan* **59**, 575 (1986).

7. A. Vairavamurthy, B. Manowitz, G.W. Luther III and Y. Jeon, *Geochim. Cosmochim. Acta* **57**, 1619 (1993).

8. M.M. Hyland and G.M. Bancroft, *Geochim. Cosmochim. Acta* **53**, 367 (1988).

9. M.E., Fleet, S.L. Chryssoulis, P.J. Maclean, R. Davison and C.G. Weisener, *Can. Mineral.* **31**, 1 (1993).

10. S. Richardson and D.J. Vaughan, *Mineral. Mag.* **53**, 213 (1989).

11. R.T. Shuey, *Semiconducting Ore Minerals*. Elsevier Publishing Company, Amsterdam, 1975.

12. D.J. Vaughan and J.R. Craig, *Mineral Chemistry of Metal Sulfides*. Cambridge University Press, Cambridge, London, 1978.

13. J.W. Anthony, R.A. Bideaux, K.W. Bladh and M.C. Nichol, *Handbook of Mineralogy, I. Elements, Sulfides and Sulfosalts*. Mineral Data Publishing, Tucson, Arizona, 1990.

14. B.K. Teo, *EXAFS: Basic Principles and Data Analysis*, Springer-Verlag, Berlin, 1986.

15. T. Tyliszczak, Ban data analysis program. Unpublished.

16. G.A. Waychunas, G.E. Brown and M.J. Apted, *Phys. Chem. Minerals* **13**, 31 (1986).

17. A.G. McKale, B.W. Veal, A.P. Paulikas, S.K. Chan and G.S. Knapp, *J. Am. Chem. Soc.* **110**, 3763 (1988).

18. J.J. Rehr, L.J. de Mustre, S.I. Zabinsky and R.C. Albers, *J. Am. Chem. Soc.* **113**, 5135 (1991).

CHAPTER 6

X-ray Absorption Spectroscopy of SiO_2 Polymorphs: Structural Characterization of Opal

6.1 Introduction

Extensive studies on phase transformations of Mg and Fe silicates at high temperature and high pressure have been made to understand the mineralogy, petrology and seismic discontinuities of the Earth's mantle. The phase transformations in $MgSiO_3$ and Mg_2SiO_4, two of the most important silicate compositions, have been established as follows[1]: with increase in pressure, the sequences of transformation are: enstatite ($MgSiO_3$) to β-spinel and stishovite, to γ-spinel and stishovite, to ilmenite, and finally to perovskite phases; forsterite (Mg_2SiO_4) to β-spinel, to γ-spinel, and finally to perovskite phases. The densification of silicates at high pressure is caused by more efficient packing of anions and/or increase in the coordination number of cations.

There are many polymorphic modifications of silicon dioxide (SiO_2) at high temperature and high pressure, including 4:2 coordinate structures (e.g. α-quartz, cristobalite, tridymite and coesite) and a 6:3 coordinate structure (stishovite). Stishovite was initially synthesized at pressure above 100 kbar[2], and subsequently discovered in an impact breccia from Meteorite Crater, Arizona[3]. Stishovite has a rutile-type structure[4]. The detailed crystal chemistry of stishovite was described by Hill et al.[5] and Ross et al.[6]. The electronic structures of α-quartz[7-17], β-cristobalite[17-20] and stishovite[19-23] have been calculated using various approaches. The calculated valence band structures were used to reasonably interpret the experimental photoelectron spectra (XPS and UPS) and x-ray emission spectra (XES). Wiech[24] and Wiech and Kurmaev[25] also studied the electronic structure of crystalline and vitreous SiO_2 using Si K XES. These studies provided important information on the valence band (VB) structure and bonding of SiO_2 polymorphs.

The Si L-edge XANES of α-quartz was first reported by Brown et al[26]. The Si K- and L-edge XES and XANES of stishovite and α-quartz have been studied comparatively[27,28]. Recently, Davoli et al.[29] also studied the Si K-edge and O K-edge XANES of densified a- SiO_2 at high pressure. However, the assignments for the XANES spectra of both α- quartz and stishovite were in conflict, and the conduction band (CB) structure and unoccupied densities of states (DOS) of SiO_2 are not fully understood.

In this chapter, high-resolution Si K- and L-edge XANES of 4:2 coordinate α-quartz, α-cristobalite, coesite and amorphous SiO_2 and opals, and 6:3 coordinate stishovite are presented, and the unoccupied electronic states of these forms of silica (SiO_2) are studied. In addition, the relation of the XANES spectra to the crystal structures of SiO_2 polymorphs and important new applications of XANES to the study of amorphous silicate materials are discussed.

6.2 Experimental

Natural and synthetic stishovite samples were provided by Professor Lin-gun Liu, Australian National University. The natural stishovite was separated from sandstone of the Meteorite Crater, Arizona, by German researchers. The synthetic stishovite was obtained by reacting coesite and graphite at 120 kbar. Natural single-crystal α-quartz and the two opal samples were from the mineral collection in the Department of Earth Sciences, University of Western Ontario (UWO). Two cristobalite samples were synthesized at room pressure and 1600 °C, while the coesite sample was synthesized at 1000 °C and 50 kbar using the 1000 ton cubic-anvil press at UWO. All samples were checked by powder x-ray diffraction (PXRD) before collection of XANES spectra. Both samples of opal were highly disordered, and nearly amorphous. Opal #1232 was a precious opal from Queensland, Australia, and has a PXRD pattern similar to sample H[30]. Opal #800 was from Virgin, Nevada, and had a PXRD pattern intermediate between that of samples G and F[30]. The Si K- and L-edge XANES spectra were collected using the DCM and Grasshopper beamlines and synchrotron radiation by Total Electron Yield.

6.3 Results and Discussion

6.3.1 Interpretation of XANES Spectra

Figure 6.3.1 shows the Si K- and L-edge XANES of α-quartz and stishovite, along with the calculated unoccupied DOS[12,15]. The L-edge spectra are aligned using the XPS Si 2p binding energy (BE) of α-quartz at 103.4 eV[31], and the Si K-edge spectra are correlated with the L-edge spectra by taking the Si $K\alpha_1$ x-ray emission line of α-quartz at 1740.0 eV. The peak positions are summarized in Table 6.3.1, in which ΔE is the difference between the XANES resonance and the corresponding Si 1s or 2p BE of α-quartz. The ΔE value for the corresponding peaks A to G in the L- and K-edge spectra of both minerals are very similar, although the relative intensities differ considerably. The slight differences in ΔE of the corresponding L- and K-edge spectral features are probably attributable to differences in L and K core-hole relaxation. The calculated DOS features also correspond reasonably well in most cases with the L- and K-edge features (Figure 6.3.1), although relative intensities differ considerably.

Si K- and L-edge XANES[27,28] of α-quartz and stishovite were reported and interpreted based on the MO calculations of SiO_4^{4-} and SiO_6^{8-} clusters. Recently, Azizan et al.[32] used the MO calculation of the SiO_4^{4-} cluster to interpret the direct and inverse photoemission spectra of crystalline and amorphous SiO_2, and to study the electronic structures of these materials. In the ground state of the SiO_4^{4-} molecule-like cluster having T_d point symmetry, the s-orbitals of the Si atom transform to an a_1 representation, the p-orbitals transform to a t_2 representation, and the d-orbitals split into triply degenerate t_2 and doubly degenerate e representations. The electric dipole selection rules governing electronic transitions in XANES spectra are $\Delta L = \pm 1$, $\Delta S = 0$ and $\Delta J = \pm 1$.

For 4:2 coordinate α-quartz, the Si XANES spectra are characteristic of a tetrahedral SiO_4 cluster. Indeed the main peaks A, C, E and G in both K- and L-edge XANES are aligned well, and can be assigned generally from the gas phase spectra of the tetrahedral analogues $Si(OCH_3)_4$ [33], SiH_4 [34] and SiF_4 [35]. Based on the molecular orbital approach mentioned above[7,27,32], peak A in the L-edge XANES corresponds to

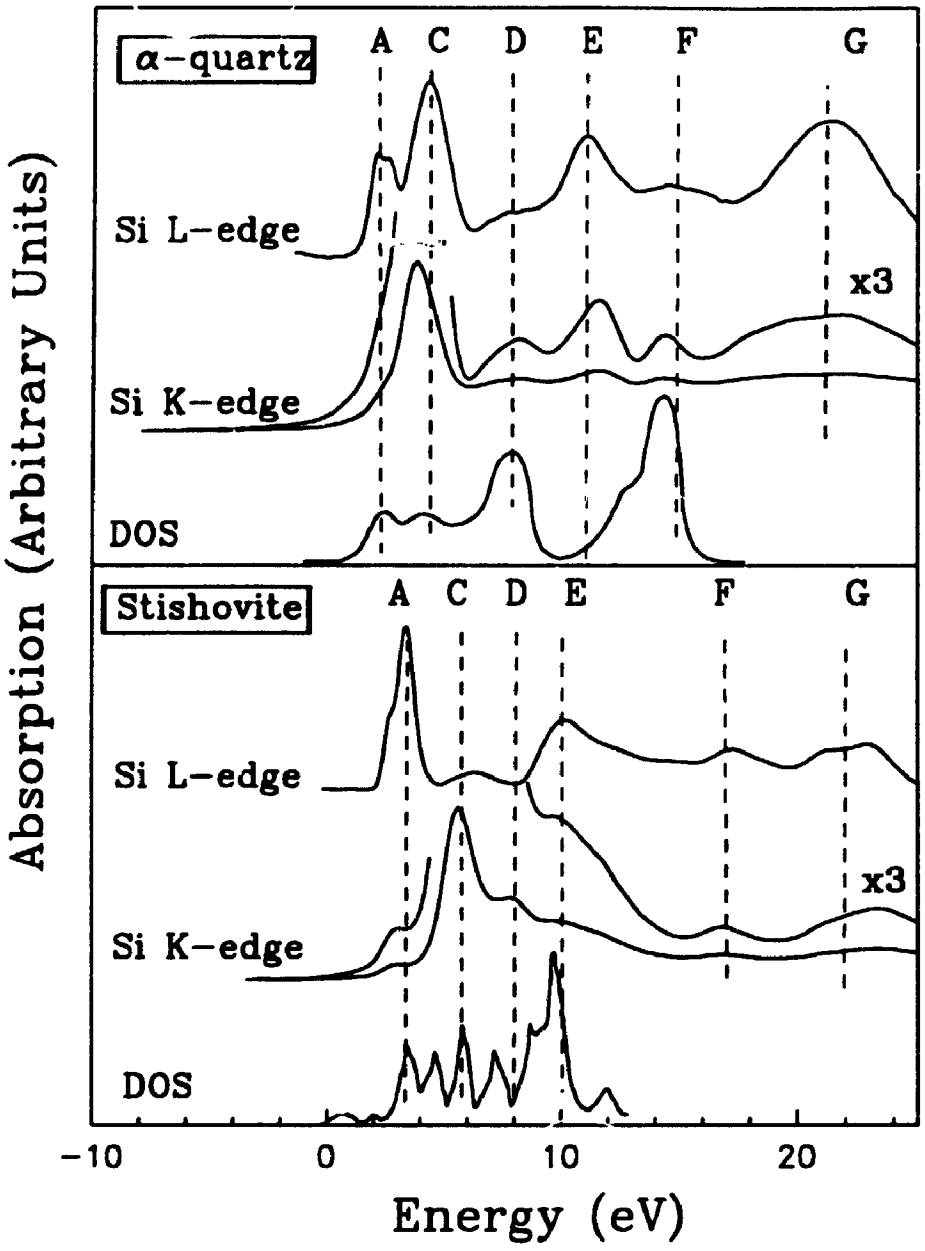

Figure 6.3.1 Si K- and L-edge XANES spectra of α-quartz and stishovite. The DOS calculated for α-quartz[12] and stishovite[13] are included for comparison.

Table 6.3.1 Si K- and L-edge XANES spectra and peak assignments of SiO_2 polymorphs

		K-edge (±0.2 eV)		Assignments*	L-edge (±0.2 eV)		Assignments*
		Peaks	ΔE**		Peaks	ΔE**	
α-quartz	A	1844.9	1.5	Si 1s → a_1 (Si 3s/3p)	105.4	2.0	Si $2p_{3/2}$ → a_1 (Si 3s/3p)
					106.0	2.6	Si $2p_{1/2}$ → a_1 (Si 3s/3p)
	C	1846.8	3.4	Si 1s → t_2 (Si 3p/3s)	107.8	4.4	Si 2p → t_2 (Si 3p/3s)
	D	1850.7	7.3	multiple scattering	111.3	7.9	multiple scattering
	E	1854.5	12.1	Si 1s → e (Si 3d/3p)	114.5	11.1	Si 2p → e (Si 3d/3p)
	F	1857.4	14.0	multiple scattering	118.5	15.1	multiple scattering
	G	1864.3	20.9	Si 1s → t_2 (Si 3d/3p)	125.0	21.6	Si 2p → t_2 (Si 3d/3p)
Cristobalite	A	1844.9	1.5	Si 1s → a_1 (Si 3s/3p)	105.6	2.2	Si $2p_{3/2}$ → a_1 (Si 3s/3p)
					106.2	2.8	Si $2p_{1/2}$ → a_1 (Si 3s/3p)
	C	1846.7	3.3	Si 1s → t_2 (Si 3p/3s)	108.0	4.6	Si 2p → t_2 (Si 3p/3s)
	D	1849.9	6.5	multiple scattering	111.3	8.3	multiple scattering
	E	1852.6	9.2	Si 1s → e (Si 3d/3p)	114.2	10.8	Si 2p → e (Si 3d/3p)
	F	1856.5	13.1	multiple scattering	115.9	12.5	multiple scattering
	G	1863.6	20.2	Si 1s → t_2 (Si 3d/3p)	127.8	21.2	Si 2p → t_2 (Si 3d/3p)
Coesite	A	1843.6	0.2	Si 1s → a_1 (Si 3s/3p)	105.9	2.5	Si $2p_{3/2}$ → a_1 (Si 3s/3p)
					106.5	3.1	Si $2p_{1/2}$ → a_1 (Si 3s/3p)
	C	1846.8	3.4	Si 1s → t_2 (Si 3p/3s)	107.8	4.4	Si 2p → t_2 (Si 3p/3s)
	D	1851.1	7.7	multiple scattering	111.3	7.9	multiple scattering
	E	1855.0	11.6	Si 1s → e (Si 3d/3p)	114.3	10.9	Si 2p → e (Si 3d/3p)
	F	1858.4	15.0	multiple scattering	116.5	13.1	multiple scattering
	G	1864.0	20.6	Si 1s → t_2 (Si 3d/3p)	125.9	22.5	Si 2p → t_2 (Si 3d/3p)

Table 6.3.1 continue

a-SiO_2	A	1844.9	1.5	Si 1s → a_1 (Si 3s/3p)	104.8	1.4	Si $2p_{3/2}$ → a_1 (Si 3s/3p)
					105.4	2.2	Si $2p_{1/2}$ → a_1 (Si 3s/3p)
	C	1846.9	3.5	Si 1s → t_2 (Si 3p/3s)	107.7	4.3	Si 2p → t_2 (Si 3p/3s)
	E	1853.4	10.0	Si 1s → e (Si 3d/3p)	114.8	11.3	Si 2p → e (Si 3d/3p)
	G	1863.8	20.4	Si 1s → t_2 (Si 3d/3p)	131.1	27.3	Si 2p → t_2 (Si 3d/3p)
Opal	A	1844.9	1.5	Si 1s → a_1 (Si 3s/3p)	105.5	2.1	Si $2p_{3/2}$ → a_1 (Si 3s/3p)
					106.2	2.8	Si $2p_{1/2}$ → a_1 (Si 3s/3p)
	C	1846.8	3.4	Si 1s → t_2 (Si 3p/3s)	108.1	4.7	Si 2p → t_2 (Si 3p/3s)
	E	1852.7	9.3	Si 1s → e (Si 3d/3p)	115.1	11.7	Si 2p → e (Si 3d/3p)
	G	1863.6	20.2	Si 1s → t_2 (Si 3d/3p)	130.4	27.0	Si 2p → t_2 (Si 3d/3p)
stishovite	A	1846.3	2.9	Si 1s → a_{1g} (Si 3s/3p)	106.0	2.6	Si $2p_{3/2}$ → a_{1g} (Si 3s/3p)
					106.8	3.4	Si $2p_{1/2}$ → a_{1g} (Si 3s/3p)
	C	1849.0	5.6	Si 1s → t_{1u} (Si 3p/3s)	109.8	6.4	Si 2p → t_{1u} (Si 3p/3s)
	D	1851.3	7.9	multiple scattering			
	E	1853.4	10.0	Si 1s → t_{2g} (Si 3d/3p)	113.6	10.2	Si 2p → t_{2g} (Si 3d/3p)
	F	1860.2	16.8	multiple scattering	120.7	17.3	multiple scattering
	G	1866.4	23.0	Si 1s → e_g (Si 3d/3p)	126.4	23.0	Si 2p → e_g (Si 3d/3p)

* The majority character of the conduction band states is given first.

** The XPS Si 2p BE of α-quartz is 103.4 eV, and the Si $K\alpha_1$ x-ray emission energy is 1740.0 eV, so that the Si 1s BE is calculated to be 1843.4 eV. The ΔE is the energy difference between the resonances and the Si 1s BE for the Si K-edge XANES and between the resonances and the Si 2p BE for the Si L-edge XANES. The reading error of the edge peak is ±0.1 eV.

transition of Si 2p electrons to the antibonding Si 3s-like a_1 states. The splitting of this peak by about 0.6 eV is attributed to the spin-orbital interaction of Si 2p orbitals. O'Brien et al.[36] determined the CB minimum of α-quartz at 106.73 eV, based on the Si L_2 XES at 97.3 eV and the known optical band gap of 9.1 eV[17]. Therefore, peak A is also called a core exciton below the CB minimum of α-quartz[38]. Peak A in the K-edge XANES is weak because the transition of Si 1s → Si 3s-like states is dipole-forbidden. Peak C in the Si K-edge spectrum is attributed to the dipole-allowed transition of S 1s electrons to the antibonding t_2 state of majority Si 3p character, and peak C in the L-edge spectra to the transition of Si 2p electrons to the t_2 state. The high intensity of peak C in the L-edge spectrum shows that even though this corresponds to a Si 2p → p-like transition, a $t_2 \rightarrow t_2$ transition is, in fact, dipole-allowed[27,39]. This is also consistent with the acentric tetrahedral symmetry, and the strong hybridization of the Si 3s/3d and 3p orbitals in α-quartz. Peaks E and G in the L-edge XANES are assigned to the empty Si 3d states[40], also called "shape resonances"[38,41,42]. In the T_d crystal field, the 3d orbitals are split into e and t_2 states, and the e states are favored in energy over t_2. Peak E is assigned to transitions to the e states, and peak G to the t_2 states. The Si 3d states in α-quartz also have contributions from Si p electron states, which are responsible for peaks E and G in the Si K-edge XANES of α-quartz.

Peaks D and F in both K- and L-edge spectra of α-quartz correspond with peaks in the DOS. However, these two peaks are not present in Si K- and L-edge XANES of a-SiO_2, the theoretical calculations of gaseous $Si(OCH_3)_4$ and $Si(CH_3)_4$ [33], and the Si L-edge XANES of SiH_4 [34] and SiF_4 [35]. On the other hand, MS calculations for zircon ($ZrSiO_4$) indicated that with increasing the size of the cluster, the p-like DOS is modified by outer shells. For the SiO_4^{4-} cluster, the calculated spectrum is similar to that of a-SiO_2. When up to seven shells are included in the MS calculation, the Si K-edge electron energy loss near-edge structure (ELNES) are reproduced[43]. The peaks, due to the MS effect, absent in the SiO_4^{4-} spectrum, correspond well to peaks D and F in the Si K-edge XANES spectrum of α-quartz. From this argument, peaks D and F are probably related to the extended energy band structure or the MS of the more distant shell atoms in the crystal structure. Davoli et al.[29] reported the Si K-edge spectra of densified vitreous

silica, however, their spectra had lower signal-to-noise ratios, and their MS calculations are not in agreement with their experimental results and their conclusions. More recently, Bart et al.[44] interpreted peaks D, E, F and G in the Si K-edge spectrum of α-quartz as the MS from the more distant atoms, using the Natoli model[45], but they did not even include the first Si-O shell in the ΔE versus $1/R^2$ correlation. Actually we tried to use this model, but it does not work for the spectra of α-quartz and many other silicate minerals.

The very different Si K- and L-edge spectra for 6:3 coordinate stishovite can be interpreted qualitatively with the help of the Si K- and L-edge spectra of octahedral SF_6[42] and the MO calculation of the SiO_6^{8-} cluster[21,27]. In octahedral symmetry, the s state transforms to an a_{1g} representation, the p state to a t_{1u} representation, and the d state is split into t_{2g} and e_g orbitals. Therefore, peak A in the L-edge spectrum is due to the transition of Si 2p electrons to the antibonding a_{1g} Si 3s-like orbital. The splitting of peak A is apparently larger than the Si 2p spin-orbit splitting of 0.6 eV, but this splitting must be mainly due to the Si 2p spin-orbit interaction. Peak A in the K-edge spectrum is relatively weak because the transition of Si 1s $\rightarrow$ 3s is dipole-forbidden. Peak C is attributed to the transition of Si 1s electrons to the antibonding Si 3p-like t_{1u} orbital. This transition is not formally allowed in the L-edge spectrum, and so peak C is very weak in the L-edge spectrum, as in the corresponding spectrum of SF_6 [42]. In addition, the hybridization of Si 3s/3d and Si 3p orbitals in stishovite is much weaker than that in α-quartz, because of the octahedral crystal field in stishovite. Peaks E and G in the L-edge spectrum can be assigned readily to the d-like shape resonance of t_{2g} and e_g character, respectively. The energy separation of the two Si 3d bands in stishovite is larger than in α-quartz as required for the present assignments, but does not obey the rule: $\Delta_{tet} = -4/9\Delta_{oct}$ [40]. The empty Si 3d bands are also mixed with some Si p-like states, which are responsible for the weak peaks E and G in the K-edge spectrum of stishovite. The origins of peak D in the K-edge XANES and peak F in the K- and L-edge spectrum of stishovite may be related also to the extended energy band structure or MS effects, as discussed for α-quartz.

The qualitative assignments of the near-edge Si K- and L-edge spectra of α-quartz

and stishovite are summarized in Table 1. These assignments are reasonably consistent, and also in reasonable agreement with calculated unoccupied DOS (see Figure 1). Unfortunately, the DOS calculations gave neither the s, p or d character of these unoccupied states nor the transition probability to these states[12,15], and it is not possible to relate the experimental and theoretical intensities even semi-qualitatively. However, a qualitative and reasonable assignment has been given to the present spectra, which gives satisfactory relative intensities.

6.3.2 XANES Spectra and Crystal Chemistry

Figure 6.3.2 shows the Si K-edge XANES spectra of cristobalite, coesite, a-SiO_2 and the two opals, in addition to α-quartz and stishovite, in which the Si 1s BE for α-quartz is indicated by a solid line an arrow on the top left. The Si K-edge spectrum of a-SiO_2 is in agreement with the results of Davoli et al. [29]. The peak positions and the assignments are also summarized in Table 1. It is immediately apparent that the XANES spectrum of the 6:3 coordinate stishovite is very different from those of 4:2 coordinate α-quartz, cristobalite and coesite. In 4:2 coordinate SiO_2, the strongest peak C at about 1846.8 eV characterizes the tetrahedral coordinate silicon (Si^{IV}) with oxygen in the Si K-edge XANES, and peak A, due to the dipole-forbidden Si 1s → Si 3s transition, is very weak. However, peak C in the stishovite K-edge spectrum has shifted by about 2.2 eV to higher energy compared to peak C in 4:2 coordinate SiO_2, and peak A is significantly intensified, even though the Si 1s → Si 3s transition is also dipole-forbidden in the octahedral field. Also peaks F and G shift to higher energy (Figure 6.3.2). Therefore, on a simple fingerprint basis, it is apparent that Si K-edge XANES spectra should be very useful for distinguishing between Si^{IV} and Si^{VI} in silicate minerals and glasses.

For 4:2 coordinate cristobalite and coesite, the general spectral profiles are similar to that of α-quartz. The four main peaks A, C, E and G are assigned to the transitions of Si 1s electrons to a_1 (Si 3s-like), t_2 (Si 3p-like), e and t_2 (Si 3d-like) states in tetrahedral symmetry. However, some apparent changes are observed in the Si K-edge spectra of these 4:2 coordinate SiO_2. First, peak A, due to dipole-forbidden Si 1s → 3s-

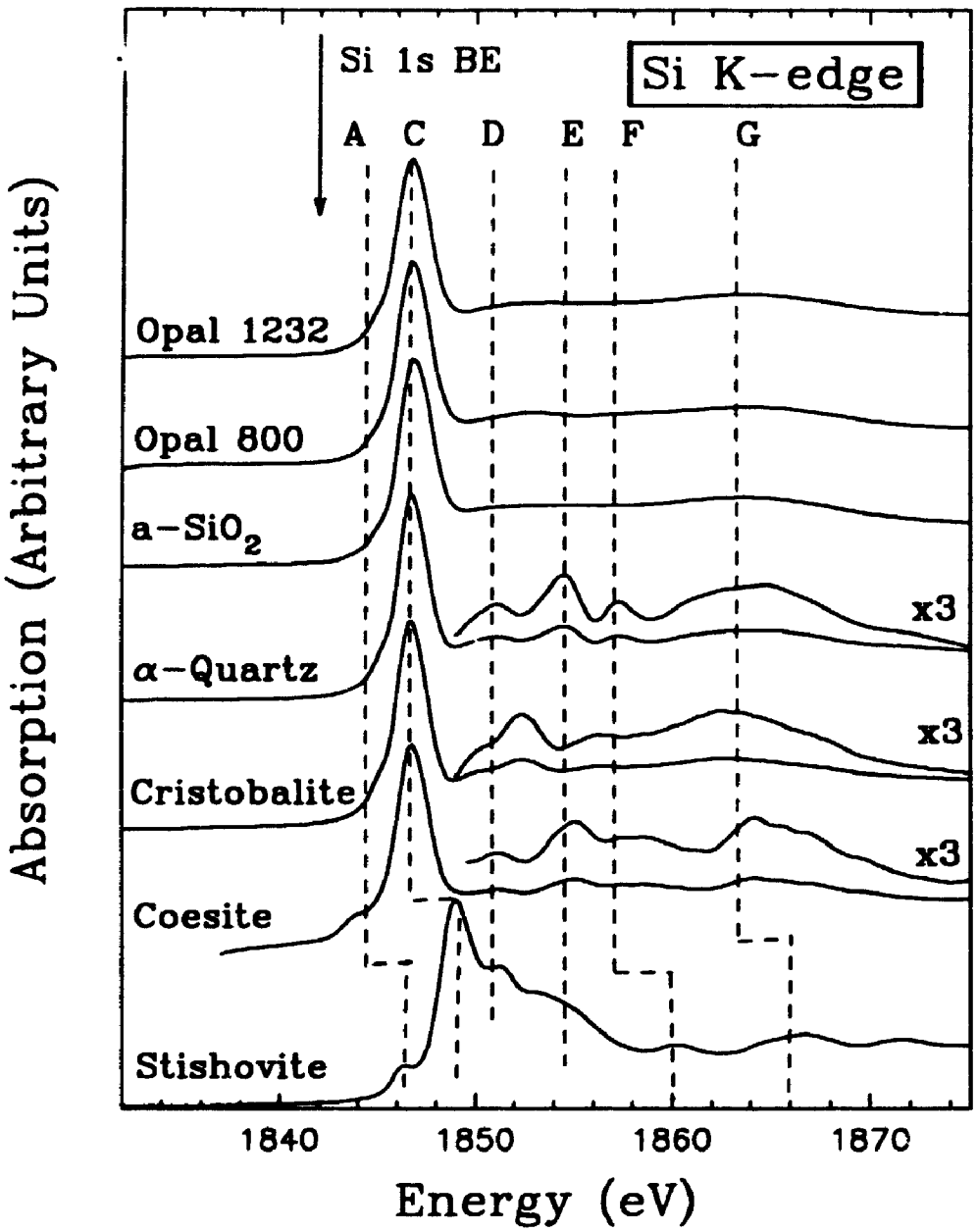

Figure 6.3.2 Si K-edge XANES spectra of α-quartz, cristobalite, coesite, stishovite and opals.

like transition, is expected to be weak in the K-edge spectra, as observed for most of the 4:2 coordinate SiO_2 materials. However, for coesite, peak A is markedly more intense, and shifts toward lower energy. The energy separation between peaks A and C for coesite is about 3.2 eV, similar to that for stishovite. The relative intensity of peak A for coesite is intermediate between α-quartz and stishovite. This indicates that the Si 3s-like states below the CB minimum are mixed with more Si 3p states in the high pressure structures. Second, peaks E and G in the cristobalite spectrum shift to lower energy, but the energy separation for these two peaks remains similar to that for α-quartz and coesite. Peaks D and F, due to the MS effect, also shift to lower energy and become weak. These differences must be related to the crystal structures of these materials.

Figure 6.3.3 shows the Si L-edge XANES of SiO_2 polymorphs, a-SiO_2 and opals, and also the Si 2p BE for α-quartz is indicated by a solid line with an arrow. The peaks are labelled as in Figure 6.3.1. The basic spectral features for α-quartz, cristobalite and coesite are qualitatively similar to each other, but differ from those of stishovite. The Si L-edge (peak A) for stishovite also shifts to higher energy by about 1 eV, compared with the SiO_2 polymorphs containing Si^{IV}. The Si L-edge spectra can also be used as a structural fingerprint to distinguish Si^{IV} and Si^{VI} in silicate minerals and glasses. For the 4:2 coordinate SiO_2 materials, the strong peak C at 107.9 ± 0.1 eV characterizes the Si^{IV} atoms in the Si L-edge XANES. However, peak A, representing an exciton below the CB minimum, appears to shifts toward higher energy in the sequence from α-quartz to cristobalite to coesite. This slight shift for peak A is related to the local structure of the Si atoms, and is also qualitatively in agreement with various crystal chemical parameters, e.g., Si-O bond length, Si-Si distance, Si-O bond valence, MAS NMR chemical shifts (also see Table 6.3.2). Comparison with the spectra of gaseous $Si(OCH_3)_4$ [31], SiH_4 [34] and SiF_4 [35] suggests that the Si L-edge absorption spectra of various SiO_2 materials are dominated by the SiO_4^{4-} cluster. Hence, the presently-resolved differences among the spectra of α-quartz, α-cristobalite and coesite, and also among the spectra between crystalline and amorphous SiO_2 materials likely represent contributions from beyond the first shell of Si; in other words, the extra features reflect the intermediate-range structure of α-quartz, α-cristobalite and coesite.

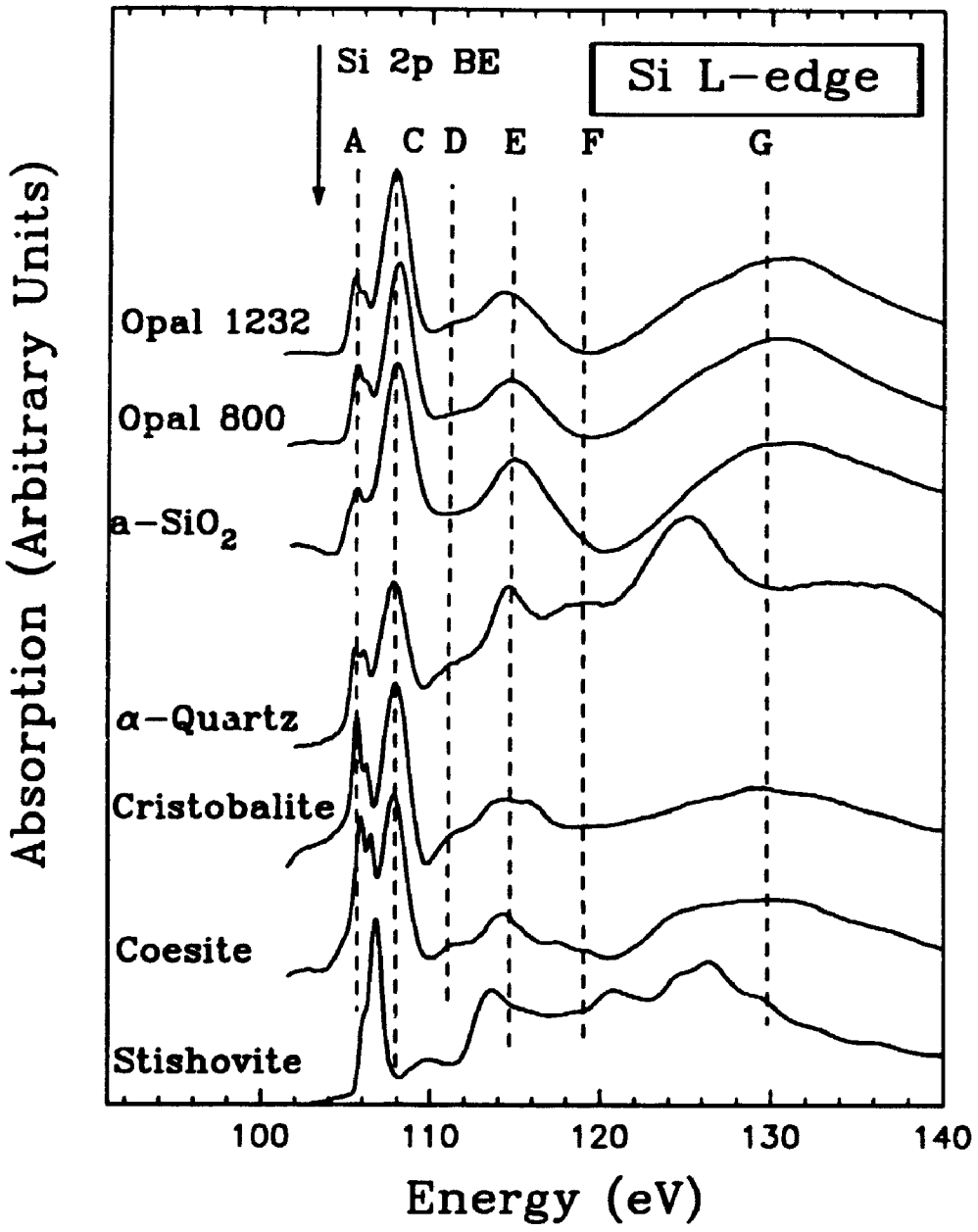

Figure 6.3.3 Si L-edge XANES spectra of α-quartz, cristobalite, coesite, stishovite and opals.

For a-SiO_2, the four main peaks A, C, E and F characterizing Si^{IV} are also present in both Si K- and L-edge XANES. Even peak E in the L-edge spectrum becomes broader and weaker. This confirms that the local structure of a-SiO_2 has tetrahedral symmetry, as in the crystalline 4:2 coordinate modifications. This is, of course, well known from the early x-ray diffraction study of a-SiO_2 [46]. On the other hand, peaks D and F are absent from both Si K- and L-edge XANES. This confirms the assignments of peaks D and F due to the MS effect related to intermediate range structure, because the MS effect from the more distant shell atoms are strongly quenched by the structural disorder.

The energy position (ΔE) for peak C in the K-edge XANES and peak A in the L-edge XANES, and some crystal-chemical parameters of the 4:2 coordinate SiO_2 materials and 6:3 coordinate stishovite are summarized in Table 6.3.2. In this Table, ΔE is defined as in Table 1, and the bond valence (s) is calculated according to the formula:

$$s = \exp[-(R-R_0)/B]$$

where R is the bond length, and R_0 and B are fitted constants for Si-O bonds[47]. The shift in the Si K-edge toward higher energy in stishovite is caused by the different effective charge on the Si atoms which is related to change of coordination number (CN) of Si, from 4 in all 4:2 coordinate SiO_2 materials to 6 in stishovite. This is also in agreement with the Si Kα x-ray emission shift and MO calculation[48]. However, the shift in the Si K-edge XANES is much more significant than that in Si Kα x-ray emission. Therefore, the Si K-edge XANES is a more sensitive fingerprint for determining the coordination of Si in silicate minerals and glasses. The Si K-edge shift toward higher energy is also related to variations of crystal-chemical parameters of stishovite and the other SiO_2 polymorphs (see Table 6.3.2): with increase in Si-O bond length, Si-Si bond distance and negative Si MAS NMR chemical shift[49] and decrease in Si-O-Si bond angle and reduction in Si-O bond valence from the 4:2 coordinate SiO_2 polymorphs to stishovite, the Si K-edge shifts toward higher energy.

Table 6.3.2 Si K- and L-edge XANES and crystal chemistry of SiO_2 polymorphs

	α-quartz	cristobalite	coesite	stishovite
ΔE for peak C in K-edge* (eV)	3.4	3.3	3.4	5.6
ΔE for peak A in L-edge* (eV)	2.3	2.5	2.8	3.0
Si:O coordination number	4:2	4:2	4:2	6:3
Si-O (Å)	1.61	1.605	1.61**	1.76 (x2) 1.81 (x4)
Si-Si (Å)	3.06	3.07	3.09**	3.24
Si-O-Si (°)	144.0	146.8	150.8**	130.7
Si-O bond valence (s)	4.23	4.29	4.22	3.82
MAS NMR δ (ppm)	-107.1	-108.5	-110.0**	-191.1

* The ΔE is the difference between the energy for peak C and Si 1s BE for Si K-edge XANES and between the energy for peak A and Si 2p BE for Si L-edge XANES.

** There are two Si sites in coesite, but the XANES has no capability to distinguish them. These data are the average of two different Si sites.

6.3.3 Structural Characterization of Opal

Opal is a compact form of natural hydrous silica ($SiO_2 \cdot nH_2O$), and has been classified by Jones and Segnit according to the nature of its PXRD pattern[30]. Amorphous opal has been further classified into glass-like network structure opal and gel-like structure opal by Langer and Flörke[50] based on PXRD, chemical, thermoanalytic and IR spectroscopic studies. Adams et al.[51] reported that chemical shifts from MAS NMR spectra do not distinguish among various types of opal, but the ^{29}Si line widths decrease with increase in structural order.

The Si K- and L-edge XANES spectra of two opal samples, opals #1232 and #800, are compared with the spectra of the other crystalline SiO_2 polymorphs in Figures 2 and 3, respectively. The Si K-edge spectra of the opal samples are similar to that of a-SiO_2, but we can see some weak features due to the long-range ordered structure,

particularly for opal #800. For example, peak E in the K-edge spectrum of opal #800 shifts toward lower energy, as in the spectrum of cristobalite, rather than that of α-quartz. The Si L-edge spectra of the opals demonstrate that the two opals are essentially similar to a-SiO_2, but also have some spectral features of cristobalite. For instance, peak A is split, and peak D becomes more significant, as in the cristobalite spectrum. In summary, the two opals essentially have the structural character of a-SiO_2, but also contain a small proportion of cristobalite structural units; features of α-quartz are not present in either Si K- or L-edge spectra of these two opals. The opal #800 has a greater component of cristobalite structural units than the precious opal #1232. These results are in good qualitative agreement with the x-ray diffraction patterns of the opals.

Composite Si K- and L-edge XANES spectra for different proportions of cristobalite and a-SiO_2 are shown in Figures 6.3.4 and 6.3.5, respectively. The most apparent feature of the composite Si K-edge spectra is that peak E, as marked by a solid triangle in Figure 6.3.4, becomes more intense, and also peaks D and F become more significant, with increase in the proportion of cristobalite. In the composite Si L-edge spectra, two apparent changes occur, as marked by solid triangles in Figure 6.3.5, with increase in the proportion of cristobalite. First, peak A shifts to higher energy, and becomes more intense, and the relative intensity of its doublet become reversed. Second, peak D becomes more significant.

The Si K-edge spectra of opals #1232 and #800 are shown as solid lines at the left hand side of Figure 6.3.6. Composite spectra of 10% cristobalite + 90% a-SiO_2 and 30% cristobalite + 70% a-SiO_2 simulate visually the spectra of the opals #1232 and #800, respectively, quite successfully. This analysis indicates that the two opal samples are essentially characterized by a-SiO_2 structural units, but also contain small proportions of the structural units of crystalline cristobalite. The precious opal #1232 contains about 10% cristobalite structural units, and the opal #800 contains about 30% cristobalite structural units. These estimates are in qualitative agreement with the PXRD which indicates that there is some crystalline cristobalite present. However, the XANES method can also provide information on the local structure and can semi-quantitatively determine the proportions of different structural units in the opals.

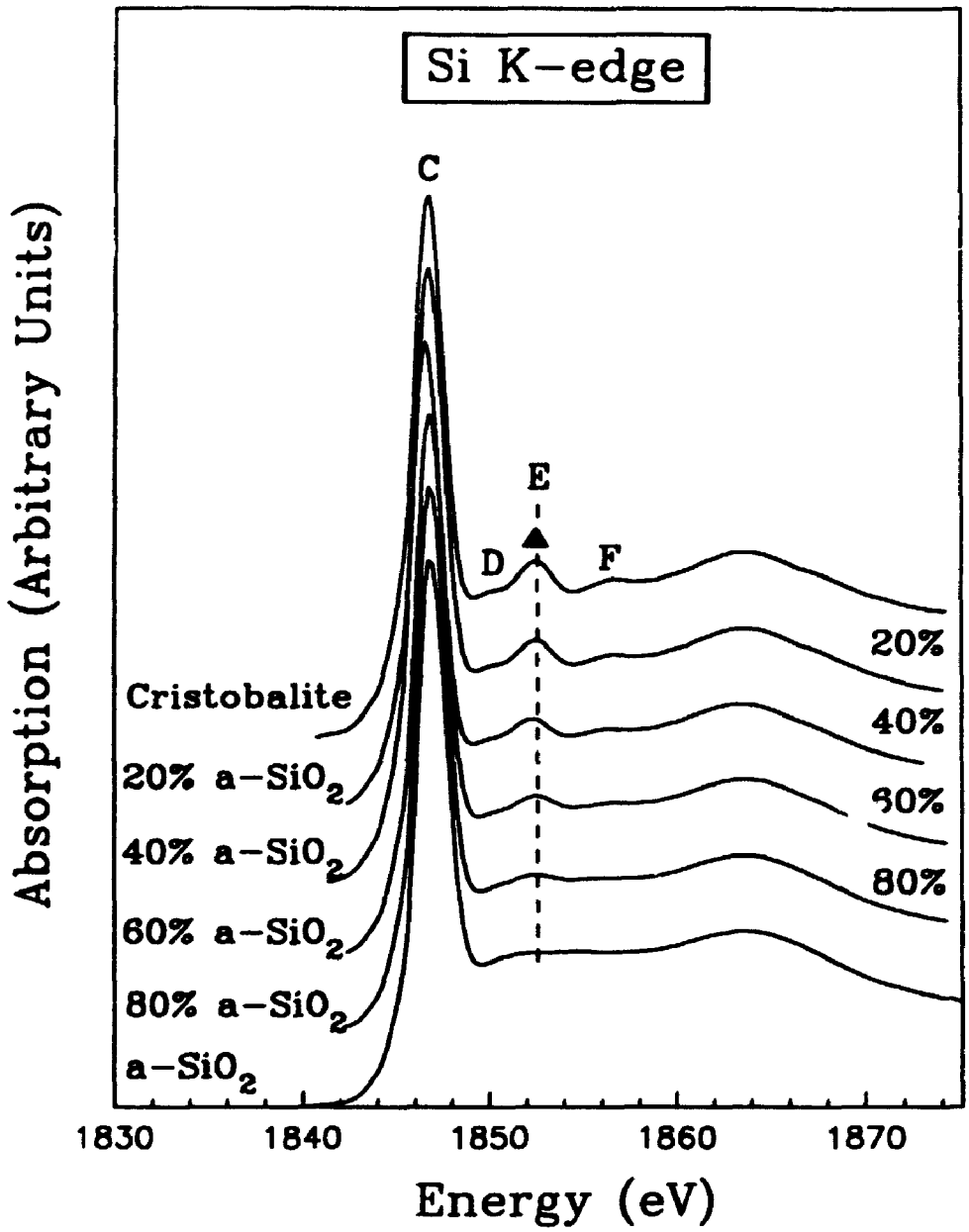

Figure 6.3.4 Si K-edge XANES spectra of cristobalite and a-SiO_2, together with the composite spectra for different proportions of cristobalite and a-SiO_2.

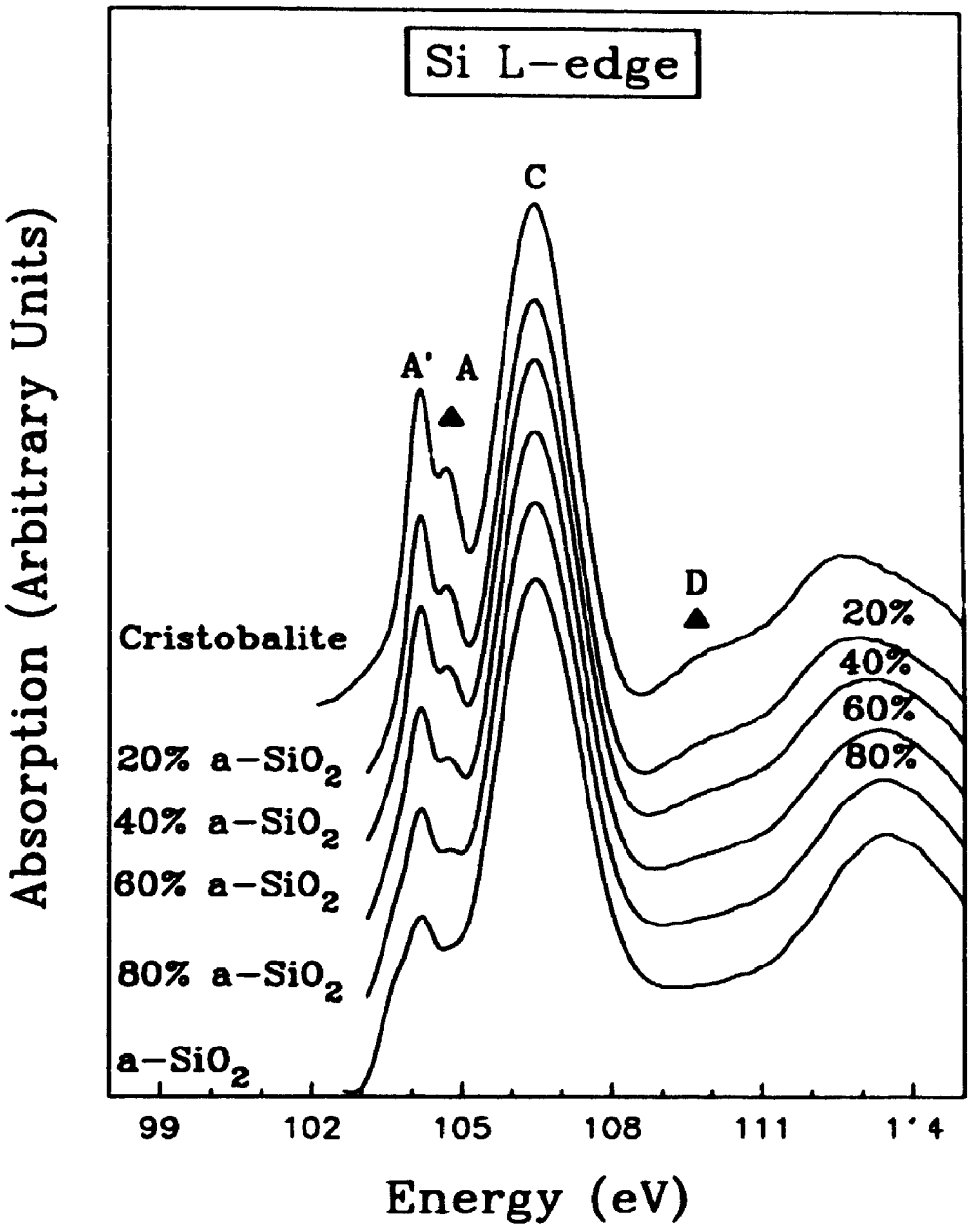

Figure 6.3.5 Si L-edge XANES spectra of cristobalite and a-SiO_2, together with the composite spectra for different proportions of cristobalite and a-SiO_2.

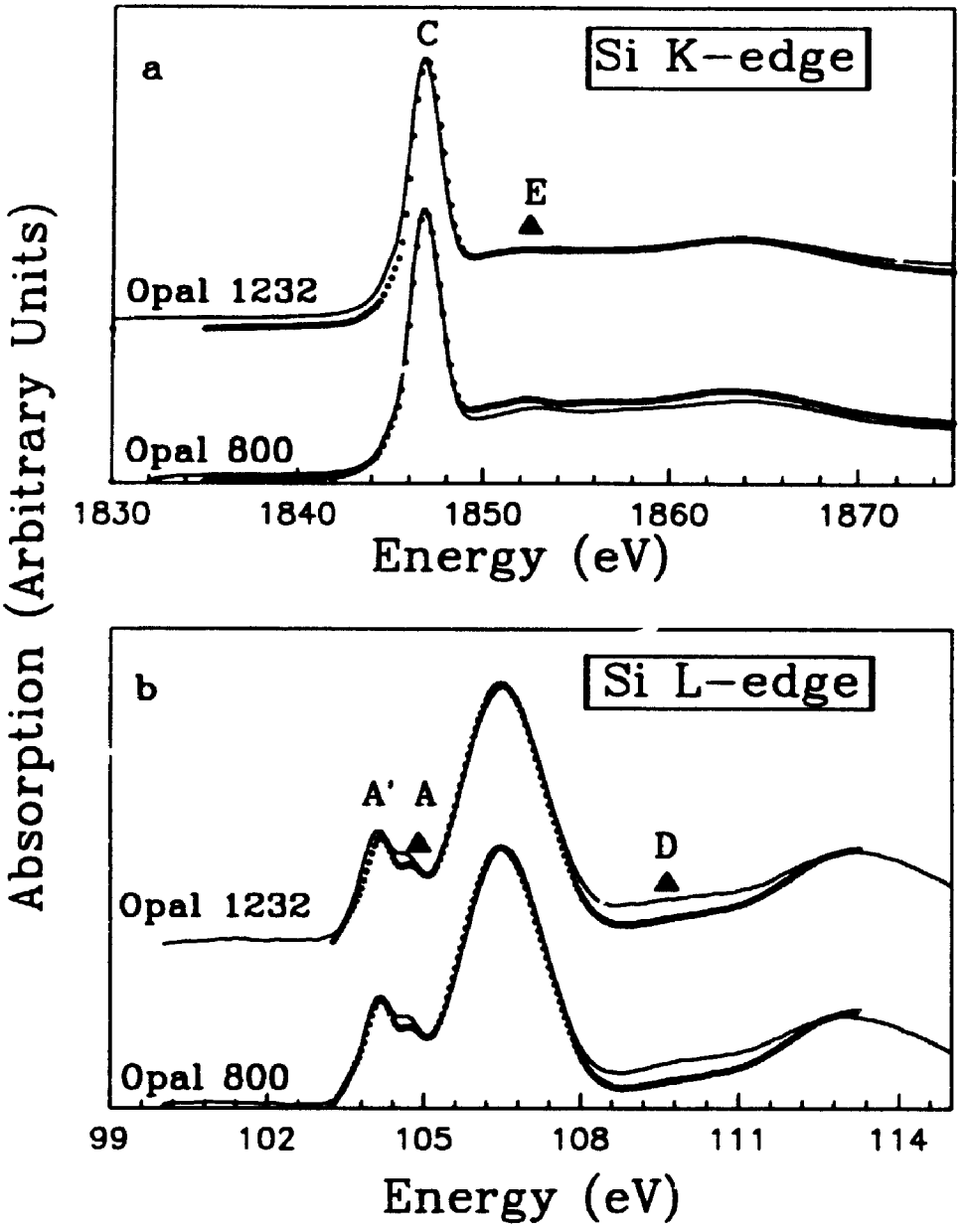

Figure 6.3.6 The Si K- (a) and L-edge (b) XANES spectra (s ·.id lines) of two opal samples, #1232 and #800 are compared with the composite spectra (solid dot lines) of different proportions of cristobalite and a-SiO_2.

The Si L-edge spectra of the two opals are shown also as solid lines at the right hand side of Figure 6.3.6. Peak A is marginally stronger, and peak D a little more significant in opal #800 than in opal #1232, qualitatively indicating that the opal #800 has more features of crystalline cristobalite. However, these two spectra are in general very similar. The composite spectrum of 40% cristobalite + 60% a-SiO_2 fits the spectra of both opals (#1232 and #800) reasonably well. Therefore, the Si L-edge spectra demonstrate that both opals #1232 and #800 contain about 40% cristobalite structural units, and are thus in qualitative, but not quantitative agreement with the Si K-edge spectra and PXRD. However, as a semi-quantitative method, Si K- and L-edge XANES shows potential applications for the characterization of the structure of opal and other partly ordered silicate materials.

6.4 Conclusions

The main features in the Si K- and L-edge XANES spectra of SiO_2 polymorphs are qualitatively interpreted based on the MO calculations of the corresponding SiO_4^{4-} and SiO_6^{8-} clusters, and the comparison with the spectra and MO calculation of other model molecules. The MS effect also contributes to the near-edge features of these materials. The Si K- and L-edge XANES of SiO_2 polymorphs qualitatively reflect the DOS of unoccupied Si s-like, p-like and d-like electronic states, and indicate the stronger covalent bonding in 4:2 coordinate SiO_2 polymorphs than in 6:3 coordinate stishovite. For 4:2 coordinate SiO_2, the Si 3s/3d and 3p orbitals are strongly hybridized. However, for 6:3 coordinate stishovite, the mixing between Si 3s/3d and Si 3p orbitals is apparently weak. The Si K- and L-edges of stishovite are shifted significantly towards higher energy compared to those of the other SiO_2 polymorphs. This shift is related to the different coordination geometries and effective charges of the Si atoms. Therefore, the Si K- and L-edge XANES can clearly distinguish Si^{IV} and Si^{IV} in silicate minerals and glasses, and may be used as a structural fingerprint. More importantly, the XANES spectra provide insight into the structure of amorphous SiO_2 and opal. For the two opal samples studied, the XANES spectra reveal that they are basically amorphous, but contain certain

proportions of α-cristobalite-like structural units.

6.5 References

1. L.G. Liu, *Nature* **258**, 510 (1975).
2. S.M. Stishov and S.V. Popova, *Geokhimiya* **10**, 837 (1961).
3. E.C.T. Chao, J.J. Fahey, J. Littler and D.J. Milton, *J. Geophys. Res.* **67**, 419 (1962).
4. W. Sinclair and A.E. Ringwood, *Nature* **272**, 714 (1978)
5. R.J. Hill, M.D. Newton and G.V. Gibbs, *J. Solid State Chem.* **47**, 185 (1983).
6. N.L. Ross, J.F. Shu, R.M. Hazen and T. Gasparik, *Am. Mineral.* **75**, 739 (1990).
7. J.A. Tossell, *J. Am. Chem. Soc.* **97**, 4840 (1975).
8. K.L. Yip and Fowler, *Phys. Rev.* **B10**, 1400 (1974).
9. J.R. Chelikowsky and M. Schlüter, *Phys. Rev.* **B15**, 4020 (1977).
10. E. Calabrese and W.B. Fowler, *Phys. Rev.* **B18**, 2888 (1978).
11. R.B. Laughlin, J.D. Joannopoulos and D.J. Chady, *Phys. Rev.* **B20**, 5228 (1979).
12. R.N. Nucho and A. Madhukar, *Phys. Rev.* **B21**, 1576 (1980).
13. W.J. Ching, *Phys. Rev. Lett.* **46**, 607 (1981).
14. E.P. O'Reilly and J. Robertson, *Phys. Rev.* **B27**, 3780 (1983).
15. Y.P. Li and W.Y. Ching, *Phys. Rev.* **B31**, 2172 (1985).
16. R. Nada, C.R.A. Catlow, R. Dovesi and C. Pisani, *Phys. Chem. Minerals* **17**, 353 (1990).
17. I. Štich, *Solid State Commun.* **58**, 705 (1986).
18. S.T. Pantelides and W.A. Harrison, *Phys. Rev.* **B13**, 2667 (1976).
19. S. Ciraci and I.P. Batra, *Phys. Rev.* **B15**, 4923 (1977).
20. P.M. Schneider and W.B. Fowler, *Phys. Rev.* **B18** 7122 (1978).
21. J.A. Tossell, *J. Phys. Chem. Solids* **36**, 1273 (1975).
22. J.K. Rudra and W.B. Fowler, *Phys. Rev.* **B28**, 1061 (1983).

23. M.A. Spackman, R.J. Hill and G.V. Gibbs, *Phys. Chem. Minerals* **14**, 139 (1987).

24. G. Wiech, *Solid State Commun.* **52**, 807 (1984).

25. G. Wiech and E.Z. Kurmaev, *J. Phys.* **C18**, 4393 (1985).

26. F.C. Brown, R.Z. Bachrach and M. Skibowski, *Phys. Rev.* **B15**, 4781 (1977).

27. Y. Iguchi, *Science of Light* **26**, 161 (1977).

28. I.A. Brytov, K.I. Konashenok and Yu.N. Romashchenko, *Geochem. Int.* **16**, 142 (1979).

29. I. Davoli, E. Paris, S. Stizza, M. Benfatto, M. Fanfoni, A. Gargano, A. Bianconi and F. Seifert, *Phys. Chem. Minerals* **19**, 17 (1992).

30. J.B. Jones and E.R. Segnit, *J. Geol. Soc. Aust.* **18**, 57 (1971).

31. C.D. Wagner, D.E. Passoja, H.F. Hillery, T.G. Kinisky, H.A. Six, W.T. Jansen and J.A. Taylor, *J. Vac. Sci. Tech.* **21**, 933 (1982).

32. M. Azizan, R. Baptist, A. Brenac, G. Chauvet and T.A. Nguyen Tan, *J. Physique* **48**, 81 (1987).

33. D.G.L. Sutherland, M. Kasrai, G.M. Bancroft, Z.F. Liu and K.H. Tan, *Phys. Rev.* **B48**, 14989 (1993).

34. H. Friedrich, B. Sonntag, P. Rabe, W. Butscher and W.H.E. Schwarz, *Chem. Phys. lett.* **64**, 360 (1979).

35. T.A. Ferrett, M.N. Piancastelli, D.W. Lindle, P.A. Heimann and D.A. Shirley, *Phys. Rev.* **A38**, 701(1988).

36. W.L. O'Brien, J. Jia, Q.Y. Dong, T.A. Callcott, J.E. Rubensson, D.L. Mueller and D.L. Ederer, *Phys. Rev.* **B44**, 1013 (1991).

37. N.M. Ravindra and J. Narayan, *J. Appl. Phys.* **61**, 2017 (1987).

38. A. Bianconi, *Surf. Sci.* **89**, 41 (1979).

39. P.L. Hansen, R. Brydson and D.M. McComb, *Microsc. Microanal. Microstr.* **3**, 213 (1992).

40. Z.F. Liu, J.N. Cutler, G.M. Bancroft, K.H. Tan, R.G. Cavell and J.S. Tse, *Chem. Phys.* **168**, 133 (1992).

41. J.L. Dehmer, *J. Chem. Phys.* **56**, 4496 (1972).

42. T.A. Ferrett, D.W. Lindle, P.A. Heimann, H.G. Kerkhoff, U.E. Necker and D.A. Shirley, *Phys. Rev.* **A34**, 1916 (1986).

43. D.W. McComb, R. Brydson, P.L. Hansen and R.S Payne, *J. Phys.: Condensed Matter*, **4**, 8363 (1992).

44. F. Bart, F. Jollet, J.P. Duraud and L. Douillard, *Phys. Status Solidi* **B176**, 163 (1993).

45. C.R. Natoli, In *EXAFS and Near-Edge Structure III* (Ed. by Hodgson, K.O., Hedman, B., and Penner-Hahn, J.E.). Springer-Verlag, Berlin, 1984, pp. 38.

46. J. Wong and C.A. Angell, *Glass Structure by Spectroscopy*. Marcel Dekker Inc., New York, 1976, pp. 53.

47. I.D. Brown, In *Structure and Bonding in Crystals II* (Ed. by O'Keeffe M. and Navrotsky A.). Academic Press, New York, 1981, pp. 1.

48. T. Okura, H. Inoue, T. Kanazawa, S. Endo, S. Fukushima and Y. Gohshi, *Spectrochim. Acta* **B45**, 711 (1990).

49. J.V. Smith and C.S. Blackwell, *Nature* **303**, 223 (1983).

50. K. Langer and O.W. Flörke, *Fortsch. Mineral.* **52**, 17 (1974).

51. S.J. Adams, G.E. Hawkes and E.H. Curzon, *Am. Mineral.* 76, 1863 (1991).

CHAPTER 7

Si K-Edge XANES Spectra of Silicate Minerals

7.1 Introduction

Silicates are classified into nesosilicates (SiO_4^{4-} - Q^0), sorosilicates ($Si_2O_7^{6-}$ - Q^1), cyclosilicates and single inosilicates (SiO_3^{2-} - Q^2), double inosilicates ($Si_4O_{11}^{6-}$ - Q^2 and Q^3), phyllosilicates ($Si_4O_{10}^{4-}$ - Q^3) and tectosilicates (SiO_2 - Q^4) based on the polymerization of SiO_4^{4-} tetrahedra[1]. With the exception of the SiO_2 polymorphs, the tectosilicates contain Al substituting for Si. The structure and bonding of silicates and aluminosilicates have been studied using x-ray photoelectron spectroscopy (XPS)[2-8], x-ray emission spectroscopy (XES)[9-13], x-ray photoelectron diffraction (XPD)[14,15], x-ray absorption spectroscopy (XAS)[9], magic-angle-spinning (MAS) nuclear magnetic resonance (NMR) spectroscopy[16-25] and molecular orbital (MO) calculation[26-28]. MAS NMR, in particular, has become a very powerful technique for distinguishing 4- and 6-coordinated Si and Al and in determining non-equivalent Si sites and degree of polymerization of SiO_4^{4-} in silicates.

In this chapter, Si K-edge XANES spectra of crystalline silicate minerals are presented in order to explore the correlations of chemical shift in the Si K-edge with the polymerization of SiO_4^{4-}, Si-O bond distance (d_{Si-O}), Si-O bond valence (s_{Si-O}), distortion of SiO_4^{4-} tetrahedra, and chemical substitution in both tetrahedral and octahedral sites.

7.2 Experimental

The silicate and aluminosilicate minerals studied were provided by the Department of Earth Sciences, UWO, and the Department of Mineralogy, ROM. All samples were shown by powder x-ray diffraction (PXRD) to be essentially single phase. The electron

microprobe analyses of the aluminosilicate minerals will be given in Table 8.2.1 (Chapter 8). Si K-edge XANES spectra were collected on the DCM and synchrotron radiation.

7.3 Results and Discussion

7.3.1 Interpretation of Si K-edge XANES Spectra

Figure 7.3.1 shows Si K-edge XANES spectra of some representative silicate minerals, forsterite ($Mg_2[SiO_4]$), grossular ($Ca_3Al_2[SiO_4]_3$), hemimorphite $Zn_4Si_2O_7(OH)_2$, enstatite ($Mg[SiO_3]$), tremolite ($Ca_2Mg_5[Si_4O_{11}]_2(OH)_2$), pyrophyllite ($Al_2[Si_4O_{10}](OH)_2$), microcline ($K[AlSi_3O_8]$) and α-quartz (SiO_2), arranged in upward sequence of increase in polymerization of SiO_4^{4-} clusters. The Si K-edge spectra of silicate minerals are complicated by crystal structure complexity and the low local symmetry of Si. However, in general, the four characteristic features assigned to the SiO_4^{4-} cluster are always present. The peaks are labelled and qualitatively interpreted by molecular orbital (MO) and multiple scattering (MS) considerations, following the assignments for α-quartz. Peak A is attributed to transition of Si 1s electrons to the antibonding 3s-like states (a_1); this transition is dipole-forbidden, so that peak A is very weak. Peak C is assigned to transition of Si 1s electrons to the antibonding 3p-like states (t_2); this transition is dipole-allowed, so that peak C is very strong, and presently referred as the Si K-edge. Peaks E and G are attributable to the transitions of Si 1s electrons to empty Si 3d-like e and t_2 states, respectively (called symmetry-forbidden "shape resonances"[29,30]). Peaks D and F are qualitatively attributable to the MS effect from more distant atom shells, in agreement with the MS calculation for zircon ($ZrSiO_4$)[31].

Peak C is assigned with some confidence, but the features above peak C are complicated by the complex MS processes and possible splitting of e (3d-like) and t_2 states (3p- and 3d-like) in crystal fields of lower symmetry. Thus, an equivalent peak might both shift in position and change in relative intensity for different silicate minerals. For example, in the Si K-edge spectra of inosilicates and phyllosilicates, peak E becomes stronger and shifts to high energy. The post-edge features clearly contain important

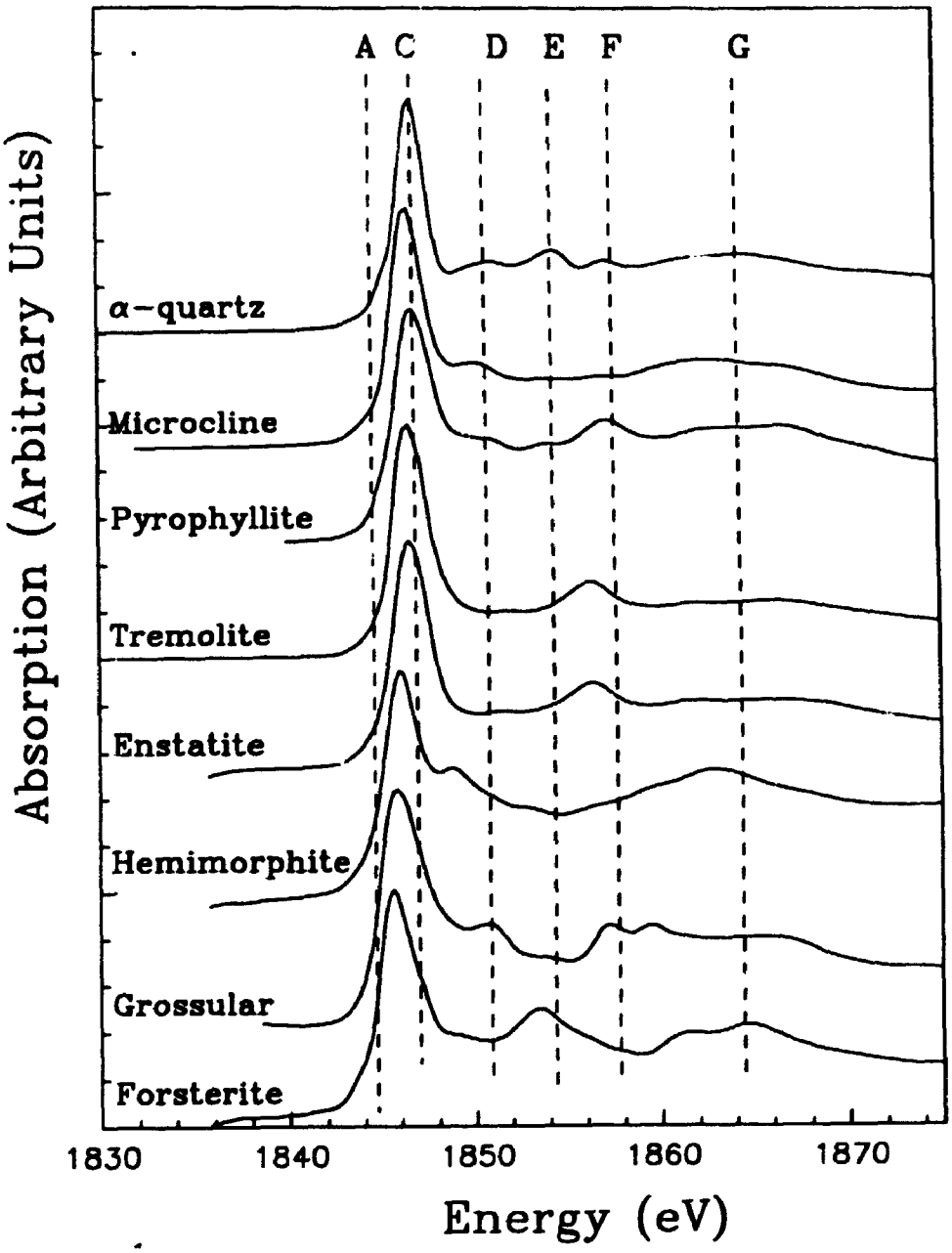

Figure 7.3.1 Si K-edge XANES spectra of some representative silicate minerals with different degrees of polymerization.

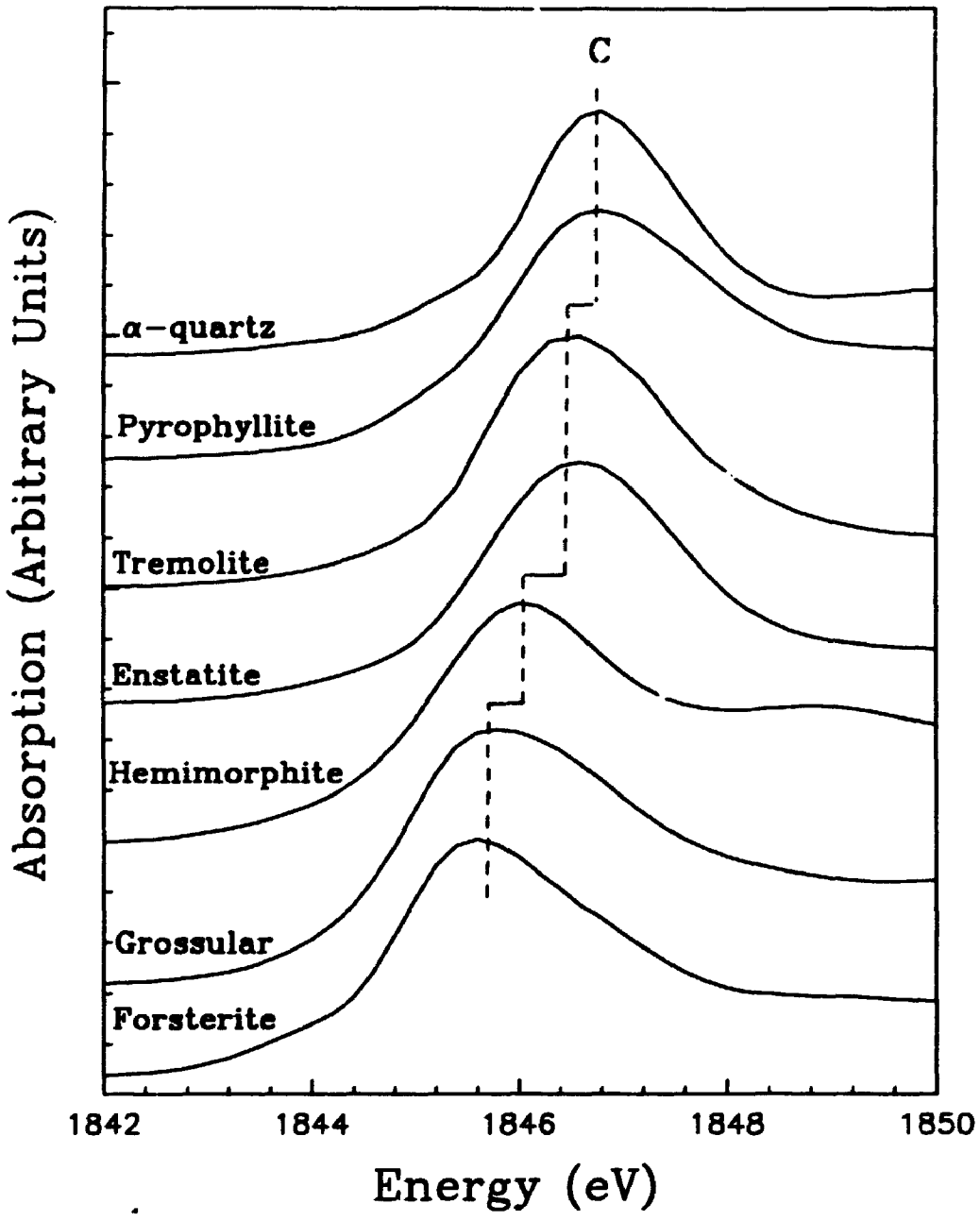

Figure 7.3.2. Si K-edge (peak C) of representative silicate minerals in an expanded scale. The Si K-edge shifts to higher energy by 1.3 eV with increase in the polymerization of SiO_4^{4-} clusters, from nesosilicates to tectosilicates.

information on the structure and bonding of silicates, but are too complicated to be meaningfully interpreted at this time. Therefore, the following discussion focuses on the chemical shift of peak C.

7.3.2 Chemical Shift of Si K-edge versus Polymerization

Figure 7.3.2 shows peak C (Si K-edge) in the Si K-edge spectra of some representative silicate minerals in an expanded scale. Peak C shifts toward high energy with increased polymerization of SiO_4^{4-} clusters, by about 1.3 eV from forsterite (nesosilicate) to α-quartz (tectosilicate). The Si K-edge position, Si-O bond distance (d_{Si-O} in Å), Si-O band valence (s_{Si-O}) and ^{29}Si MAS NMR chemical shifts (δ in ppm) of the silicate minerals studied are given in Table 7.3.1, where the d_{Si-O} values are cited from Smyth and Bish[32] and references therein, the s_{Si-O} values are calculated using Brown's formula[33] and the δ values are cited from Sherriff and Grundy[24] and Sherriff et al.[25] and references therein.

Figure 7.3.3 shows the variation of the Si K-edge with the O:Si ratio and polymerization of all the silicate and aluminosilicate minerals studied. Q^n is the degree of polymerization of TO_4 tetrahedra, and mineral labels are after Kretz[34]. In general, for silicate minerals, the Si K-edge shifts to higher energy with decrease in the O:Si ratio and with increase in polymerization. For example, for magnesium silicates, the Si K-edge shifts from 1845.5 eV for forsterite (Q^0) to 1846.5 eV for enstatite (Q^2) and 1846.9 eV for talc (Q^3). However, considering all the silicate minerals, there is considerable overlapping of the Si K-edge shift for silicates of the same polymerization type, due to the effect of other cations and crystal structure complexity.

Table 7.3.1 Si K-edge (±0.1 eV) and crystal chemical parameters of silicates

Minerals	Formula	Peak C	d_{Si-O} *	s_{Si-O} *	NMR δ**
Nesosilicates (Q^0)					
Fayalite	$Fe_2[SiO_4]$	1846.6	1.636	3.934	
Olivine	$(Mg,Fe)_2[SiO_4]$	1846.1	1.636	3.934	-62.0
γ-Mg_2SiO_4		1846.2	1.655	3.732	
Forsterite	$Mg_2[SiO_4]$	1845.5	1.636	3.934	
Pyrope	$Mg_3Al_2[SiO_4]_3$	1845.7	1.635	3.945	
Almandine	$Fe_3Al_2[SiO_4]_3$	1846.0	1.628	4.022	
Spessartine	$Mn_3Al_2[SiO_4]_3$	1846.3	1.636	3.934	
Grossular	$Ca_3Al_2[SiO_4]_3$	1845.8	1.645	3.837	
Andalusite	$Al_2[SiO_4]O$	1846.4	1.631	3.989	-79.8
Kyanite	$Al_2[SiO_4]O$	1846.3	1.636	3.934	-82.8
Sillimanite	$Al_2[SiO_4]O$	1846.4	1.626	4.045	-86.4
Topaz	$Al_2[SiO_4](OH,F)_2$	1846.7	1.643	3.838	-85.6
Phenacite	$Be_2[SiO_4]$	1846.3	1.631	3.898	-74.2
Titanite	$CaTi[SiO_4]O$	1846.5	1.645	3.837	-79.0
Zircon	$Zr[SiO_4]$	1846.7	1.623	4.079	-81.6
Neso- and sorosilicates (Q^0 + Q^1)					
Epidote	$Ca_2Al_2Fe[SiO_4]_3(OH)$	1846.3	1.626	4.045	
Clinozoisite	$Ca_2Al_3[SiO_4]_3(OH)$	1846.3	1.628	4.022	
Vesuvianite	$Ca_{10}(Mg,Fe)_2Al_4[Si_2O_7]_2$ $[SiO_4]_5(OH,F)_4$	1845.9	1.638	3.912	
Sorosilicate (Q^1)					
Hemimorphite	$Zn_4[Si_2O_7](OH)_2 \cdot H_2O$	1846.2	1.624	4.067	-80.0
Cyclo-silicates (Q^2)					
Beryl	$Be_3Al_2[SiO_4]_6$	1846.7	1.608	4.252	-102.2
Tourmaline	$Na(Mg,Fe,Al)_3Al_6$ $[SiO_3]_6[BO_3]_3(OH,F)_4$	1846.5	1.620	4.113	-88.1
Dioptase	$Cu_6[SiO_3]_6.6H_2O$	1846.6	1.627	4.034	
Cordierite	$Mg_2[Al_4Si_5O_{18}]$	1846.5	1.619	4.124	

Table 7.3.1 continue

Single ino-silicates (Q^2)					
Spodumene	$LiAl[SiO_3]_2$	1846.6	1.619	4.124	-91.4
Omphacite	$(Na,Ca)Al[SiO_3]_2$	1846.4	1.633	3.967	-85.4
Diopside	$CaMg[SiO_3]_2$	1846.7	1.635	3.945	-84.7
Enstatite	$Mg[SiO_3]$	1846.7	1.628	4.022	-83.0
Rhodonite	$Mn[SiO_3]$	1846.3	1.622	4.090	
Double inosilicates (Q^2 + Q^3)					
Tremolite	$Ca_2Mg_5[Si_4O_{11}]_2(OH)_2$	1846.6	1.632	3.978	-89.2
Hornblende	$Ca_2Na(Mg,Fe)_4(Al,Fe)[(Si,Al)_4O_{11}]_2(OH)_2$	1846.4	1.639	3.901	
Glaucophane	$Na_2Mg_3Al_2[Si_4O_{11}]_2(OH)_2$	1846.5	1.628	4.022	
Phyllosilicates (Q^3)					
Talc	$Mg_3[Si_4O_{10}](OH)_2$	1846.9	1.623	4.079	-97.2
Pyrophyllite	$Al_2[Si_4O_{10}](OH)_2$	1846.8	1.618	4.136	-94.0
Biotite	$KMg_3[AlSi_3O_{10}](OH)_2$	1846.5	1.642	3.869	-86.0
muscovite	$KAl_2[AlSi_3O_{10}](OH)_2$	1846.4	1.645	3.837	-85.5
margarite	$CaAl_2[Al_2Si_2O_{10}](OH)_2$	1846.1	1.628	4.022	-76.0
serpentine	$Mg_6[Si_4O_{10}](OH)_8$	1846.7	1.638	3.912	
kaolinite	$Al_4[Si_4O_{10}](OH)_8$	1846.6	1.622	4.090	-91.5
chlorite	$(Mg,Al,Fe)_{12}[(Si,Al)_8O_{20}](OH)_{16}$	1846.6	1.651	3.773	
Tectosilicates (Q^4)					
α-quartz	SiO_2	1846.8	1.609	4.240	-107.1
Cristobalite	SiO_2	1846.7	1.606	4.276	-108.5
Coesite	SiO_2	1846.8	1.613	4.193	-111.0
Microcline	$K[AlSi_3O_8]$	1846.5	1.612	4.205	-97.1
Orthoclase	$K[AlSi_3O_8]$	1846.6	1.629	4.011	
Albite	$Na[AlSi_3O_8]$	1846.5	1.618	4.136	-98.2
Anorthite	$Ca[Al_2Si_2O_8]$	1846.3	1.613	4.193	-84.8
Nepheline	$KNa_3[Al_4Si_4O_{16}]$	1846.3	1.614	4.182	-86.9
Sodalite	$Na_8[AlSiO_4]_6Cl_2$	1846.6	1.628	4.022	-84.9
Cancrinite	$Na_6Ca_2[AlSiO_4]_6[CO_3,SO_4](OH)_2$	1846.6	1.615	4.170	-86.3

* d_{Si-O} is average Si-O distance in Å and cited from Smyth and Bish[32] and references therein; s_{Si-O} is average Si-O band valence calculated using Brown's formula[33].

** ^{29}Si MAS NMR chemical shifts (in ppm) are cited from Sherriff and Grundy[24], Sherriff et al.[25] and references therein.

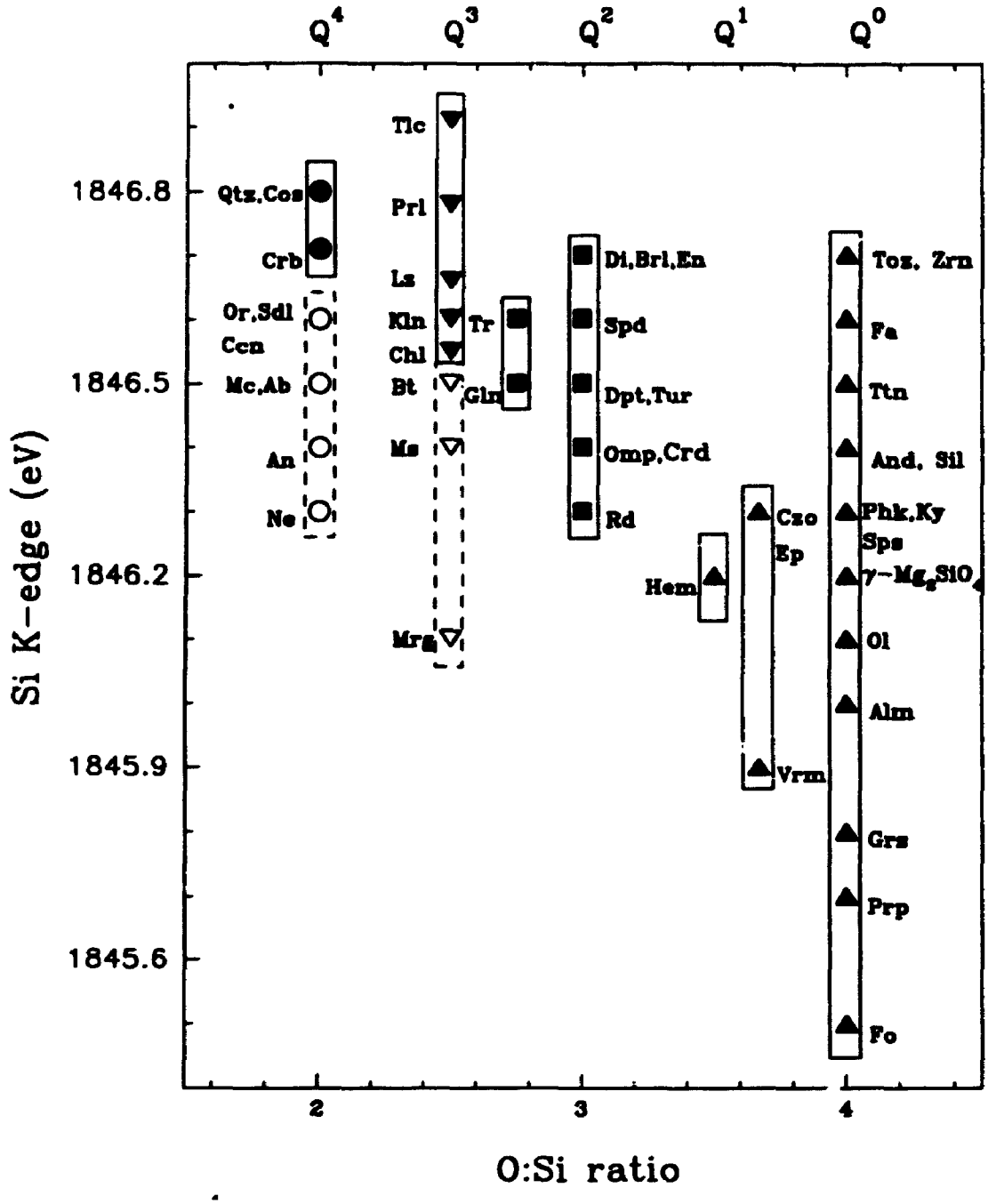

Figure 7.3.3 Variation of Si K-edge position with polymerization and O:Si ratio of silicates. Nesosilicates (Q^0) and sorosilicate (Q^1), cyclo- and inosilicate (Q^2), phyllosilicates (Q^3) and tectosilicates (Q^4) are labelled as filled upward-triangles, squares, downward-triangles and circles, respectively. Corresponding aluminosilicates are labelled with empty symbols.

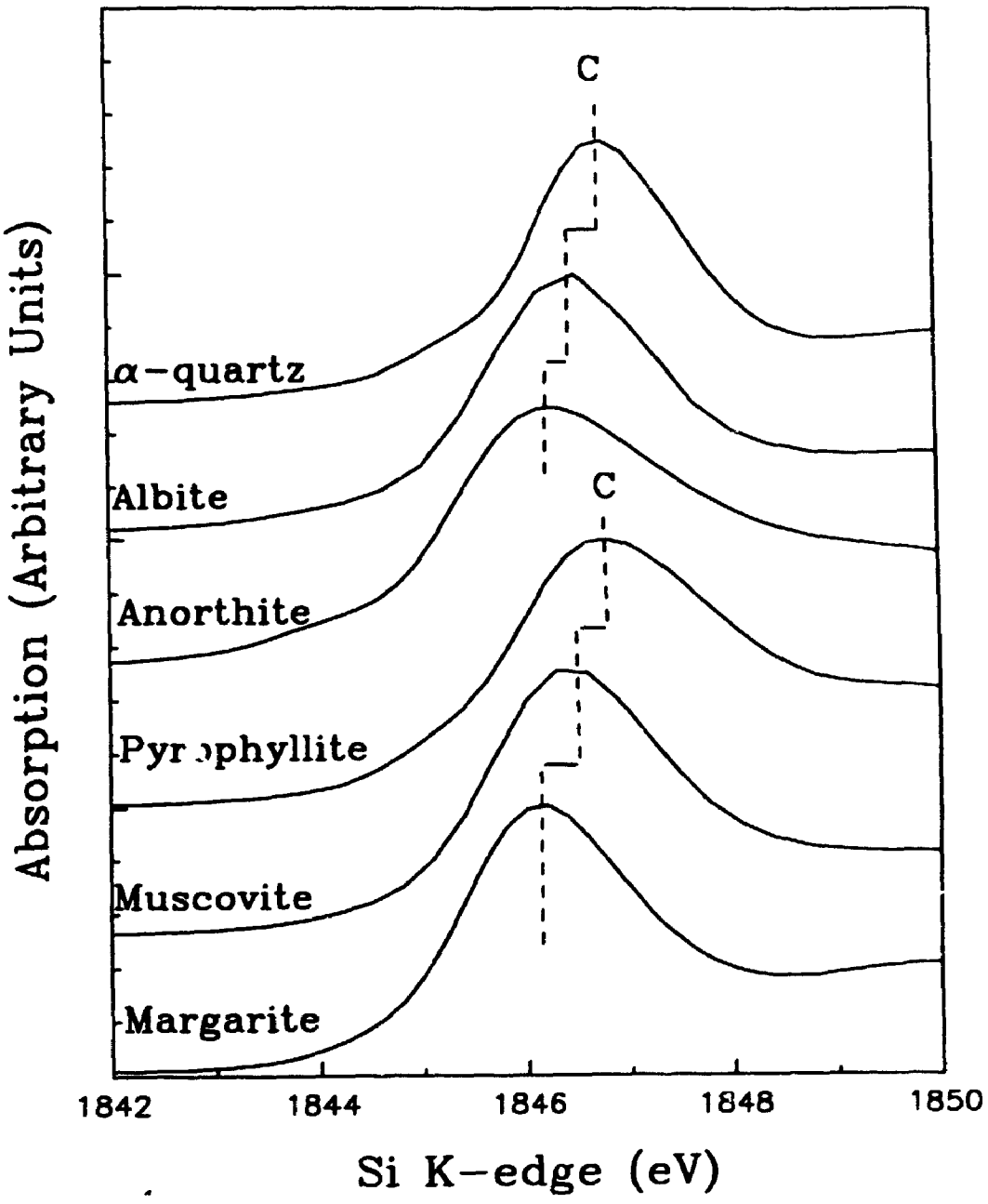

Figure 7.3.4 Shifts of Si K-edge to lower energy with substitution of Al for Si, from α-quartz (SiO_2) to albite ($Na[AlSi_3O_8]$) and anorthite ($Ca[Al_2Si_2O_8]$) for Q^4 series, and from pyrophyllite ($Al_2[Si_4O_{10}](OH)_2$) to muscovite ($KAl_2[AlSi_3O_{10}](OH)_2$) and margarite ($CaAl_2[Al_2Si_2O_{10}](OH)_2$) for Q^3 series.

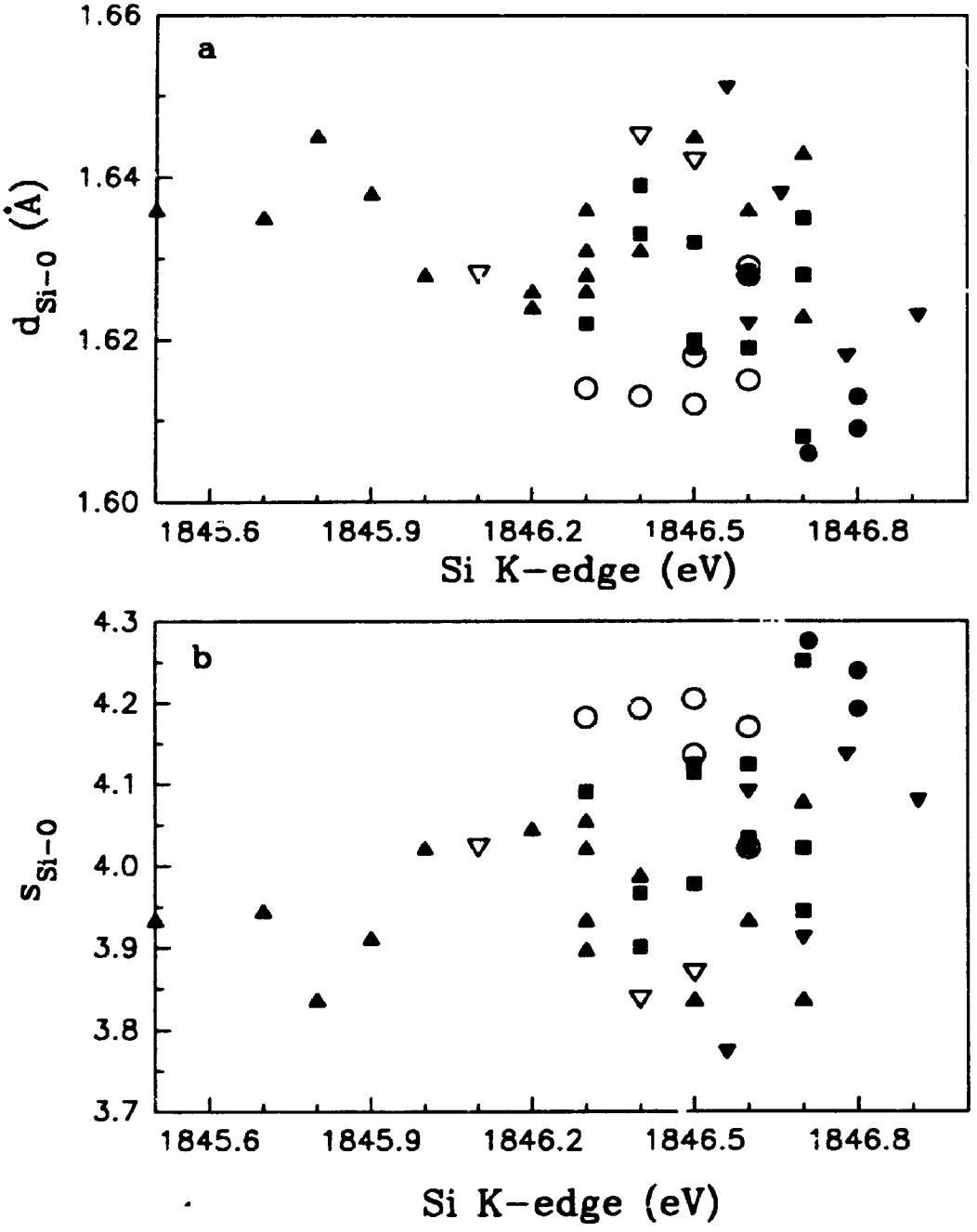

Figure 7.3.5 Correlation of Si K-edge with Si-O bond distance (d_{Si-O}) (a), Si-O bond valence (b).

7.3.3 Chemical Shift of Si K-edge versus Substitution of Al for Si

Figure 7.3.4 also shows that the substitution of Al for Si shifts the Si K-edge to lower energy for silicates and aluminosilicates with the same polymerization. The Si K-edges of tectosilicates [Q^4; α-quartz (SiO_2), albite ($NaAlSi_3O_8$) and anorthite ($CaAl_2Si_2O_8$)], and phyllosilicates [Q^3; pyrophyllite ($Al_2[Si_4O_{10}](OH)_2$, muscovite ($KAl_2[AlSi_3O_{10}](OH)_2$ and margarite $CaAl_2[Al_2Si_2O_{10}](OH)_2$] are compared in Figure 7.3.4. The Si K-edge shifts from 1846.8 eV for α-quartz to 1846.5 eV for albite and 1846.3 eV for anorthite, and shifts from 1846.8 for pyrophyllite to 1846.4 eV for muscovite and 1846.1 eV for margarite. The Si K-edge shifts toward lower energy with increase in the substitution of Al for Si, in agreement with the trends in ^{29}Si MAS NMR chemical shift and again consistent with a decrease in effective charge on the absorber atom.

7.3.4 Chemical Shift of Si K-edge versus d_{Si-O} and s_{Si-O}

Figure 7.3.5 shows correlations of Si K-edge positions with average values for d_{Si-O} (a) and s_{Si-O} (b). In general, both of these two correlations are very weak for all silicate minerals and silicates of the same polymerization type. This is attributed mainly to crystal structure complexity (multisite structures, polyhedral distortion, variations in neighbor shells, etc.).

7.3.5 Chemical Shift of Si K-edge and Cations in More Distant Atom Shells

As shown in Figure 7.3.3, the ranges of variation in Si K-edge position tend to become smaller with increase in polymerization and decrease in number of non-bridging oxygen (NBO), indicating that the Si K-edge position is influenced by the cations connecting the Si oxyanions. For nesosilicates containing isolated SiO_4^{4-}, the range in Si K-edge shifts is 1.2 eV, most likely attributable to the different cations in the second shell. For example, the Si K-edge shifts from 1845.5 eV for forsterite (Mg_2SiO_4) to

1846.2 eV for olivine ($(Mg,Fe)_2SiO_4$ and 1846.6 eV for fayalite (Fe_2SiO_4). For garnet minerals, the Si K-edges of pyrope ($Mg_3Al_2[SiO_4]_3$) and grossular ($Ca_3Al_2[SiO_4]_3$) are at lower energy than those of almandine ($Fe_3Al_2[SiO_4]_3$) and spessartine ($Mn_3Al_2[SiO_4]_3$). These results appear to indicate that, in silicates of similar crystal structures, the heavier M^{2+} cations, for example, 3d transition metal cations, lead to a shift of the Si K-edge to higher energy. With increase in polymerization of Si oxy-anions, the effect of the more distant cation shells on the Si K-edge tends to decrease.

The substitution of Al for Mg in octahedral sites also result in shift of the Si K-edge. This is best exemplified by trioctahedral and dioctahedral phyllosilicates. Figure 7.3.6 compares the Si K-edge shift for talc ($Mg_3[Si_4O_{10}](OH)_2$) - pyrophyllite ($Al_2[Si_4O_{10}](OH)_2$), biotite ($K(Mg,Fe)_3[AlSi_3O_{10}](OH)_2$) - muscovite ($KAl_2[AlSi_3O_{10}](OH)_2$), serpentine ($Mg_6[Si_4O_{10}](OH)_8$ - kaolinite ($Al_4[Si_4O_{10}](OH)_8$, and diopside ($(Ca,Mg)_2[Si_2O_6]$) - spodumene ($LiAl[SiO_3]_2$) with d_{Si-O} and substitution of Mg for Al in octahedral sites. These pairs of silicate minerals have similar crystal structures, and differ only in the substitution of Al for Mg in the octahedral sites, with corresponding decrease in d_{Si-O}.

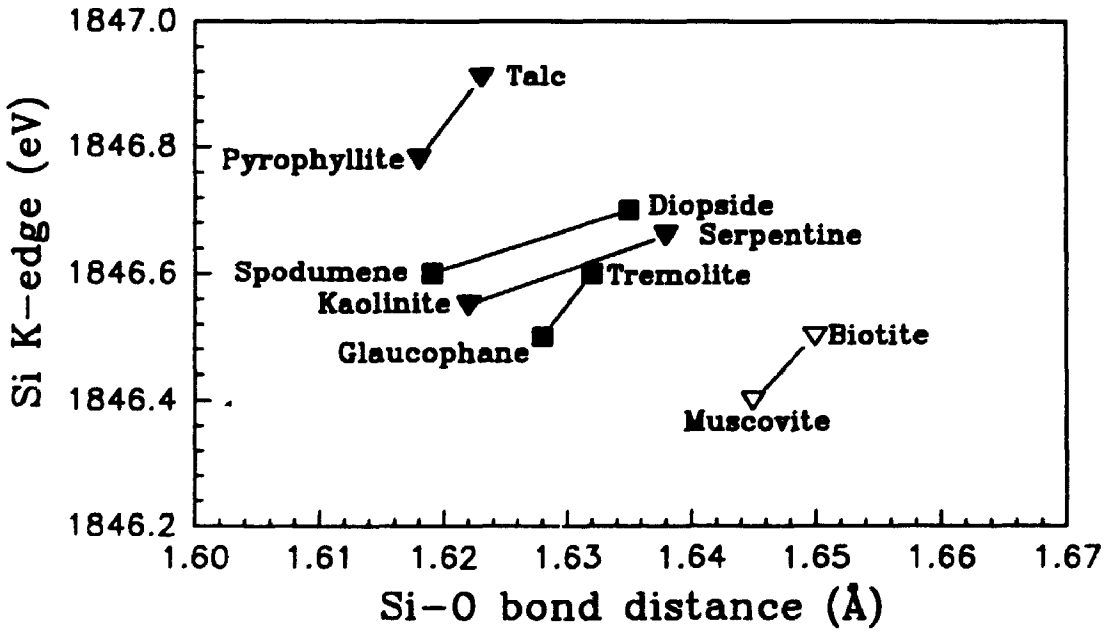

Figure 7.3.6 Si K-edge shift and substitution of Al for Mg in octahedral sites in various Q^3 and Q^2 structures.

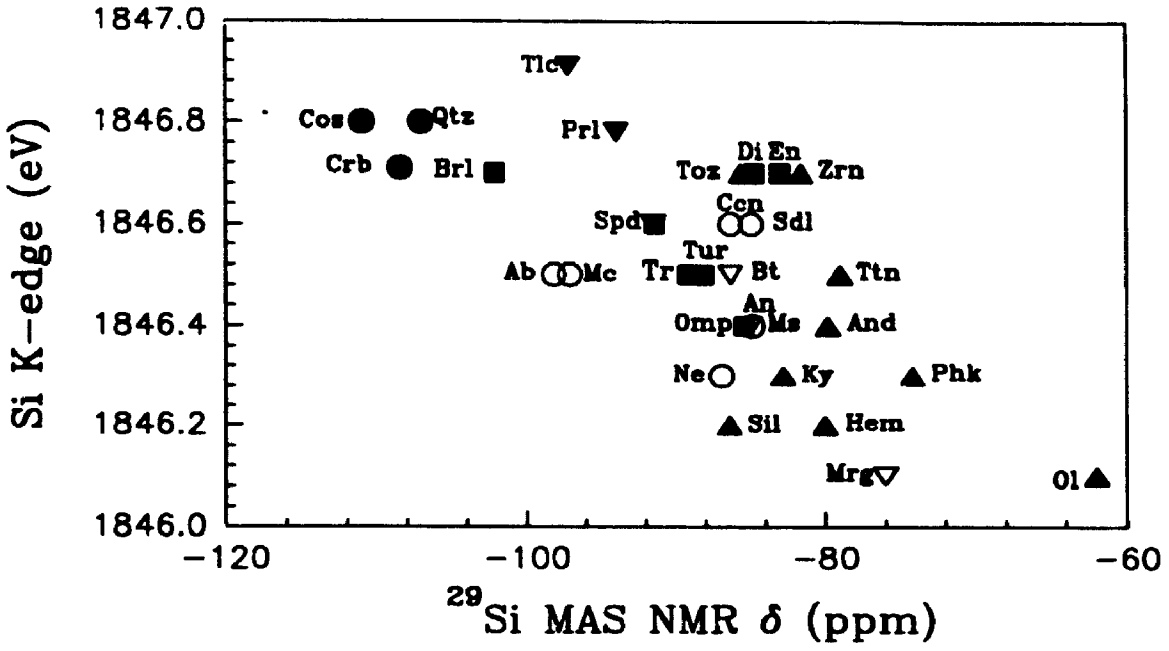

Figure 7.3.7 Correlation of Si K-edge (eV) with ^{29}Si MAS NMR chemical shift, δ (ppm). The values of δ are from Sherriff and Grundy[24] and Sherriff et al.[25] and references therein.

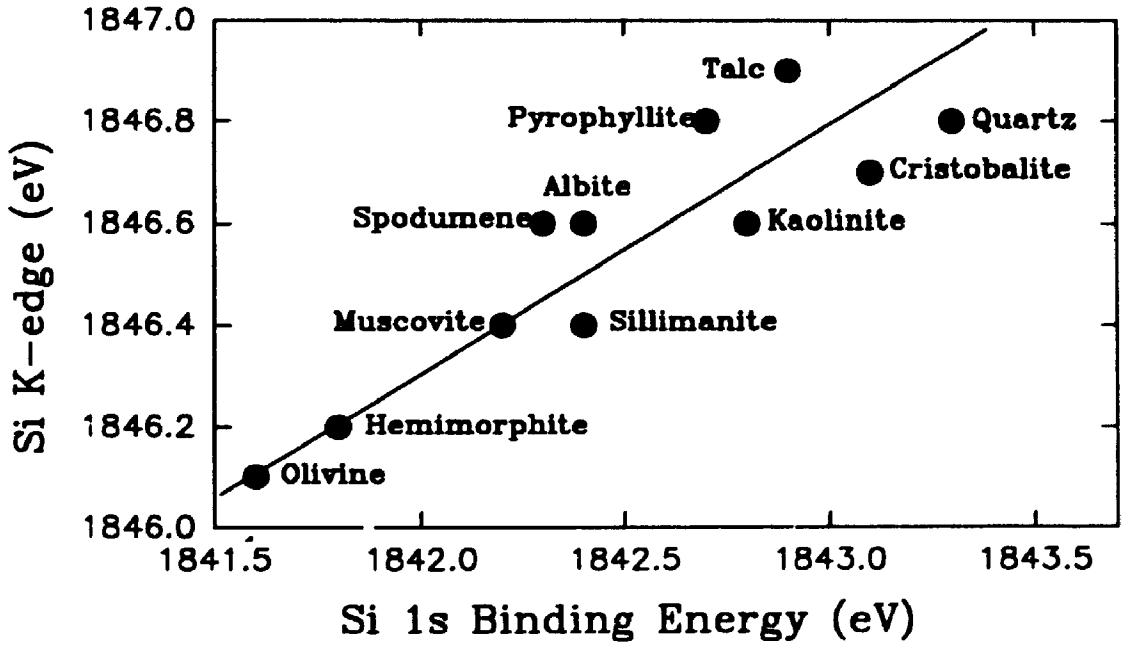

Figure 7.3.8 Correlation of Si K-edge (eV) and Si 1s BE for some silicate minerals. The Si 1s BE is calculated by adding Si 2p BE from XPS[4] and Si $K\alpha_1$ x-ray emission energy .

7.3.6 Comparison of Si K-edge XANES technique with ^{29}Si NMR and XPS

The ^{29}Si chemical shift moves to more negative values with increase in the polymerization of silicates[18,20]. Ranges of chemical shift partially overlap for silicates of different polymerization. Figure 7.3.7 shows the correlation between the ^{29}Si NMR chemical shift and the Si K-edge of silicate minerals. Even though the correlation between the Si K-edge and ^{29}Si MAS NMR shifts is quite weak, the Si K-edge does indeed shift to higher energy with increase in the polymerization and shielding of Si atoms. The latter is equivalent to a progressive increase in effective charge on the Si atoms with increase in Q^n. The Si K-edge spectra for silicates are generally in good agreement with the ^{29}Si MAS NMR results.

Figure 7.3.8 shows the correlation between the Si K-edge and Si 1s binding energy (BE) of some silicate minerals for which the Si 2p BE data from XPS are available. The Si 1s BE is calculated by adding the Si 2p BE and Si $K\alpha_1$ emission energy at 1740.0 eV, and Si 2p BE values are cited from Wagner et al.[4]. In general, Si K-edge shifts to higher energy and the Si 1s BE increases with increase in the polymerization of silicates. This figure also indicates that the shift of Si K-edge to higher energy is essentially due to the increase of the Si 1s BE, even though it is surprising that the change of the Si 1s BE is even larger than the shift of Si K-edge for the silicate minerals presented. The reason for this is that with increase in the polymerization of SiO_4^{4-} clusters, the screening of core electrons by valence electrons is reduced, the core energy levels becomes more tightly bound, and Si atoms have slightly higher positive charge. This result is also in agreement with the ^{29}Si MAS NMR chemical shift.

Comparing ^{29}Si MAS NMR spectroscopy, XPS and x-ray absorption spectroscopy, these three techniques can provide important information on the coordination and local structure of Si in minerals and glasses. Indeed ^{29}Si MAS NMR spectroscopy is a powerful technique for studying geometrical sites, electronic structure and bonding of silicates, and it can even distinguish nonequivalent Si atoms in silicates. The disadvantage of this technique is that it requires a large amount of samples, because of

the low abundance of ^{29}Si. XPS can be used to study microscopic samples and is very sensitive to the surface structures of elements. However, for insulating silicate samples, XPS method has a big problem with the surface charge. This is also the reason why the XPS data of silicates are very limited. Although x-ray absorption spectroscopy has little capability to distinguish nonequivalent Si atoms in silicate mineral, this technique just needs very small amount of sample, and also it has no problem with the surface charge for the study of insulating silicate samples. Therefore, Si K-edge XANES spectroscopy is a very powerful technique for studying the coordination and local structure of silicate minerals and glasses.

7.4 Conclusions

Si K-edge XANES spectra of silicates are qualitatively interpreted within the MO scheme of the SiO_4^{4-} cluster. Because of the crystal structure complexity of silicate minerals and multiple factors effecting the x-ray absorption processes, all spectral features cannot be completely interpreted. Even though Si atoms are four-coordinated in the silicates and aluminosilicates investigated, Si K-edge XANES provides important information on their structure and bonding. Firstly, the Si K-edge shifts to higher energy with increase in the polymerization of SiO_4^{4-} clusters, but with considerable overlap, in agreement with the trends in ^{29}Si MAS NMR chemical shift (δ). Secondly, substitution of Al for Si in tetrahedral sites leads to a shift of the Si K-edge to lower energy for aluminosilicates. Thirdly, substitution of Al for Mg in octahedral sites among dioctahedral and trioctahedral phyllosilicates causes a shift of the Si K-edge toward lower energy. The Si K-edge for nesosilicates is more strongly influenced by cations in the second coordination shells than for the other silicates and aluminosilicates; substitution by heavier metal cations shifts the Si K-edge to higher energy. Fourthly, the correlations of Si K-edge with Si-O bond distance and Si-O bond valence are very weak both for all silicates and silicates of the same polymerization type. Si K-edge XANES spectroscopy can provide information comparable to that from ^{29}Si MAS NMR spectroscopy, however, the advantage of Si K-edge spectroscpy is that it requires a very small amount of sample.

7.5 References

1. F. Liebau, *Structural Chemistry of Silicates: Structure, Bonding and Classification*. Springer-Verlag, Berlin, 1985.
2. I.M. Adams, J.M. Thomas and G.M. Bancroft, *Earth Planet. Sci. Lett.* **16**, 429 (1972).
3. I.M. Adams, S. Evans, P.I. Raid, J.M. Thomas and M.J. Walters, *Anal. Chem.* **49**, 2001 (1977).
4. C.D. Wagner, H.A. Six, W.T. Jansen and J.A. Taylor, *Appl. Surf. Sci.* **9**, 203 (1981).
5. C.D. Wagner, D.E. Passoja, H.F. Hillery, T.G. Kinisky, H.A. Six, W.T. Jansen and J.A. Taylor, *J. Vac. Sci. Tech.* **21**, 933 (1982).
6. R.H. West and J.E. Castle, *Surf. Interf. Anal.* **4**, 68 (1982).
7. H. Seyama and M. Soma, *J. Chem. Soc. Faraday Trans. I* **81**, 485 (1985).
8. V.I. Nefedov, V.G. Yarzhemsky, A.V. Chuvaev and E.M. Trishkina, *J. Electron Spectrosc. Relat. Phenom.* **46**, 381 (1988).
9. I.A. Brytov, K.I. Konashenok and Yu.N. Romashchenko, *Geochem. Int.* **16**, 142 (1979).
10. B. Pitault, E. Belin, D. Boutouaba and C. Senemaud, *Chem. Phys. Lett.* **81**, 123 (1981).
11. G. Wiech and E.Z. Kurmaev, *J. Phys. C: Solid state Phys.* **18**, 4393 (1985).
12. J. Purton and D.S. Urch, *Mineral. Mag.* **53**, 239 (1989).
13. D.S. Urch, *Mineral. Mag.* **53**, 153 (1989).
14. S. Evans, I.M. Adams and J.M. Thomas, *Phil. Trans. R. Soc. Lond.* **A292**, 563 (1979).
15. S. Evans and E. Raftery, *Solid State Commun.* **33**, 1213 (1980).
16. E. Lippmaa, M. Mägi, A. Samoson, G. Engelhardt and A.R. Grimmer, *J. Am. Chem. Soc.* **102**, 4889 (1980).
17. A.R. Grimmer, R.P. Fechner and G. Molgedey, *Chem. Phys. Lett.* **77**, 331

(1981).

18. K.A. Smith, R.J. Kirkpatrick, E. Oldfield and D.M. Henderson, *Am. Mineral.* **68**, 1206 (1983).
19. J. Klinowski, *Progress in NMR Spectroscopy* **16**, 237 (1984).
20. M. Mägi, E. Lippmaa, A. Samoson, G. Engelhardt and A.R. Grimmer, *J. Phys. Chem.* **88**, 1518 (1984).
21. R.A. Kinsey, R.J. Kirkpatrick, J. Hower, K.A. smith and E. Oldfield, *Am. Mineral.* **70**, 537 (1985).
22. C.A. Weiss, S.P. Altaner, R.J. Kirkpatrick, *Am. Mineral.* **72**, 935 (1987).
23. R.J. Kirkpatrick, In *Spectroscopic Methods in Mineralogy and Geology* (Ed. by Hawthorne F.C.). Mineralogical Society of America, 1988, pp.341.
24. B.L. Sherriff and H.D. Grundy, *Nature* **332**, 819 (1988).
25. B.L. Sherriff, H.D. Grundy and J.S. Hartman, *Eur. J. Mineral.* **3**, 751 (1991).
26. J.A. Tossell, *J. Phys. Chem. Solids* **34**, 307 (1973).
27. J.A. Tossell, *J. Am. Chem. Soc.* **97**, 4840 (1975).
28. Yu.P. Dikov, E.I. Debolsky, Yu.N. Romashenko, S.P. Dolin and A.A. Levin, *Phys. Chem. Minerals* **1**, 27 (1977).
29. J.L. Dehmer, *J. Chem. Phys.* **56**, 4496 (1972).
30. T.A. Ferrett, D.W. Lindle, P.A. Heimann, H.G. Kerkhoff, U.E. Becker and D.A. Shirley, *Phys. Rev.* **A34**, 1916 (1986).
31. D.W. McComb, R. Brydson, P.L. Hansen and R.S. Payne, *J. Phys.: Condensed Matter* **4**, 8363 (1992).
32. J.R. Smyth and D.L. Bish, *Crystal Structures and Cation Sites of the Rock-Forming Minerals*. Allen & Unwin, Boston, 1988.
33. I.D. Brown, In *Structure and Bonding in Crystals II* (Ed. by O'Keeffe M. and Navrotsky A.). 1985, pp. 1.
34. R. Kretz, *Am. Mineral.* **68**, 277 (1983).

CHAPTER 8

Al K-edge XANES Spectroscopy of Aluminosilicates

8.1 Introduction

The structural coordination of Al in crystalline aluminosilicate minerals has been studied by x-ray crystallography[1], x-ray emission spectroscopy (XES)[2], x-ray photoelectron spectroscopy (XPS)[3,4], magic-angle-spinning (MAS) nuclear magnetic spectroscopy (NMR)[5-9] and Al K-edge XANES[10-13]. Al in aluminosilicates is normally 4- and/or 6-coordinated with oxygen, but Al is also known to be 5-coordinated in andalusite ($Al^{VI}Al^{V}SiO_5$)[14-17]. Therefore, Al can act as both a network former (Al^{IV}) and a network modifier (Al^{VI}) in aluminosilicate glasses and melts.

In this chapter, Al K-edge XANES spectra of a range of crystalline aluminosilicate minerals are reported. The purposes are: (1) to interpret the Al K-edge spectra based on the MO calculation and comparison with the Si K-edge spectra of 4-coordinated α-quartz and 6-coordinated stishovite; (2) to explore qualitative correlations of chemical shift in the Al K-edge to the coordination of Al, Al-O bond distance ($d_{Al\text{-}O}$), bond valence ($s_{Al\text{-}O}$), the distortion ($\Delta_{Al\text{-}O}$) of the coordination polyhedra, and chemical compositions of the first and second shells; (3) to document a semi-quantitative relationship between the intensity of the Al K-edge and the content of Al in both octahedral and tetrahedral sites and to investigate the partition of Al in tetrahedral and octahedral sites. These studies will establish a foundation for the use of the Al K-edge XANES method in the study of the structure of the structural role of Al in glasses and melts.

Table 8.2.1 Electron microprobe analyses (wt%) of aluminosilicate minerals

Minerals	SiO_2	Al_2O_3	MgO	CaO	Na_2O	K_2O	FeO	MnO	TiO_2	Cr_2O_3	Cl	F	Total
Anorthite	44.2.	34.83		19.38	0.55		0.56						99.52
Microcline	65.00	18.22			0.61	16.04	0.03						99.89
Sodalite	37.07	31.46		0.01	24.49	0.03					7.21		100.30
Biotite[a]	38.00	10.31	13.30		0.54	8.95	17.89	0.90	2.07		0.19	2.57	94.74
Cordierite	49.65	33.24	9.50		0.33		5.44	0.07					98.21
Spodumene[b]	64.35	26.70			0.05			0.06					91.23
Pyrope	42.30	21.92	18.58	5.31			8.66	0.44	0.09	2.22			99.51
Almandine	39.34	22.06	10.54	5.11			21.84	0.49	0.11				99.50
Spessartine	36.39	20.12	0.09	3.74			8.07	31.55	0.12				100.10
Grossular	39.06	22.89		35.35	0.03		1.52	0.59	0.12				98.52
Clinozoisite[c]	37.92	26.08	0.01	23.51			8.93	0.07	0.19	0.01			96.72
Epidote[c]	37.01	23.13	0.06	23.01	0.01		13.63	0.20	0.19				97.23
Kyanite	37.03	62.21	0.01				0.17	0.04					99.46
Topaz	31.79	55.78										12.33	99.65
Beryl[b]	62.77	16.87			0.92				0.01				80.57
Tourmaline[b]	38.10	40.41		0.89	1.59		0.01	0.29				0.64	81.93
Corundum		99.48					0.37			0.27			100.10
Muscovite[a]	45.13	33.10	0.83	0.03	0.57	10.25	2.73		0.39			0.85	93.88
Omphacite	57.24	13.18	7.51	12.09	7.53		2.12	0.04	0.08	0.02			99.82
Sillimanite	37.19	62.46					0.29						99.94
Andalusite	37.26	62.65					0.23						100.10

[a] H_2O in these two minerals can not detected by EMPA.

[b] Li in spodumene, Be in beryl are B in tourmaline can not be detected by EMPA.

[c] Fe in these two minerals is Fe_2O_3, rather than FeO.

8.2 Experimental

Aluminosilicate mineral samples were largely from the collection in the Department of Earth Sciences, UWO. The samples were characterized by optical petrography, powder x-ray diffraction (PXRD) and electron microprobe analyses (EMPA). The EMPA results were given in Table 8.2.1. The sodalite sample was a mixture of sodalite and K-rich nepheline. The sillimanite was impure fibrolite, and apparently a mixture of fibrolite, other aluminosilicate and hydrous alteration phases. All other minerals were single phases, departing from ideal end-member compositions only because of expected solid solutions.

Al K-edge XANES spectra of the aluminosilicate minerals were collected on the Double Crystal Monochromator (DCM) beamline. Two α-quartz crystals, cut along the orientation $(10\bar{1}0)$ (2d = 8.512 Å), were employed as the monochromator crystals, giving a resolution of about 0.7 eV. However, the intensity of the photon flux in energy range of the Al K-edge was very weak; even less than one percent of that from InSb monochromator for the Si K-edge measurement. The spectra were taken at room temperature and chamber pressure of about 10^{-7} torr, using the Aladdin synchrotron radiation operating at 800 meV or 1 GeV.

The aluminosilicate minerals were ground into fine powder of about 10 μm in size, and the powder samples were pressed uniformly on electric carbon tape supported on a stainless steel sample holder for XANES measurements. The Al K-edge spectra were recorded by Total Electron Yield (TEY) over the energy ranges 1565-1572 eV (0.1 eV for each data point) and 1572-1600 eV (0.25 eV for each data point). The spectra were normalized by I/I_0, where I is the intensity of TEY, and I_0 is the intensity of photon flux. The signal-to-noise ratios for some spectra are poor, due to the low photon flux from the α-quartz $(10\bar{1}0)$ monochromator crystals. The Al K-edge spectra shown below in Figures 8.3.1 and 8.3.2 are averages of five scans and smoothed once after two adjacent data points were added together. The spectra were also calibrated with the K-edge of Al metal at 1560 eV, and a similar linear pre-edge background has been removed for each spectrum.

8.3 Results and Discussion

8.3.2 Al K-edge XANES spectra of 4-coordinated Al (Al^{IV})

Figure 8.3.1 compares Al K-edge XANES spectra (solid dot lines) of anorthite, microcline and biotite with Si K-edge spectra (solid line) of these minerals and α-quartz. The Al K-edge spectra of the other aluminosilicate minerals containing Al^{IV}, such as sodalite, cancrinite and cordierite, are very similar to those of anorthite, microcline and biotite. The peak positions for these aluminosilicate minerals containing Al^{IV} and α-quartz are given in Table 8.3.1. To enable comparison of the spectra, the Al and Si K-edge spectra are aligned by setting peak C to zero in energy scale. The intensity of peak C increases in the sequence of biotite, microcline and anorthite. ΔE in Table 8.3.1 is the energy difference between each peak and peak C.

The Al K-edge spectra of these Al^{IV} minerals are qualitatively very similar, and correspond closely to the previously published Al K-edge spectrum of albite[11,12]. Peaks C, D, E and G lie at similar ΔE values for all the six minerals. Peak C ranges from 1566.5 eV for microcline to 1567.3 eV for sodalite. The Si K-edge spectrum of α-quartz exhibits peaks C, D, E and F (see Chapter 7). Interestingly, the Al K-edge spectra are qualitatively very similar to the Si K-edge spectra of the same mineral, and similar to the Si K-edge spectrum of α-quartz (see Figure 8.3.1). The ΔE values for corresponding peaks are very similar in both Si and Al K-edge spectra (see Table 8.3.1). The similarity of the Al and Si K-edge spectra are not surprising, perhaps because Si and Al reside in the same tetrahedral site. In addition, α-quartz exhibits a distinct shoulder (peak A) on the higher energy side of peak C, which is not readily seen in the Al or Si K-edge spectra of the other minerals.

XANES spectroscopy of solids involves complicated processes that are not fully understood theoretically. The accurate interpretation of the Al K-edge XANES spectra is impossible without sophisticated theoretical calculation. This kind of calculation is often very difficult for aluminosilicates. However, as discussed in chapter 6, Si K- and L-edge XANES spectra of α-quartz were qualitatively interpretable based on Xα multiple

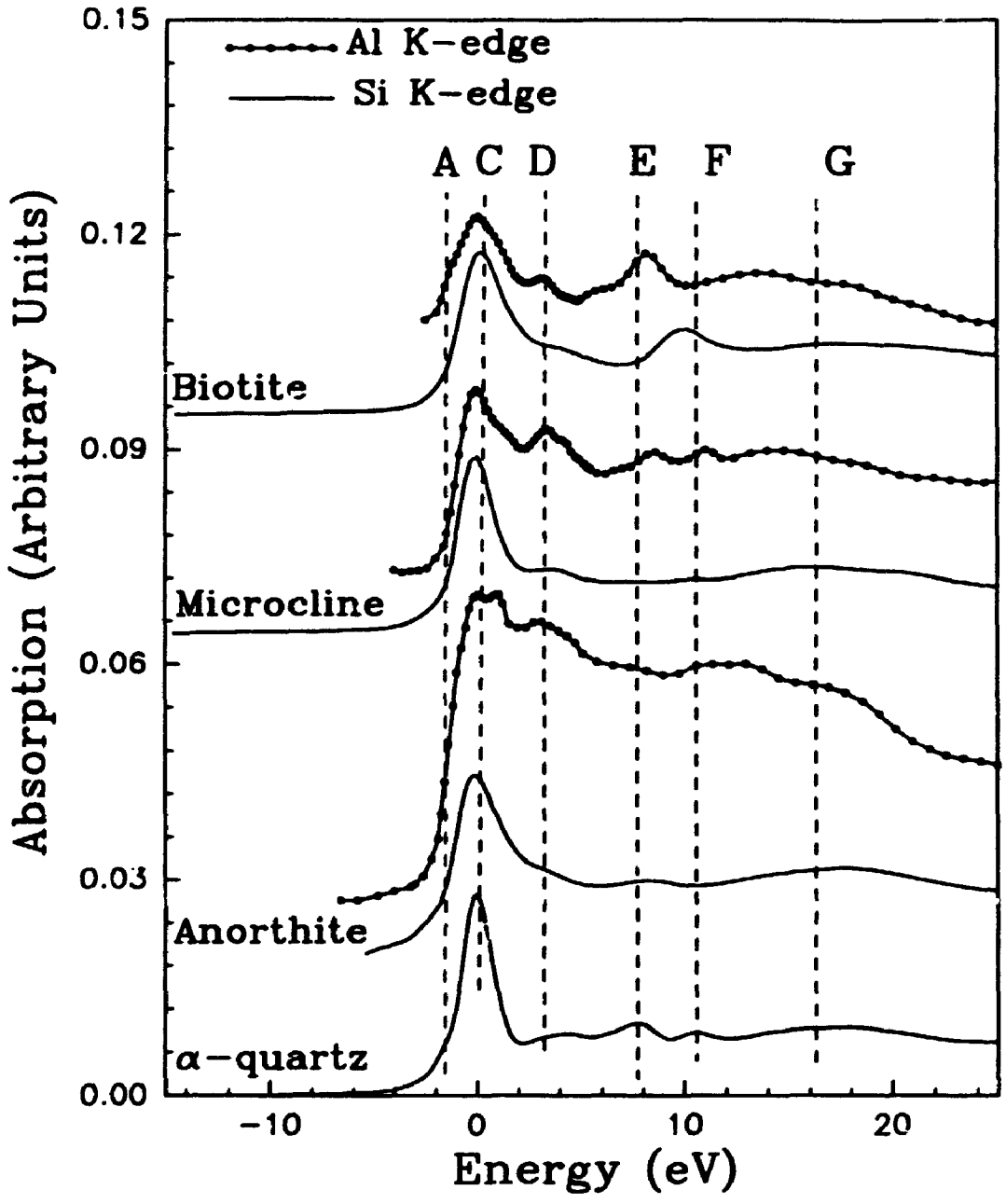

Figure 8.3.1 Al K-edge XANES spectra (solid dot lines) of anorthite, microcline and biotite, compared to Si K-edge spectra (solid lines) of these minerals and α-quartz. The Al and Si K-edge spectra are aligned on a common scale by calibration of peak C to zero in energy scale.

Table 8.3.1 Assignments of Al K-edge XANES of aluminosilicates containing 4-coordinated Al

Assignments		Al K-edge XANES (±0.2 eV)*										Si K-edge (±0.2 eV)*	
		Anorthite		Microcline		Sodalite		Cordierite		Biotite		α-quartz	
		Peaks	ΔE	Peaks	ΔE	Peaks	ΔE	Peaks	ΔE	Peaks	ΔE	Peaks	ΔE
A	1s → a_1 (3s-like)											1844.9	-1.9
C	1s → t_2 (3p-like)	1566.9	0.0	1566.5	0.0	1567.3	0.0	1567.0	0.0	1567.0	0.0	1846.8	0.0
D	MS effect	1569.9	3.0	1569.9	3.4	1570.5	3.2	1570.1	3.1	1570.2	3.2	1850.7	3.9
E	1s → e (3d-like)	1574.3	7.4	1575.0	8.5	1575.6	8.3	1572.7	5.7	1575.2	8.0	1854.5	7.7
F	MS effect	1579.2	12.3	1577.5	11.0	1580.4	13.1	1580.5	13.5	1857.4	10.6		
G	1s → t_2 (3d-like)	1584.1	17.2	1582.0	15.5	1584.2	16.9	1582.3	15.3	1584.5	17.5	1864.3	17.5

* ΔE is energy difference between each peak and peak C, rather than that between each peak and the 1s binding energy as for α-quartz in Chapter 6. The reading error of the edge peak is ±0.1 eV.

scattering MO calculation and XANES spectra of model gas phase molecules. These assignments were in good agreement with the interpretation of the Si L-edge XANES spectra of gas phases SiH_4 [18], SiF_4 [19] and $Si(OCH_3)_4$ [20], and of Si L-edge electron energy loss spectra (EELS) of some silicates[21]. Because 4-coordinated Al and Si have similar structural environments in aluminosilicate, and AlO_4^{5-} and SiO_4^{4-} clusters are isoelectronic, the 4-coordinated Al and Si K-edge XANES spectra are expected to be similar, and may be interpreted in a similar way.

Therefore, as shown in Table 8.3.1, the Al K-edge XANES spectra of aluminosilicates containing Al^{IV} are qualitatively interpreted by comparison with the Si K-edge spectrum of α-quartz and the MO calculation of the AlO_4^{5-} cluster[22]. Peak A is very week in the Al K-edge spectra, because it is due to the dipole-forbidden Al 1s $\rightarrow a_1$ (3s-like) transition. Peak C is assigned to the allowed transition of Al 1s to the antibonding t_2 (3p-like) state. Peak E and G are attributed to the transitions of Al 1s electrons to the e and t_2 (3d-like) states, respectively, the so-called "symmetry-forbidden shape resonances"[23,24]. Peaks D and F are attributable to multiple scattering (MS) from the more distant atom shells (see Chapter 6). Certainly, peak G must include a contribution of the MS effect from the more distant atom shells. The splitting of peak C in the anorthite spectrum (see Figure 8.3.1) is unexpected, but is probably related to the fact that Al has four nonequivalent positions in primitive anorthite.

8.3.2 Al K-edge XANES spectra of 6-coordinated Al (Al^{VI})

Figure 8.3.2 compares the Al K-edge XANES spectra (solid dot lines) of some representative aluminosilicate minerals containing Al^{VI}—— almandine, spodumene, pyrophyllite, tourmaline, kaolinite, topaz, kyanite and corundum with Si K-edge spectra (solid lines) of stishovite containing Si^{VI}. The peak positions for spodumene, pyrophyllite, kyanite, topaz, corundum and stishovite are given in Table 8.3.2. The Al K-edge spectra of the other aluminosilicate minerals containing Al^{VI} are very similar to those shown in Figure 8.3.2. Again the Al and Si K-edge XANES spectra are aligned by the calibration of peak C to zero in energy scale, and the intensity of peak C in the

Al K-edge spectra increases in the sequence from the upper to the bottom of this figure. The Al K-edge spectra of topaz and corundum are similar to previous results[11].

Peak A is weak, but resolved in the spectra of most aluminosilicates containing Al^{VI}. Peak C is the main Al K-edge. Peak D, which is prominent in the Si K-edge spectrum of stishovite, is not apparent in the spectra of most aluminosilicates containing Al^{VI}. On the other hand, peak E shifts to lower energy and becomes more prominent in all the Al^{VI} K-edge spectra than in the stishovite Si K-edge spectrum. A possible cause is that peaks D and E merge and overlap. The relative intensity between peaks C and E varies dramatically. Peak C is stronger than peak E for corundum, topaz and kyanite, while peak E becomes more prominent than peak C for spodumene, almandine and kaolinite.

The Al^{VI} in aluminosilicates has a similar structural environment to that of Si in stishovite, and the AlO_6^{9-} and SiO_6^{8-} clusters are isoelectronic. Based on comparison with the Si K-edge spectrum of stishovite and MO calculation of the AlO_6^{9-} cluster[25], the Al^{VI} K-edge XANES spectra are interpreted as follows. The weak peak A is due to the dipole-forbidden transition of Al 1s electrons to the antibonding 3s-like a_{1g} states. This forbidden peak appears, because the distortion of the coordination octahedra permits a mixture Al s and p states. The intensity of peak A increases qualitatively in order of almandine, tourmaline, spodumene, epidote, corundum, pyrophyllite, kaolinite, topaz and kyanite, and is related to the local symmetry of Al. However, it is very difficult to evaluate the correlation between the intensity of peak A and the distortion of the Al coordination, even on a semi-quantitative basis. Peak C, of course, is assigned to the allowed transition of Al 1s electrons to the antibonding 3p-like t_{1u} (3p-like) states. Peaks E and G are attributed to transitions of Al 1s electrons to the 3d-like t_{2g} and e_g (3d-like) states, respectively, or the symmetry-forbidden "shape resonances"[23,24]. Also, as indicated above, peaks E and G certainly reflect the contribution of the MS effect from the more distant atom shells. Peak D, due to the MS effect in the stishovite spectrum, is resolved only in epidote, clinozoisite, beryl and omphacite spectra, and is not resolved for most aluminosilicates containing Al^{VI}. It is suggested that peak D merges with peak E, making peak E appear more complicated. The MS effect may enhance peak E; this

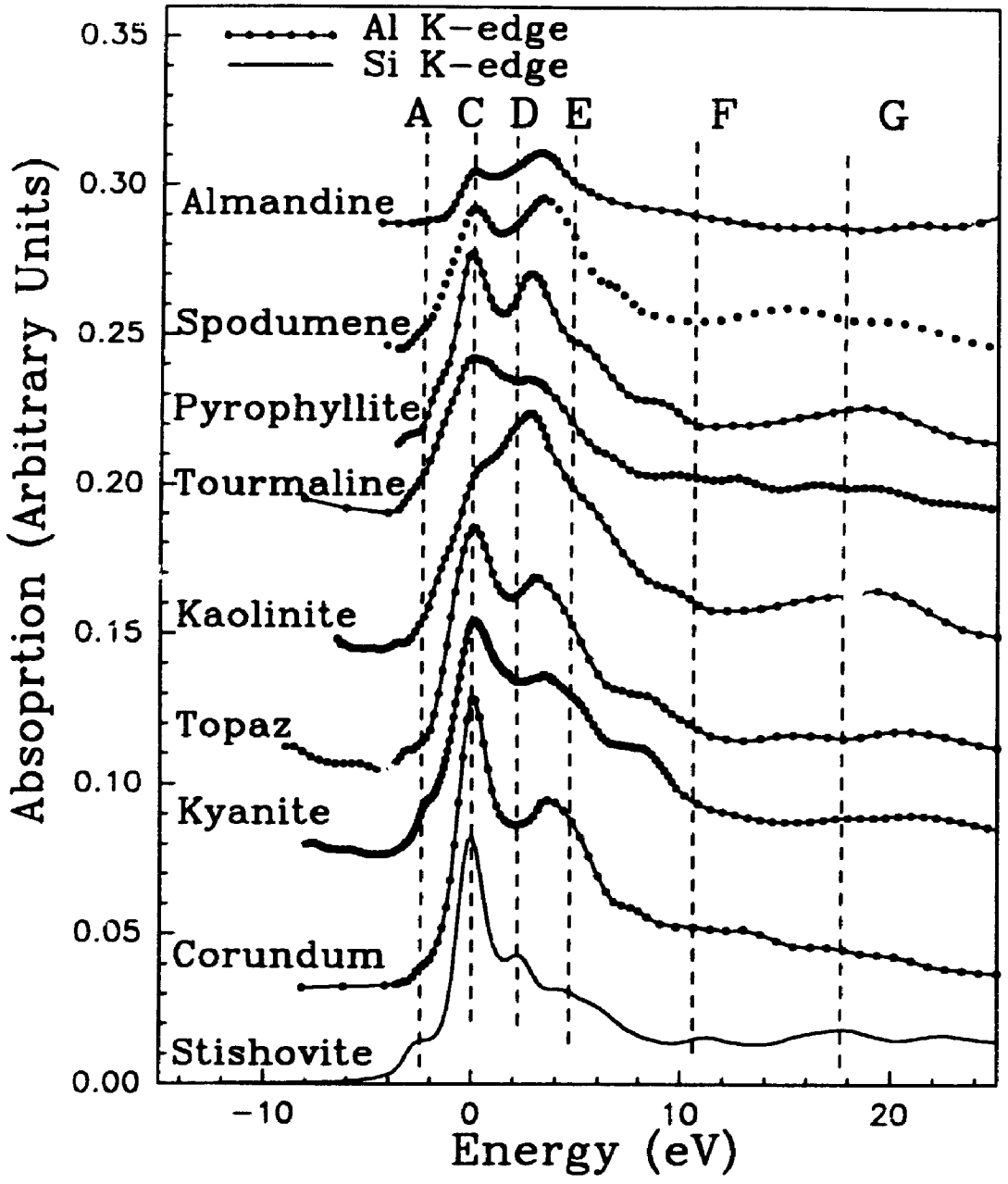

Figure 8.3.2 Al K-edge XANES spectra (solid dot lines) of some representative aluminosilicates containing Al^{VI}, compared to Si K-edge spectrum (solid line) of 6-coordinated stishovite.

Table 8.3.2 Assignments of Al K-edge XANES of representative aluminosilicates containing 6-coordinated Al

		Al K-edge XANES (±0.2 eV)*										Si K-edge (±0.2 eV)*	
Assignments		Spodumene		Pyrophyllite		Kyanite		Topaz		Corundum		Stishovite	
		Peaks	ΔE	Peaks	ΔE	Peaks	ΔE	Peaks	ΔE	Peaks	ΔE	Peaks	ΔE
A	$1s \rightarrow a_{1g}$ (3s-like)	1565.9	-2.8	1565.4	-3.3	1565.7	-2.5	1565.8	-3.3	1566.0	2.7	1846.3	-2.7
C	$1s \rightarrow t_{1u}$ (3p-like)	1568.7	0.0	1568.7	0.0	1568.2	0.0	1569.1	0.0	1568.7	0.0	1849.0	0.0
D	MS effect			1571.5	2.8					1851.3	2.3		
E	$1s \rightarrow t_{2g}$ (3d-like)	1572.0	3.3	1574.1	5.4	1571.8	3.6	1572.7	3.4	1572.4	3.7	1853.4	4.4
F	MS effect	1575.4	6.7	1577.8	9.1	1580.3	13.7	1577.4	8.3	1576.8	7.9	1860.2	11.2
G	$1s \rightarrow e_g$ (3d-like)	1583.7	15.0	1584.6	15.9	1585.0	16.8	1584.4	15.3	1582.2	13.5	1866.4	17.4

* ΔE is energy difference between each peak and peak C, rather than that between each peak and the 1s binding energy as for stishovite in Chapter 6. The reading error of the edge peak is ±0.1 eV.

interpretation is in good agreement with the MS calculation of the Al K-edge spectra[13]. These qualitative assignments of Al K-edge XANES of representative aluminosilicates containing Al are summarized in Table 8.3.2, and again ΔE is the energy difference between each peak and peak C.

8.3.3 Chemical Shift of Al K-edge and Coordination Number of Al

Figure 8.3.3 compares Al K-edge spectra of microcline (Al^{IV} only), andalusite (both Al^{V} and Al^{VI}), corundum (Al^{VI} only) and omphacite, sillimanite and muscovite (both Al^{IV} and Al^{VI}). As stated above, the Al K-edge shifts by about 2.2 eV from 1566.5 eV for microcline to 1568.7 eV for corundum. The two major peaks in the muscovite spectra are at 1566.4 and 1568.6 eV. The lower energy peak corresponds to Al^{IV}, and the higher energy peak to Al^{VI}. For andalusite, the main peak at 1567.8 eV, intermediate between Al^{IV} and Al^{VI}, is assigned to Al^{V}. The edge peak for Al^{VI} in andalusite is not clearly resolved, and probably shifts to lower energy and merges with the peak for Al^{V}, so that the peak at 1567.8 eV for andalusite is very strong and broad. The two prominent peaks in the sillimanite spectrum apparently indicate the presence of Al^{IV} and Al^{VI}. However, the two peaks consistently shift to lower energy, so that the Al^{VI} edge peak is close to the Al^{V} edge peak in the andalusite spectrum. Indeed, for the three polymorphs of Al_2SiO_5, kyanite, sillimanite and andalusite, the Al K-edge spectra appear not be interpreted completely, and probably provide some new information on the structural coordination of Al. The extent to which the present anomalies in the spectrum of sillimanite are attributable to impurities, or more interestingly, to the fibrolite problem[26], is unknown.

The Al K-edge data and crystal-chemical parameters, such as $d_{Al\text{-}O}$ (Å), $s_{Al\text{-}O}$, and $\Delta_{Si\text{-}O}$, coordination number (CN) of Al, relative intensity of Al K-edge, and Al content (wt%) of the aluminosilicates are summarized in Table 8.3.3, together with ^{27}Al MAS NMR chemical shift δ (ppm)[5-8]. The $s_{Al\text{-}O}$ was calculated using the formula[27]:

$$s = \exp[-(R-R_0)/B]$$

where for the Al-O polyhedron, R_0 = 1.62 Å and B = 0.37. The distortion parameter

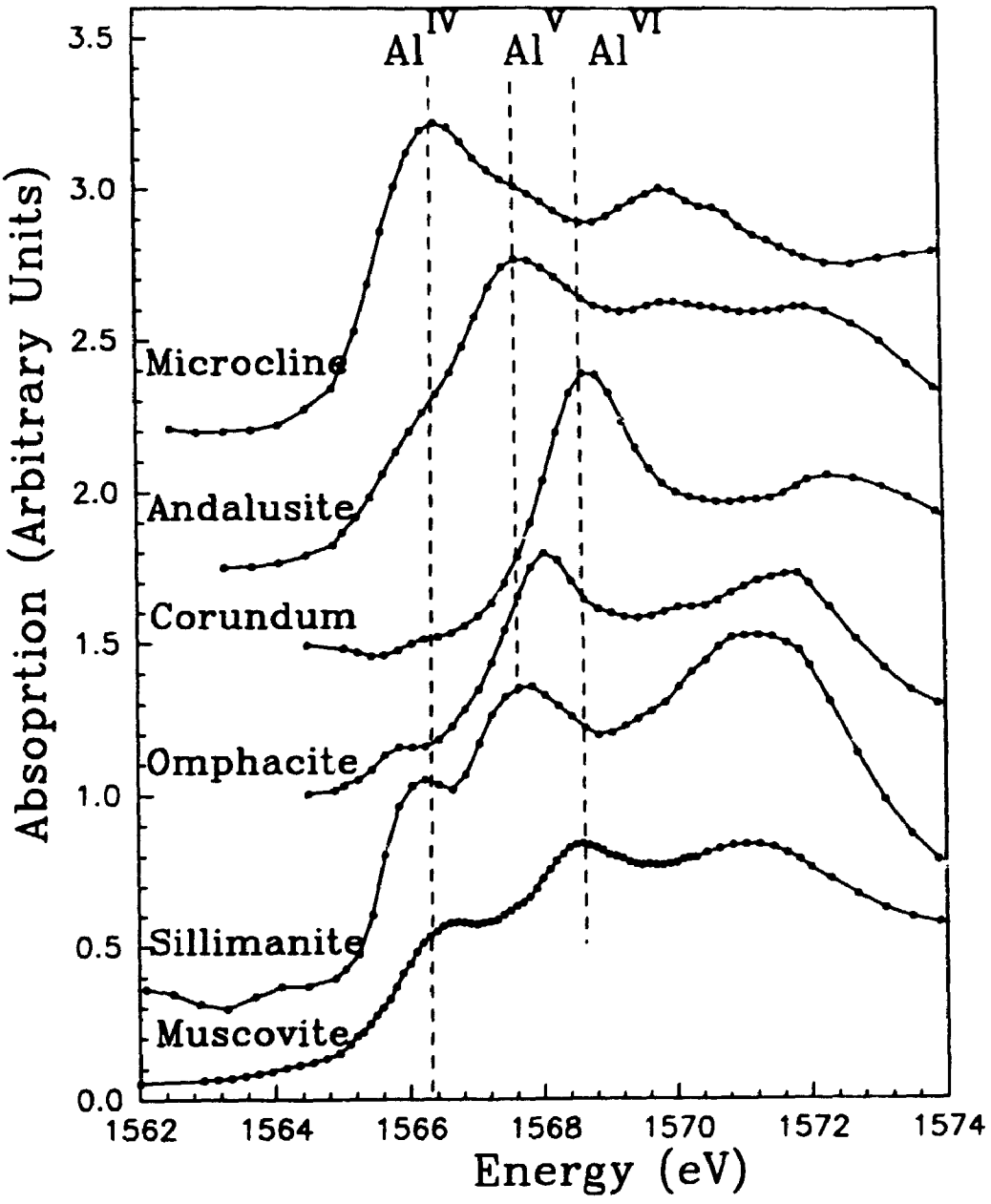

Figure 8.3.3 Al K-edge XANES spectra of microcline (Al^{IV} only), andalusite (both Al^{IV} and Al^{V}), corundum (Al^{VI} only), and omphacite, sillimanite and muscovite (both Al^{IV} and Al^{VI}).

Table 8.3.3 Al K-edge, crystal-chemical parameters, NMR δ (ppm) and the content of Al (wt%) of aluminosilicates

Mineral	Formula	Al K-edge (±0.1 eV)	d_{Al-O} (Å)	s_{Al-O}	Δ_{Al-O}	CN	NMR δ	Al (expt.)	I
Anorthite	$Ca[Al_2Si_2O_8]$	1566.9	1.747	2.87	1.79E-4	4		18.4	0.43
Microcline	$K[AlSi_3O_8]$	1566.5	1.742	2.89	2.39E-6	4	60.9	9.7	0.32
Sodalite	$Na_8[AlSiO_4]_6Cl_2$	1567.3	1.728	2.99		4	64.5	16.7	0.43
Cancrinite	$Na_6Ca_2[AlSiO_4]_6SO_4(OH)_2$	1566.6	1.742	2.88	3.28E-5	4		15.3	0.41
Biotite	$K(Mg,Fe)_3[AlSi_3O_{10}](OH)_2$	1567.0				4	63.5	5.5	0.17
Cordierite	$Mg_2[Al_4Si_5O_{18}]$	1567.0	1.750	2.82	3.47E-4	4		17.6	0.45
Pyrophyllite	$Al_2[Si_4O_{10}](OH)_2$	1568.7	1.912	2.73	7.65E-5	6	1.0	15.2	0.55
Kaolinite	$Al_4[Si_4O_{10}](OH)_8$	1568.5				6	4.0	20.3	0.64
Spodumene	$LiAl[Si_2O_6]$	1568.7	1.919	2.73	1.53E-4	6		14.2	0.51
Pyrope	$Mg_3Al_2[Si_3O_{12}]$	1567.9	1.887	2.92		6		11.6	0.23
Almandine	$Fe_3Al_2[Si_3O_{12}]$	1568.0	1.896	2.85		6		11.7	0.20
Spessartine	$Mn_3Al_2[Si_3O_{12}]$	1568.2	1.901	2.81		6		10.7	0.19
Grossular	$Ca_3Al_2[Si_3O_{12}]$	1568.1	1.924	2.64		6		11.9	0.28
Clinozoisite	$Ca_2AlAl_2[SiO_4][Si_2O_7]O(OH)$	1568.0	1.892	2.90	3.12E-4	6		13.8	0.19
Epidote	$Ca_2FeAl_2[SiO_4][Si_2O_7]O(OH)$	1567.8	1.895	2.87	2.70E-4	6		11.1	0.17
Kyanite	$Al_2[SiO_4]O$	1568.2	1.907	2.79	6.34E-4	6	7.5	32.9	0.81
Topaz	$Al_2[SiO_4]F_2$	1569.1	1.871			6		29.5	0.72
Beryl	$Be_3Al_2[Si_6O_{18}]$	1568.3	1.906	2.77		6	-3.2	8.9	0.30
Tourmaline	$NaMg_3Al_6[Si_6O_{18}][BO_3]_3(OH)_4$	1568.6	1.922	2.67	3.99E-4	6		21.4	0.58
Corundum	Al_2O_3	1568.7	1.913	2.75	8.72E-4	6		52.7	1.00
Muscovite	$KAl_2[AlSi_3O_{10}](OH)_2$	1566.4				4	67.0	5.9	0.21
		1568.6	1.940	2.53	3.87E-5	6	1.5	11.7	0.32
Omphacite	$(Na,Ca)Al[(Al,Si)_2O_6]$	1566.0				4			0.05
		1568.1	1.940	2.49	7.18E-4	6		7.0	0.23
Sillimanite	$Al^{IV}Al^{VI}[SiO_4]O$	1566.0	1.764	2.73	4.04E-4	4	64.5	16.3	0.28
		1567.8	1.912	2.74	3.38E-4	6	4.0	16.7	0.39
Andalusite	$Al^{V}Al^{VI}[SiO_4]O$	1567.8	1.836	2.80	3.18E-4	5,6	36.0	33.2	0.77

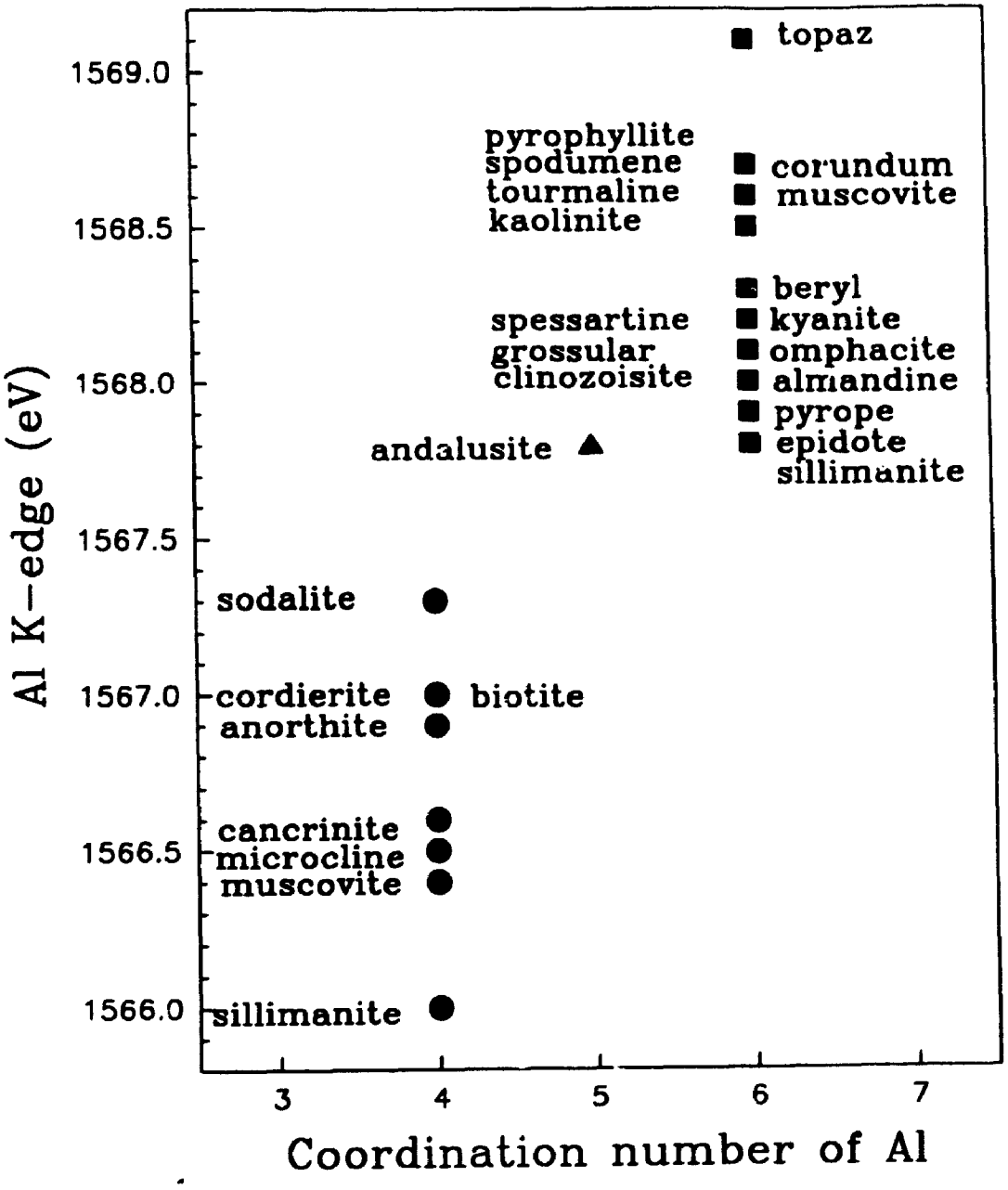

Figure 8.3.4 Chemical shifts of Al K-edges for all studied aluminosilicates with the coordination number of Al.

(Δ) calculated using the empirical formula[28]:

$$\Delta = 1/N \cdot \sum_{i=1}^{N} (R_i - R_0)^2$$

where R_i and R are the individual and average radii for a polyhedron, respectively, and N is 4, 5 and 6 for Al^{IV}, Al^{V} and Al^{VI}, respectively. The relative intensity (arbitrary units) of the Al K-edge is approximately represented by the normalized height of peak C in the Al K-edge XANES spectra. The values of the relative intensity of peak C shown in Table 8.3.3 are derived, using the Al K-edge spectrum of corundum as the external standard of which the normalized intensity of Al K-edge for corundum is calibrated to one unit. The content (wt%) of Al were determined by EMPA.

Figure 8.3.4 shows the variation of the position of peak C with the coordination number (CN) of Al. In general, the Al K-edge shifts by about 1.6 eV with increase in the CN of Al, from 1566.7 eV for Al^{IV} (average for 8 samples) to 1568.3 eV for Al^{VI} (average for 17 samples), which is also in good agreement with the shift (2.2 eV) of Si K-edge for α-quartz and stishovite. The Al K-edge for Al^{V} is 1567.8 eV (1 sample), intermediate between Al^{IV} and Al^{VI}. The shift in the Al K-edge toward higher energy with increase in the CN of Al is attributable to increase in the effective charge of the Al atoms. Qualitatively, the $d_{Al\text{-}O}$ is larger, the Al-O bonding is weaker, the $s_{Al\text{-}O}$ is smaller. The effective charge on Al atoms is higher in aluminosilicates containing Al^{VI} than in aluminosilicates containing Al^{IV}, and the Al^{VI} 1s binding energy (BE) is higher than the Al^{IV} BE.

Figure 8.3.5 shows the correlation of the Al K-edge position with ^{27}Al MAS NMR chemical shift δ (ppm) for some aluminosilicates. The δ values were cited from Kirkpatrick et al.[7] for anorthite, microcline, muscovite and spodumene; from Kinsey et al.[6] for kaolinite and pyrophyllite; from Lippmaa et al.[8] for sodalite, sillimanite, andalusite and kyanite; from Sanz and Serratosa[5] for biotite; and from Sherriff et al.[29] for beryl (see Table 8.3.3). The δ value for Al^{VI} is -3.2 to 7.5 ppm, while the δ for Al^{IV} is 57 to 72 ppm, indicating that Al^{VI} is less shielded than Al^{IV}. This means that Al-O bond for Al^{VI} is more ionic, parallel to the increase in effective charge on Al calculated

from XPS and Auger energy[30]. Therefore, the Al K-edge shifts to higher energy with increase in the CN of Al, parallel to decrease in the ^{27}Al NMR δ and increase in the effective charge on Al atom.

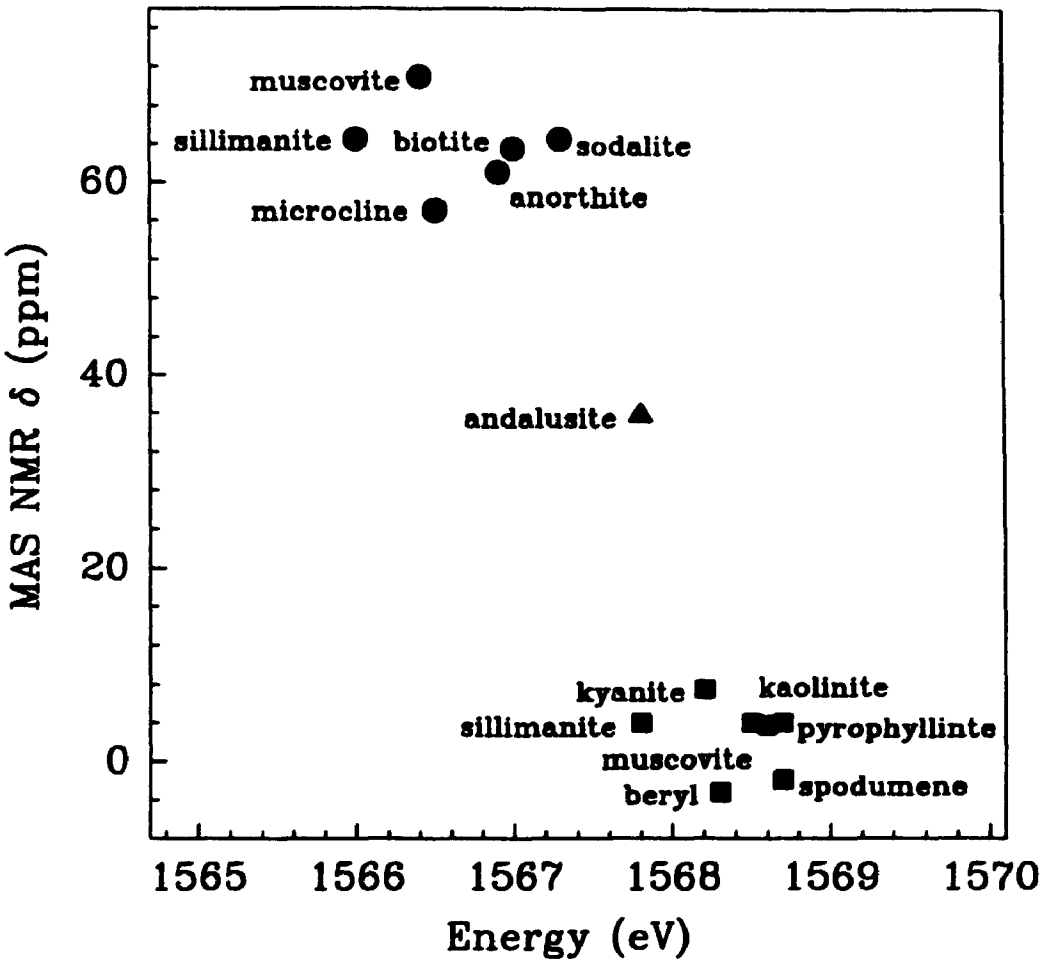

Figure 8.3.5 Correlation of Al K-edges with the MAS NMR chemical shift for Al^{IV}, Al^{V} and Al^{VI} in aluminosilicates.

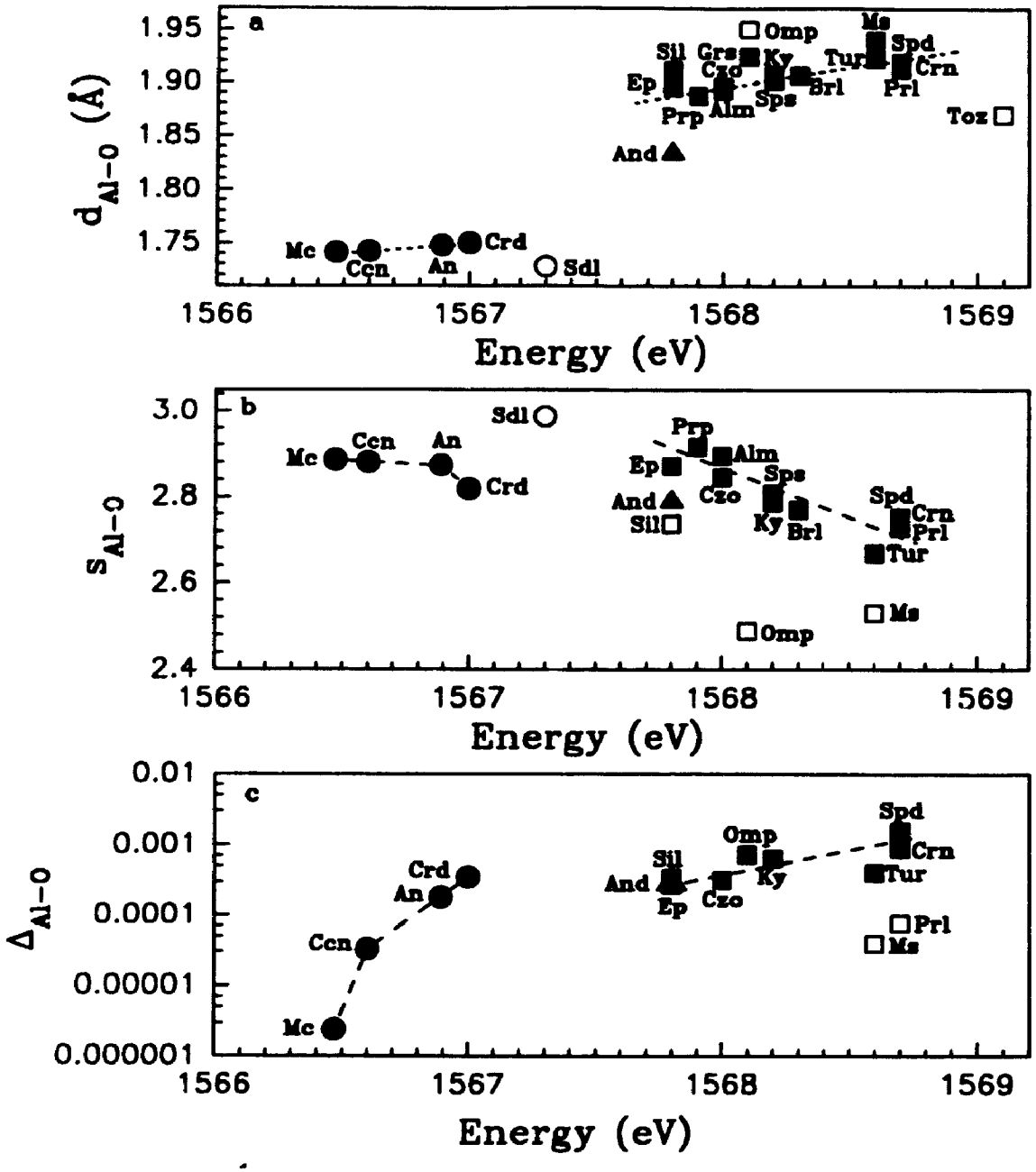

Figure 8.3.6 Correlations of Al K-edge with d_{Al-O} (a), s_{Al-O} (b) and Δ_{Al-O} (c) of aluminosilicates. The keys used in this figure are after Kretz[32].

8.3.4 Shift of Al K-edge versus d_{Al-O}, s_{Al-O}, Δ_{Al-O} and Chemical Effect

Figure 8:3.4 and Table 8.3.3 indicate that even for aluminosilicates in which the coordination number of Al is the same, significant shifts in the Al K-edge occur. For example, the Al K-edge shifts by 1.3 eV for aluminosilicates containing either Al^{IV} or Al^{VI} investigated. Therefore, the shift of the Al K-edge must be related to other factors, as well as the CN of Al.

Figure 8.3.6 shows correlations of Al K-edge with d_{Al-O} (a), s_{Al-O} (b) and Δ_{Si-O} (c). The data for the d_{Al-O} are largely from Smyth and Bish[1] and references therein. In general, the Al K-edge shifts to higher energy with increase in d_{Al-O} and Δ_{Al-O}, and with change in the coordination of Al from 4 to 6, in agreement with the above discussion. There is a slight change in the position of peak C with the s_{Al-O}. On the other hand, as seen in Figure 8.3.6, for microcline, cancrinite, anorthite and cordierite in which Al occupies the 4-coordinated site, the Al K-edge shifts to higher energy markedly with increase in Δ_{Al-O}, and slightly to higher energy with increase in d_{Al-O} and with decrease in s_{Al-O}. These trends are also generally observed for aluminosilicates containing Al^{VI} only, but correlations are generally weaker for obvious reasons. For example, the discrepancy for omphacite ($(Na,Ca)Al[(Al,Si)_2O_6]$) is probably related to the substitution of Fe^{2+} and Fe^{3+} for Al in the $M_1(1)$ and $M_1(H)$ sites that leads to a larger d_{Al-O} [31]. The discrepancies for topaz ($Al_2[SiO_4]F_2$) and sodalite ($Na_8[AlSiO_4]_6Cl_2$) are attributable to more electronegative F and Cl in the first and second neighboring shells of these minerals, respectively. The shifts to lower energy of the Al K-edges for Al^{IV} and Al^{VI} in sillimanite are unexplained.

8.3.5 The Intensity of Al K-edge and the Content of Al

As noted previously, Figures 8.3.1 and 8.3.2 showed that the intensity of peak C increases from the top to the bottom of these two figures. The intensity of this peak correlates well with increasing Al content for both Al^{IV} and Al^{VI} aluminosilicate minerals (see Table 8.3.3). It is possible to make this correlation more quantitative, so that the

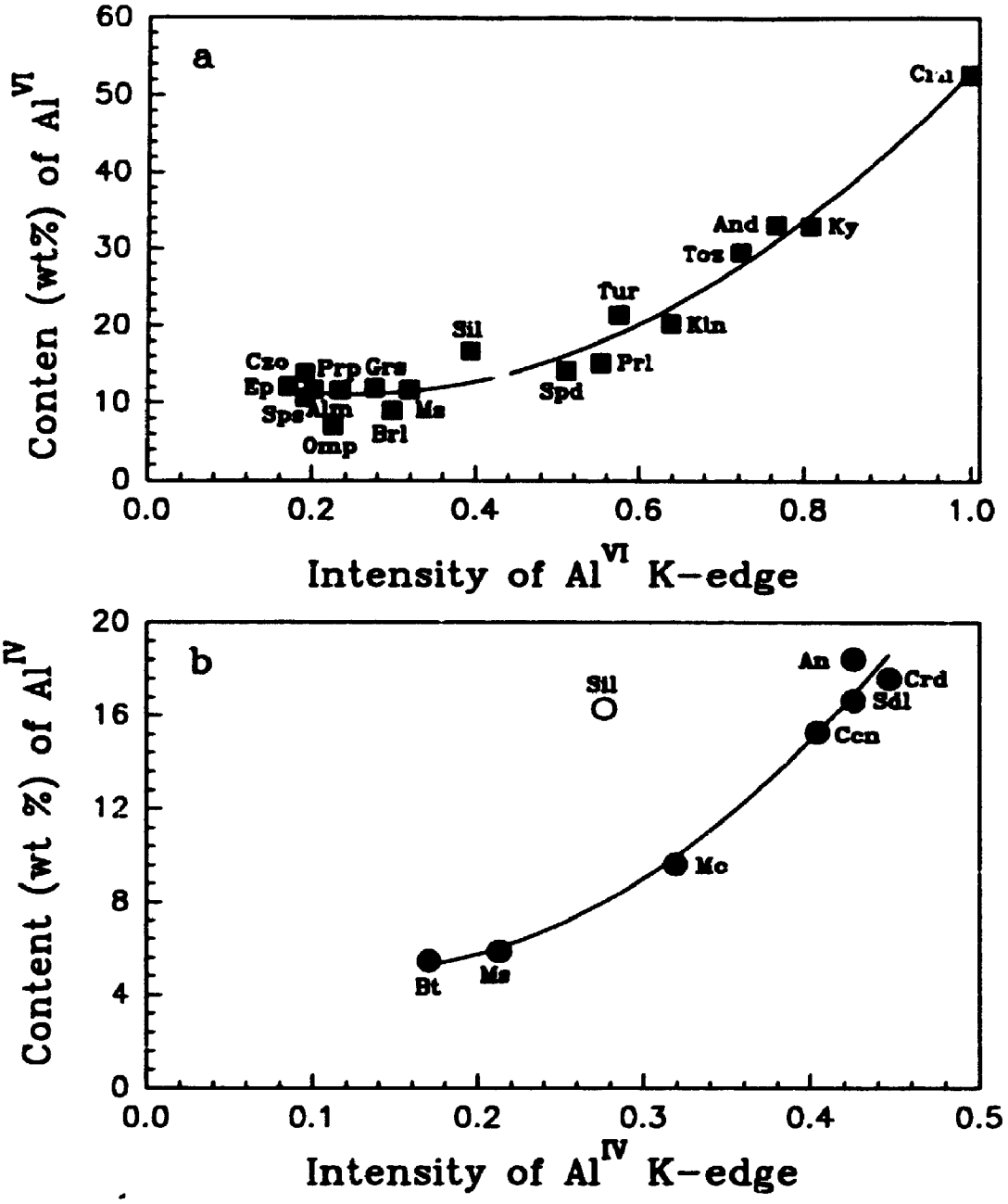

Figure 8.3.7 Correlations of the intensity of Al K-edge with the content (wt%) of Al in octahedra (a) and tetrahedral sites.

intensity of peak C could be used to estimate the Al^{IV} and Al^{VI} content of minerals and glasses semi-quantitatively. Figure 8.3.7 shows the correlations between the intensity of peak C in the Al K-edge XANES spectra of aluminosilicates containing Al^{VI} (a) and Al^{IV} (b) and the content (wt%) of Al in octahedral and tetrahedral sites, respectively. The peak intensity is in arbitrary units and relative to one unit of the height of peak C in the corundum spectrum. For both Al^{VI} and Al^{VI}, the intensity of peak C generally increases with the content of Al in the respective octahedral and tetrahedral sites.

Theoretically, the absorption coefficient, μ, is proportional to the number of absorbing Al atoms, N_{Al}, and the absorption cross section. The TEY should also be proportional to N_{Al}. Although it is not easy to prepare uniform samples for all minerals, considerable care was taken to prepare finely ground and uniform samples, as described in the experimental section. Extrapolating a linear background from the pre-edge before peak C, the height of peak C was measured (the height of peak C in the corundum spectrum is 1) and the correlation of the Al^{IV} and Al^{VI} content in wt% versus the height of peak C are plotted in Figure 8.3.7. For both Al^{IV} and Al^{VI}, the intensity of the Al K-edge generally increase with increase in Al content. However, these two correlations are not linear, and are probably best fitted by an equation of this type $y = ax^2 + bx + c$, where y is the content (wt%) of Al, and x is the normalized intensity. The correlation equations are $y = 74.34x^2 - 37.00x + 15.66$ for Al^{VI}, with correlation coefficient of 0.9827, and $y = 132.40x^2 - 33.39x + 7.13$ for Al^{IV}, with correlation coefficient of 0.9902. Sillimanite is the only discrepant data point: this is most likely attributable to either impurity or alteration of the fibrolite sample presently investigated.

These semi-quantitative correlations between the Al K-edges for Al^{IV} and Al^{VI} and the content (wt%) of Al in respective tetrahedral and octahedral sites are significant, and provide a possible approach for estimating the distribution of Al between 4- and 6-coordinated sites in aluminosilicate minerals and glasses. For example, in muscovite that contains both Al^{IV} and Al^{VI}, the contents of Al in tetrahedral and octahedral sites are 6.0 wt% and 11.4 wt%, respectively, based on the relative intensity of the Al K-edge, and very close to the EMPA results. The ratio of Al^{IV} and Al^{VI} is 0.53, also very close to the ideal value of 0.5. For omphacite, $(Na,Ca)Al[(Al,Si)_2O_6]$, the x-ray crystal structure

refinement could not determine the distribution of Al between the tetrahedral and octahedral sites[31]. The Al K-edge XANES spectrum of omphacite indicates the presence of some Al^{IV} (see Figure 8.3.3). The intensity ratio of Al^{IV} and Al^{VI} is about 1:5, demonstrating that for the omphacite sample presently investigated, about 1.0 wt% Al substitutes for Si. Of course, the occupancy of Al in tetrahedral sites is overestimated, because peak C for Al^{IV} is enhanced due to the overlap of peak A, assigned to $1s \rightarrow 3s$ transition for Al^{VI}.

8.4 Conclusions

The Al K-edge spectra of aluminosilicates containing Al^{IV} and Al^{VI} are qualitatively interpreted by comparison with the Si K-edge spectra of α-quartz and stishovite, and MO calculation for tetrahedral and octahedral clusters, respectively. Some near-edge features are attributed to the MS effect of the more distant shell atoms. The Al K-edge shifts toward higher energy with increase in the CN of Al, from 1566.7 eV for Al^{IV} (averaged for 8 samples) to 1568.3 eV for Al^{VI} (averaged for 17 samples), and 1567.8 eV for Al^{V}, intermediate between Al^{IV} and Al^{VI}. For respective 4- and 6-coordinated aluminosilicates, the Al K-edge shifts to higher energy with increase in $d_{Al\text{-}O}$ and $\Delta_{Al\text{-}O}$, and with decrease in $s_{Al\text{-}O}$. For topaz and sodalite, the Al K-edge shifts to higher energy dramatically, related to the more electronegative F and Cl atoms in the first and second coordination shells around Al, respectively. Also for respective 4- and 6-coordinated Al, the relative intensity of the Al K-edge is semi-quantitatively correlated with the content (wt%) of Al in tetrahedral and octahedral sites, pointing to the potential of Al K-edge spectroscopy as a new technique for determination of the distribution of Al between 4- and 6-coordinated sites. Therefore, Al K-edge XANES spectroscopy provides important information on coordination geometries and local structures of Al, comparable to that from ^{27}Al MAS NMR spectroscopy. Al K-edge spectroscopy is even superior to ^{27}Al MAS NMR spectroscopy, because features in the latter are often poorly resolved, because of quadruple broadening.

8.5 References

1. J.R. Smyth and D.L. Bish, *Crystal structures and cation sites of the rock-forming minerals*. Allen & Unwin, Boston, 1988.
2. K. Suzuki, H. Noro, A. Miyake, Y. Yamamoto and K. Yokoi, *Prelim. Rep. Afr. Stud.*, 135 (1983).
3. R.H. West and J.E. Castle, *Surf. Interface Anal.* **4**, 68 (1982).
4. C.D. Wagner, D.E. Passoja, H.F. Hillery, T.G. Kinisky, H.A. Six, W.T. Jansen and J.A. Taylor, *J. Vac. Sci. Tech.* **21**, 933 (1983).
5. J. Sanz and J.M. Serratosa, *J. Am. Chem. Soc.* **106**, 4790 (1984).
6. R.A. Kinsey, R.J. Kirkpatrick, J. Hower, K.A. Smith and E. Olefield, *Am. Mineral.* **70**, 537 (1985).
7. R.J. Kirkpatrick, R.A. Kinsey, K.A. Smith, D.M. Henderson and E. Oldfield, *Am. Mineral.* **70**, 106 (1985).
8. E. Lippmaa, A. Samoson and M. Magi, *J. Am. Chem. Soc.* **108**, 1730 (1986).
9. R.J. Kirkpatrick R.J., In *Spectroscopic Methods in Mineralogy and Geochemistry* (Ed. by Hawthorne F.C.). Mineralogical Society of America, 1988, pp. 341.
10. I.A. Brytov, K.I. Konashenok and Yu.N. Romashchenko, *Geochem. Int.* **16**, 142 (1979).
11. G.E. Brown, F.D. Dikman and G.A. Waychunas, *SSRL Report* No. 1983/01, Proposal No. 741 (1983).
12. D.A. McKeown, G.A. Waychunas and G.E. Brown, *J. Non-Cryst. Solids* **74**, 349 (1985).
13. D.A. McKeown, *Phys. Chem. Minerals* **16**, 678 (1989).
14. J.K. Winter and S. Ghose, *Am. Mineral.* **64**, 573 (1979).
15. M.C. Cruickshank, L.S. Dent Glasser, S.A.I. Barri and I.J.F. Poplett, *J. Chem. Soc., Chem. Commun.*, 23 (1986).
16. L.B. Alemany and G.W. Kirker, *J. Am. Chem. Soc.* **108**, 6158 (1986).
17. S.F. Dec, J.J. Fitzgerald, J.S. Frye, M.P. Shatlock and G.E. Maciel, *J. Mag.*

Res. **93**, 403 (1991).

18. H. Friedrich, B. Sonntag, P. Rabe, W. Butscher and W.H.E. Schwarz, *Chem. Phys. Leit.* **64**, 360 (1979).
19. T.A. Ferrett, M.N. Piancastelli, D.W. Lindle, P.A. Heimann and D.A. Shirley, *Phys. Rev.* **A38**, 701 (1988).
20. D.G.J. Sutherland, M. Kasrai, G.M. Bancroft, Z.F. Liu and K.H. Tan, *Phys. Rev.* **48**, 14989 (1993).
21. P.L. Hansen, R. Brydson and D.M. McComb, *Microsc. Microanal. Microstr.* **3** 213 (1992).
22. J.A. Tossell, *J. Am. Chem. Soc.* **97**, 4840 (1975).
23. J.L. Dehmer, *J. Chem. Phys.* **56**, 4496 (1972).
24. T.A. Ferrett, D.W. Lindle, P.A. Heimann, H.G. Kerkhoff, U.E. Becker and D.A. Shirley, *Phys. Rev.* **A34**, 1916 (1986).
25. J.A. Tossell, *J. Phys. Chem. Solids* **36**, 1273 (1975).
26. D.E. Kerrick, *The Al_2SiO_5 polymorphs.* Mineralogical Society of America, 1990.
27. I.D. Brown, In *Structure and Bonding in Crystals* **II** (Ed. by O'Keeffe M. and Navrotsky A.). 1985, pp. 1.
28. M.E. Fleet, *Mineral Mag.* **40**, 531 (1976).
29. B.L. Sherriff, H.G. Grundy, J.S. Hartman, F.C. Hawthorne and P. Cerny, *Can. Mineral.* **29**, 271 (1991).
30. V.I. Nefedov, V.G. Yarzhemsky, A.V. Chuvaev and E.M. Trishkina, *J. Electron Spectrosc. Relat. Phenom.* **46**, 381 (1988).
31. J.R. Clark J.J. Papike, *Am. Mineral.* **53**, 840 (1968).
32. R. Kretz, *Am. Mineral.* **68**, 277 (1983).

CHAPTER 9

Local Structures of Silicon and Phosphorus in Glasses

9.1 Introduction

Crystalline silicon diphosphate (c-SiP_2O_7) is one of several compounds in which silicon has been shown to be six-coordinated with oxygen at atmospheric pressure, and has three different modifications: a cubic Pa3 phase and monoclinic $P2_1/c$ and $P2_1/n$ phases[1]. The infrared (IR) and Raman spectra of c-SiP_2O_7 were measured and interpreted by normal coordinate analyses[2]. The ^{29}Si magic-angle-spinning (MAS) NMR spectra of c-SiP_2O_7 have also been reported[3-7]. The higher energy shift of the Si Kα x-ray emission line in c-SiP_2O_7, compared to that for 4-coordinated Si, was calculated by MO method[8].

Phosphorus-containing silicate glasses and melts have been the subject of intensive study for their high-technology and geochemical applications. High-silica glasses containing P_2O_5 have been recognized as the most promising fiber material for optical communication systems[9]. Also, P_2O_5 has a profound effect on the evolution of magma systems[10-17]. For example, the addition of P_2O_5 to magma can lead to liquid immiscibility in magma systems[18,19], significantly depresses the liquidus temperature of magmatic liquids[20,21], strongly affects the partitioning of elements between crystals and liquid, and between liquid and liquid[22,23], and reduces the viscosity of heplogranitic liquids[24].

Glasses containing phosphorus have been studied by IR spectroscopy for SiO_2-P_2O_5 compositions[25], Raman spectroscopy for SiO_2-P_2O_5 [26], Na_2O-SiO_2-P_2O_5 [27-30], Na_2O-Al_2O_3-SiO_2-P_2O_5 [27,31], SiO_2-B_2O_3-P_2O_5 [32], K_2O-Al_2O_3-SiO_2-P_2O_5 [33], and $CaMgSi_2O_6$-$CaAl_2Si_2O_8$ [27] and MAS NMR spectroscopy for SiO_2-P_2O_5 [5,34], $CaSiO_3$-$CaAl_2Si_2O_8$ [35,36], Na_2O-Al_2O_3-SiO_2-P_2O_5 [37,38], SiO_2-B_2O_3-P_2O_5 [32], and K_2O-Al_2O_3-SiO_2-P_2O_5 [33]. However, the local structure and solution mechanism of P_2O_5 in glasses and melts are controversial.

In this chapter, high-resolution Si and P K- and L-edge XANES spectra of c-

SiP_2O_7, and SiO_2-P_2O_5 and Na_2O-SiO_2-P_2O_5 glasses are presented using synchrotron radiation, and qualitatively interpreted within an MO framework. The coordination and local structure of Si and P in these glass systems are studied, in order to help resolve the structural roles of P and Na in these systems.

9.2 Experimental

The c-SiP_2O_7 sample was synthesized by reacting high purity amorphous SiO_2 and excess H_3PO_4 in an open silica-glass tube at initially 230 °C and finally about 950 °C, and identified as the monoclinic $P2_1/n$ phase by powder x-ray diffraction (PXRD). Glasses with compositions in the systems SiO_2-P_2O_5 and Na_2O SiO_2-P_2O_5 were prepared from c-SiP_2O_7, and a mixture of a-SiO_2, and H_3PO_4 and Na_2CO_3, respectively, melted at 1250-1550 °C in a small Pt dish and quenched in air and water. Unfortunately, some of P_2O_5 and Na_2O were lost from the glass preparations during melting. Glasses were examined by optical microscopy and PXRD, and glass compositions were determined by electron microprobe analysis (EMPA) (see Table 9.3.2). Si and P K-edge XANES spectra were measured using the DCM with InSb (111) monochromators. The Si and P L-edge spectra were collected using the Grasshopper beamline. Both K- and L-edge spectra were recorded by Total Electron Yield (TEY).

9.3 Results and Discussion

9.3.1 Interpretation of Spectra

Figure 9.3.1 shows the Si K- and L-edge XANES spectra of c-SiP_2O_7 and a-SiO_2-P_2O_5 with 75 mol% SiO_2 and 25 mol% P_2O_5. The Si L-edge spectra are shown by the solid lines, and the Si K-edge spectra by the solid lines with dots. The Si K- and L-edge spectra are aligned on a common scale by the Si $K\alpha_1$ x-ray emission energy at 1740.0 eV. The peak positions and assignments are given in Table 9.3.1, in which ΔE for the Si K-edge spectra is the difference between each peak and the Si $K\alpha_1$ x-ray emission

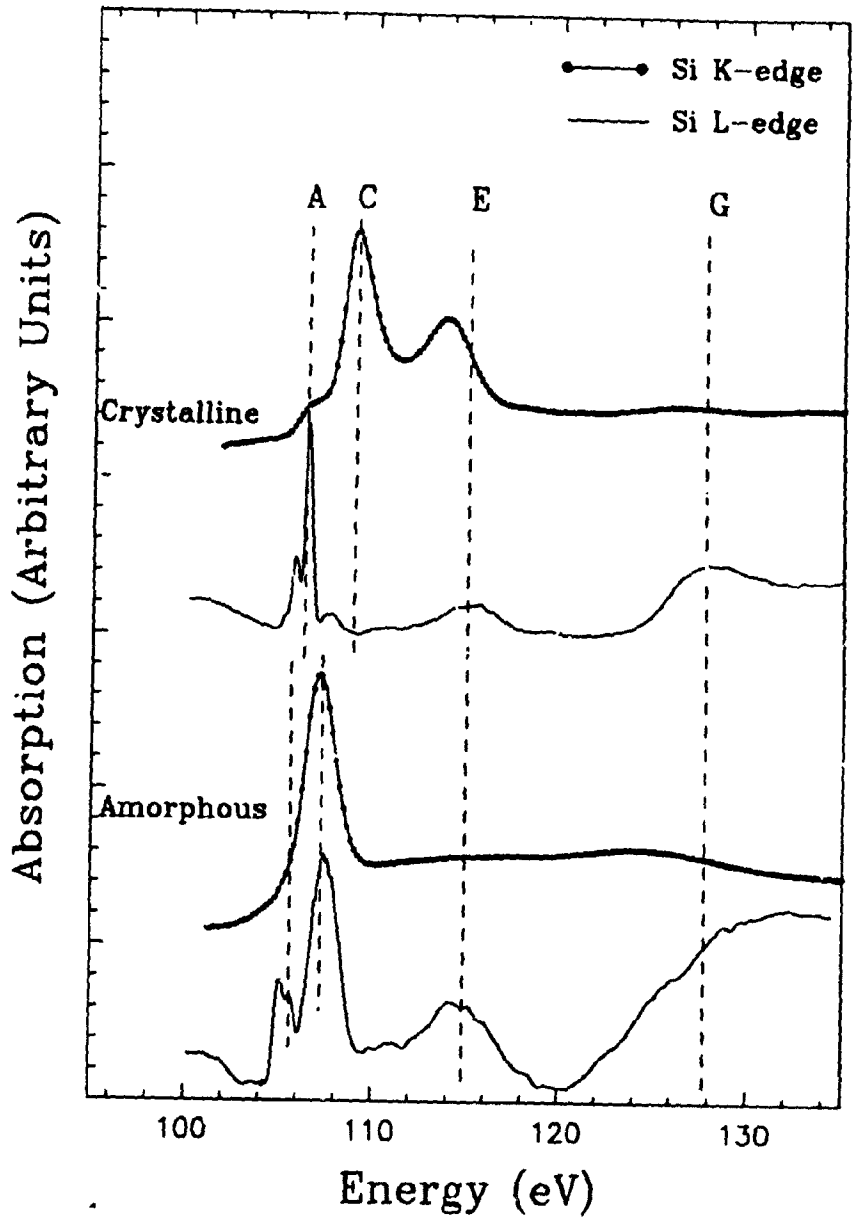

Figure 9.3.1 Si K- and L-edge XANES spectra of c-SiP_2O_7 and SiO_2-P_2O_5 glass.

Table 9.3.1 Assignments for Si K- and L-edge spectra of c-SiP_2O_7 and a-SiP_2O_7

	K-edge (±0.2 eV)			L-edge (±0.2 eV)	
	Peaks (eV)*	ΔE (eV)	Assignments	Peaks (eV)*	Assignments
			c-SiP_2O_7		
A	1846.2	106.2	Si 1s → a_{1g} (3s-like)	106.0	Si $2p_{3/2}$ → a_{1g} (3s-like)
				106.6	Si $2p_{1/2}$ → a_{1g} (3s-like)
C	1848.9	108.9	Si 1s → t_{1u} (3p-like)	107.8	Si 2p → t_{1u} (3p-like)
E	1853.7	113.7	Si 1s → t_{2g} (3d-like)	115.2	Si 2p → t_{2g} (3d-like)
G	1866.3	126.3	Si 1s → e_g (3d-like)	128.2	Si 2p → e_g (3d-like)
			a-SiO_2-P_2O_5		
A	1844.6	104.6	Si 1s → a_1 (3s-like)	105.2	Si $2p_{3/2}$ → a_1 (3s-like)
				105.8	Si $2p_{1/2}$ → a_1 (3s-like)
C	1846.9	106.9	Si 1s → t_2 (3p-like)	107.6	Si 2p → t_2 (3p-like)
E	1854.3	114.3	Si 1s → e (3d-like)	114.9	Si 2p → e (3d-like)
G	1863.7	123.7	Si 1s → t_2 (3d-like)	129.8	Si 2p → t_2 (3d-like)

* The reading error of the edge peak is ±0.1 eV.

energy at 1740.0 eV. Si K- and L-edge XANES spectra of c-SiP_2O_7 are essentially similar to those for stishovite (see Chapter 6), characterizing 6-coordinated Si. The linewidth of peak A in the Si L-edge spectrum is about 0.38 eV, which is the best resolution ever reported for solid state samples, to my knowledge. Peak a in the Si L-edge spectrum is assigned to the dipole-allowed transition of Si 2p electrons to 3s-like a_{1g} states[39,40]. It is split by about 0.65 eV, due to the spin-orbit interaction of Si 2p orbitals. Peak C is attributable to the transition of Si 2p electrons to 3p-like t_{1u} states; it is weak, because this transition is dipole-forbidden in an octahedral field. Peaks E and G are assigned to the transitions of Si 2p electrons to empty Si 3d-like t_{2g} and e_g states, respectively (so-called "shape resonances"[41]).

Peaks A, C, E and G in the Si K-edge spectrum align reasonably well with the

corresponding peaks in the Si L-edge spectrum. Peak A is assigned to the transition of Si 1s electrons to 3s-like a_{1g} state; it is weak, since this transition is forbidden for octahedral symmetry. Peak C is attributed to the dipole-allowed transition of Si 1s electrons to 3p-like t_{1u} states. Peaks E and G are assigned to transitions of Si 1s electrons to t_{2g} and e_g states, respectively, or called symmetry-forbidden "shape resonances"[42,43]. Peak E becomes strong, and peak D, which was assigned to multiple scattering (MS) in the stishovite K-edge spectrum, disappears, probably indicating that peak E also includes significant contribution from the MS of the more distant atom shells. Other peaks, attributed to the MS effect in the stishovite spectrum are weak in the c-SiP_2O_7 spectra.

Just as the Si K- and L-edge spectra of c-SiP_2O_7 are very similar to those of stishovite, the Si K- and L-edge spectra of a-SiO_2-P_2O_5 are very similar to the corresponding spectra of both α-quartz and a-SiO_2. In particular, peak C in the Si K-edge spectra shifts by 2.0 eV, from 1848.9 eV for c-SiP_2O_7 to 1846.9 eV for a-SiO_2-P_2O_5. This is very convincing evidence for 4-coordinated Si in a-SiO_2-P_2O_5, in good agreement with MAS NMR results from Weeding et al.[5].

The Si K- and L-edge XANES spectra of a-SiO_2-P_2O_5 can be readily assigned according to the MO scheme for a tetrahedral crystal field. In the Si L-edge spectrum, peak A is assigned to dipole-allowed transition of Si 2p electrons to 3s-like a_1 states[40,44], and its splitting of about 0.61 eV is apparently due to the spin-orbit interaction of Si 2p orbitals. Peak C is attributed to the transition of Si 2p electrons to 3p-like t_2 states; the p → p transition is dipole-allowed in the tetrahedral field[45], and consequently, peak C is very strong. Peaks E and G are attributed to the transition of Si 2p electrons to empty Si 3d-like e and t_2 states (the "shape resonances"). Peaks in the Si K-edge spectra of a-SiO_2-P_2O_5 are assigned as follows: peak A, due to dipole-forbidden Si 1s → 3s-like a_1 states, is too weak to be observed; peak C is assigned to the dipole allowed transition S 1s → 3p-like t_2 states; and peaks E and G to transitions of Si 1s → 3d-like e and t_2, respectively (so-called symmetry-forbidden "shape resonances"[42,43]). Also, the features due to the MS effect from the more distant atom shells in the α-quartz spectra essentially disappear in the glass spectra, no doubt related to the loss of long-range order in the vitreous sample.

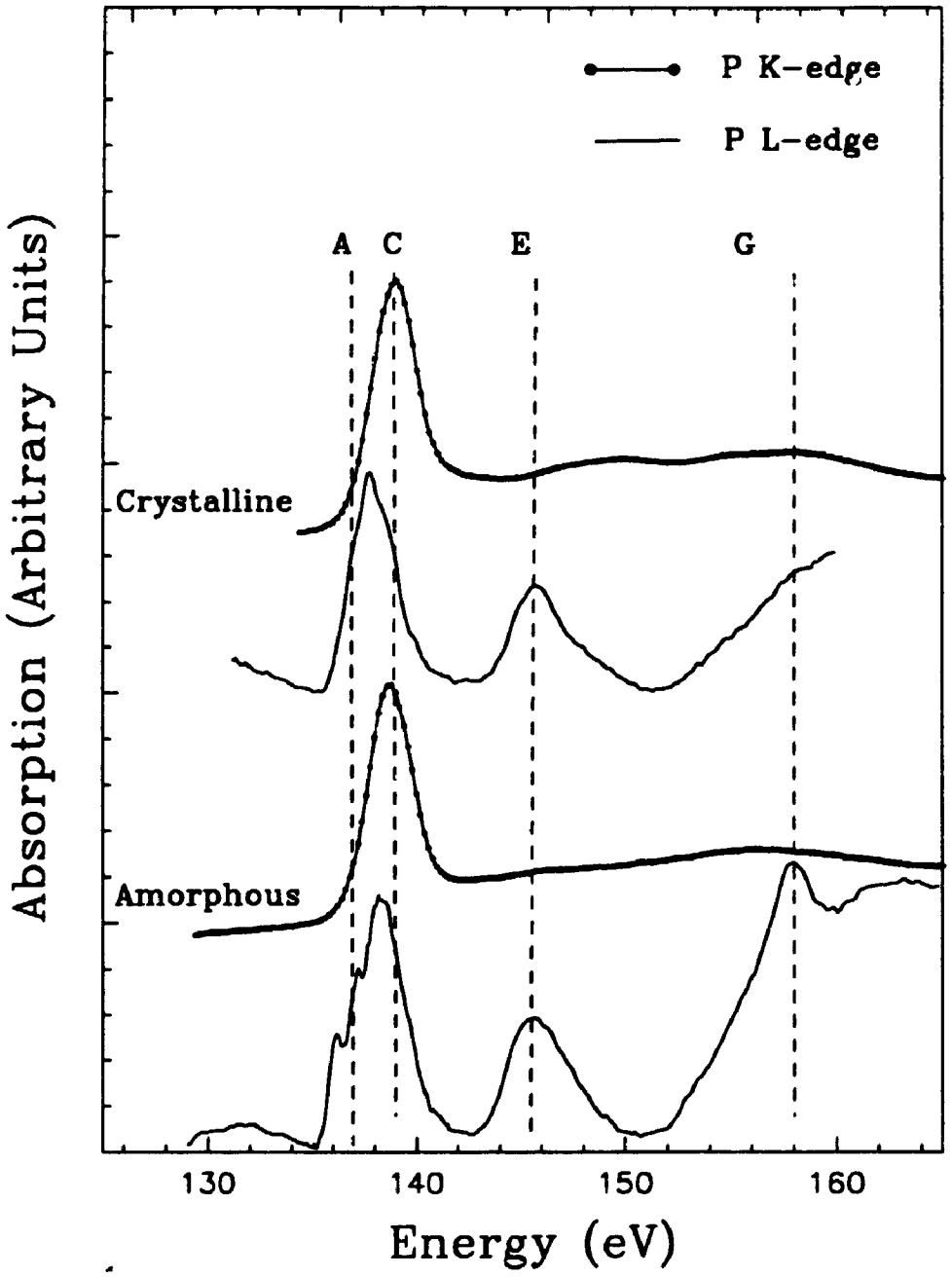

Figure 9.3.2 P K- and L-edge XANES spectra of c-SiP_2O_7 and SiO_2-P_2O_5 glass.

Figure 9.3.2 shows the P K- and L-edge XANES spectra of c-SiP_2O_7 and a-SiO_2-P_2O_5. The P L-edge spectra are shown as solid lines, and the P K-edge spectra as solid line and dot curves. The P K- and L-edge spectra are aligned on a common scale by the P $K\alpha_1$ x-ray emission energy at 2013.7 eV, and the peaks are assigned as for Si K- and L-edge spectra of a-SiO_2-P_2O_5. P K- and L-edge spectra indicate that the local structure of P in both c-SiP_2O_7 and a-SiO_2-P_2O_5 is tetrahedral. However, compared to the Si L-edge spectrum, peaks A and C are not resolved in the P L-edge spectrum for c-SiP_2O_7, and peak G is very broad; while for a-SiO_2-P_2O_5, peaks A and C, (and even the spin-orbit splitting of peak A) are very well resolved and peak G is much sharper.

9.3.2 Structure of SiO_2-P_2O_5 Glasses

Features of the Si K- (a) and L-edge (b) spectra of SiO_2-P_2O_5 glasses are shown in Figure 9.3.3. The positions of the Si K- and L-edges, and P L-edge and the contents of SiO_2 and P_2O_5 are summarized in Table 9.3.2. The Si K- and L-edges for all the SiO_2-P_2O_5 glasses show little shift with increase in the content of P_2O_5 up to 30 mol%, indicating no change in the coordination of Si. Moreover, the silicate units appear to remain fully polymerized. Ryerson and Hess[12] have shown that in SiO_2-P_2O_5 glasses, PO_4^{3-} and SiO_4^{4-} groups are copolymerized, so that addition of P_2O_5 into silicate glasses breaks Si-O-Si linkages and disassembles the silicate network. On the other hand, Si K-edge XANES spectra of silicate minerals showed that Si K-edge shifts to lower energy with decrease in the degree of polymerization of SiO_4^{4-} groups (see Chapter 8), and the absence of a similar shift in the present glass spectra with addition of P_2O_5 possibly points to another compensating factor causing an increase in net charge on Si atoms and shifting the Si K-edge to higher energy. For example, the substitution of Al for Si in aluminosilicates shifts the Si K-edge to lower energy (see Chapter 8), and correspondingly, the interconnection of PO_4^{3-} and SiO_4^{4-} groups should shift the Si K-edge to higher energy. Hence, there is inferential evidence in the XANES spectra for the interconnection of SiO_4^{4-} and PO_4^{3-} groups. This is in a good agreement with the IR spectra[25] and Raman[26,27] spectra of SiO_2-P_2O_5 glasses, which indicate that the relative

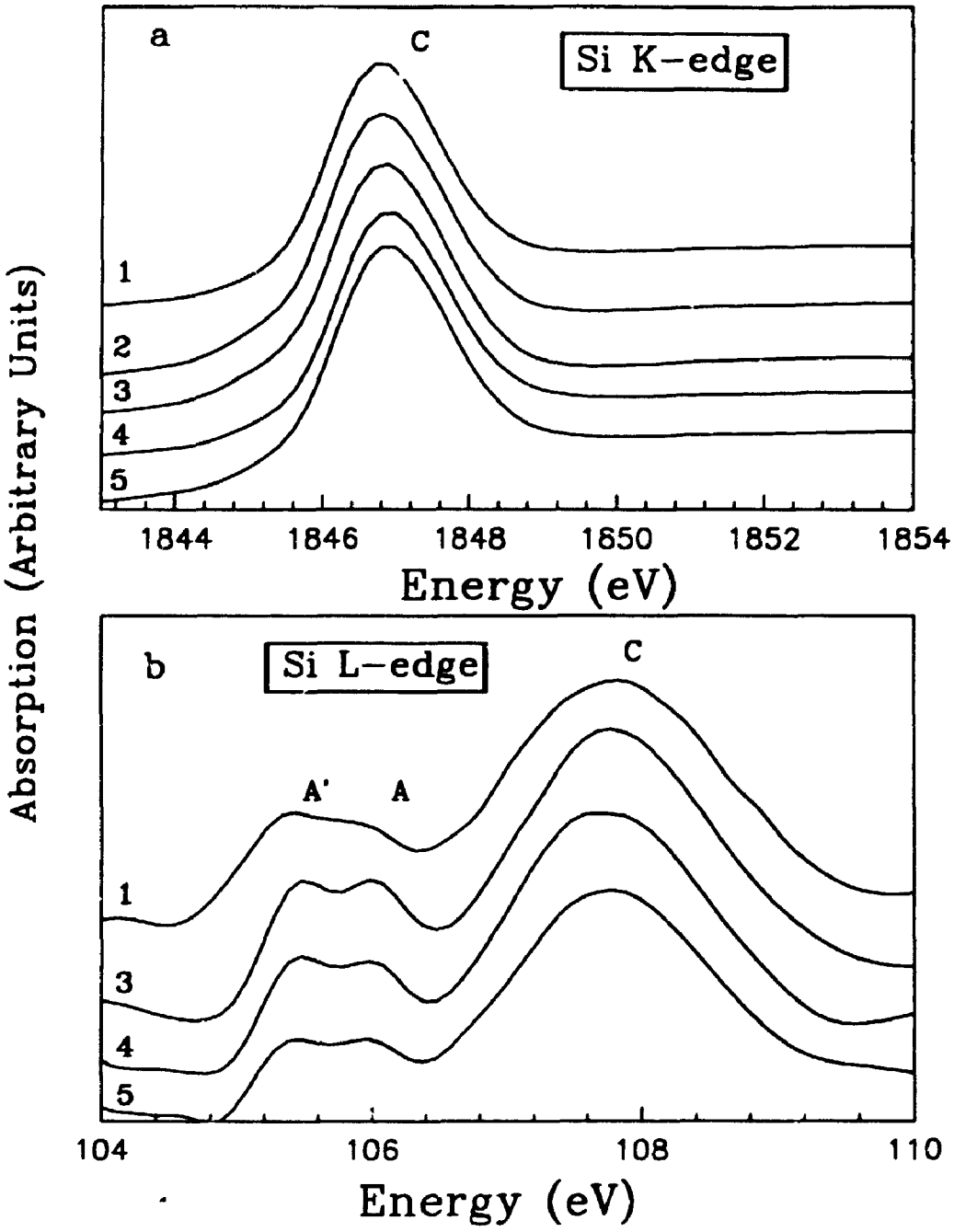

Figure 9.3.3 The near-edge features in Si K- (a) and L-edge (b) XANES spectra of SiO_2-P_2O_5 glasses.

Table 9.3.2 Si K- and L-edges, P L-edge and chemical composition of glasses

	XANES spectra (±0.1 eV)					Composition (mol%)		
	Si K-edge	Si L-edge		P L-edge				
	C	A'	A	A'	A	C	SiO_2	P_2O_5	Na_2O
c-SiP_2O_7								
	1848.9	105.93	106.59	135.9	136.9	138.4	50.0	50.0	
SiO_2-P_2O_5 glasses								
1	1846.8	105.2	105.8	135.9	137.0	138.0	87.2	12.8	
2	1846.9			135.9	136.9	138.3	79.1	20.9	
3	1846.9	105.3	105.9	136.0	136.9	137.9	76.3	24.8	
4	1847.0	105.3	105.9	135.9	136.9	138.2	72.7	27.3	
5	1847.0	105.3	105.9	135.9	136.9	137.8	72.4	27.7	
Na_2O-SiO_2-P_2O_5 glasses									
6	1846.6	105.0		134.9	135.9	137.9	69.9	3.2	26.9
7	1946.8						80.0	1.6	18.4
8	1847.0	105.2	105.8	135.8	136.8	138.0	74.5	20.7	4.8
9	1847.1	105.2	105.8	135.7	136.7	137.9	60.8	29.0	10.2

intensity of the 1145 cm^{-1} band that results from P-O-Si bond stretching increases with increasing concentration of P.

The P K-edge XANES spectra of a selection of model compounds reveal little information on the local environment of P, except for the oxidation state of P, but the P L-edge spectra are very sensitive to the local structure of P [46]. Figure 9.3.4 shows the P L-edge XANES spectra of SiO_2-P_2O_5 glasses, and peak positions are summarized in Table 9.3.1, and the chemical compositions of these glasses are given in Table 9.3.2. The P L-edge spectra of these glasses are generally similar, even though features in the P L-edge spectrum of sample 1 are poorly resolved. Peaks A' and A become well resolved for samples 2 and 5, and their relative intensity increases, but the peak positions remain fairly constant. Based on the study of model phosphate compounds, Yin et al.[46] have concluded that peaks A and A' in the P L-edge spectra shift to higher energy from orthophosphate, pyrophosphate to metaphosphates, and the relative intensity of peaks A' and A increases markedly with the length of the metaphosphate chains, especially from PO_4^{3-} to $P_{15}O_{46}^{17-}$. The P L-edge spectra of these glasses are very similar to those of the two model metaphosphates $Na_7P_5O_{16}$ and $Na_{17}P_{15}O_{46}$ [46], and their detailed features are intermediate between these two model compounds. Therefore, phosphate species in glasses are dominantly metaphosphates, and the metaphosphates polymerize to form chains of different length, depending on the content of P_2O_5. Using a similar analysis, the metaphosphates in the present glasses are most likely intermediate between $P_5O_{16}^{7-}$ and $P_{10}O_{31}^{12-}$.

The Si K- and L-edge and P L-edge XANES spectra provide important information on the local structure of SiO_2-P_2O_5 glasses, which permits us to discuss the solution mechanism of P_2O_5 in silicate melts and glasses and the structure of the glasses. The ionic radii for P^{5+} (0.35 Å) and Si^{4+} (0.42 Å) are similar. Both P and Si are coordinated with four oxygen atoms to form tetrahedral phosphate and silicate anions (PO_4^{3-} and SiO_4^{4-}), which can polymerize to form chain, layer and framework structures. The essential difference between PO_4^{3-} and SiO_4^{4-} is that SiO_4^{4-} has four single Si-O bonds, while PO_4^{3-} has only three single P-O bonds and one double P=O bond, so that SiO_4^{4-} is capable of polymerizing to form four bridging-oxygen bonds, but PO_4^{3-} can form

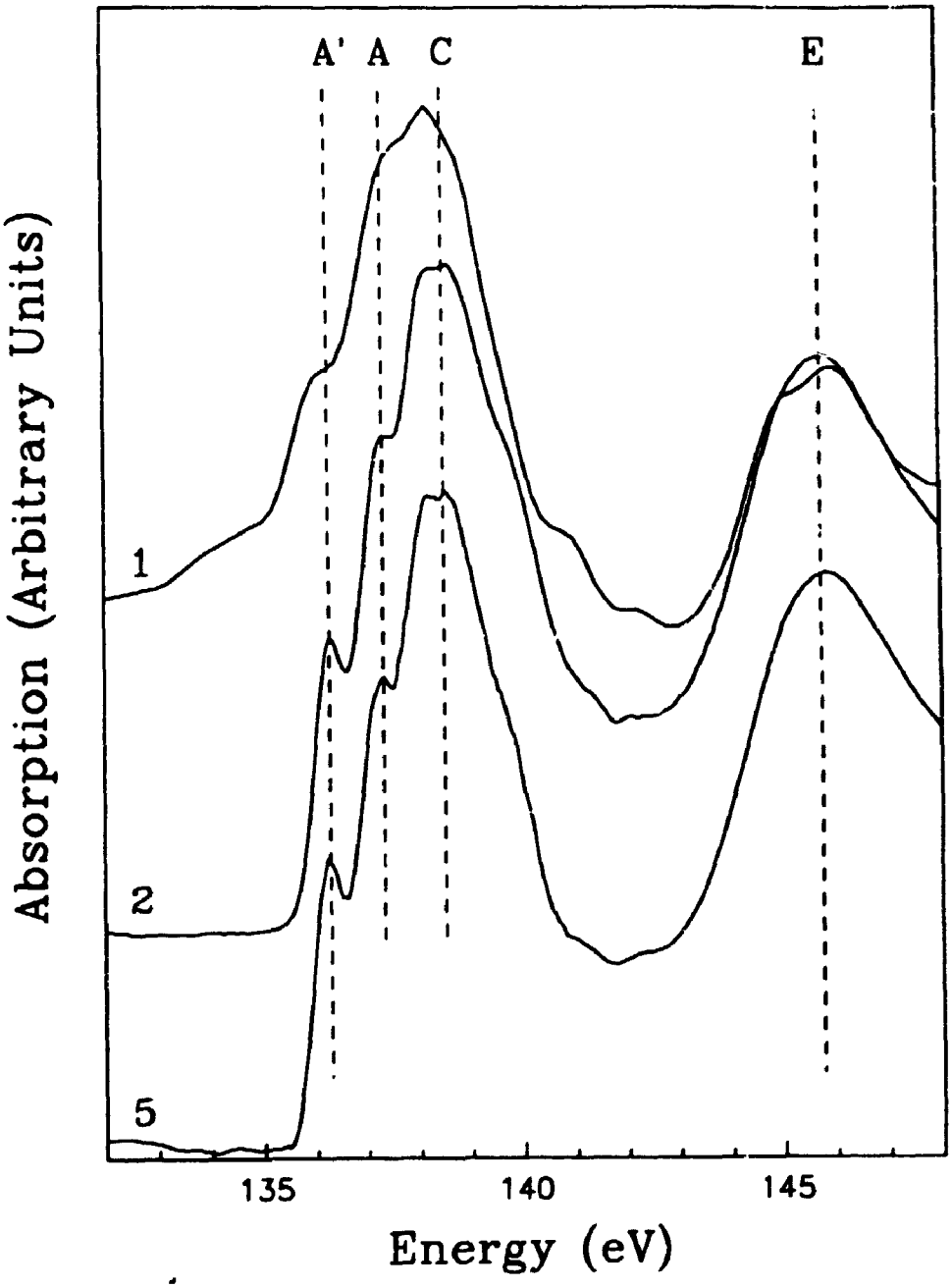

Figure 9.3.4 P L-edge spectra of SiO_2-P_2O_5 glasses, the compositions of these samples (1, 2 and 5) are given in Table 9.3.2.

only three bridging-oxygen bonds. The SiO_4^{4-} groups form a silicate network in SiO_2-P_2O_5 glasses. The PO_4^{3-} and SiO_4^{4-} groups may be capable of copolymerization, and P^{5+} may substitute for Si^{4+} in the silicate glasses and melts, particularly, when the content of P_2O_5 is low (e.g. $\leq$5 mol%). However, the P=O double bond in PO_4^{3-} greatly limits the capability of PO_4^{3-} in the cross-linkage to form three-dimensional structures, and thus SiO_4^{4-} and PO_4^{3-} can not form complete solutions in the glasses. When the content of P_2O_5 increases, the PO_4^{3-} groups tend to polymerize to form chain metaphosphates. The metaphosphate chains with different lengths are connected with the silicate network. Therefore, PO_4^{3-} actually forms chains of different length in SiO_2-P_2O_5 glasses and melts, but the metaphosphate chains are randomly distributed in the silicate network.

This structural model of SiO_2-P_2O_5 glasses is essentially confirmed by Si K- and L-edge and P L-edge XANES spectra, as well as previous IR, Raman and MAS NMR spectra. Also, this model is consistent with the fact that the high P_2O_5 content leads to the formation of liquid immiscibility, reduces the activity of SiO_2 and depresses the liquidus temperature of magmatic liquids in the SiO_2-P_2O_5 system.

9.3.3 Structure of Na_2O-SiO_2-P_2O_5 Glasses

The near-edge features of the Si K- and L-edges of Na_2O-SiO_2-P_2O_5 glasses are shown in Figure 9.3.5. Both Si K- and L-edges shift markedly to higher energy from sample #6 to #9 by about 0.5 eV. The variation of the Si K-edge position with the contents of SiO_2, P_2O_5 and Na_2O are shown in the inset of Figure 9.3.5a. The positions of the Si K- and L-edges, and P L-edge and the contents of SiO_2, P_2O_5 and Na_2O in the Na_2O-SiO_2-P_2O_5 glasses are also given in Table 9.3.2. Both Si K- and L-edges generally shift to higher energy with increase in the content of P_2O_5 and decrease in the content of Na_2O.

Figure 9.3.6 shows the P L-edge spectra of several Na_2O-SiO_2-P_2O_5 glasses, in sequence of increase in the content of P_2O_5. The P L-edge spectrum of sample #6 with just 3.2 mol% P_2O_5 is distinct from the other two glasses in that peaks A' and A are shifted to lower energy by about 0.8 eV, and their relative intensity decreases: peak A

in particular is not well resolved. These features are very similar to those in the P L-edge of the model compound $Na_4P_2O_7$ [47], indicating that the P species in sample #6 is dominantly pyphosphate. The P L-edge spectra of samples #8 and 9 are similar to those of samples #2 and #5 of SiO_2-P_2O_5 glasses, and of the model metaphosphates $Na_7P_5O_{16}$ and $Na_{17}P_{15}O_{46}$ [46], and demonstrate that the P is present dominantly as metaphosphates. Compared with the spectra of the two model compounds, the P L-edge spectra of these glasses are most consistent with metaphosphate species between $P_5O_{16}^{7-}$ and $P_{10}O_{31}^{12}$.

The higher energy shifts of both Si K- and L-edges are not clearly understood, but they are not correlated with the coordination change of Si. Figure 9.3.7 shows the near-edge features of Si K-edge spectra of c-SiP_2O_7 that contains six-fold coordinated Si (Si^{VI}) and SiO_2-P_2O_5 glass containing four-fold coordinated Si (Si^{IV}), and the composite near-edge spectra simulated with different proportions of Si^{VI} and Si^{IV}. First, if the coordination of a small amount of Si changes from 4 to 6, a shoulder at about 1849.0 eV in the Si K-edge spectrum should be observed at the position of the arrow, and the edge peak C should broaden. These features are observed in the Si K-edge spectra of wadeite-structure $K_2Si^{VI}Si_3^{IV}O_9$, in which 25% of Si is Si^{VI} [47], and in the high pressure $K_2Si_4O_9$, $Na_2Si_4O_9$ and $Na_2Si_2O_5$ glasses in which the coordination change of Si is pressure-induced[48]. However, no shoulder is observed at about 1849.0 eV in the Si K-edge spectra of all these Na_2O-SiO_2-P_2O_5 glasses, and the edge peak C tends to become narrower with the shift of Si K-edge toward higher energy. Also, as shown in Figure 9.3.7, the edge peak C for Si^{IV} shows little shift to higher energy with increase in the proportion of Si^{VI}, and only the relative intensities of the edge peaks for Si^{IV} and Si^{VI} change, which is not in agreement with our observations for these glasses.

The structure of Na_2O-SiO_2 glass is fairly well known[49]; the addition of Na_2O, as a network modifier, depolymerizes the SiO_2 melt and glass. This depolymerization mechanism may be represented as $Na_2O + SiO_2 \rightarrow Na_2SiO_3$; or equivalently, Si-O-Si + Na-O-Na → 2Si-O-Na. Therefore, the Si K-edge is expected to shift to lower energy for Na_2O-SiO_2 glass, in good agreement with the observation of Si K-edge at 1846.6 eV for sample #6, which contains 26.9 mol% Na_2O and only 3.2 mol% P_2O_5. Addition of P_2O_5 into the Na_2O-SiO_2-P_2O_5 glasses has two consequences. First, the behavior of P_2O_5 in

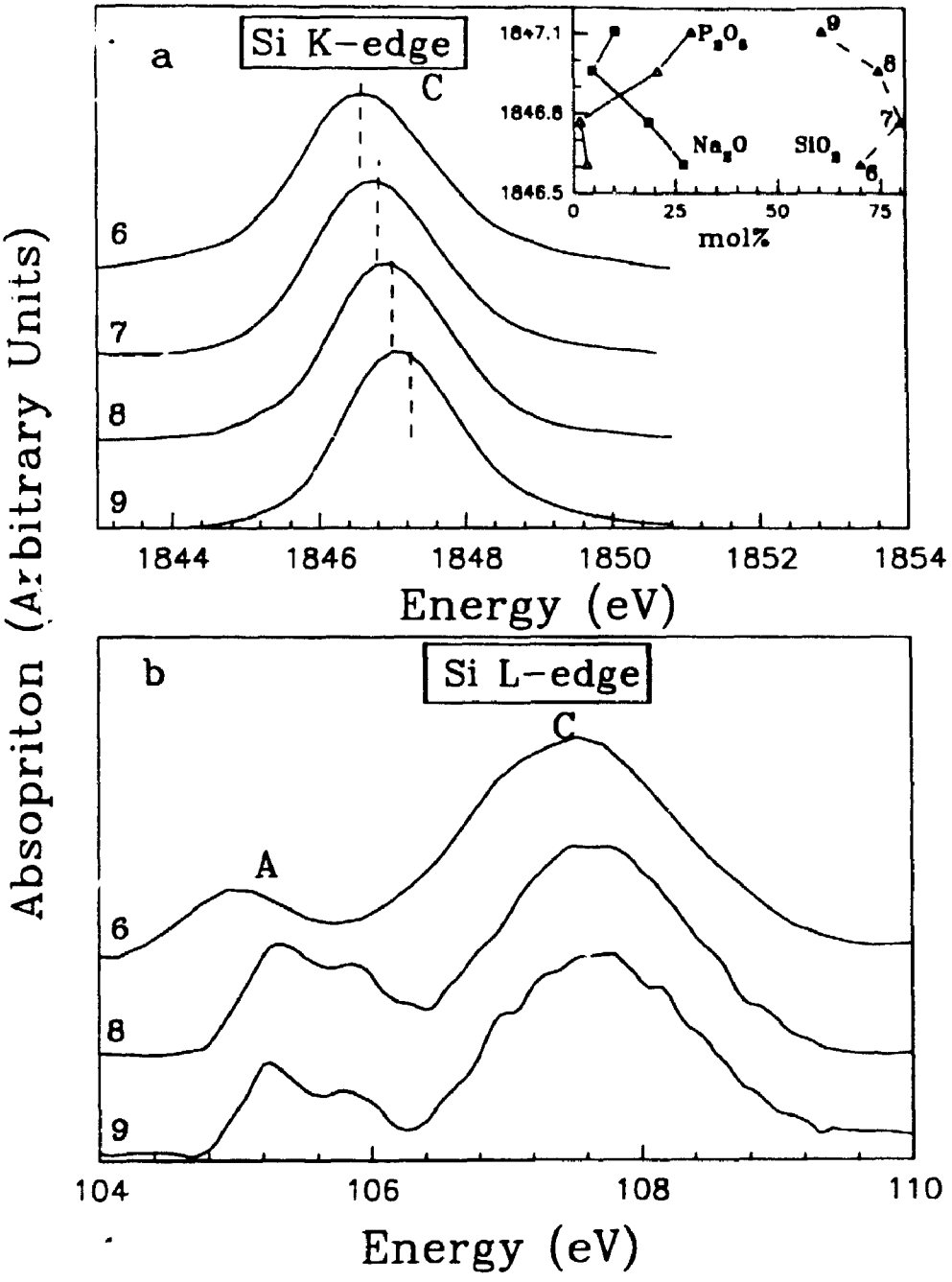

Figure 9.3.5 The near-edge features in Si K- (a) and L-edge (b) XANES spectra of Na_2O-SiO_2-P_2O_5 glasses. Variations of the Si K-edge position with the content of Na_2O, SiO_2 and P_2O_5 is shown in the inset of Figure 9.3.5a.

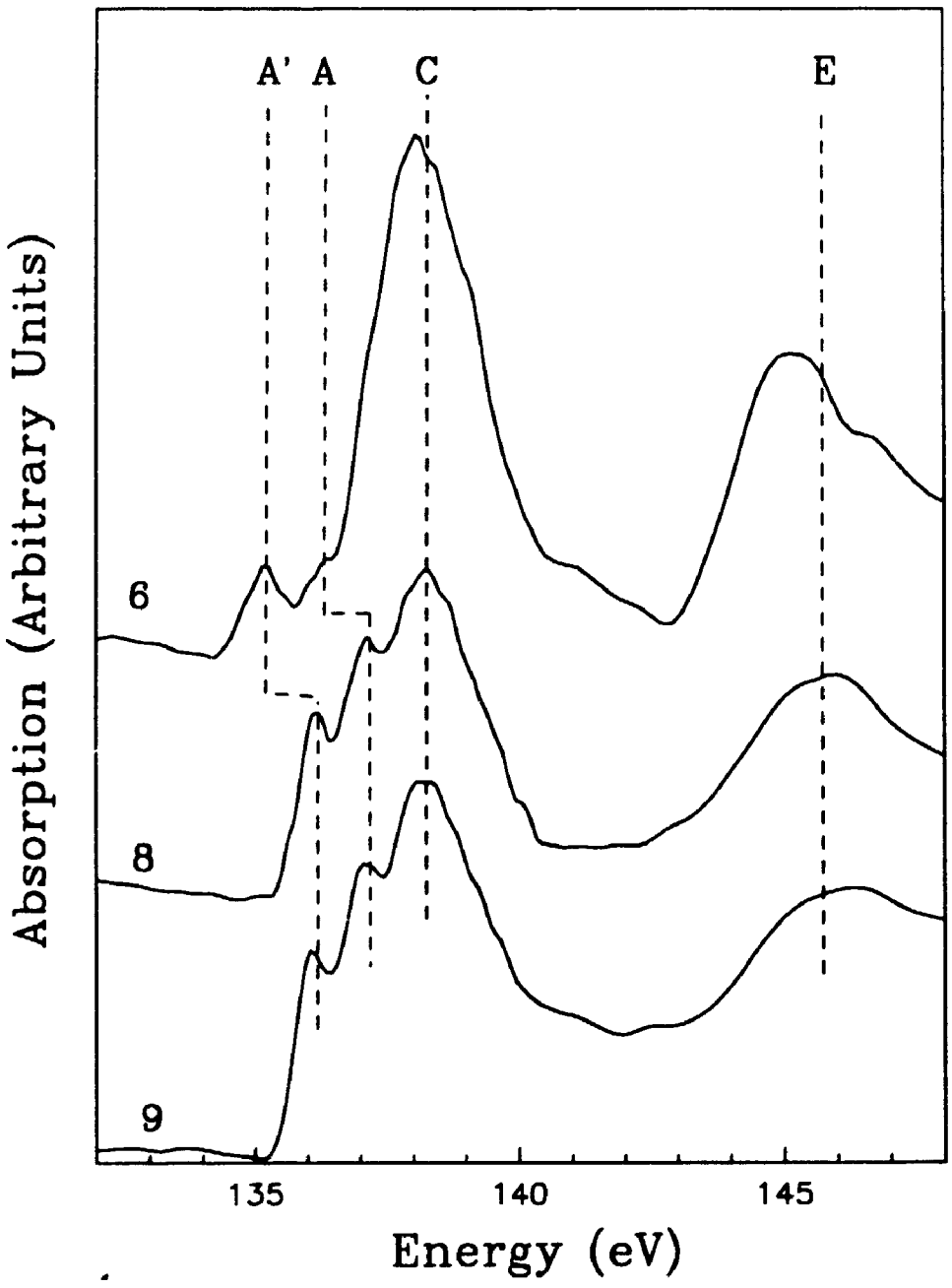

Figure 9.3.6 P L-edge spectra of Na_2O-SiO_2-P_2O_5 glasses.

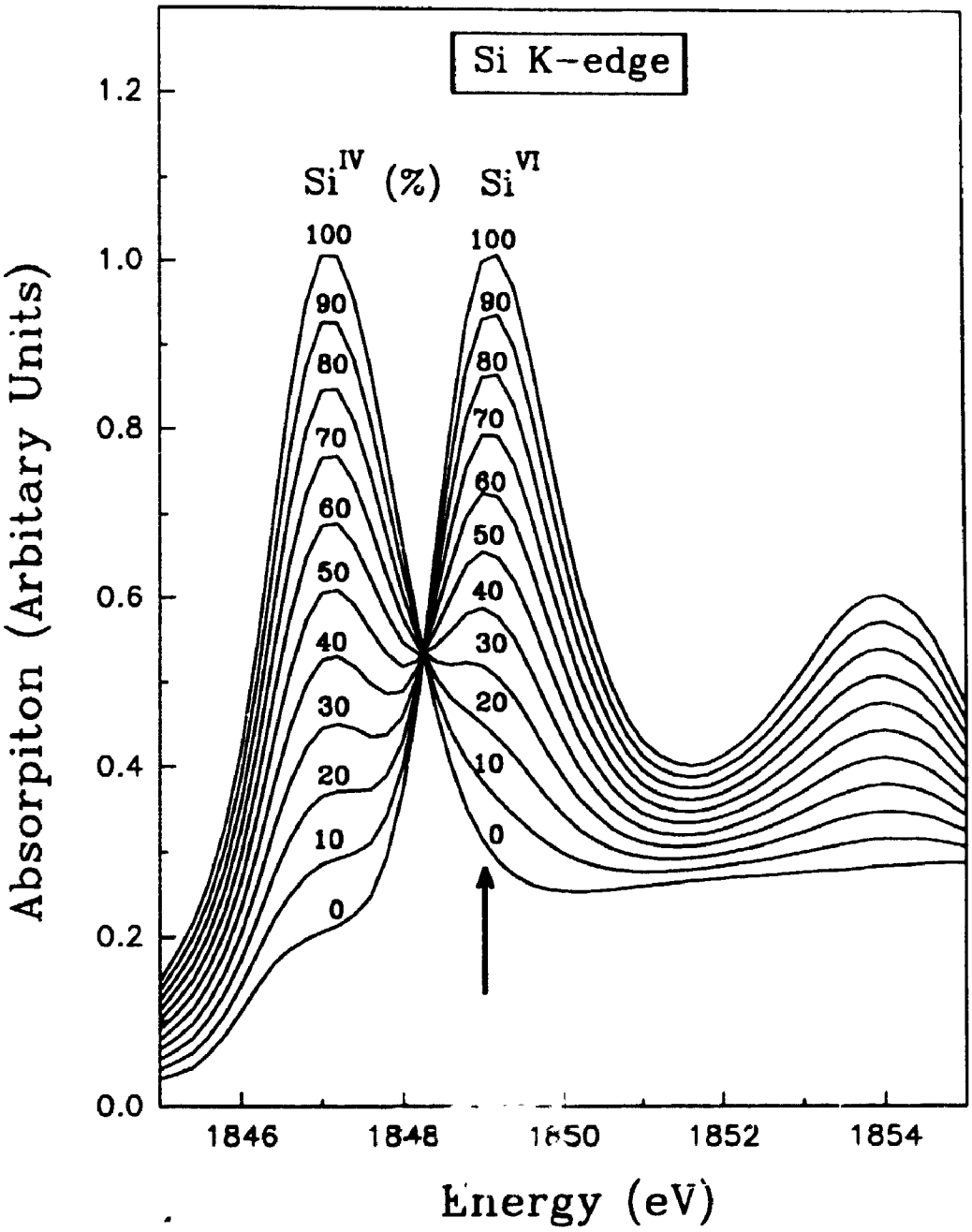

Figure 9.3.7 Composite Si K-edge spectra of Si^{VI} and Si^{IV}, simulated with different proportions of c-SiP_2O_7 containing Si^{VI} and SiO_2-P_2O_5 glass containing Si^{IV}.

Na_2O-SiO_2-P_2O_5 glass differs from that in SiO_2-P_2O_5 glass, and the addition of P_2O_5 polymerizes the Na_2O-SiO_2 glass, and shifts the Si K-edge to 1846.8 eV, as observed for fully polymerized SiO_2 glass. Second, the further shift of the Si K-edge to higher energy must be related to interconnection between SiO_4^{4-} and PO_4^{3-} groups.

Addition of P_2O_5 to Na_2O-SiO_2-P_2O_5 melts and glasses strips Na_2O from the silicate network and polymerizes the glass system. The general solution mechanism of P_2O_5 is:

$(n+2)\ Na_2SiO_3 + n\ P_2O_5 \rightarrow 2\ Na_{n+2}P_nO_{3n+1} + (n+2)\ SiO_2$ ($n = 1, 2, 3, 4.....$). where n increases, and the P speciation changes from isolated phosphate to pyrophosphate and to metaphosphates of different chain length with increase in the content of P_2O_5. Phase separation occurs in this glass system. The sodium phosphate phases separate from the sodium silicate network when the content of Na_2O is greater than that of P_2O_5, or from the silica-phosphate network when the content of Na_2O is lower than that of P_2O_5.

Evidence that the addition of P_2O_5 in the Na_2O-SiO_2-P_2O_5 glasses strips Na_2O from the silicate network has been reported previously from other techniques of investigation. First, enthalpy of formation data[50] indicate that the phosphate anion has a greater affinity for metal cations than the corresponding silicate anion. Second, although Na is distributed between silicate and phosphate anions, it is more likely to be affiliated with the latter[12]. Third, MAS NMR spectroscopy shows that addition of P_2O_5 to sodium silicates causes repolymerization of the silicate network and the formation of sodium phosphate units[38]. Fourth, Raman spectra of Na_2O-SiO_2-P_2O_5 glasses pointed to a similar conclusion[28,29] and even demonstrated that the devitrification products of xNa_2O-$(50-x/2)SiO_2$-$(50-x/2)P_2O_5$ glasses also contain $3SiO_2 \cdot 2P_2O_5$ and $Na_4P_2O_7$ crystals[30]. However, the Si K- and L-edge and P L-edge XANES spectra more accurately determine the P species and better correlate the P speciation with the content of P_2O_5.

9.4 Conclusions

Si K- and L-edge and P L-edge XANES spectra of SiO_2-P_2O_5 and Na_2O-SiO_2-P_2O_5

glasses provide important information on the coordination and local structures of Si and P. Both Si and P are four-fold coordinated with oxygen atoms. However, the SiO_4^{4-} group has four single bonds and can polymerize to form network structures, while the PO_4^{3-} cluster has only three single bonds and one double bond which limits the degree of polymerization of the PO_4^{3-} groups. The P species formed in these glasses are isolated phosphate, pyrophosphate and metaphosphates, depending on the content of P_2O_5; the metaphosphate are most likely species intermediate between $P_5O_{16}^{7-}$ and $P_{10}O_{31}^{12-}$. In SiO_2-P_2O_5 glasses, the P species are connected with the silicate network, but randomly distributed. However, PO_4^{3-} and SiO_4^{4-} do not form complete solutions, and the PO_4^{3-} groups tend to polymerize into metaphosphate chains of different length with increase in the content of P_2O_5. In Na_2O-SiO_2-P_2O_5 glasses, the addition of P_2O_5 strips Na_2O from the silicate network to form separate sodium phosphate, pyrophosphate and metaphosphate entities, also depending on the content of P_2O_5. The degree of polymerization of the SiO_4^{4-} groups depends on the relative content of P_2O_5 and Na_2O. When the content of Na_2O is higher than P_2O_5, the SiO_4^{4-} clusters are not fully polymerized and form sodium silicate entities; and conversely when the content of Na_2O is lower than P_2O_5, the SiO_4^{4-} groups are fully polymerized and SiO_2-P_2O_5 entities form.

XANES spectroscopy, like Raman and MAS NMR spectroscopy, can provide structural information for glasses, based on comparison with model compounds. However, XANES spectroscopy has several advantages and can provide new structural information, and information compatible with that from Raman and MAS NMR spectroscopy. There are difficulties in the assignments of vibrational bands in the Raman spectra of glasses, because of band overlap, for example, bands for SiO_4^{4-} and PO_4^{3-} groups always overlap. One advantage of XANES spectroscopy is that it is element-specific, so that separate Si and P K- and L-edge XANES spectra may be collected. ^{29}Si and ^{31}P MAS NMR spectroscopy is indeed a very powerful technique for studying the local structure of Si and P in glasses and melts. However, ^{31}P MAS NMR spectroscopy does not provide detailed information about the metaphosphates formed in glass systems. In contrast, XANES spectroscopy provides information on not only the structure and bonding in the first coordination shell, but also the extended structure, via the multiple

scattering effect. Thus, P L-edge XANES spectra are very sensitive to the local structure and the chain length of metaphosphate, and provide evidence for the speciation and intermediate-range order of phosphate species in glasses and melts.

9.5 References

1. F. Liebau, *Structural Chemistry of Silicates: Structure, Bonding and Classification*, Springer-Verlag, Berlin, 1985.
2. I.N. Chakraborty, R.A. Condrate, J.R. Ferraro and C.F. Chenuit, *J. Solid State Chem.* **68**, 94 (1987).
3. J.M. Thomas, J.M. Gonzalez-Calbert, C.A. Fyfe, G.C. Gobbi and M. Nicol, *Geophys. Res. lett.* **10**, 91 (1983).
4. I.L. Mudrakovskii, V.M. Mastikhin, V.P. Smachkova and N.S. Kotsarenko, *Chem. Phys. Lett.* **120**, 424 (1985).
5. T.L. Weeding, B.H.W.S. de Jong, W.S. Veeman and B.G. Aitken, *Nature* **318**, 352 (1985).
6. A.R. Grimmer, F. Von Lampe and M. Mägi, *Chem. Phys. Lett.* **132**, 549 (1986).
7. J.F. Stebbins and M. Kanzaki, *Science* **251**, 294 (1991).
8. T. Okura, H. Inoue, T. Kanazawa, S. Endo, S. Fukushima and Y. Gohshi. *Spectrochim. Acta* **45B**, 711(1990).
9. T. Miya, Y. Terunuma, T. Hosaka and T. Miyashita, *Electron Lett.* **14**, 534 (1978).
10. I. Kushiro, *Am. J. Sci.* **275**, 411 (1975).
11. E. Roedder, *Geochim. Cosmochim. Acta* **42**, 1746 (1978).
12. F.J. Ryerson and P.C. Hess, *Geochim. Cosmochim. Acta* **44**, 611 (1980).
13. F.J. Ryerson, *Geochim. Cosmochim. Acta* **49**, 637 (1985).
14. D. London, *Geochim. Cosmochim. Acta* **51**, 403 (1987).
15. D. London, P. Černý, J.L. Loomis and J.J. Pan, *Can. Mineral.* **28**, 771 (1990).
16. D. London, *Am. Mineral.* **77**, 126 (1992).

17. D. London, G.B. Morgan VI, H.A. Babb and J.L. Loomis, *Contrib. Mineral. Petrol.* **113**, 450 (1993).

18. W. Visser and A.F.K. Van de Groos, *Am. J. Sci.* **279**, 970 (1979).

19. W. Visser and A.F.K. Van de Groos, *Am. J. Sci.* **279**, 1160 (1979).

20. T.Y. Tien and F.A. Hummel, *J. Am. Ceram. Soc.* **45**, 422 (1962).

21. P.J. Willie and O.F. Tuttle, *Am. J. Sci.* **262**, 930 (1964).

22. E.B. Watson, *Contrib. Mineral. Petrol.* **56**, 119 (1976).

23. E.B. Watson, *Geochim. Cosmochim. Acta* **41**, 1363 (1977).

24. D.B. Dingwell, R. Knoche and S.L. Webb, *Eur. J. Mineral.* **5**, 133 (1993).

25. J. Wong and C.A. Angell, *Glass Structure by Spectroscopy*. Marcel Dekker Inc., New York, 1976.

26. N. Shibata, M. Horigudhi and T. Edahiro, *J. Non-Cryst. Solids* **45**, 115 (1981).

27. B.O. Mysen, F.J. Ryerson and D. Virgo, *Am. Mineral.* **66**, 106 (1981).

28. C. Nelson and D.R. Tallant, *Phys. Chem. Glasses* **25**, 31 (1984).

29. C. Nelson and D.R. Tallant, *Phys. Chem. Glasses* **26**, 119 (1985).

30. I.N. Chakraborty and R.A. Condrate, *Phys. Chem. Glasses* **26**, 68 (1985).

31. D.R. Tallant and C. Nelson, *Phys. Chem. Glasses* **27**, 75 (1986).

32. J.E. Dickinson Jr. and B.H.W.S. de Jongs, *J. Non-Cryst. Solids* **102**, 196 (1988).

33. H. Gan and P.C. Hess, *Am. Mineral.* **77**, 495 (1992).

34. T. Sekiya, N. Mochida, A. Ohtsuka and K. Uchida, *Nippon Seramikkusu Kyokai Gakujutsu Ronbunshi* **96**, 571 (1988).

35. W.H. Yang and R.J. Kirkpatrick, *Eos* **66**, 95 (1985).

36. W.H. Yang, R.J. Kirkpatrick and G. Turner, *J. Am. Ceram. Soc.* **69**, C222 (1986).

37. R. Dupree, D. Holland and M.G. Mortuza, *Nature* **328**, 416 (1987).

38. R Dupree, D. Holland, M.G. Mortuza, J.A., Collins and M.W.G. Lockyer, *J. Non-Cryst. Solids* **112**, 111 (1989).

39. J.A. Tossell, *J. Am. Chem. Soc.* **97**, 4840 (1975).

40. Y. Iguchi, *Science of Light* **26**, 161 (1977).

41. Z.F. Liu, J.N. Cutler, G.M. Bancroft, K.H. Tan, R.G. Cavell and J.S. Tse, *Chem. Phys.* **168**, 133 (1992).

42. J.L. Dermer, *J. Chem. Phys.* **56**, 4496 (1972).

43. T.A. Ferrett, D.W. Lindle, P.A. Heimann, H.G. Kerkhoff, U.E. Becker and D.A. Shirley, *Phys. Rev.* **A34**, 1916 (1986).

44. J.A. Tossell, *J. Phys. Chem. Solids* **36**, 1273 (1975).

45. P.L. Hansen, R. Brydson and D.W. McComb, *Microsc. Microanal. Microstruc.* **3**, 213 (1992).

46. Z.F. Yin, M. Kasrai, G.M. Bancroft, K.H. Tan and X.H. Feng, To be submitted to *Phys. Rev.* **B** (1994).

47. D.K. Swanson and C.T. Prewitt, *Am. Mineral.* **68**, 581 (1983).

48. D. Li, M.E. Fleet, G.M. Bancroft, M. Kasrai and G.S. Henderson, *Eos* **75**, 370 (1994).

49. B.O. Mysen, *Structure and properties of silicate melts*. Elsevier, Amsterdam, (1988), pp. 354.

50. F.D. Richardson, *Physical Chemistry of melts in metallurgy*. Academic Press, New York, 1974.